FOSSIL

DOE/PC/80752-T15(Vol.1)
(DE91000990)

DETAILED MODEL FOR PRACTICAL PULVERIZED COAL FURNACES AND GASIFIERS

Volume 1

General Technical Report

Final Report

By
Philip J. Smith
L. Douglas Smoot

August 1989

Work Performed Under Contract No. FG22-85PC80752

For
U.S. Department of Energy
Pittsburgh Energy Technology Center
Pittsburgh, Pennsylvania

By
Brigham Young University
Provo, Utah

DISCLAIMER

This report has been reproduced directly from the best available copy.

Available to DOE and DOE contractors from the Office of Scientific and Technical Information, P.O. Box 62, Oak Ridge, TN 37831; prices available from (615)576-8401, FTS 626-8401.

Available to the public from the National Technical Information Service, U. S. Department of Commerce, 5285 Port Royal Rd., Springfield, VA 22161.

Price: Printed Copy A16
Microfiche A01

Printed in the United States of America, Office of Scientific and Technical Information, Oak Ridge , Tennessee

DOE/PC/80752--T15-Vol.1

DE91 000990

FINAL REPORT

DETAILED MODEL FOR PRACTICAL PULVERIZED COAL FURNACES AND GASIFIERS
Volume I
General Technical Report

August, 1989

Contract No.: DE-FG22-85PC80752

Prepared By:

Brigham Young University
Department of Chemical Engineering
350 CB
Provo, UT 84602

Principal Investigators
Philip J. Smith and L. Douglas Smoot

Notice

Abstract

This volume, which summarizes all of the technical work accomplished under a consortium agreement during the study period from May 1, 1985 through August 31, 1989, is one of a three-volume final report. Consortium members were Babcock and Wilcox, Combustion Engineering, Consolidation Coal Co., Electric Power Research Institute, Empire State Electric Energy Research Corp., Foster Wheeler Development Co., Tennessee Valley Authority, Pittsburgh Energy Technology Center (DOE) and Utah Power and Light Co. The objective of this study was to improve and extend a generalized combustion model for application to large-scale, three-dimensional furnaces. Tasks included 3-D model development, model evaluation, and submodel development. Key accomplishments of the 52-month study include:

1. Development of a new, three-dimensional code for application to turbulent, non-reacting, gas-particle systems and combusting gaseous systems.

2. Important numerical advances included identification of a preferred solution algorithm with weighting factors, a new differencing formulation for irregular grids, a substantial decrease in computation time through vectorization, and use of multigrid methods (in two dimensions).

3. Key combustion model parameters (particularly those for coal devolatilization and char oxidation) were identified.

4. 3-D model predictions were successfully compared with limiting analytical solutions.

5. A summary of three-dimensional data for model evaluation was completed (summarized herein and published in detail in Volume III).

6. 3-D model predictions were compared with measured, non-reacting flow data from the data book for pilot-scale tangential and wall-fired furnaces. General elements of agreement are apparent while effects of turbulence model options are illustrated.

7. Development of discrete ordinates radiation codes for 2-D and 3-D systems were completed and demonstrated.

8. A new submodel for particle dispersion in a turbulent gas was completed and evaluated. The basic model shows significant promise of more efficient and realistic treatment of particle dispersion.

9. The NO_x formation model for coal systems was improved and applied to 30 new coal combustion and gasification cases with positive results.

10. Improved methods for organizing and interpreting coal devolatilization and char oxidation data were developed while work on carbon monoxide formation and nonlinear turbulence modeling provided new insights for turbulent combusting systems.

11. A first version of a new fouling and slagging submodel was developed and evaluated to describe coal mineral transformation and deposition.

Fourteen consortium study reports were prepared and distributed and three annual review meetings were hosted. Plans were made for a 3-D code workshop. In addition, several papers were presented and published during this study period based on this consortium-sponsored research.

This pioneering consortium study provided a foundation for the organization and funding of a new Advanced Combustion Engineering Research Center (ACERC), which started one year after the consortium funding and is now in its fourth year. ACERC has provided an organizational structure, resources, and facilities for continuation of vital research in this general area of fossil fuels combustion, including comprehensive modeling. Plans include expansion of the 3-D code developed under this study to even larger-scale coal combustion systems. Most of the consortium members have continuing membership in ACERC.

Acknowledgements

This report summarizes work conducted at Brigham Young University on a research study on detailed modeling for practical pulverized coal furnaces and gasifiers. The study was funded by a consortium of nine separate industrial and governmental sponsors. Each organization, their representative, and their address is given in Table 0.1. The support of these institutions is greatly appreciated.

Foreword

Work under this study has been reported in three volumes. This document, Volume 1, provides a summary of all technical work accomplished under this study. Volume II is the User's Manual for PCGC-3. Volume III is the data book for three-dimensional model evaluation. This report summarizes technical accomplishments made during the entire four-year reporting period for a study conducted for a consortium of governmental and industrial organizations. This period extended from May 1, 1985 to August 31, 1989. Work was accomplished under the direction of Dr. L. Douglas Smoot, project director, and Dr. Philip J. Smith, principal investigator. Dr. Scott Brewster, Dr. A.S. Jamaluddin, and Dr. Subrata Sen have been senior investigators during this study. Subcontract work at Los Alamos National Laboratory was performed under the direction of Dr. Scott C. Hill.

Graduate students who have contributed to the progress reported herein include Larry Baxter, Joseph Smith, Paul Gillis, Knute Christensen, Robert Colson, Steven Phillips, Paul Davies, Mary Rasband, and Richard Boardman. Michael R. King, Cindy A. Stevens, Ruth Dodson and May Tiu have provided administrative assistance, typing, and drafting services.

This study was a foundation for the development of a new Advanced Combustion Engineering Research Center (ACERC) which is funded by the National Science Foundation, the State of Utah, and the U.S. Department of Energy and twenty-five industrial organizations. ACERC was started on May 1, 1986, one year after the initiation of work on this consortium study. All sponsors of this work automatically became associate members of ACERC for the remaining three-year period of the consortium study to August 31, 1989. Further, new associate members in ACERC have immediate access to this

set of consortium final reports and to the 3-D code. These members include Advanced Fuel Research Co., Convex Computer Corp., Dow Chemical USA, Gas Research Institute, and Morgantown Energy Technology Center of DOE.

Table 0.1: Summary of Participating Organizations and Technical Contacts for Consortium Study on "Detailed Model for Practical Pulverized Coal Furnaces and Gasifiers".

Organization/Contact/Address	
Babcock & Wilcox Mr. Wm. Oberjohn, Supervisor 1562 Beeson Street Alliance, OH 44601	Combustion Engineering Co. Mr. Gordon Robinson 1000 Prospect Hill Road Windsor, CT 06095-0550
Consolidation Coal Co. Dr. Stanley Harding 4000 Brownsville Road Library, PA 15129	Electric Power Research Institute Quality Fossil Fuel Power Plant Dept. Dr. Arun Mehta, Project Manager 3412 Hillview Avenue Palo Alto, CA 94303
Empire St. Elec. Energy Res. Corp. New York State Elec. & Gas Corp. Mr. Rick Mancini, Manager P.O. Box 3607 Binghamton, NY 13902-3607	Foster Wheeler Development Corp. Dr. K.S. Ahluwalia 12 Peach Tree Hill Road Livingston, NJ 07039
Tennessee Valley Authority Solids Waste Group Dr. Chao-Ming Huang 1150 Chestnut Street, Tower II Chattanooga, TN 37401	U.S. Department of Energy Pittsburgh Energy Tech. Center Comb. Project Management Div. Coal Mr. James Hickerson P.O. Box 10940 Pittsburgh, PA 15236
Utah Power and Light Co. Combustion Research Dr. Dee P. Rees, Manager 1407 West North Temple Salt Lake City, UT 84110	

Contents

List of Figures

List of Tables

Nomenclature

Arabic Symbols

Symbol	Units	Definition
a	—	Constant associated with second order slip
a	$m\ s^{-2}$	Acceleration function
a	--	Number of atoms in a molecule
a	$kg(kg-mol)^{-1}$	Atomic weight
a	$kg\ s^{-1}$	Left tridiagonal matrix element
a	—	Asymmetry factor
A	m^2	Area
A	m	Van Driest damping parameter
A	$kg\ s^{-1}$	Combined convection/diffusion coefficient for tranport equations
A	—	Fourier coefficients
$\mathcal{A}$	m^2	Area
B	m^2	Area
B	—	Fourier coefficients
b	$kg\ s^{-1}$	Center tridiagonal matrix element
c	—	empirical constant
c	$kg\ s^{-1}$	Right tridiagonal matrix element
C	$kg\ s^{-1}$	Convection coefficient for transport equations
C	m^2	Area
C	—	Dimensionless constant
C	$kg\ m^{-3}$	Concentration,
C	*varies*	Viscous slip coefficient
d	m	Diameter
D	$m^2\ s^{-1}$	Fickian diffusivity
D	*varies*	Coefficient for various transport equations
D	$m^2\ s^{-1}$	Brownian diffusivity
D	m	Diameter of the enclosure
D	s^{-1}	Deformation tensor
e	—	Recursion coefficient in Thomas algorithm
E	—	Law of the Wall constant
f	—	Mixture fraction
f	—	Skin friction factor
f	—	Differencing factor

Arabic Symbols

Symbol	Units	Definition
f	—	Recursion coefficient in Thomas algorithm
F	*varies*	Facial variable values
F	$kg\ m\ s^{-2}$	Thermophoretic force
g	—	Variance of mixture fraction
g	—	Einstein functions
g	—	Relaxation parameter in Thomas algorithm
$\mathbf{g}$	$m\ s^{-2}$	Gravitational acceleration
G	$kg\ m^{-1}\ s^{-3}$	Generation of turbulent kinetic energy
G	—	Transformation function
h	$J\ kg^{-1}$	Specific enthalpy
H	m	Height of the furnace
ΔH	$J\ kg^{-1}$	Heat of vaporization/reaction
i	—	Iterative index
I	$Wm^{-2}sr^{-1}$	Radiation intensity
(INT)	—	Value of integral
k	$m^2\ s^{-2}$	Turbulent kinetic energy
k	$kg\ m^{-4}s^{-1}$	Mass transfer coefficient
k	$kg\ m^2s^{-2}\ K^{-1}$	Boltzmann constant
k_s	m	Equivalent sand roughness
k	$W(m\ K)^{-1}$	Thermal conductivity
k	m^{-1}	Radiation coefficients
K	—	Knudsen number
l	m	Turbulent length scale
L	m	Turbulent length scale
L	m	Length of the furnace
$\mathcal{L}$	s	Integral time scale
m	kg	Mass, molecular mass
M	$kg\ s^{-1}$	Mass flow rate
M	$s\ kg^{-1}$	Mobility
$\mathbf{M}$	—	Tridiagonal matrix
n	—	Index
N	—	Total number of points, nodal variable values
N	$kg\ m^{-2}s^{-1}$	Mass flux
O	—	Nodal variable values in opposite direction
O	—	Oxygen
p	$N\ m^{-2}$	Pressure

Arabic Symbols

Symbol	Units	Definition
p	—	Parameter
$P(\Omega, \Omega')$	—	Scattering phase function
$\mathbf{n}$	—	Unit vector normal to surface (outward-directed)
q	$W\ m^{-2}$	Hemispherical flux
Q	$N\ m^{-2}s^{-1}$	Heat flux
r	m	Radial distance
R	*varies*	Equation error/residual
R	—	Generalized correlation function
Re	—	Reynolds number
s	—	Conserved scalar
s	—	Search variable
s	m	Particle stop distance
S	$kg\ m^{-2}s^{-2}$	Source term for transport equations
S	—	Single partial variance
S_f	—	Fractional surface coverage
S	*varies*	Source term
Sc	—	Particle Schmidt number
t	s	Time
T	s	Time duration which is large compared to the time scale of the local turbulence
T	K	Temperature
u	$m\ s^{-1}$	Axial/x component of velocity
v	$m\ s^{-1}$	Radial/y component of velocity
$\mathbf{v}$	$m\ s^{-1}$	Velocity vector
vol	m^3	Cell volume
V	m^3	Volume of the computational cell
w	$m\ s^{-1}$	Tangential/z component of velocity
w	sr	Angular quadrature weight
W	m	Width of the furnace
x	—	Mass fraction
x	m	Cartesian coordinate direction
y	m	Cartesian coordinate direction
y	m	Distance from the wall
z	m	Cartesian coordinate direction

Greek Symbols

Symbol	Units	Definition
α	—	Under-relaxation factor
α	m	Weighting distance
β	m	Weighting distance
γ	—	Large number (10^{25})
Γ	$kg\ m^{-1}\ s^{-1}$	Diffusive transport coefficient
Γ	*varies*	Arbitrary exchange coefficient
δ	m	Computational distance between subscript locations
δ	*varies*	Small perturbation, Dirac function
δ_{ij}	—	Kronecker delta
ϵ	$m^2\ s^{-3}$	Dissipation rate of turbulent kinetic energy
ϵ	$m\ s^{-2}$	Momentum eddy diffusivity
ε	—	Emissivity
ζ	m	Weighting distance
η	—	Coal gas mixture fraction
η	—	Direction cosine
θ	—	TDMA acceleration parameter
θ	*rads*	Tangential distance
θ	—	Blowing factor correction
κ	—	Turbulent boundary condition constant
μ	$kg\ m^{-1}s^{-1}$	Viscosity
μ	$kg\ m^{-1}s^{-1}$	Dynamic viscosity
μ	—	Direction cosine
μ	$kg\ m^{-1}s^{-1}$	Dynamic viscosity of the gas
ν	m^2s^{-1}	Kinetmatic viscosity
ξ	—	Direction cosine
ρ	$kg\ m^{-3}$	Density
σ	—	Schmidt or Prandtl number
σ	*varies*	Standard deviation
τ	s	Time scale
τ	$kg\ m^{-1}\ s^{-2}$	Shear stress
ϕ	*varies*	Arbitrary variable

Greek Symbols

Symbol	Units	Definition
ϕ	*rads*	Angle between incident and scattered intensities
Φ	s^{-2}	Dissipation function
φ	*rads*	Angle between flow and grid structure
χ	*varies*	Weighted variable of interest
ψ	*varies*	Truncation error parameter
ω	—	Scattering albedo
ω	*rads* s^{-1}	Angular frequency
Ω, Ω'	—	Outward and inward directions of radiation

Subscripts

Symbol	Definition
a	Absorption
b	Bulk
b	Black body
b	Buffer layer
b	At, from, or to bottom face
B	At, from, or to bottom node
BC	At, from, or to boundary node
c	Devolatilization, convective
cou	For Couette flow
C	Convective component of coefficient
d	Directional index
d	Direction along the coordinates
D	Diffusive component of coefficient
e	Effective
e	At, from, or to east face
E	At, from, or to east node
f	Mixture fraction
fal	False or numerical
F	Face or surface values
g	Variance
g	Medium, gas
g	Variance in mixture fraction
h	Oxidation, enthalpy
i	Matrix element
i	Coordinate direction, arbitrary
i	Integer index for x direction, coordinate index
in	Inlet
j	Integer index for y direction
k	Integer index for z direction
l	Liquid
l	Laminar sublayer

Subscripts

Symbol	Definition
l	L'th parameter
m	Mixing
m, m'	Directions of the discrete ordinates
n	At, from, or to north face
N	At, from, or to north node
O	Node in opposite direction
p	p-cell
p	Particle
pr	Primary
P	At, from, or to principal cell node
r	Radial component
r	Radiative
res	Residual
s	Surface
s	Scattering
s	At, from, or to south face
sc	Secondary
S	At, from, or to south node
t	Turbulent
t	At, from, or to top face
th	Thermophoretic
T	At, from, or to top node
U	Non-linearizable source term
v	Vaporization
w	Wall
w	At, from, or to west face
W	At, from, or to west node
WW	At, from, or to second west node
x	Cartesian/axial coordinate component
y	Cartesian coordinate component
z	Cartesian coordinate component

Subscripts

Sumbol	Definition
0	Initial value
1	First
2	Second
1,2	Arbitrary numbers
ϵ	Dissipation of turbulent kinetic energy
η	Mixture fraction η
θ	Tangential component
μ	Viscosity
μ	Prandtl-Kolmogorov
ϕ	Variable of interest
ϕ	Pertaining to variable ϕ
$*$	Friction

Superscripts

Symbol	Definition
$+$	Positive, dimensionless variable for wall function
$+$	Dimensionless
$-$	Negative
BE	Best estimate
c	Correction
f	f mixture fraction
h	Enthalpy
i	Irregular grid
K	Known solution
L	Lagrangian
m	Total mass
m	m'th output function
M	Mass balance
n	Iteration index
new	Updated value
o	Individual node point
O	Original (PCGC-2) formulation
p	Pressure equation
p^c	Pressure correction equation
P	Evaluated at pressure (main) cell node
u	For x/axial momentum equation
u	Axial velocity
v	For y/radial momentum equation
v	Radial velocity
w	For z/tangential momentum equation
w	Tangential velocity
η	η mixture fraction
ϕ	Equation of interest
ψ	Truncation error

Executive Summary

Objectives and Accomplishments

This study has been supported by a consortium of nine industrial and governmental sponsors. Work was initiated on May 1, 1985 and completed August 31, 1989. The central objective of this work was to develop, evaluate and apply a practical combustion model for utility boilers, industrial furnaces and gasifiers. During this four-year effort, key accomplishments have included:

1. Development of an advanced first-generation, computer model for combustion in three dimensional furnaces,
2. Development of a new first generation fouling and slagging submodel,
3. Detailed evaluation of an existing NOx submodel,
4. Development and evaluation of an improved radiation submodel,
5. Preparation and distribution of a three-volume final report:
    a. Volume 1: General Technical Report
    b. Volume 2: PCGC-3 User's Manual
    c. Volume 3: Data Book for Evaluation of Three-Dimensional Combustion Models
6. Organization of a user's workshop on the three-dimensional code

The furnace computer model developed under this study requires further development before it can be applied generally to all applications; however, it can be used now by specialists for many specific applications, including non-combusting systems and combusting geseous systems. During the course of this study, a new combustion center was organized and work was initiated to continue the important research effort initiated by this study. Additional information on these key accomplishments follows.

Practical Combustion Model Development

A practical, comprehensive combustion model has been developed, entitled PCGC-3 (Pulverized Coal and Gasification Combustion Model in 3-dimensions), which includes submodels and numerical methods based on developments over the last decade and half at this laboratory. Furnace models

have a very large number of potential uses. An illustrative list includes the following:

1. For planning test programs, where test variables or sample locations need to be identified.

2. For evaluating the effects of key furnace parameters such as changes in coal type, coal size or preheat temperature.

3. For interpreting test data for applications such as scaling of pilot plant data to larger sizes.

4. For examining boiler fouling and slagging effects.

5. For assistance in designing new furnaces or retrofitting existing furnaces.

6. For analyzing potential effects of new burners, such as reduction in NOx emissions.

7. For examining furnace operations such as regions where erosion due to coal particle impingement might be of concern.

The number of potential applications of computer models goes beyond this illustrative list. Those modelscan ba applied non-combusting systems, such as in the design of equipment to recover SOx sorbent particles, to gaseous combustion systems, such as in a natural gas industrial boiler, and to solids combustion systems such as a utility coal-fired boiler or an entrained coal gasifier.

By the end of this contracted study, the 3-D combustion model had incorporated computational turbulent fluid dynamics, gaseous reaction, heat transfer, and non-reacting particulate transport. A user's manual was prepared (Vol. II) for delivery to all consortium members. This model predicts the local velocity, composition and thermal fields inside gas-fired and coal-fired furnaces.

Our past efforts were deliberately focused on the development of a laboratory-scale (two-dimensional, axi-symmetric) model that provided for all of that physical and chemical effects that occurred in still more complex configurations while minimizing computer costs for development and evaluation. A 2-D combustion model (PCGC-2) was developed, evaluated through extensive comparisons with measurements, and applied to selected problems. Extensive comparisons with measurements from coal gasification and combustion reactors were generally favorable, considering the complexity of these processes.

Based on the demonstrated utility of the 2-D work, this consortium study

was focused on developing the key components that are essential to the extension of this technology to large-scale and three-dimensional furnaces and gasifiers. Not all of the physical and chemical issues had been resolved in this previous small scale work and therefore, the thrust of this study also included further work on subcomponents and of reviewing and incorporating on-going research by other investigators.

The end goal of developing a 3-D furnace combustion model has been greatly assisted by using the 2-D code as a significant development tool. While the large-scale 3-D applications require numerical methods and evaluation that may be unique, the chemically- and physically-based submodels are as applicable to smaller-scale 2-D geometries as to industrial 3-D configurations. The more proven and established 2-D combustion model previously developed has provided a more computationally efficient method for incorporating, testing, and evaluating most physical and chemical submodels and to some extent even for exploring new computational strategies.

Submodel Development

A practical furnace model contains several components, called submodels, that describe the various physical and chemical processes, such as coal particle motion, radiation, fouling or slagging by minerals, NOx formation and the like. Further development and independent evaluation was conducted on several important submodels necessary for the 3-D model: radiation, char oxidation, turbulent dispersion of particles, nitrogen oxide formation, carbon monoxide formation, coal devolatilization, and turbulence. The radiation and turbulence submodels have been formulated in 3-D geometries. The other submodels have been implemented only in 2-D, axisymmeric geometries. Further discussion of submodel development accomplishments follows.

Radiation Submodel. A study has been completed on the development of a discrete-ordinates radiative heat transfer submodel. Radiative heat transfer has been shown to be increasingly more important as the scale of the furnace increases. The need for obtaining an accurate calculation of radiation in an efficient way for large-scale systems has dictated this new submodel development. A new radiation submodel was developed and applied to 2-and-3-dimensional cylindrical and Cartesian geometries. It has been compared to

experimental data and to other more rigorous numerical solutions, showing improved accuracy and efficiency over conventional flux methods.

Coal and Char Reactions. The char oxidation submodel accuracy was improved by re-examining the original data from which the chemical kinetic rates were obtained. Several char oxidation data sets were re-correlated with advance methods for several coals. This non-linear method of data analysis differs substanatially from that most commonly used linear approximation to correlate data with the Arrhenius law. A generalized framework for coal devolatilization has also been developed which includes most of the published devolatilization models. It is organized around the concept of incorporating fundamental descriptions of coal into a kinetic reaction scheme which predicts the product distributions.

Coal Particle and Gaseous Flows. A fundamental approach to describing coal particle flow and dispersion was developed. This submodel requires no adjustable parameters and is independent of any particular turbulence model. This submodel has been evaluated by comparison to exact solutions, alternative models, and experimental data. The new submodel was shown to be an accurate and efficient method of describing particle flow.

Improvements were also made in the description of the gaseous flows. A generalized form of a commonly used turbulence model, called the k-ϵ model, was adapted for future use in the 3-D code. This nonlinear k-ϵ model describes turbulent flows where the variation in the normal stresses are signficant. This method has been shown to provide a better estimate of the velocity field. The model has successfully predicted secondary flows in ducts and channels where the standard k-ϵ model has failed.

Nitrogen Oxide Formation. The submodel for predicting NOx concentrations in coal-fired furnaces has been evaluated for a wide variety of operating conditions. Comparisions of NOx predictions for 30 additional sets of data provided a broad evaluation of the NOx submodel. The NOx submodel provided reliable predictions for pulverized-fuel gasification and combustion for bituminous and subbitminous coals at moderately and extremely fuel-rich conditions. The effect of pressure was also properly predicted for the gasification of Utah bituminous coal.

Carbon Monoxide Formation. The inability of coal combustion models to accurately predict carbon monoxide (CO) concentrations was thought to be partly caused by ignoring rate-limiting chemical reactions. A rigorous kinetic treatment of all chemical processes occurring in the reactor was found to

require too great an increase in computational time to be practical with the current generation of computer technology. Use of a simplified method was found to account for most of the kinetic effects with an acceptable increase in computational time.

Fouling and Slagging. A study was conducted to develop a fouling and slagging submodel. Although many mechanisms in the mineral matter transformation processes have not been completely defined,this model incorprated current technology. Particle fragmentation, particle deposition, capture processes and deposit heat transfer were treated in this new submodel. Results from the initial evaluation of the submodel emphasized the importance of the thermal characteristics of the deposit.

Furnace Model Evaluation

An evaluation has been conducted to explore the predictive capabilities of the 3-D furnace combustion model with its integrated submodels. In this evaluation, we have made extensive use of both the 2-D and 3-D versions of the model. The evaluation has included: (1) a sensitivity analysis of key model parameters for a laboratory-scale, axi-symmetric, coal-fired furnace, (2) an analysis of the numerical methods of the 3-D model using several approaches including identification of mesh-size independent solutions for the fully-coupled equation set, (3) comparisons with known exact solutions for highly simplified cases, (4) a compilation and evaluation of available 3-D data, and (5) extensive comparisons of model predictions with experimental data.

The 3-D model has been evaluated at the largest scale by comparing non-reacting flow predictions with measurements from two-pilot-scale furnaces, a tangentially-fired furnace operated by Combustion Engineering Incorporated, and a wall-fired, pilot-scale furnace operated by Consolidation Coal Company. These comparative evaluations indicated that the computational methods and physical approximations were appropriately balanced to predict flow patterns and velocities to within engineering adequacy for the two furnaces.

Technology Transfer

The practical furnace model is based on generalized mathematical equations and includes detail physical and chemical submodels. It is solved through use of advanced numberical methods and requires a large computer. Thus, routine use by practicing engineers is not currently practical. It is best used by a graduate-level engineer with specific training and experience in use of comprehensive models. Recognizing this challenge, we have completed several tasks to facilitate the use of this model including the following:

1.A detailed User's Manual has been published (Volume II, Final Report).

2.A workshop has been scheduled at our laboratory for August of 1990, to train consortium members in the use of the 3-D model.

3. Participating companies were offered the computerized 3-D model for on-site use.

4. Twelve quarterly reports, three annual reports and a three volume final report were prepared and distributed. Also, forteen technical presentations were made and twenty-two publications were completed based on this work, with others in process.

5. Methods for providing technical services on 3-D model use have been identified. Consulting services of faculty can be obtained. Also, a new company involving the professionals in code development has been organized to provide technical services. Thus, use of this new technology is readily available to consortium members regardless of their interest in using the code in-house.

Future Work

Even though substantial progress was made during this four year contract study, much work must be completed in order to produce an effieient, practical combustion code with very broad application. Recognizing this need, we orgainized a new Advanced Combustion Engineering Research Center (ACERC). On May 1, 1986, Brigham Young University and the University of Utah jointly began research work in ACERC with a major National Science Foundation grant. This consortium study was used as the foundational

framework on which ACERC was built. As a result, all consortium sponsors automatically became ACERC associate members during the period of the consortium contract, and thus received research results and products of ACERC that go well beyond the consortium tasks. These research results have been communicated to all consortium sponsors through separate ACERC communications.

The results of this consortium study have formed the basis for further 3-D combustion model development under ACERC sponsorship that has continued beyond the completion of this study. ACERC is now well established and most of the original consortium members are associate members. Work among 125 faculty, professionals and students is continuing in six thrust areas, with a focus on clean and efficient use of low-quality fossil fuels: (1) fuel structure and reaction mechanisms, (2) fuel minerals, fouling and slagging, (3) pollutant control and solid-waste incineration, (4) turbulent, reactive flows, (5) comprehensive model development and (6) evaluation data and process strategies.

Among these projects, a major objective is to develop, evaluate and implement an advanced, next-generation, 3-D combustion model for practical furnaces, combustors and gasifiers. Among the important research tasks that must be accomplished include:

1.Application of improved numerical methods that work for very large furnaces.

2.Discovering the relationships between coal structure and its reactions so that general coal reaction models can be included.

3.Incorporation of improved NOx/SOx, fouling/slagging, radiation and turbulent flow submodels into the furnace combustion model.

4.Measurements from inside large boilers and pilot combustors for model evaluation.

5.Development of efficient graphical methods for managing required input parameters and model output predictions.

6.Further developement of technology transfer methods in order to make the new technology readily available to all potential users.

Section 1

Research Task 1 - Practical Full-Scale Model

1.1 Background

Past modeling at this laboratory resulted in the development of a computational model for coal combustion entitled PCGC-2 which is a steady-state model, formulated for axi-symmetric, cylindrical coordinates. To be of practical value to full-scale furnace and gasifier geometries it had to be extended to general, three-dimensional coordinates. Also, numerical methods applicable to large-scale systems had to be incorporated. Since steady-state and gasifier furnace operation is of major interest, and since past transient modeling has suggested that steady-state solutions may be impractical with transient codes, work was conducted to extend the steady-state model to three-dimensions.

It is recognized that there are many difficulties associated with the three-dimensional systems, applied to large-scale reactors.

1. There are difficulties in obtaining a computational mesh that is fine enough to sufficiently resolve the details of mixing and reaction around individual inlets and burners, yet coarse enough to maintain acceptable computational run times.

2. With the increased computational time required for the large number of nodes needed for three-dimensional systems, it was

important to incorporate the most efficient and accurate mathematical technique available for solving the coupled partial differential equations.

3. Since one of the objectives of this work was to make this available to industrial users, it was important to target the computer program to computers available to the potential industrial user.

4. The computational output from a 3-D model must be presented in easily understood graphical form.

Each of these four challenges has been addressed in this task.

1.2 Model Formulation

1.2.1 Submodel Description of PCGC-3

Several submodels have been identified for incorporation into the 3-D code. These include all submodels in the existing 2-D code. Additionally, several submodels have been identified for needing significant improvement and others that were not previously in the 2-D code need to be developed and incorporated (i.e., mineral matter transformation). All of the submodels targeted for improvement or development over the past four years are discussed in detail in Section 3 with the exception of the fouling and slagging submodel. That new submodel development is reported as a separate task in Section 4 of this report. All submodel development was initiated and tested in the 2-D code first, then advanced and implemented in the 3-D code.

This section reviews the research, development and status of PCGC-3. This is the 3-D embodiment of the submodels and numerical methods of the last decade and a half at this laboratory. The 2-D code remains a useful tool for evaluating submodels and for analysis of simple furnaces. As such, the 2- and 3-D codes are considered as a set of tools for analyzing combustion chambers.

The 3-D code developed in this study has incorporated computational fluid dynamics, gaseous reaction, heat transfer, and non-reacting particulate transport all in turbulent environments. In moving to calculations in larger chambers, a new set of computational constraints have emerged. Differencing schemes, solution procedures, coupling algorithms and other numerical

methods have had to be reevaluated in light of the temporal and spatial scales that need resolving in larger furnaces. These are discussed in this section. Graphical interfaces are often the only way of gaining access to the input and output data of large or complex geometries in combustion. The graphics pre- and post-processors developed for this study and continuing under ACERC sponsorship are summarized in this chapter.

The coupling of multiple chemical and physical processes has been a major emphisis of this research. Particularly, when the coupling occurs in a statistically fluctuating field when the processes are usually highly nonlinear. The fluid turbulence that produces these fluctuations is a continued emphasis of this research and that is made more apparent in several sections throughout this report (i.e. subsection 2.4, subsection 3.3, subsection 3.7, Section 4). The 3-D code has incorporated this coupling from the initial conception. For example, the energy transport is affected strongly by turbulent transport and fluctuations, and by all other processes in the system (i.e. fluid dynamics, gaseous reaction, boundary conditions, geometry, etc.). All of these have been incorporated in the development of the 3-D code and centered around the calculation and evaluation of the 3-D enthalpy field in the 3-D code.

The problems associated with increasing the scale of the calculation has introduced need for new procedures and methods. At different furnace scales, different physical processes dominate. The 3-D code has only been applied to pilot-scale furnaces and smaller in this study. Applications to yet larger systems will be forthcoming with independent funding, but will require more careful evaluation and undoubtedly a further evaluation of appropriate numerical methods and of submodel adequacy. Like scale-up of real physical furnaces, the scale-up of the furnace model requires a systematic development path.

Development of complex tools where the understanding of basic physics and chemistry are still evolving requires an iterative approach to the application of the scientific method. Hypothesizing an approach, testing and evaluating this approach leads to new hypotheses and new testing. Future work will advance the existing 3-D code to include the reacting particle fields, and to further advances in numerical methods and improved submodels.

1.2.2 Numerical Description

The model assumes that the flow field is a laminar or turbulent continuum field that can be described locally by general conservation equations. The flow is assumed to be steady-state and gas properties are determined through local mixing calculations. The fluid is assumed to be Newtonian and dilatation is neglected. The comprehensive model uses an Eulerian framework and is coded to handle either Reynolds- or Favre-averaging. This code, referred to as PCGC-3 (Pulverized Coal Gasification or Combustion-three-dimensional) couples the momentum and continuity equations with variations of the SIMPLE algorithm (Patankar, 1980), utilizes a combined first-order upwind and weighted central differencing scheme, and iteratively solves the difference coefficient matrices by approximating them as tridiagonal systems, which are solved with the Thomas algorithm (Davis, 1984).

The SIMPLE (Semi-Implicit Method for Solving Pressure Linked Equations) algorithm is a technique for solving the equations of motion and continuity in a decoupled fashion. It requires an initial guess of the pressure field which is then updated through the calculation of a pressure correction. This iterative procedure can require more than one thousand iterations to converge on the correct pressure field. Several variations of the SIMPLE algorithm were implemented in PCGC-3.

Although both PCGC-3 and PCGC-2 employ a first-order upwind differencing scheme, several important changes have been introduced in PCGC-3. The upwind differencing has been reformulated to reduce the approximations which cause numerical diffusion. Furthermore, the central differencing in PCGC-2 was designed primarily for uniform grids. A new flux-weighted formulation was required to allow PCGC-3 to correctly central difference the highly irregular grid structures needed to model industrial furnace geometries.

The differencing scheme in PCGC-3 results in the formation of heptadiagonal coefficient matrices. Each matrix is first approximated as a series of three tridiagonal matrices. These matrices are then solved successively with the Thomas algorithm, and the solution procedure is repeated several times to resolve the coupling in the three coordinate directions. This procedure is a variation of the Alternating Direction Iterative (ADI) method (Davis, 1984). These iterations on a specific variable are termed "micro-iterations" and are typically done in a line-by-line fashion. PCGC-3 performs these "micro-

iterations" in a plane-by-plane manner to aid vectorization. Generally, fewer than five "micro-iterations" are necessary to converge each variable, with the exception of the pressure variables. Figure 1.1 provides a basic flow diagram of the iterative loops in the overall solution algorithm. Steps 4 through 7 in this figure constitute a "micro-iteration."

The differential equations for each variable are solved in succession in a decoupled manner. This procedure usually begins with a component of velocity and ends with a turbulence model variable. A "macro-iteration" is completed after the complete set of variables has been calculated once. This is illustrated by Steps 2 through 10 in Figure 1.1. Coupling of the equation set is achieved through these "macro-iterations." Several hundred macro-iterations are usually required to completely converge the reacting flow field.

1.2.3 Differential Equation Set

The equations modeled in PCGC-3 can be classified as Eulerian, steady-state, second-order, nonlinear, elliptical partial differential equations. All the equations were cast into a standard equation format. This allows a single finite differencing and greatly simplifies the solution technique and model coding. The standard equation form for the cylindrical equations follows:

$$r\frac{\partial(\bar{\rho}\tilde{u}\phi)}{\partial x}+\frac{\partial(\bar{\rho}r\tilde{v}\phi)}{\partial r}+\frac{\partial(\bar{\rho}\tilde{w}\phi)}{\partial\theta}- r\frac{\partial}{\partial x}\left(\Gamma_\phi\frac{\partial\phi}{\partial x}\right)-\frac{\partial}{\partial r}\left(r\Gamma_\phi\frac{\partial\phi}{\partial r}\right)-\frac{\partial}{\partial\theta}\left(\frac{\Gamma_\phi}{r}\frac{\partial\phi}{\partial\theta}\right)=S_\phi \tag{1.1}$$

Both the Cartesian and cylindrical coordinate system equations can be modeled with PCGC-3. The Cartesian equations are a subset of the cylindrical system and only the derivation of the more complex cylindrical equations will be presented in this report. The standard equation format for the Cartesian equations can be found by equating all radius terms in Equation 1.1 with unity. A short discussion of the equations simulated in PCGC-3 follows. These equations are presented in their Favre-averaged state.

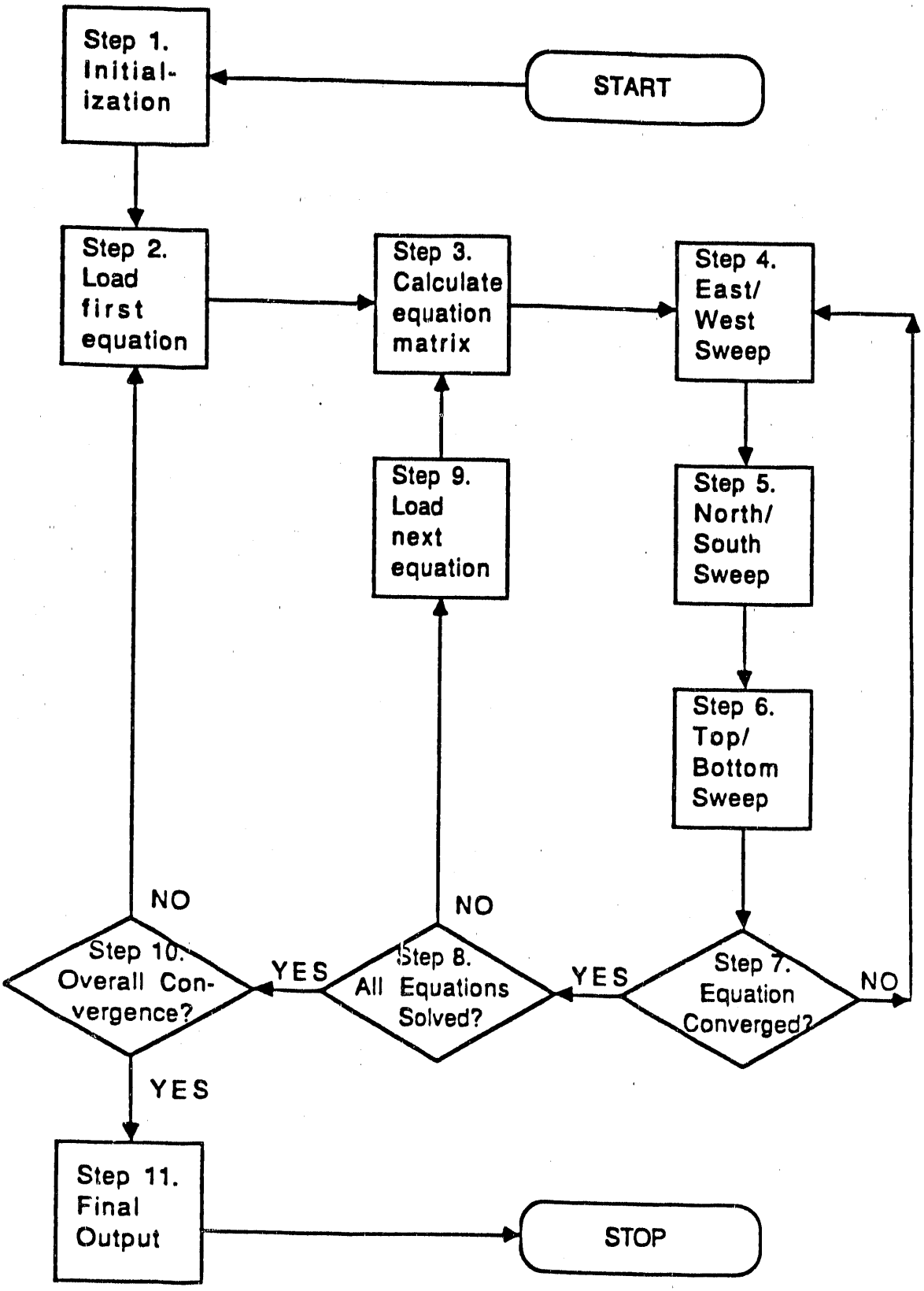

Figure 1.1: Iterative Procedure in PCGC-3.

Continuity an ' Momentum

The instantaneous gas-phase equations of continuity and momentum (Bird, 1960) are given below.

$$\frac{D\rho}{Dt} = -\rho(\nabla \cdot \mathbf{v}) \tag{1.2}$$

$$\rho\frac{D\mathbf{v}}{Dt} = -\nabla p - \nabla \cdot \tau + \rho\mathbf{g} \tag{1.3}$$

The equations may be simplified by assuming steady-state and considering only Newtonian fluids. In the expansion of Equation 1.3 the dilatation of the fluid is minimal at low velocities (less than 0.25 Mach Number) and is neglected (Bird, 1960; Smoot and Pratt, 1979).

The differential equations are Favre-averaged and the resulting Reynolds stress terms are modeled with an eddy diffusivity. Equations 1.2 and 1.3 can be expanded in cylindrical coordinates to equal:

$$\frac{\partial(\bar{\rho}\tilde{u})}{\partial x} + \frac{1}{r}\frac{\partial(r\bar{\rho}\tilde{v})}{\partial r} + \frac{1}{r}\frac{\partial(\bar{\rho}\tilde{w})}{\partial \theta} = 0 \tag{1.4}$$

$$\begin{aligned} r\frac{\partial(\bar{\rho}\tilde{u}\tilde{w})}{\partial x} + \frac{\partial(\bar{\rho}r\tilde{v}\tilde{w})}{\partial r} + \frac{\partial(\bar{\rho}\tilde{w}\tilde{w})}{\partial \theta} - \\ r\frac{\partial}{\partial x}(\mu_e\frac{\partial\tilde{w}}{\partial x}) - \frac{\partial}{\partial r}(r\mu_e\frac{\partial\tilde{w}}{\partial r}) - \frac{\partial}{\partial \theta}(\frac{\mu_e}{r}\frac{\partial\tilde{w}}{\partial \theta}) = \\ -\frac{\partial p}{\partial \theta} + r\frac{\partial}{\partial x}(\frac{\mu_e}{r}\frac{\partial\tilde{u}}{\partial \theta}) + \frac{\partial}{\partial r}(\mu_e\frac{\partial\tilde{v}}{\partial \theta} - \mu_e\tilde{w}) + \\ \frac{\partial}{\partial \theta}[(\frac{\mu_e}{r})(\frac{\partial\tilde{w}}{\partial \theta} + 2r\frac{\partial\tilde{v}}{\partial r})] + \mu_e(\frac{\partial\tilde{w}}{\partial r} + \frac{1}{r}\frac{\partial\tilde{v}}{\partial \theta} - \frac{\tilde{w}}{r}) - \bar{\rho}\tilde{v}\tilde{w} + r\bar{\rho}g_\theta \end{aligned} \tag{1.5}$$

Mixture Fraction Equations

For cases where there are two identifiable streams or states that have uniform properties, it is convenient to describe a conservative scalar f, the mixture fraction:

$$f = \frac{M_{pr}}{M_{pr} + M_{sc}} \tag{1.6}$$

This variable is equal to mass fraction of fluid atoms originating in the primary stream. The advantage of the mixture fraction approach lies in its ability to calculate any conserved scalar, s, from the local value of f:

$$s = f s_{pr} + (1 - f) s_{sc} \tag{1.7}$$

A transport equation for the time-averaged distribution of the mixture fraction (first moment about the origin) is given by Equation 1.8.

$$\begin{aligned} &\frac{r\partial}{\partial x}(\overline{\rho}\tilde{u}\tilde{f}) + \frac{\partial}{\partial r}(r\overline{\rho}\tilde{v}\tilde{f}) + \frac{\partial}{\partial \theta}(r\overline{\rho}\tilde{w}\tilde{f}) - \\ &\frac{r\partial}{\partial x}(\frac{\mu_e}{\sigma_f}\frac{\partial \tilde{f}}{\partial x}) - \frac{\partial}{\partial r}(\frac{r\mu_e}{\sigma_f}\frac{\partial \tilde{f}}{\partial r}) - \frac{\partial}{\partial \theta}(\frac{\mu_e}{r\sigma_f}\frac{\partial \tilde{f}}{\partial \theta}) = 0 \end{aligned} \tag{1.8}$$

The variance (second moment about the mean, or the mean-square fluctuation) of the mixture fraction is defined by Equation 1.9.

$$\tilde{g} = \overline{(f - \tilde{f})^2} = \frac{1}{T}\int_0^T [f(t) - \tilde{f}]^2 dt \tag{1.9}$$

Launder and Spalding (1972) show how a transport equation for g can be derived and appropriate terms modeled in a manner analogous to, and consistent with the other two equations in the k-ϵ turbulence model. The Favre-averaged differential equation for the transport of the mixture fraction variance, g, is given below:

$$\begin{aligned} &\frac{r\partial}{\partial x}(\overline{\rho}\tilde{u}\tilde{g}) + \frac{\partial}{\partial r}(r\overline{\rho}\tilde{v}\tilde{g}) + \frac{\partial}{\partial \theta}(r\overline{\rho}\tilde{v}\tilde{g}) - \\ &\frac{r\partial}{\partial x}(\frac{\mu_e}{\sigma_g}\frac{\partial \tilde{g}}{\partial x}\tilde{f}) - \frac{\partial}{\partial r}(\frac{r\mu_e}{\sigma_g}\frac{\partial \tilde{g}}{\partial r}\tilde{f}) - \frac{\partial}{\partial \theta}(\frac{\mu_e}{r\sigma_g}\frac{\partial \tilde{g}}{\partial \theta}\tilde{f}) = \\ &rc_{g1}\frac{\mu_e}{\sigma_g}[(\frac{\partial \tilde{f}}{\partial x})^2 + (\frac{\partial \tilde{f}}{\partial r})^2 + (\frac{\partial \tilde{f}}{r\partial \theta})^2] - rc_{g2}\frac{\overline{\rho}\epsilon\tilde{g}}{k} \end{aligned} \tag{1.10}$$

Summary of Equations

The preceding sections outlined a basis for the equations modeled by the current version of PCGC-3. The complete differential equation set for both the Cartesian and cylindrical coordinate systems is given in Tables 1.1 and

1.2. These tables begin with the standard equation form which is followed by ϕ and source term assignments which allow the standard equation to represent each differential equation. A close comparison of Table 1.1 and Table 1.2 will reveal that the Cartesian equations can be represented through a simplification of the cylindrical set. If the radius, r, is equated with unity in Table 1.2 and several radial and tangential momentum source terms are neglected, the equation sets become identical. This similarity simplified the coding of PCGC-3. The differential equation set was validated by comparing it with the equation set used in the other three-dimensional models (Turan, 1978; Fiveland and Wessel, 1986).

1.2.4 Computational Mesh

Each of the differential equations summarized in Tables 1.1 and 1.2 must be cast in finite difference form and solved over some appropriate grid spacing. A series of grid lines orthogonal to the coordinate directions define node points at their intersections. Values of the dependent variables are identified with these node points. Roache (1976) has reviewed solutions of the flow equations using various possible mesh systems and showed that in the primitive variable formulation, the variables u, v and w are most conveniently and accurately evaluated with node points lying on cell boundaries and with p and ρ being placed at cell centers. The staggered-mesh system implemented in PCGC-3 is shown in Figure 1.2. The grid spacing may be non-uniform with grid points concentrated in areas of steep gradients or unusual boundary configurations. This non-uniform grid spacing can increase the convergence rate and accuracy of the computations. PCGC-3 locates all cell faces midway between node points. Flux-weighted interpolation is used to obtain physical property values at mesh boundaries between node points. Completely arbitrary grid spacing is permitted.

Figure 1.2 shows a typical computational cell. Attention is focused on the node point P and its nearest neighbors (N,S,E,W,T,B) which were named for the four points of a compass plus top and bottom. The pressure, along with other variables, is calculated for these nodes. The velocity components associated with this node point are calculated at cell faces. The u velocity component for this cell is located at the w location in Figure 1.2. The v and w velocities are found on the cell faces at s and b. This staggered grid

Table 1.1: Cartesian Differential Equation Set.

$$\frac{\partial(\bar{\rho}\tilde{u}\phi)}{\partial x}+\frac{\partial(\bar{\rho}\tilde{v}\phi)}{\partial y}+\frac{\partial(\bar{\rho}\tilde{w}\phi)}{\partial z}-\frac{\partial}{\partial x}\left(\Gamma_\phi\frac{\partial\phi}{\partial x}\right)-\frac{\partial}{\partial y}\left(\Gamma_\phi\frac{\partial\phi}{\partial y}\right)-\frac{\partial}{\partial z}\left(\Gamma_\phi\frac{\partial\phi}{\partial z}\right)=S_\phi$$

Equation	ϕ	Γ_ϕ	S_ϕ
Continuity	1	0	$S_{pf}+S_{p\eta}$
X Momentum	$\tilde{u}$	μ_e	$-\frac{\partial\bar{P}}{\partial x}+\frac{\partial}{\partial x}\left(\mu_e\frac{\partial\tilde{u}}{\partial x}\right)+\frac{\partial}{\partial y}\left(\mu_e\frac{\partial\tilde{v}}{\partial x}\right)+\frac{\partial}{\partial z}\left(\mu_e\frac{\partial\tilde{w}}{\partial x}\right)+\bar{\rho}g_x-\frac{2}{3}\bar{\rho}\tilde{k}+S_{pu}$
Y Momentum	$\tilde{v}$	μ_e	$-\frac{\partial\bar{P}}{\partial y}+\frac{\partial}{\partial x}\left(\mu_e\frac{\partial\tilde{u}}{\partial y}\right)+\frac{\partial}{\partial y}\left(\mu_e\frac{\partial\tilde{v}}{\partial y}\right)+\frac{\partial}{\partial z}\left(\mu_e\frac{\partial\tilde{w}}{\partial y}\right)+\bar{\rho}g_y-\frac{2}{3}\bar{\rho}\tilde{k}+S_{pv}$
Z Momentum	$\tilde{w}$	μ_e	$-\frac{\partial\bar{P}}{\partial z}+\frac{\partial}{\partial x}\left(\mu_e\frac{\partial\tilde{u}}{\partial z}\right)+\frac{\partial}{\partial y}\left(\mu_e\frac{\partial\tilde{v}}{\partial z}\right)+\frac{\partial}{\partial z}\left(\mu_e\frac{\partial\tilde{w}}{\partial z}\right)+\bar{\rho}g_z-\frac{2}{3}\bar{\rho}\tilde{k}+S_{pw}$
Turbulent Energy	$\tilde{k}$	$\frac{\mu_e}{\sigma_k}$	G - $\bar{\rho}\tilde{\epsilon}$
Dissipation Rate	$\tilde{\epsilon}$	$\frac{\mu_e}{\sigma_\epsilon}$	$\left(\frac{\tilde{\epsilon}}{\tilde{k}}\right)(C_1G-C_2\bar{\rho}\tilde{\epsilon})$
Mixture Fraction	$\tilde{f}$	$\frac{\mu_e}{\sigma_f}$	S_{pf}
Mixture Fraction Variance	$\tilde{g}_f$	$\frac{\mu_e}{\sigma_{g_f}}$	$C_{g1}\frac{\mu_e}{\sigma_{g_f}}\left[\left(\frac{\partial\tilde{f}}{\partial x}\right)^2+\left(\frac{\partial\tilde{f}}{\partial y}\right)^2+\left(\frac{\partial\tilde{f}}{\partial z}\right)^2\right]-C_{g2}\bar{\rho}\tilde{g}_f\frac{\tilde{\epsilon}}{\tilde{k}}$
Enthalpy	$\tilde{h}$	$\frac{\mu_e}{\sigma_h}$	$q'_{rg}+\tilde{u}\frac{\partial\bar{P}}{\partial x}+\tilde{v}\frac{\partial\bar{P}}{\partial y}+\tilde{w}\frac{\partial\bar{P}}{\partial z}+S_{ph}$

where:

$$G=\mu_e\left\{2\left[\left(\frac{\partial\tilde{u}}{\partial x}\right)^2+\left(\frac{\partial\tilde{v}}{\partial y}\right)^2+\left(\frac{\partial\tilde{w}}{\partial z}\right)^2\right]+\left(\frac{\partial\tilde{u}}{\partial y}+\frac{\partial\tilde{v}}{\partial x}\right)^2+\left(\frac{\partial\tilde{u}}{\partial z}+\frac{\partial\tilde{w}}{\partial x}\right)^2+\left(\frac{\partial\tilde{v}}{\partial z}+\frac{\partial\tilde{w}}{\partial y}\right)^2\right\}$$

Table 1.2: Cylindrical Differential Equation Set.

$$\frac{\partial(\bar{\rho}\tilde{u}\phi)}{\partial x}+\frac{\partial(\bar{\rho}r\tilde{v}\phi)}{r\partial r}+\frac{\partial(\bar{\rho}\tilde{w}\phi)}{r\partial\theta}-\frac{\partial}{\partial x}\left(\Gamma_\phi\frac{\partial\phi}{\partial x}\right)-\frac{\partial}{r\partial r}\left(r\Gamma_\phi\frac{\partial\phi}{\partial r}\right)-\frac{\partial}{r\partial\theta}\left(\frac{\Gamma_\phi}{r}\frac{\partial\phi}{\partial\theta}\right)=S_\phi$$

Equation	ϕ	Γ_ϕ	S_ϕ
Continuity	1	0	$S_{pf}+S_{pu}$
X Momentum	$\tilde{u}$	μ_e	$\frac{\partial\bar{P}}{\partial x}+\frac{\partial}{\partial r}\left(\mu_e\frac{\partial\tilde{u}}{\partial x}\right)+\frac{1}{r}\frac{\partial}{\partial x}\left(\mu_e r\frac{\partial\tilde{v}}{\partial x}\right)+\frac{1}{r}\frac{\partial}{\partial\theta}\left(\mu_e\frac{\partial\tilde{w}}{\partial x}\right)+\bar{\rho}g_x-\frac{2}{3}\bar{\rho}\tilde{k}+S_{p\eta}$
R Momentum	$\tilde{v}$	μ_e	$\frac{\partial\bar{P}}{\partial r}+\frac{\partial}{\partial x}\left(\mu_e\frac{\partial\tilde{u}}{\partial r}\right)+\frac{1}{r}\frac{\partial}{\partial r}\left(\mu_e r\frac{\partial\tilde{v}}{\partial r}\right)+\frac{\partial}{r\partial\theta}\mu_e\left(\frac{\partial\tilde{w}}{\partial r}-\frac{\tilde{w}}{r}\right)-\frac{2\mu_e}{r^2}\left(\frac{\partial\tilde{w}}{\partial\theta}-\tilde{v}\right)+\frac{\bar{\rho}\tilde{w}^2}{r}+\bar{\rho}g_r-\frac{2}{3}\bar{\rho}\tilde{k}+S_{pv}$
θ Momentum	$\tilde{w}$	μ_e	$\frac{1}{r}\frac{\partial\bar{P}}{\partial\theta}+\frac{\partial}{\partial x}\left(\frac{\mu_e}{r}\frac{\partial\tilde{u}}{\partial\theta}\right)+\frac{1}{r}\frac{\partial}{\partial r}\left(\mu_e\frac{\partial\tilde{v}}{\partial\theta}-\mu_e\tilde{w}\right)-\frac{\bar{\rho}\tilde{v}\tilde{w}}{r}+\frac{1}{r}\frac{\partial}{\partial\theta}\left[\left(\frac{\mu_e}{r}\right)\left(\frac{\partial\tilde{w}}{\partial\theta}+2\tilde{v}\right)\right]+\mu_e\left(\frac{\partial\tilde{w}}{r\partial r}+\frac{\partial\tilde{v}}{r\partial\theta}-\frac{\tilde{w}}{r^2}\right)+\bar{\rho}g_\theta-\frac{2}{3}\bar{\rho}\tilde{k}+S_{pw}$
Turbulent Energy	$\tilde{k}$	$\frac{\mu_e}{\sigma_k}$	$G-\bar{\rho}\tilde{\epsilon}$
Dissipation Rate	$\tilde{\epsilon}$	$\frac{\mu_e}{\sigma_k}$	$\left(\frac{\tilde{\epsilon}}{\tilde{k}}\right)(C_1G-C_2\bar{\rho}\tilde{\epsilon})$
Mixture Fraction	$\tilde{f}$	$\frac{\mu_e}{\sigma_f}$	S_{pf}
Mixture Fraction Variance	$\tilde{g}_f$	$\frac{\mu_e}{\sigma_{g_f}}$	$C_{g1}\frac{\mu_e}{\sigma_{g_f}}\left[\left(\frac{\partial\tilde{f}}{\partial x}\right)^2+\left(\frac{\partial\tilde{f}}{\partial r}\right)^2+\left(\frac{\partial\tilde{f}}{r\partial\theta}\right)^2\right]-C_{g2}\,\bar{\rho}\tilde{g}_f\frac{\tilde{\epsilon}}{\tilde{k}}$
Enthalpy	$\tilde{h}$	$\frac{\mu_e}{\sigma_h}$	$q'_{rg}+\tilde{u}\frac{\partial\bar{P}}{\partial x}+\tilde{v}\frac{\partial\bar{P}}{\partial r}+\frac{\tilde{w}}{r}\frac{\partial\bar{P}}{\partial\theta}+S_{ph}$

where:

$$G=\mu_e\left\{2\left[\left(\frac{\partial\tilde{u}}{\partial x}\right)^2+\left(\frac{\partial\tilde{v}}{\partial r}\right)^2+\left(\frac{\partial\tilde{w}}{r\partial\theta}+\frac{\tilde{v}}{r}\right)^2\right]+\left(\frac{\partial\tilde{u}}{\partial r}+\frac{\partial\tilde{v}}{\partial x}\right)^2+\left(\frac{\partial\tilde{u}}{r\partial\theta}+\frac{\partial\tilde{w}}{\partial x}\right)^2+\left(\frac{\partial\tilde{v}}{r\partial\theta}+\frac{\partial\tilde{w}}{\partial r}-\frac{\tilde{w}}{r^2}\right)^2\right\}$$

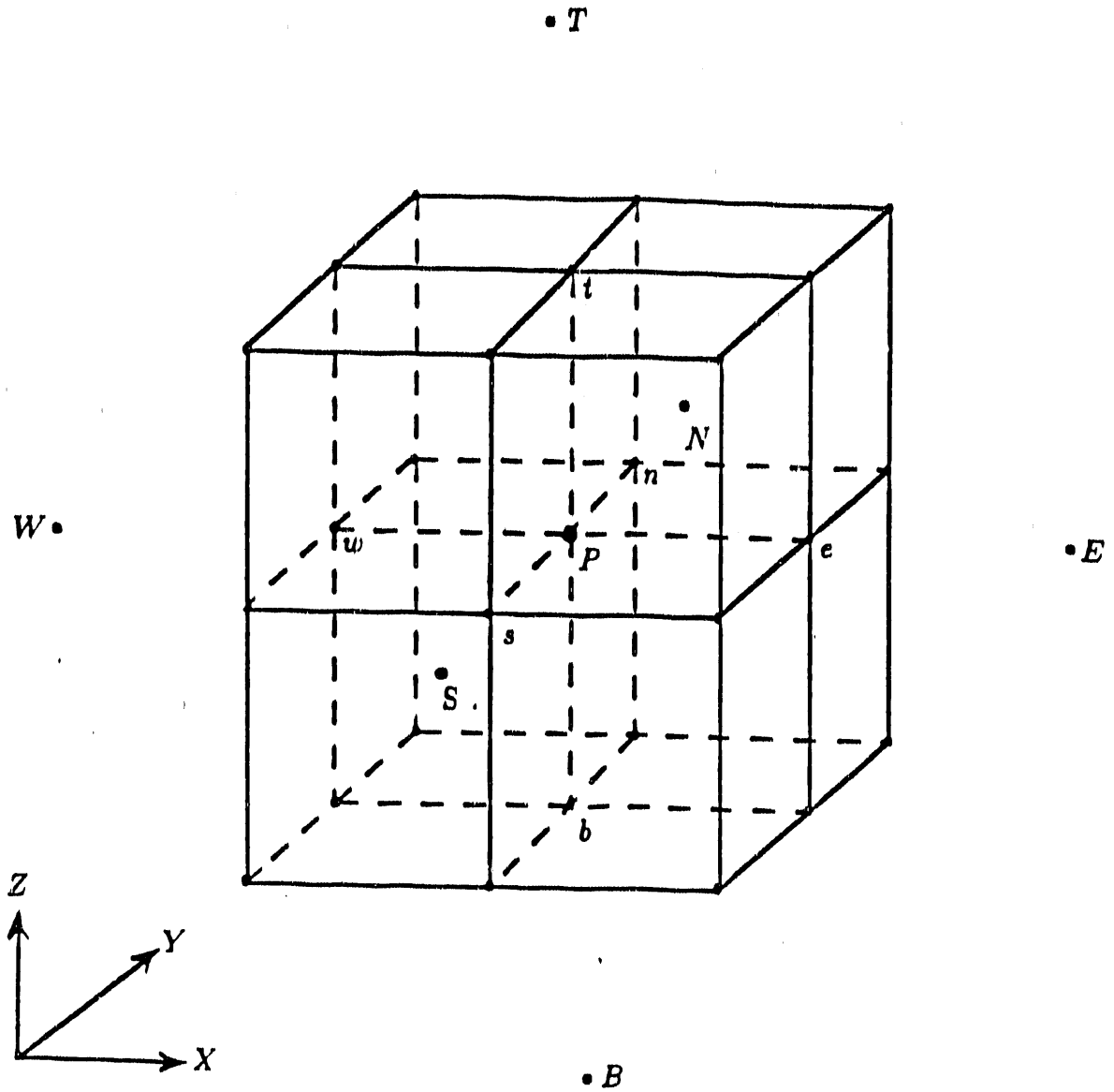

Figure 1.2: Labeled Main or Pressure Cell.

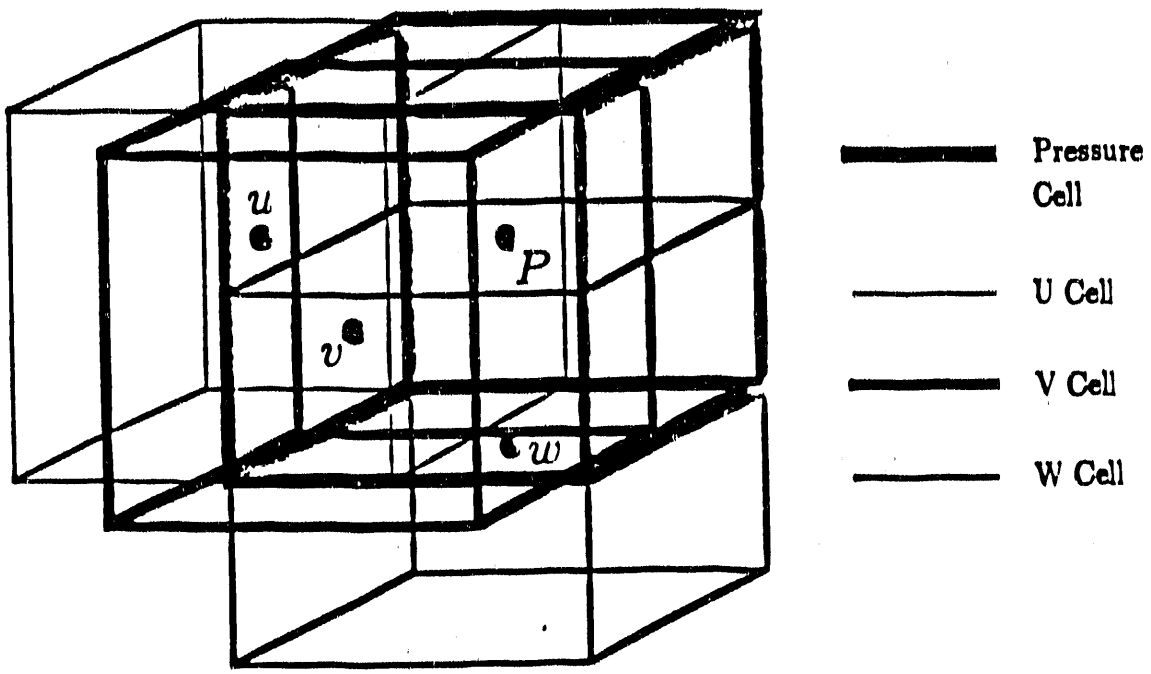

Figure 1.3: Relationship of Various Cell Types on a Staggered Grid.

is conducive to the solution of the cell mass conservation equation since the required velocities are located at the cell faces.

There are several types of cells in the computational domain. The various cells are centered at the point of definition of the variable of interest and extend halfway to the six adjacent (in three-dimensional) neighboring node points. There are four cell systems, one for each component of velocity and a main cell system, where pressure and physical property variables are stored. Thus, a cell is referred to as a p-cell (pressure or main cell), u-cell, v-cell, or w-cell. The geometric relationship among the different cell types is illustrated in Figure 1.3. Due to the complexity of describing the geometric parameters, the finite differencing techniques will be discussed for a single dimension.

1.2.5 Finite Difference Scheme

Due to the number and complexity of the partial differential equations in PCGC-3, the finite differencing technique will only be demonstrated on a one-

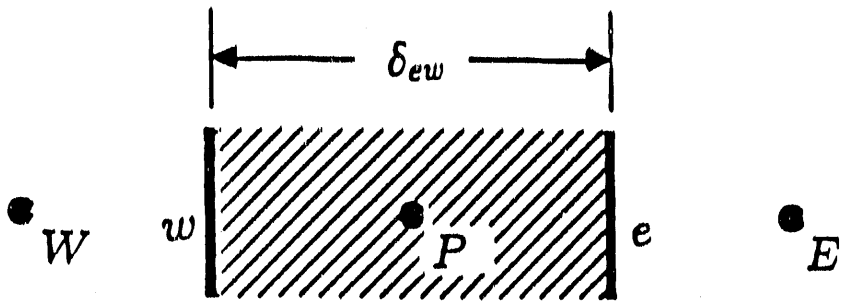

Figure 1.4: Cell Notation on a Regular Grid.

dimensional scalar transport equation. This equation follows and contains both a convective term and a diffusion term.

$$\frac{\partial(\rho u\phi)}{\partial x} - \frac{\partial}{\partial x}\left(\Gamma\frac{\partial\phi}{\partial x}\right) = 0 \tag{1.11}$$

Central Differencing

The finite-difference form of the convection term, $\frac{\partial(\rho u\phi)}{\partial x}$, found in Equation 1.11 can be expressed without any difficulty by the central difference operator. The geometric locations and distances used in these differencing schemes are labeled in Figure 1.4. Thus,

$$\frac{\partial(\rho u\phi)}{\partial x} = \frac{(\rho u)_e\phi_e - (\rho u)_w\phi_w}{\delta_{ew}} \tag{1.12}$$

The convective coefficients representing this differencing are mass fluxes and can be defined as:

$$C_E^O = \frac{(\rho u)_e}{\delta_{ew}}, \quad C_W^O = \frac{(\rho u)_w}{\delta_{ew}} \tag{1.13}$$

Similarly, the diffusion term $\frac{\partial}{\partial x}\left(\Gamma\frac{\partial\phi}{\partial x}\right)$ in Equation 1.11 can be expressed by a central-difference operator.

$$\frac{\partial}{\partial x}\left(\Gamma\frac{\partial\phi}{\partial x}\right) = \frac{\Gamma_e\frac{\partial\phi}{\partial x}|_e - \Gamma_w\frac{\partial\phi}{\partial x}|_w}{\delta_{ew}} \tag{1.14}$$

This can be expanded to equal:

$$\frac{\partial}{\partial x}\left(\Gamma\frac{\partial\phi}{\partial x}\right) = \frac{\Gamma_e\frac{\phi_E-\phi_P}{\delta_{PE}} - \Gamma_w\frac{\phi_P-\phi_W}{\delta_{PW}}}{\delta_{ew}} \tag{1.15}$$

On a regular grid, δ_{PE} equals δ_{PW}. This allows Equation 1.15 to be rewritten as:

$$\frac{\partial}{\partial x}\left(\Gamma\frac{\partial\phi}{\partial x}\right) = \frac{\Gamma_e\frac{\phi_E}{\delta_{PE}} + \Gamma_w\frac{\phi_W}{\delta_{PW}}}{\delta_{ew}} \tag{1.16}$$

The following diffusion coefficients result:

$$D_E^o = \frac{\Gamma_e}{\delta_{PE}\delta_{ew}}, \quad D_W^o = \frac{\Gamma_w}{\delta_{PW}\delta_{ew}} \tag{1.17}$$

The convective and diffusive coefficients can be combined to yield overall coefficients.

$$A_E = D_E^o - \frac{C_E^o}{2} \tag{1.18}$$

$$A_W = D_W^o + \frac{C_W^o}{2} \tag{1.19}$$

Upwind Differencing

Stability analysis of this differencing scheme requires that for stability and zero overshoot, the cell Reynolds number ($\frac{u_i\delta x}{\Gamma}$) must be less than 2. Less rigorously, but conceptually correct, this stability problem can be seen by noting that Equation 1.18 will calculate a negative value of A_E when the cell Reynolds number exceeds 2. A large negative velocity will cause the same problem in Equation 1.19. Negative transport coefficients, such as A_E and A_W, can result in solution instabilities. Consequently, upwind formulations are used to promote stability. The upwind differencing employed in PCGC-3 follows:

$$\frac{\partial(\rho u\phi)}{\partial x} = \frac{\rho_P u_P(\phi_P - \phi_W)}{\delta_{PW}}, \quad u_P > 0 \tag{1.20}$$

$$\frac{\partial(\rho u\phi)}{\partial x} = \frac{\rho_P u_P(\phi_E - \phi_P)}{\delta_{PE}}, \quad u_P < 0 \tag{1.21}$$

This results in the following convection coefficients:

$$C_E^P = \frac{u_P}{\delta_{EP}}, \quad C_W^P = \frac{u_P}{\delta_{PW}} \tag{1.22}$$

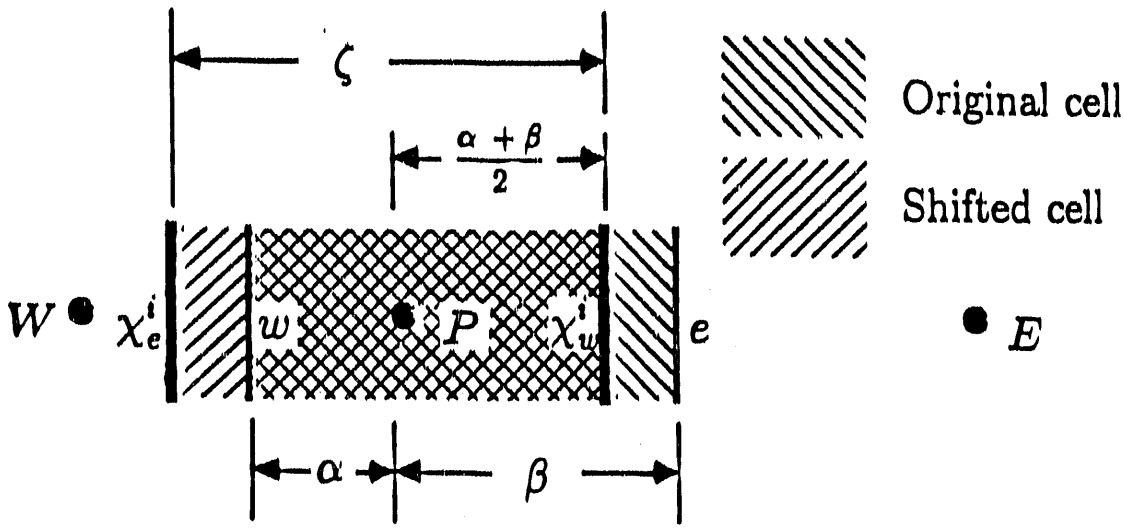

Figure 1.5: Cell Distances on an Irregular Grid.

These upwind formulations are only first-order accurate compared with the second-order accuracy of central differencing. The motivation behind this particular upwind formulation and a discussion of alternative upwind schemes is given in the numerical diffusion subsection of the numerical evaluation section.

Weighted Central Differencing

The differencing schemes just described assume that the distance between grid points remains constant and that cell centers are located half way between cell faces. The ability to handle highly irregular grids is important in industrial modeling applications to allow for the maximization of grid points around the burners, while holding the total number of grid points (and convergence time) to a minimum. Figure 1.5 illustrates the geometric parameters used in the irregular central differencing scheme.

For the irregular grid shown in Figure 1.5, the central differenced convection term is:

$$\frac{\partial(\rho u\phi)}{\partial x} = \frac{(\rho u)^i_e \phi^i_e - (\rho u)^i_w \phi^i_w}{\delta_{ew}} \tag{1.23}$$

The values of any variable, χ, at the new cell faces can be found through a linear interpolation scheme, given in Equations 1.24 and 1.25.

$$\chi_e^i = \frac{\beta - \alpha}{2\zeta}\chi_w + \frac{3\alpha + \beta}{2\zeta}\chi_e \tag{1.24}$$

$$\chi_w^i = \frac{\alpha - \beta}{2\zeta}\chi_e + \frac{3\alpha + \beta}{2\zeta}\chi_w \tag{1.25}$$

Substituting these relations into Equation 1.23 results in Equation 1.27.

$$\frac{\partial(\rho u\phi)}{\partial x} = \frac{1}{\zeta}\left\{\left[\left(\frac{\beta-\alpha}{2\zeta}\right)(\rho u)_w + \left(\frac{3\alpha+\beta}{2\zeta}\right)(\rho u)_e\right]\right. \tag{1.26}$$
$$\left[\left(\frac{\beta-\alpha}{2\zeta}\right)\phi_w + \left(\frac{3\alpha+\beta}{2\zeta}\right)\phi_e\right] - \left[\left(\frac{\alpha-\beta}{2\zeta}\right)(\rho u)_e + \left(\frac{3\beta+\alpha}{2\zeta}\right)(\rho u)_w\right]$$
$$\left.\left[\left(\frac{\alpha-\beta}{2\zeta}\right)\phi_e + \left(\frac{3\beta+\alpha}{2\zeta}\right)\phi_w\right]\right\}$$

Through considerable algebraic manipulation, this equation can be simplified to Equation 1.27.

$$\frac{\partial(\rho u\phi)}{\partial x} = \frac{1}{\zeta}\left\{\left(\frac{-2\beta}{\zeta}\right)(\rho u)_w\phi_w + \left(\frac{2\alpha}{\zeta}\right)(\rho u)_e\phi_e + \right. \tag{1.27}$$
$$\left.\left(\frac{\beta-\alpha}{\zeta}\right)[(\rho u)_e\phi_w + (\rho u)_w\phi_e]\right\}$$

By defining the following weighting coefficients,

$$C_E^w = \frac{2\beta}{\zeta}, \quad C_W^w = \frac{2\alpha}{\zeta}, \quad C_{WE}^w = \frac{C_E^w + C_W^w}{2} \tag{1.28}$$

a relationship between this scheme and the regular grid differencing can be seen.

$$C_E = C_E^w C_E^O + C_{WE}^w C_W^O, \quad C_W = C_W^w C_W^O - C_{WE}^w C_E^O \tag{1.29}$$

The diffusion terms for an irregular grid can be determined in a similar manner.

$$\frac{\partial}{\partial x}\left(\Gamma\frac{\partial\phi}{\partial x}\right) = \frac{\Gamma_{ie}\left(\frac{\phi_E-\phi_P}{\delta_{PE}}\right)_{ie} - \Gamma_{iw}\left(\frac{\phi_P-\phi_W}{\delta_{PW}}\right)_{ie}}{\delta_{ew}} \tag{1.30}$$

Diffusion coefficients can be defined as follows:

$$D_E = C_E^w D_E^O + C_{WE}^w D_W^O \frac{\delta_{PW}}{\delta_{PE}}, \quad D_W = C_W^w D_W^{\cup} - C_{WE}^w D_E^O \frac{\delta_{PE}}{\delta_{PW}} \tag{1.31}$$

so that the weighting parameters used in the convective coefficient can also be employed in the diffusion differencing.

$$\frac{\partial}{\partial x}\left(\Gamma \frac{\partial \phi}{\partial x}\right) = [D_e(\phi_E - \phi_P) - D_w(\phi_P - \phi_W)]\frac{1}{\delta_{ew}} \tag{1.32}$$

The $\frac{\delta_{PW}}{\delta_{PE}}$ and $\frac{\delta_{PE}}{\delta_{PW}}$ terms are needed to provide correct geometric parameters for the nested derivative in the diffusion terms.

The upwind differencing scheme also requires some property interpolation modifications to handle irregular grid structures. Figure 1.5 depicts an irregular cell, where the cell node is not centrally located between the east and west faces. Properties are first averaged to obtain their values on the cell faces. These values are then interpolated by using the inverse lever arm rule to find their values at the cell center.

Combined Differencing

Although central differencing is more accurate than upwind differencing, it suffers from poor stability at high Reynolds numbers. In order to minimize this problem, a combined differencing approach is taken which alternates between the two differencing schemes according to cell Reynolds number. This procedure is illustrated by the following set of equations.

$$A_E = D_E - \frac{C_E}{2} \quad when\ Re\ < 2 \tag{1.33}$$

$$A_E = D_E - C_E^P \quad when\ Re\ > 2 \tag{1.34}$$

$$A_W = D_W + \frac{C_W}{2} \quad when\ Re\ < 2 \tag{1.35}$$

$$A_W = D_W + C_W^P \quad when\ Re\ > 2 \tag{1.36}$$

Re represents the cell Reynolds number in the direction of differencing. Mixed upwind and central differencing is possible. For example, upwind differencing could be used in the x-direction, while central differencing is employed in the other two directions.

Conservative Equation Format

Momentum equations can be solved in their conservative form or non-conservative form in PCGC-3. Tables 1.1 and 1.2 presented the momentum equations in their conservative form. The non-conservative form is obtained by subtracting the product of ϕ and the continuity equation from the conservative form. Because the continuity equation equals zero, this subtraction does not alter the validity of the momentum equations.

Roach (1976) suggests that the conservative form might increase stability of the solution algorithm. PCGC-3 contains the option to use either the conservative or non-conservative form of the momentum equations. Neither method clearly showed superior properties over the other. The code default is the conservative form. The conservative form is modeled by incorporating the cell mass balance to either A_P or S_U, depending on the sign of S_P^M.

$$S_P^M = C_E - C_W + C_N - C_S + C_T - C_B \tag{1.37}$$

$$C_P^+ = max\ \{0.0,\ S_P^M\} \tag{1.38}$$

$$C_P^- = min\ \{0.0,\ S_P^M\} \tag{1.39}$$

$$S_U = S_U - C_P^- \phi_P \tag{1.40}$$

$$A_P = A_P - S_P + C_P^+ \tag{1.41}$$

In order for the matrix solver to function properly, the finite difference coefficients must form a diagonally dominant matrix. This is the reason for the use of two equations, Equations 1.40 and 1.41, to add the continuity term into the momentum equations. Source terms in Tables 1.1 and 1.2 are also placed in the coefficient A_P when these terms are linear functions of the variable being solved. This is only performed for negative source terms to prevent the diagonal element of the matrix, A_P, from becoming less than the sum of the off-diagonal elements. This linearization improves convergence characteristics.

Final Form of Difference Equation

The final form of the ϕ-finite-difference equation in PCGC-3 is:

$$A_P\phi_P = A_E\phi_E + A_W\phi_W + A_N\phi_N + A_S\phi_S + A_T\phi_T + A_B\phi_B + S_U \tag{1.42}$$

where,

$$A_P = A_E + A_W + A_N + A_S + A_T + A_B + C_P^+ - S_P \tag{1.43}$$

$$A_N = D_N - \frac{C_N}{2} \quad for\ N\ =\ E,\ N,\ T\ \ when\ Re\ < 2 \tag{1.44}$$

$$A_N = D_N - C_N^P \quad for\ N\ =\ E,\ N,\ T\ \ when\ Re\ > 2 \tag{1.45}$$

$$A_N = D_N + \frac{C_N}{2} \quad for\ N\ =\ W,\ S,\ B\ \ when\ Re\ < 2 \tag{1.46}$$

$$A_N = D_N + C_N^P \quad for\ N\ =\ W,\ S,\ B\ \ when\ Re\ > 2 \tag{1.47}$$

$$D_N = C_N^w D_N^O + C_{ON}^w D_O^O \frac{\delta_{OP}}{\delta_{PN}}, \quad for\ N = E,N,T;\ O = W,S,B \tag{1.48}$$

$$D_N = C_N^w D_N^O - C_{NO}^w D_O^O \frac{\delta_{PO}}{\delta_{PN}}, \quad for\ N = W,S,B;\ O = E,N,T \tag{1.49}$$

$$D_N^O = \frac{\Gamma_F}{\delta_{PN}\delta_{cell}}, \quad for\ N = E,N,T;\ F = e,n,t \tag{1.50}$$

$$C_N = C_N^w C_N^O + C_{ON}^w C_O^O \quad for\ N = W,S,B;\ O = E,N,T \tag{1.51}$$

$$C_N = C_N^w C_N^O - C_{ON}^w C_O^O \quad for\ N = E,N,T;\ O = W,S,B \tag{1.52}$$

$$C_N^O = \frac{\rho u_F}{\delta_{cell}}, \quad for\ N = E,W,N,S,T,B;\ and\ F = e,w,n,s,t,b \tag{1.53}$$

$$C_N^P = \frac{u_P}{\delta_{PN}}, \quad for\ N = E,W,N,S,T,B \tag{1.54}$$

$$S_P^M = C_E - C_W + C_N - C_S + C_T - C_B \tag{1.55}$$

$$C_P^+ = max\ \{0.0,\ S_P^M\} \tag{1.56}$$

$$C_P^- = min\ \{0.0,\ S_P^M\} \tag{1.57}$$

$$S_U = S_U + D_\phi(p_d - p_P) - C_P^- \phi_P, \quad for\ \phi\ =\ \tilde{f},\tilde{g},\tilde{k},and\ \tilde{\epsilon} \tag{1.58}$$

$$S_U = S_U - C_P^- \phi_P, \quad for\ \phi\ =\ \tilde{u},\tilde{v},and\ \tilde{w} \tag{1.59}$$

1.2.6 Matrix Solution Procedure

PCGC-3 creates a large system of linear algebraic finite-difference equations and many solution techniques are available. Roache (1976) presents some of the more popular methods. Matrix inversion and other direct techniques are usually unacceptable because of the large number of equations involved and the matrix size; therefore, iterative methods are normally employed. The formulation of Gosman (1969), in terms of vorticity and stream function, utilized a Gauss-Seidel algorithm. This is a point-by-point method in which the equations are solved one at a time, passing from node point to node point throughout the flow field. New values of the variables are used as soon as they become available, and the complete flow field is solved for each dependent variable before going to the next dependent variable.

The technique originally used in PCGC-3 simultaneously solved a line of node points in a so-called line-by-line method. This technique, as implemented in an efficient Tri-Diagonal Matrix Algorithm (TDMA), follows the form of Equation 1.60.

$$b_i\phi_i = a_i\phi_{i-1} + c_i\phi_{i+1} + d_i, \tag{1.60}$$

The TDMA can be implemented to solve Equation 1.42 by considering the equations for all the control volumes along a grid line with the last or best estimates for the values of ϕ along the neighboring grid lines, and hence constructing a tridiagonal equation set which can be solved by the TDMA. In this manner, the first traverse can proceed along all the grid lines in the x-direction. Then, using this solution as the best estimate, proceed along grid lines in the y-direction and finally, the z-direction.

For the initial x-direction sweep, Equation 1.42 is written as:

$$A_P\phi_P = A_E\phi_E + A_W\phi_W + (A_N\phi_N + A_S\phi_S + A_T\phi_T + A_B\phi_B + S_U) \tag{1.61}$$

For the y-direction sweep and z-direction sweep, Equation 1.42 is written as:

$$A_P\phi_P = A_N\phi_N + A_S\phi_S + (A_E\phi_E + A_W\phi_W + A_T\phi_T + A_B\phi_B + S_U) \tag{1.62}$$

$$A_P\phi_P = A_T\phi_T + A_B\phi_B + (A_E\phi_E + A_W\phi_W + A_N\phi_N + A_S\phi_S + S_U) \tag{1.63}$$

The terms in parenthesis in each of these equations are considered known so that the TDMA can be applied. Each sweep through the matrix updates the

values of ϕ_i. The relationship between Equation 1.42 and Equation 1.60 can now be clarified. In each of the three tridiagonal systems, four (the terms in parenthesis in Equations 1.61, 1.62, and 1.63) of the six directional difference coefficients are incorporated into the source term, d_i. The A_P term is renamed to be b_i, leaving the backward and forward coefficients in the sweep direction to be a_i and c_i. Equation 1.42 is thus transformed to be Equation 1.60. The later equation may be transformed into typical tridiagonal format through simple algebra. Equation 1.64 represents this change and Equation 1.65 describes the resulting matrix.

$$-a_i\phi_{i-1} + b_i\phi_i - c_i\phi_{i+1} = d_i \tag{1.64}$$

$$\mathrm{M}\phi = \mathrm{d}, \quad where \ \mathrm{M} = f(a,b,c) \tag{1.65}$$

Two significant improvements were implemented in this matrix solution technique. The TDMA algorithm was changed from a line-by-line method to a plane-by-plane method. Typically, the tridiagonal matrix algorithm is recursive and thus prevents code vectorization. This was remedied by performing simultaneous line sweeps throughout an entire plane. The innermost loop of the TDMA is inverted with one of the two outer loops, removing the recursion from the inner loop. This loop repositioning required several arrays to be changed from one to two dimensions.

A second major change in the TDMA was suggested by Van Doormaal (1984). This involved the implementation of an acceleration technique similar to Stone's partial cancellation (Stone, 1968). The technique can be simply described as an under-relaxation of the ϕ update. First, $\phi^{BE}_{i,j+1,k}$, a better estimate of $\phi_{i,j+1,k}$ was defined as follows:

$$\phi^{BE}_{i,j+1,k} = \phi^{old}_{i,j+1,k} + \theta(\phi_{i,j+1,k} - \phi^{old}_{i,j+1,k}) \tag{1.66}$$

This expression was then approximated through the following simplification.

$$\phi^{BE}_{i,j+1,k} \approx \phi^{old}_{i,j+1,k} + \theta(\phi_{i,j,k} - \phi^{old}_{i,j,k}) \tag{1.67}$$

It can be noted that θ is an under-relaxation parameter that must be specified between 0 and 1. If θ is set to 1, this procedure reverts to the normal TDMA procedure.

These changes alter the equation previously described. Equation 1.34 becomes:

$$[A_P - \theta\ (A_N + A_S + A_T)]\phi_P = A_E\phi_E + A_W\phi_W + \qquad (1.68)$$
$$[A_N(\phi_N - \theta\phi_P^{old}) + A_S(\phi_S - \theta\phi_P^{old}) + A_T(\phi_T - \theta\phi_P^{old}) + A_B\phi_B + S_U]$$

The equations in the TDMA solution algorithm require reformulation. The TDMA derivation provided throughout this section applies only to the x-directional sweeps. Similar equations were derived and implemented for the other two directional sweeps. It must be remembered that the TDMA is an iterative solution technique to solve the finite-difference equations, the coefficients of which are only tentative and require updating to account for the changes in the values of the variables. The number of sweeps needed for an accurate solution of the finite-difference equations before the coefficients are recalculated is arbitrary and problem-dependent. Originally, four sweeps of each variable were conducted. A convergence evaluation scheme was incorporated to determine the number of sweeps for each equation.

1.2.7 Vectorization

PCGC-3 was developed on a series of CONVEX computers which possessed the ability to process vectors. Numerous coding changes were implemented to take advantage of the vector processing architecture. The matrix solver was initially observed to account for up to 65% of the model's overall run time on a CONVEX C-1 computer. This was due to the inability of the FORTRAN compiler to vectorize the TDMA solver due to the recursion. This motivated the loop inversion described in the preceding section. Moving the recursion to the middle loop in the TDMA allowed the inner loop to be vectorized. If the recursion is placed in the outer loop, both of the inside loops can be combined and a full vectorization can take place. This method requires much additional redimensioning of arrays. Both the full and partial vectorization schemes were coded and tested.

Table 1.3 presents the results of a factorial experiment with three cases and three matrix solvers. The partial or single loop inversion was the fastest method for the cases tested. The full vectorization suffered from increased data storage and retrieval which could not make up for the additional vector lengths.

Table 1.3: Vectorization Results.

Number of Nodes	Vector-ization	Solver Time [s]	Percent Change	Run time [s]	Percent Change	$\frac{\text{Solver time}}{\text{Run time}}$ [%]
CASE A	None	129	0.0	406	0.0	31.8
12x12x22	Part	41	68.2	327	19.5	12.5
(3168)	Full	81	37.2	358	11.8	22.5
CASE B	None	3079	0.0	7017	0.0	43.9
31x31x40	Part	874	71.6	4911	30.0	17.8
(38440)	Full	2768	37.2	6709	4.4	41.2
CASE C	None	5883	0.0	14140	0.0	41.6
35x45x65	Part	1857	68.4	10273	27.6	18.1
(102375)	Full	5296	10.0	13790	2.5	38.4

Table 1.4: Extent of Vectorization.

Size	Iterations	Scalar [s]	Vector [s]	Speed-up
25x15x3	100	78.31	22.60	3.47
40x20x21	10	1008.61	184.26	5.47
80x50x50	10	9952.14	1486.82	6.69

Additional code alterations were made to increase code vectorization. The matrix solver vectorization resulted in $\sim$ 40% reduction in simulation time. A further 50% reduction was achieved through extensive recoding of the model's subroutines. The two most significant general changes were the scalar specification for all boundary condition loops and the removal of most "IF" statements that were nested in inner loops. The extent of code vectorization is illustrated in Table 1.4. This table displays simulation times for three cases involving both a scalar run and a vector run.

1.2.8 Model Geometric Capabilities

The model allows for simulations to be made in either the Cartesian or polar coordinate system. Initial validation of the model was made through comparisons with PCGC-2, which has been extensively evaluated (Smith, *et al.*,

1981). A case was first run and documented with the axi-symmetric model. This axi-symmetric geometry was then input and flow was simulated with the three-dimensional model for both coordinate systems. Predictions from the 3-D cylindrical case were indistinguishable from the PCGC-2 results. Cartesian predictions were similarly validated through comparison. These comparisons were made before significant changes in the finite differencing scheme were implemented.

All boundary conditions are controlled by a single three-dimensional array which specifies each cell (computational node) as being part of an inlet, flow field, or a wall (intrusion). Complex geometries can be easily modeled through specification of this geometric description array. Inlets and outlets on all six faces of the computational domain can be set up in this same array. There is no limitation to the number of inlets or outlets on any one face, nor the number of faces having inlets, outlets, or both. However, if an outlet is located within a recirculation zone, an overall mass balance cannot be adequately closed and the case will not fully converge. The model will also handle structural intrusions at any point in the flow field. Intrusions are needed to model such important features as inlet quarls, ash bins, tube banks, clipped corners, and the furnace nose. Test cases, which included constricted exits, flow around successive baffles, and bluff bodies surrounded on all six sides by the flow field, have successfully converged.

A subroutine has been included in the model that checks each simulation for common errors. This error checking occurs at three different stages of each simulation. Initially, the input data is evaluated to find if any inconsistent variable specifications have occurred. The initial inlet velocities and final converged velocities are checked to see if velocities high enough to cause compressible flow are being predicted. This subroutine also checks for recirculating flow in the outlet regions.

1.2.9 Coding Structure of Model

The model consists of a main driver and fifty-three subroutines, each made up of an average of about 170 lines of FORTRAN coding. This modular structure allows each subroutine to be task-specific. This design aids the individual who wishes to better understand code elements and also eases the incorporation of submodels. The model was designed to call most subroutines from a central program. This allows the user a clearer picture of the

information flow within PCGC-3.

The comprehensive model has been coded to strictly adhere to FORTRAN 77 standards. This allows complete portability of the code. The model has been successfully compiled on Convex systems, Sun Microsystem computers, and a Silicon Graphics workstation. PCGC-2 was developed using VAX FORTRAN extensions, which necessitated several coding changes in order to produce operational versions for other computing systems.

During the development of PCGC-3, all code enhancements were included as model options. This allows previous and less complex simulations to be performed to monitor model progress and isolate coding errors. This procedure was based on difficulties with PCGC-2. For example, the turbulence model cannot be normally turned off in PCGC-2. Several coding changes are required to simulate laminar flows with PCGC-2. PCGC-3 does not suffer from these problems due to its formulation.

A user's manual for PCGC-3 is in preparation and will be available for detailed documentation of all options within the code. This user's manual will provide information on using the code as well as sample problems.

1.2.10 PCGC-2 Enhancements

This subsection will explain some of the major differences between PCGC-3 and PCGC-2.

Boundary Condition Generality

PCGC-2 was designed to model axi-symmetrical laboratory combustion systems and its boundary conditions are restricted in many ways. Inlets were only allowed on the west and north faces and an outlet was required on the east face. A centerline with symmetry boundary conditions was placed along the south side of the computational domain.

Due to the wide diversity of three-dimensional furnaces and gasifiers, the boundary conditions for PCGC-3 were designed with maximum versatility. Inlets, outlets, and symmetry boundary conditions can be placed anywhere on the outside faces of the computational domain. Furthermore, flow field obstructions (intrusions) can be specified at any exterior or interior node point.

Symmetry boundary conditions can be placed on any face of the computational domain. This option provides a means for two-dimensional simulations. Some industrial furnaces contain planes of symmetry and tremendous computational saving can be achieved through partitioning the furnace into symmetric sections. Some cross-fired geometries can be separated into symmetrical quadrants.

Weighted Central Differencing

The differencing scheme employed in PCGC-2 was designed for regular grid systems. Slightly irregular grid structures could be employed without introducing significant numerical error. The degree of irregularity allowed in PCGC-2 was a 10% reduction or increase in spacing between neighboring nodes. In order to efficiently handle the large disparity of scales found in three-dimensional furnace configurations, more freedom in the grid spacing was needed. A weighted central differencing scheme, described earlier in this section, was implemented to allow highly irregular grids.

Nodal Upwind Differencing

The simple upwind differencing employed in PCGC-2 suffers from false or numerical diffusion. Patankar (1980) has extensively documented and evaluated the extent of this problem. The subsection on numerical evaluation will explain and quantify the inaccuracies associated with this diffusion. The accuracy of a new upwind scheme will also be shown. This new scheme was described previously in this section.

Matrix Solver

The TDMA employed in the three-dimensional code contains two major differences from PCGC-2. An acceleration parameter was incorporated into the algorithm to relax variable updates. The improvement in convergence associated with this change will be demonstrated in a later section. The TDMA was also rewritten through the inverting of loops to allow for vectorization. This resulted in significant reductions in simulation times.

Pressure-Velocity Coupling Algorithms

PCGC-2 allowed the user to specify either the SIMPLE or SIMPLER algorithm to handle the coupling between the velocity and pressure calculations. PCGC-3 contains four coupling options: SIMPLE, SIMPLEC, SIMPLER, and SIMPLEST. Furthermore, more than one option can be specified, i.e., SIMPLERC. A comparison of these algorithms and an evaluation of their respective performances will be given later.

Buoyancy

PCGC-2 does not model the effect of gravity on the gas phase. Buoyancy terms have been added to the source terms for the momentum equations (see Tables 1.1 and 1.2 in PCGC-3). Buoyancy effects are more significant in large flow systems such as industrial furnaces and gasifiers.

Turbulence Modeling

While PCGC-2 was restricted to always using the k-ϵ turbulence model, PCGC-3 provides three options. The first is the use of a constant eddy diffusivity. Laminar flows can be simulated by specifying eddy viscosity with the value of the laminar viscosity. A mixing length model and the standard k-ϵ turbulence model are the other two options. A low Reynolds flow relaminarization calculation can also be performed in conjunction with the k-ϵ turbulence option. An additional term, $-\frac{2}{3}\rho k$, was incorporated into the momentum equations to account for augmentation to the normal Reynolds stresses due to the turbulent field.

Other Changes

The outlet boundary conditions were changed from quadratic extrapolation to a symmetry or zero-gradient condition. Unrealistic values calculated in the extrapolation schemes motivated this change. An error checking subroutine was incorporated to notify the user of typical problems encountered with incorrect data specification. Significant vectorization was achieved in the model through rigorous recoding. The initialization procedure was altered and values for turbulence submodel variables were included in the initializa-

tion. PCGC-3 can utilize either the conservative or non-conservative form of the momentum equations.

1.3 Advanced Nurnerical Methods for Coal Combustion Simulations

1.3.1 Introduction

The combustion of coal has historically provided significant contributions to the world's energy requirements. Computer simulations can provide a means of designing, evaluating and optimizing these coal furnaces, in addition to providing insights into the combustion processes. However, the complexities of coal combustion introduce significant challenges in making simulations. Gas fluid dynamics, turbulence, homogeneous and heterogeneous phase chemical kinetics, convective and radiative heat transfer, and particle dispersion are processes which are highly coupled and increase the computational requirements for coal combustion simulations. The large disparity in scales which exist in these furnaces, with overall dimensions of hundreds of feet and inlet jets on the order of inches, strain computational abilities of current computer technology.

Very efficient numerical methods are essential if these types of predictions are to be made in any practical time frame, even on Cray class computers. For example, a bench-scale, axi-symmetric comprehensive combustion code simulation (1,600 nodes) using *older* numerical techniques requires approximately 10 CPU hours on a CONVEX C120 vector computer. For industrial furnace predictions, it is estimated that 1,000,000 node calculations will be necessary (Gillis and Smith, 1988). The run times for this type of simulation without efficient numerical methods from extrapolation of the older method would require four million CPU hours.

The current effort is aimed at the development of an industrial scale, three-dimensional, coal combustion model (Gillis and Smith, 1988; Smith and Gillis, 1988; and Smith and Gillis, 1988), based on past development of two-dimensional, axi-symmetric codes used to simulate laboratory-scale furnaces (Smoot and Smith, 1985). This subsection examines potential improvements in computational efficiency for 3-D simulations by using multigrid methods. In order to evaluate the potential of these improvements, a 2-D axi-symmetric

Table 1.5: Axi-symmetric Navier-Stokes Equations with Non-Constant ρ and μ.

$$\frac{\partial}{\partial x}(r\rho uu) + \frac{\partial}{\partial r}(r\rho vu) - 2\frac{\partial}{\partial x}(r\mu\frac{\partial u}{\partial x}) - \frac{\partial}{\partial r}(r\mu\frac{\partial u}{\partial r}) - \frac{\partial}{\partial r}(r\mu\frac{\partial v}{\partial x}) = -\frac{\partial p}{\partial x} + S_u \qquad (1.69)$$

$$\frac{\partial}{\partial x}(r\rho uv) + \frac{\partial}{\partial r}(r\rho vv) - \frac{\partial}{\partial x}(r\mu\frac{\partial v}{\partial x}) - 2\frac{\partial}{\partial r}(r\mu\frac{\partial v}{\partial r}) - \frac{\partial}{\partial x}(r\mu\frac{\partial u}{\partial r}) + \frac{2\mu v}{r} = -\frac{\partial p}{\partial r} + S_v \qquad (1.70)$$

$$\frac{\partial}{\partial x}(r\rho u) + \frac{\partial}{\partial r}(r\rho v) = S_m \qquad (1.71)$$

multigrid fluid dynamics code was developed which could be compared with the fluid dynamics portion of a 2-D comprehensive coal combustion code.

1.3.2 Numerical Scheme

The derivation and analysis of multigrid methods are fully presented in many other sources, for example: Brandt, 1979, 1984; Hackbush and Trottenberg, 1982. Only those aspects which are unique to this application will be discussed here.

Throughout this subsection of the report, the density ρ and viscosity μ are held constant for all simulations. However, equations of motion which are employed (Table 1.5) do not require this restriction (Bird, et al., 1960).

To solve these equations, a full approximation scheme/full multigrid algorithm (FAS/FMG) is used with W(1,1) cycles (Brandt, 1984). The multigrid algorithm is an efficient *solver*, but requires an efficient *smoother*. That is, the purpose of each iteration is to smooth the solution so that it can be well approximated on a coarser grid. This smoothing operation is done as

efficiently as possible in the context of the entire coupled system of equations.

Historically, SIMPLE-based methods (Patankar, 1980) have been used quite extensively to couple the momentum and continuity equations. For this multigrid application, a *distributive relaxation* (Brandt, 1984) method has been chosen to maximize efficiency in smoothing. This method can also be used to properly couple additional equations, such as those which describe fluid turbulence. For only the momentum and continuity equations, the distributive relaxation and SIMPLE methods are quite similar, although their derivations are quite different. In both cases, each momentum equation is sequentially smoothed or relaxed for its corresponding velocity component, based on existing pressure and velocity fields. Then corrections to the velocity and pressure fields are made such that continuity is satisfied. These correction equations are where the two methods differ. For distributive relaxation, the correction equations for the above system of equations are listed in Table 1.6 (Christensen, 1988). These corrections are made in a cell-by-cell manner, rather than globally as usually practiced when using the SIMPLE-based techniques. Performing the corrections in this manner insures that the residuals for each velocity node remain unchanged, and the smoothing properties for the system of equations is efficient.

1.3.3 Results

One important geometrical consideration for combustion flow conditions is the aspect ratio, or the ratio of the dimensions of the reactor. Figure 1.6 illustrates a typical bench-scale furnace simulation with an aspect ratio of 8.0. If equal numbers of nodes are used in both directions, this aspect ratio will have an impact on the convergence rates of the multigrid solver. Certainly, the error of the solution will be affected also. Figure 1.7 shows the effect of increasing aspect ratio on the convergence rates of the multigrid method. In this case, the smoothing algorithm for the momentum equations was done by solving radial lines of nodes implicitly. This is an effective smoother when the coefficients which correspond to one dimension are much larger than those in the other dimension(s) (Thole and Trottenberg, 1985). As the aspect ratio is increased from 1.0, convergence rates decrease due to the increased relative magnitude of the coefficients in the radial direction. Unfortunately, the dominant flow is in the axial direction and for aspect ratios greater than

Table 1.6: Velocity and Pressure Correction Equations used by Distributive Relaxation on a Staggered Grid, where R_c^0 is the Residual of Continuity before the Corrections are made, and A_X and C_x are the Coefficients from the Momentum and Continuity Discretizations, Respectively.

$$u_{i,j} = u_{i,j} - \frac{\Delta r}{\Delta x(C_n + C_s) + \Delta r(C_e + C_w)} R_c^0, \tag{1.72}$$

$$u_{i+1,j} = u_{i+1,j} + \frac{\Delta r}{\Delta x(C_n + C_s) + \Delta r(C_e + C_w)} R_c^0, \tag{1.73}$$

$$v_{i,j} = v_{i,j} - \frac{\Delta x}{\Delta x(C_n + C_s) + \Delta r(C_e + C_w)} R_c^0, \tag{1.74}$$

$$v_{i,j+1} = v_{i,j+1} + \frac{\Delta x}{\Delta x(C_n + C_s) + \Delta r(C_e + C_w)} R_c^0. \tag{1.75}$$

$$p_{i-1,j} = p_{i-1,j} - A_{E_{i-1,j}} \frac{\Delta x \Delta r}{\Delta x(C_n + C_s) + \Delta r(C_e + C_w)} R_c^0, \tag{1.76}$$

$$p_{i+1,j} = p_{i+1,j} - A_{W_{i+1,j}} \frac{\Delta x \Delta r}{\Delta x(C_n + C_s) + \Delta r(C_e + C_w)} R_c^0, \tag{1.77}$$

$$p_{i,j-1} = p_{i,j-1} - A_{N_{i,j-1}} \frac{\Delta x \Delta r}{\Delta x(C_n + C_s) + \Delta r(C_e + C_w)} R_c^0, \tag{1.78}$$

$$p_{i,j+1} = p_{i,j+1} - A_{S_{i,j+1}} \frac{\Delta x \Delta r}{\Delta x(C_n + C_s) + \Delta r(C_e + C_w)} R_c^0, \tag{1.79}$$

$$p_{i,j} = p_{i,j} + A_{P_{i,j}} \frac{\Delta x \Delta r}{\Delta x(C_n + C_s) + \Delta r(C_e + C_w)} R_c^0. \tag{1.80}$$

4.0, the axial flow cannot *diffuse* properly throughout the domain resulting in deteriorating convergence properties.

For the reactor illustrated in Figure 1.6, a comparison of the performance of the multigrid and SIMPLE techniques was made. One prediction was performed using distributive relaxation and multigriding. Another calculation was obtained using the SIMPLER (Patankar, 1980) pressure correction algorithm on one grid. In both cases, viscosity was chosen to be 0.2 cP, reflecting a constant eddy diffusivity for turbulence. Both solutions were obtained on a 66x66 node mesh. For the SIMPLER calculation, under-relaxation factors of 0.7 were used for the two momentum equations. Run times were normalized by the amount of computational time required to make one complete calculation (both momentum equations and continuity) on the finest grid using distributive relaxation. The run time comparison between these two simulations is shown in Figure 1.8. The convergence of the multigrid code is fast and constant, demonstrating a significant improvement over the SIMPLER algorithm.

1.3.4 Conclusions

A substantial improvement in computational time has been demonstrated for a two-dimensional, axi-symmetric flow problem over traditional methods. The reason for this improvement is the multigrid error correction algorithm. Even for complex flows and geometries, the multigrid algorithm is able to avoid numerical stalling, and convergence is constant and fast. Some aspects of complex geometry in combustion chambers contribute to degradations in the optimum convergence rate.

1.4 Graphics Pre-Processor

1.4.1 Introduction

As the computer increases in its ability to make computations and store data, finite element and finite difference models increase in size and complexity. In the beginning, the geometric input parameters or graphics model were small and not very complex, and they could be entered into a data file in a few hours. But as the size and complexity of the geometric models has increased,

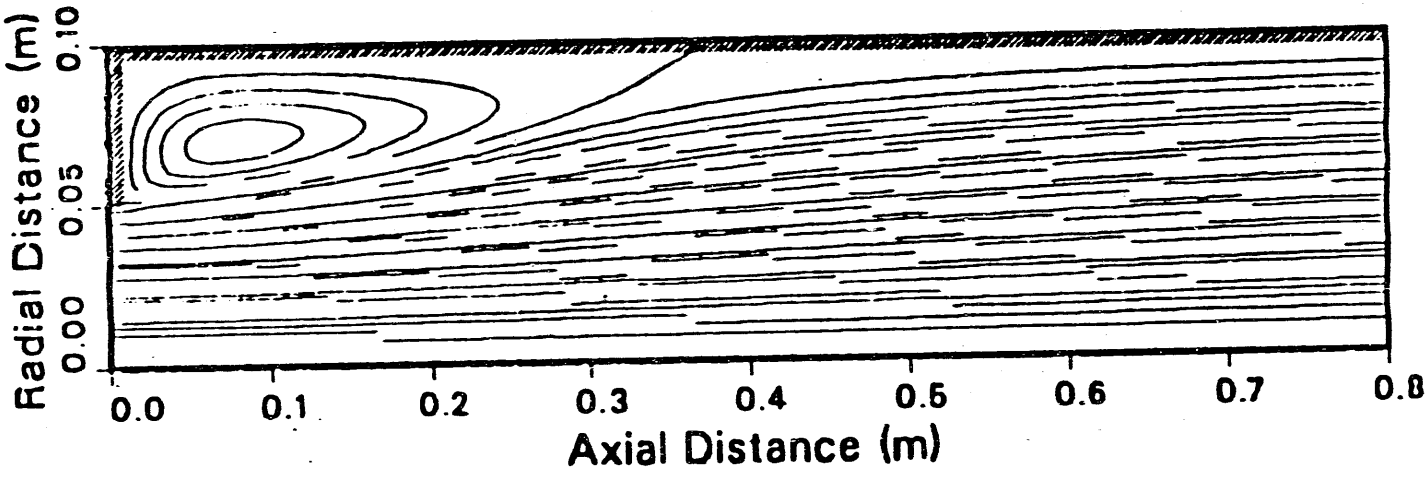

Figure 1.6: Reactor Geometry and Flow Pattern of a Bench-Scale Furnace Used in Multigrid Comparisons with Maximum Inlet Velocities on the Order of 30.0 m/s.

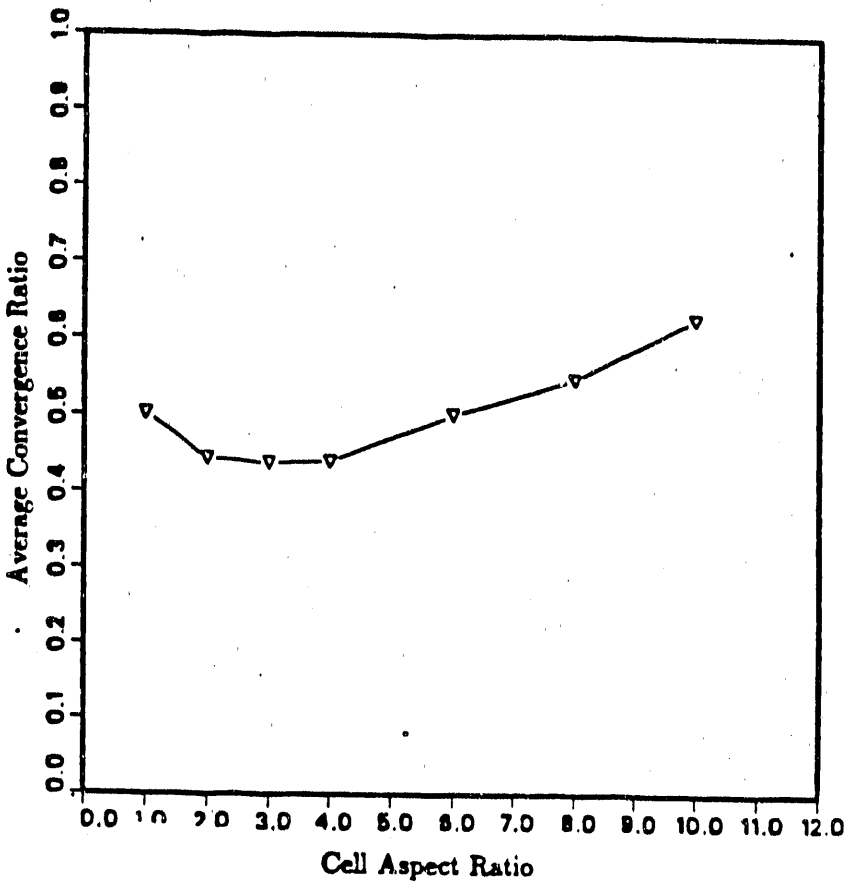

Figure 1.7: Effect of Varying Aspect Ratio on Convergence Rates in Multigrid Calculations.

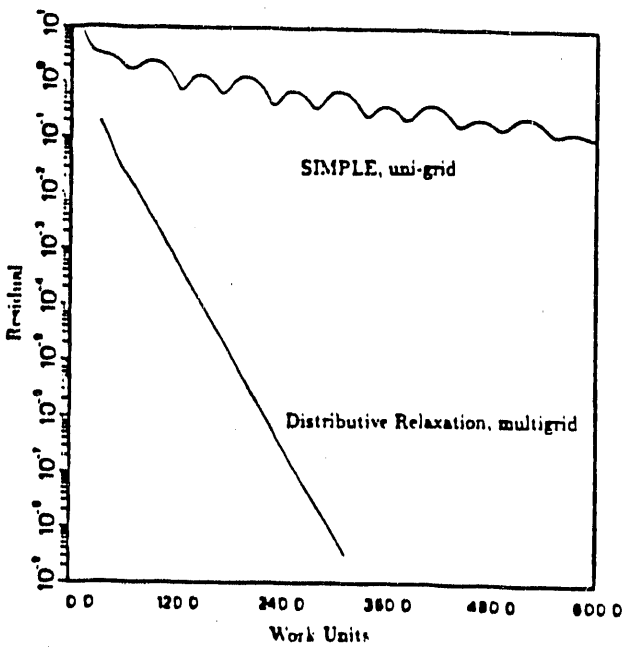

Figure 1.8: Comparisons of Computational Run Times for an Axi-symmetric Flow Case Using a Multigrid Code and a Single Grid Code.

the time needed to create an accurate model has increased dramatically. The tedious, error-prone way of searching through huge data files, trying to make sure the input for a model is correct, prevents the engineer from accomplishing the more important task of analyzing, debugging, and testing of new techniques, not to mention the limited number of test models that are being used to debug and test codes before they are released. The ability to make fast, accurate models is crucial to the production of finite element and finite difference codes. The pre-processor allows one to define this mesh graphically with menu and mouse driven inputs.

1.4.2 Versatility of the Pre-Processor

With hardware technologies changing every 14-18 months, the need for proven, robust codes that will run on a wide range of computers is crucial to the longevity and usability of a code. Therefore, this pre-processor's graphics and button/menu selection is all PHIGS (Programmers Hierarchical Interactive Graphics System) based, making the program portable to a wide range of hardware systems. Figure 1.9 is an example of the pre-processor display.

1.4.3 3-D Plane Modeling Pre-Processor

The pre-processor is written in planar form. This means it can only display one plane of the model at a time. Its display capabilities to do 3-D picks are limited only by PHIGS, not by the abilities of the current computers on the market. The pre-processor is written in planar form to match the lattice structure of the combustion model. The planes are defined as follows.

Z-Plane $=xy$ axis
X-Plane $=yz$ axis
Y-Plane $=zx$ axis

The planes are viewed one at a time and go from 1 to n levels of the model. The user can move up and down through the levels of the model with the *UP* and *DOWN* button controls. One can also move directly to a plane by clicking on the plane level number in the control button and entering the level number. To toggle between the different levels (X, Y, Z) of the model, simply click on the plane being displayed in the button control.

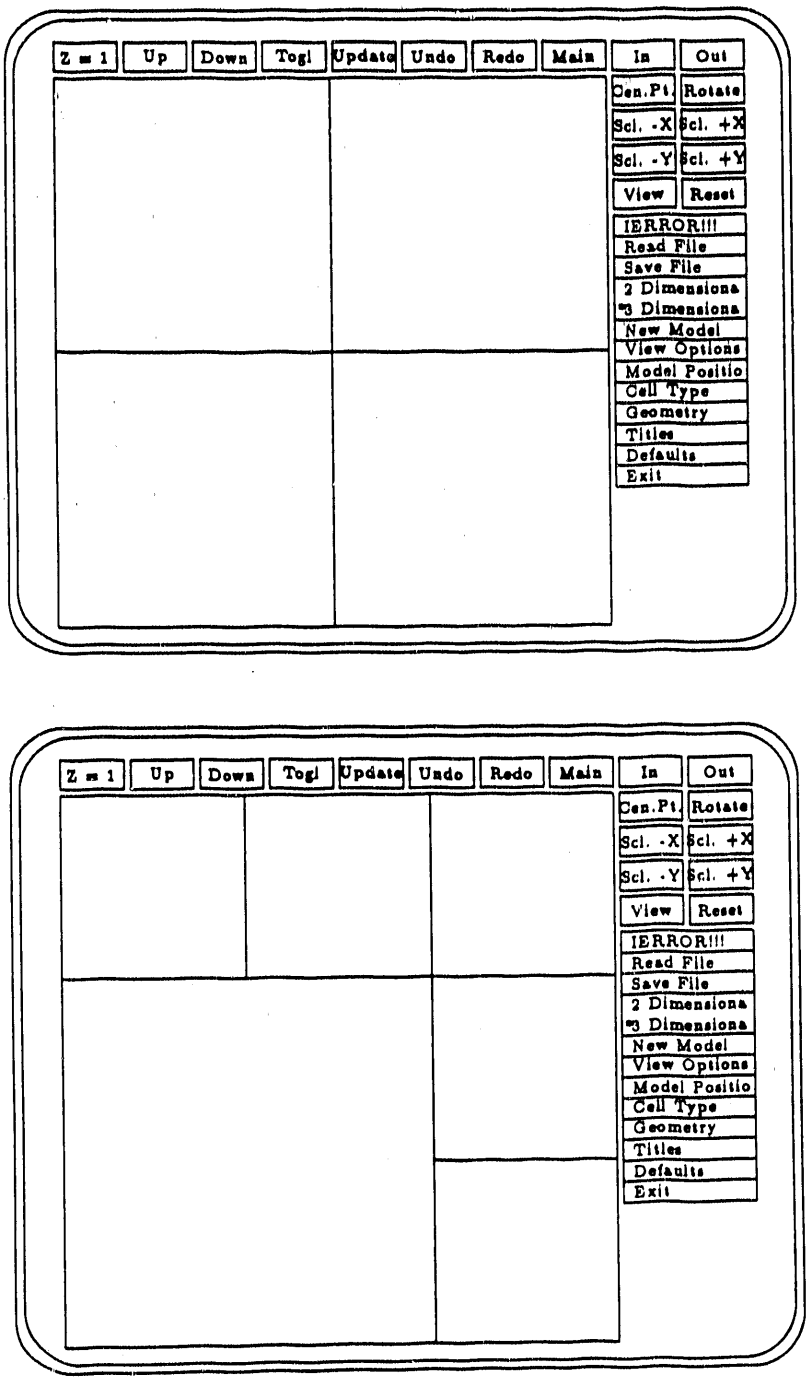

Figure 1.9: Pre-Processor Display.

1.4.4 Multiple Window Pre-Processor

The multiple window pre-processor (MWPP) has the ability to display up to six windows. At the click of a button the user can have the active window enlarged to cover the entire screen, and by clicking again, it will redisplay all the windows. This is a convenient feature when there are a lot of small windows on the screen and the user needs to get a closer look at a view without disturbing the other windows.

The benefit of MWPP is that multiple windows are displayed on the screen. Using the mouse, selections can be made from any of the windows. For an example, assume that window number 1 is currently active. With the mouse, the user activates window number 2. At this time, all menu selections, transformation, and button controls are activated for window number 2. This makes it quick and easy to display the desired model without having to search through the menus then make a selection.

1.4.5 I/O of Pre-Processor

The production of the geometric input data file is the single most important part of the pre-processor. The creation of large and complex geometry input files was previously performed by typing in information regarding each individual cell.

Input

The pre-processor can create a data file from scratch, or read in an existing file that is in either the pre-processor format, or the post-processor format. This gives the user the convenience of modifying old models into more complex and larger data files, without worrying about putting it into the correct format.

Output

If the pre-processor could not create a data file it would be worthless. The pre-processor outputs all data files in the standard pre-processor format. An added feature of the pre-processor is its ability to write out any plane of a 3-D model in 2-D format. This could be very useful in the production and testing of a 3-D code by pulling a plane out of a 3-D model, and checking the 3-D results with an older and more robust 2-D code.

1.4.6 Ongoing Enhancements

The pre-processor was designed to aid in the making of the data files, which include the geometry of the model, and the cell definition. Currently, the 2-D and 3-D codes set the initial values of the inlets of the furnace. Since the initial condition mapping is so dependent on the geometry definition of the model, this function will also be incorporated into the pre-processor in the future.

1.5 Graphics Post-Processor

1.5.1 Introduction

As the size and complexity of computer simulation problems increase, proper visualization tools become ever more important to the analyst in evaluating modeling results and trends within the simulation. The graphics post-processor developed in conjunction with the simulation code attempts to give the user a relatively simple way to interact graphically with the simulation model and properly interpret the results.

1.5.2 Features

The post-processor system includes many features to enhance productivity. As many as six separate graphics windows can be invoked, each with a totally independent database and viewing attributes. Commands are easily entered from menus, using the mouse. Additionally, both the graphics windows and menus are created using standard PHIGS (Programmers Hierarchical Interactive Graphics System) commands, making the program highly portable to a wide variety of hardware platforms. Renderings can be made with either two or three-dimensional data, and more than 75 functions are allowed per database. Several methods for data visualization are supported by the program. These are described below.

1.5.3 Visualization Capabilities

One-dimensional plotting capabilities include the option to display graphs of any function along arbitrary straight lines in space. These plots are simple

line graphs of the function versus distance. Multiple functions can be incorporated on the same plot, but care must be taken when analyzing variables with different units to avoid misinterpretation.

1.5.4 Two-Dimensional Capabilities

Two-dimensional capabilities include planar representations and warped surfaces. Planar surfaces can be rendered using a two-dimensional database, or by disregarding a plane from a three-dimensional database. Functions are represented on the surface by plotting iso-valued function contours, or by color coding the surface according to function value (color fringing). The colors used feature cool colors (blue and green) for low function values and warmer colors (yellow, orange, and red) for the higher function values. The program provides a color legend to allow proper correlation of color with function value. The warped surface representation is often called a '2 1/2 D' rendering, where the planar surface is rendered in three dimensions, with the third dimension or height of the surface proportional to the function value at each point. Warped surfaces give useful visual clues to function plots. Also, it is possible to plot two variables on a single image by using colored contours or fringes for one variable, and surface height for the second.

1.5.5 Three-Dimensional Capabilities

Three-dimensional capabilities of the post-processor include full 3-D images and 3-D vector field renderings. The 3-D image option renders a correct geometric volume of a three-dimensional data base. Rendering modes include line drawing, hidden line, and shaded. Sectioning of the model is an important and powerful feature of the system. The model can be sectioned along any or all of the three axes of the model and unwanted planes discarded, so that interior surfaces can be clearly seen and function contours or fringes displayed. The model can be rotated and viewed from any arbitrary direction.

The vector field capability allows one to view a complete vector function field in three-dimensional space. The model is rendered in outline form, and vector arrows rendered in space to show the characteristics of the vector function at each point. The direction of the vector function is given by the

arrow direction, while the vector magnitude is indicated by a color coding similar to color fringing.

1.5.6 Hardware Requirements

The graphics post-processor was designed to be compatible with a wide range of hardware. The minimum requirements for a hardware platform are 256 colors, no z-buffer, and capability to process PHIGS graphics commands, either in hardware or software. The program is currently supported on the Sun 4/110 and Silicon Graphics Personal Iris workstations. The program should be portable to other systems meeting these minimum requirements.

1.5.7 Ongoing Research

The current post-processor system uses surface representations to evaluate functions in a 3-D model. While useful to a wide range of problems, viewing only the surfaces in a model can limit the amount of information which can be gained from the simulation. Current research focuses on a volumetric rendering system which will allow viewing of a complete three dimensional function field in a single view. The new system will use advanced ray-tracing and voxel rendering techniques to provide transparency, depth cueing, and other visual clues to give a holistic view of the data field.

1.5.8 Conclusions

The Graphics Post Processor is a computer tool which allows the user to quickly visualize the numerical results from two- and three-dimensional combustion simulations. Using a menu/mouse interface system, the user creates graphical representations of simulation models, and analyzes them using contours, color fringes, and other visualization techniques. It allows the user to quickly assimilate information from large-scale simulations.

1.6 Summary of Practical Full-Scale Model Development

This section reviews the research, development, and status of a Pulverized Coal and Gasification Combustion model in three dimensions (PCGC-3). This is the 3-D embodiment of the submodels and numerical methods of the last decade and a half at this laboratory. The 2-D code remains a useful tool for evaluating submodels and for analysis of simple furnaces. As such, the 2- and 3-D codes are considered as a set of tools for analyzing combustion chambers.

To date the 3-D code has incorporated computational fluid dynamics and gaseous particulate transport, in turbulent environments. In moving to calculations in larger chambers a new set of computational constraints have emerged. Differencing schemes, solution procedures, coupling algorithms and other numerical methods have had to be reevaluated in light of the temporal and spatial scales that need resolving in larger furnaces. These are discussed in this section. Graphical interfaces are often the only way of gaining access to the input and output data of large or complex geometries in combustion. The graphics pre- and post-processors developed for this study and continuing under ACERC sponsorship are summarized in this section.

The coupling of multiple chemical and physical processes has been a major emphasis of this research. Particularly, the coupling occurs in a statistically fluctuating field when the processes are usually highly nonlinear. This coupling has been incorporated in the development of the 3-D code and centered around the calculation and evaluation of the 3-D enthalpy field in the 3-D code.

The problems associated with increasing the scale of the calculation has introduced need for new procedures and methods. At different furnace scales, different physical processes dominate. To date, the 3-D code has only been applied to pilot-scale furnaces and smaller. Applications to yet larger systems are forthcoming but will require more careful evaluation and undoubtedly further evaluation of appropriate numerical methods and of submodel adequacy. Like scale-up of real physical furnaces, the scale-up of the furnace model requires a systematic development path.

Development of complex tools where the understanding of basic physics and chemistry are still evolving requires an iterative approach to the appli-

cation of the scientific method. Hypothesizing an approach, and testing and evaluating those approaches, leads to new hypotheses and new testing.

Previous work at BYU laid the foundation for this work. Several comprehensive models (such as PCGC-2) and submodels had been previously developed and evaluated. An extensive literature review was conducted to evaluate applicable numerical algorithms and techniques. A review of existing 3-D combustion models revealed their common basis on the SIMPLE algorithm and their lack of demonstration with fine grid simulations. Iterative, decoupled numerical techniques were found to be the most applicable to this problem because of low computer memory requirements and compatibility with turbulence submodels. PCGC-2 was extended to three dimensions for an evaluation of its numerical techniques and a comparison of the SIMPLE-based algorithm variations. The major observations of this section are:

1. The modeling of flow in industrial furnaces is a very complex process. Turbulence modeling must be included. It can dominate the solution of the Navier-Stokes equations (also discussed in Section 3). The disparity of scales encountered in industrial geometries requires highly-irregular grid structures and requires finite-difference formulation minimizing false diffusion and non-uniform grid-differencing errors. Numerous changes were required in the numerical techniques employed in PCGC-2. Table 1.7 summarizes some of the major changes.

2. A weighted, central-difference formulation is needed to handle irregular grids. This formulation moves control-volume faces to new locations, centering the node point in the cell. The new formulation dramatically reduces exact solution errors on non-uniform grids.

3. Numerical diffusion is, in part, caused by the incorrect evaluation of cell face velocities. A nodal differencing scheme was developed which significantly reduced equation error. This nodal scheme was not characterized by the poor convergence properties of higher order upwind differencing schemes.

4. A decrease in computation time was achieved through extensive vectorization of the code. The reduction was case dependent, but was approximately a factor of four. A major increase in efficiency resulted from changing the TDMA solver from a line-by-line method to a plane-by-plane method. This change removed the recursion in the TDMA subroutine. Additional convergence acceleration was obtained by over-relaxing the matrix solver to

Table 1.7: GAS3D Enhancements over PCGC-2.

Change	Significance
1. Boundary Condition Generality	All configurations possible
2. Weighted Central Differencing	Grid flexibility, highly-irregular grids
3. Nodal Upwind Formulation	Reduces false diffusion, robust
4. Accelerated TDMA	Decreases code convergence times
5. SIMPLE-variation options	Improves speed and flexibility
6. Turbulence Submodels	Additional options, laminar flows
7. Vectorization	Increases speed on vector machines
8. Equation Error Normalization	Convergence can be monitored
9. Equation Convergence Criteria	Improves efficiency
10. Known Solution Option	Identifies coding/algorithmic errors
11. Domain Decomposition Option	Reduces memory requirements
12. Modular Structure	Increases code friendliness
13. Standard FORTRAN	Provides code portability
14. Buoyancy Calculations	Includes gravitational effects
15. Conservative Form Option	Greater numerical flexibility
16. Turbulence Initialization	Improves early convergence
17. Outlet Boundary Conditions	Improves code robustness

become more implicit.

5. The turbulence submodel can dominate the overall convergence process in highly turbulent flows. Studies of computational fluid dynamics (CFD) numerical methods are conducted with a coupled turbulence submodel since the importance of turbulence/velocity coupling tends to increase with increasing Reynolds numbers.

6. An exact solution case was formulated to evaluate finite-differencing errors in the model. This procedure led to several improvements in the differencing scheme and facilitated the removal of numerous coding problems. This technique is an important tool in model development.

7. Convergence evaluations are aided through the normalization of equation errors. This allows comparison of equation errors and the identification of the equation(s) slowing overall convergence. The proximity of convergence to computer round-off error is also provided through this computation.

8. Domain decomposition methods can greatly reduce computer storage requirements at the expense of computational time. The value of subdomaining depends on the memory swapping ability of the computer.

9. Grid resolution requirements were established for three test cases. It was found that corner-fired furnaces require substantially fewer node points than wall-fired furnaces. Grid-independent simulations of a tangential-fired furnace were achieved for grid structures exceeding 15,000 nodes. Complex furnace flows can require up to 500,000 grid points.

10. Several variations of the SIMPLE algorithm were tested for robustness and speed. Convergence rates are strongly dependent on under-relaxation factors. Simulating highly-turbulent flows reduces the significance of algorithm selection on solution time. The determination of optimal algorithm and under-relaxation factors was found to be case dependent. Higher Reynolds number flows require lower under-relaxation factors. The SIMPLEC, SIMPLER, and SIMPLERC algorithms provided the best speed and robustness. This study recommends the use of SIMPLERC with an under-relaxation factor of 0.8.

11. Numerical constraints on large-scale problems require improved numerical methods to avoid numerical stalling in traditional iterative elliptic solvers and to avoid enormous memory requirements of traditional direct solvers.

12. About one order-of-magnitude enhancement in computational efficiency has been demonstrated for 2-D, axi-symmetric flow problems by using the multigrid process. Even for complex geometries and flow conditions, the multigrid algorithms were shown to avoid numerical stalling to produce constant and fast convergence.

13. Preparing geometry input files for 3-D code calculations is tedious and error prone unless an automated computer graphics pre-processor is used. Such a tool has been developed and assists significantly in preparing complex files quickly and correctly through a menu-driven, user-friendly, graphics pre-processor.

14. Access to the large output data base from predictions generated by the 3-D code has been facilitated by a graphics-based post-processor.

Chapter 2

Research Task 2 - Evaluation

2.1 Introduction

Computational combustion calculations have often been questioned since so many engineering approximations are required when describing and coupling multiple physical and chemical processes and when the subprocesses themselves are based on inexact science. Constant evaluation is necessary to identify errant mechanisms and to qualify accuracy. The evaluation procedure is most effective when carried out in conjunction with model development and performed continuously throughout the process. Continual evaluation, revision, and redefinition of the problem statement reassures a more accurate and useful product.

In this study, the evaluation of individual submodels or numerical methods has been performed along with the development of each. This phase of the evaluation has been done as independent as possible from coupling other effects. The results of this level of evaluation are discussed in conjunction with the description of each submodel or numerical method in Sections 1, 3 and 4.

Additionally, evaluations are conducted of the effects of coupling multiple processes. These evaluations have involved comparison of untuned predictions with local measurements from carefully controlled experiments. The experiments are selected to explore a spectrum of complexity including non-reacting gaseous flow (laminar and turbulent), non-reacting, particle-laden flows, reacting gaseous flows, reacting coal flames, etc. We have also at-

tempted to perform evaluations on a continuing spectrum of geometric complexity. These have included 2-D axi-symmetric systems, where the scale has allowed for more complete and accurate data collection, and 3-D systems up to pilot-scale units. This section reports on both the 2-D and 3-D evaluations, both of which are significant components in the analysis and evaluation of the final 3-D product.

Since so many of the subprocesses in coal combustion contain significant amounts of empiricism, we have conducted a nonlinear sensitivity analysis to quantify the impact of uncertainty in input parameters on output functions. This sensitivity study has also been useful in identifying which subprocesses contribute the most error to a prediction and thus may need model improvement. Since the nonlinear sensitivity study is so computationally intensive and since the 3-D code was not completely ready for analysis, the sensitivity analysis was performed with the 2-D code. The results are presented in the next subsection and have helped guide the direction of our research. As shown in that subsection, this newly developed tool will be further used at this laboratory to study different combustion systems and to analyze the 3-D code.

An evaluation by comparing computed simulations with experimental data is not adequate to assure accuracy of the numerical algorithm or to provide confidence that the computer code is free of programming errors. Numerical experiments have been used to explore computational accuracy. In the numerical analysis of the new 3-D code, we have performed a number of numerical tests to evaluate accuracy and robustness. Comparisons of exact solutions with predictions from the computer model have provided an evaluation of algorithmic and coding errors. This evaluation helped quantify the effects of numerical diffusion and the like. Grid resolution requirements were also studied to demonstrate how fine the finite difference mesh must be to assure that discretization error does not overshadow the accuracy of the prediction.

Finally, the section reports on ongoing work to identify and evaluate available 3-D data for model evaluation. At the outset of this study, it was recognized that we would have to rely on data from outside this laboratory for 3-D evaluation. Our attempt to find and to critique these data is presented at the end of this chapter.

2.2 Computational Evaluation - Sensitivity Analysis

2.2.1 Overview of Sensitivity Analysis

Sensitivity analysis has its early roots in stability analysis in ordinary differential equations related to classical mechanics (Tomovic and Vokobratovic, 1972). More recently, sensitivity analysis has been associated with error analysis (Frank, 1978). One of the greatest benefits of a sensitivity analysis is the physical understanding of a complex process gained by performing the analysis.

The general sensitivity problem can be stated as:

$$Lu(x,\alpha) = S \tag{2.1}$$

L represents the general mathematical operator, $u = (u_1, u_2, u_3, ..., u_n)$ represents the vector of model outputs which are determined by the independent variables $x = (x_1, x_2, x_3, ..., x_n)$ and the model parameters $\alpha = (\alpha_1, \alpha_2, \alpha_3, ..., \alpha_n)$. $S = (S_1, S_2, S_3, ..., S_n)$ represents the source terms or forcing functions corresponding to the respective equations in the set. All parameters represented by α have some degree of uncertainty over a range:

$$\alpha_i^- < \alpha_i^o < \alpha_i^+ \tag{2.2}$$

i=1,2,3,.,.,number of parameters which can be represented by some probability density function (pdf) f(α_i), such that the probability (P) that $\alpha-$ and α_i+ is:

$$P(\alpha_i^o) = \int_{\alpha_i^-}^{\alpha_i^+} f(\alpha_i) d\alpha_i \tag{2.3}$$

For completely independent parameters, the probability functions for each parameter can be combined to form a joint pdf representing the most probable parameter space:

$$f(\alpha) = \Pi_{i=1}^{n} f_i(\alpha_i) \tag{2.4}$$

The main goal of a sensitivity analysis is to simultaneously vary all parameters over all probable combinations (representing parameter uncertainty) and to quantify the effects this variation has on a specific model output. Better estimates of the key parameters, representing less parametric uncertainty, can then be used to obtain more realistic model predictions.

During the initial development stages of a numerical model of a particular system, one must invariably test the model for a finite number of parameter values which characterize the system. This represents a crude form of sensitivity analysis and would represent a global sensitivity analysis if the model were tested at all possible parameter values. Of course, this type of analysis is not feasible for realistic problems so various types of sensitivity analysis techniques have been developed to approximately examine the total parameter space. These techniques include one-at-a-time ("brute force") methods, local [finite differences, direct differential and adjoint (Green's function)] methods, and global nonlinear (Fourier Amplitude Sensitivity Test [FAST] and stochastic) methods.

One-at-a-time methods are commonly referred to as trend analysis. This entails holding all parameters but one constant and observing the effects variations in one parameter have on a specific model prediction. Linear methods require one to vary parameters between a high and a low value to approximate the sensitivity coefficient ($du_i/d\alpha_j$) for the i^{th} output function with respect to the j^{th} parameter. This method is limited to small parameter ranges because of the linear difference approximation to the sensitivity coefficient. Finally, global nonlinear methods are applied over all probable parameter values which allows one to investigate the sensitivity of mode predictions to simultaneous variations in two or more parameters. Each method has its place and can provide information about model sensitivity to parametric uncertainty.

Early global sensitivity techniques required great computational expense. However, recent development of efficient global methods have made it more feasible to conduct comprehensive sensitivity analysis of complex models, such as PCGC-2. Efficient techniques, described in the literature, include direct methods (Atherton, et al., 1975; Dickinson and Gelinas, 1976; Caracotsios and Stewart, 1985; Dunker, 1981), orthogonal polynomial methods (Cukier, et al., 1978; Pierce and Cukier, 1981), and methods based on Green's function (Hwang, et al., 1978; Dougherty and Rabitz, 1979; Kramer, et al., 1981; Rabitz, et al., 1983). Most sensitivity work has focused on examining mechanistic chemical kinetic systems (Cukier, et al., 1973; Boni and Penner, 1977; Pierce and Cukier, 1981; Hwang, et al., 1978; Hwang, 1983; Smooke, et al., 1986; Rabitz, 1981). Other work has focused on reaction-diffusion systems (Coffee and Heimerl, 1983; Reuven, et al., 1986) and on simple of

combustion systems (Smith, J.D., 1984). The work described herein concerns a sensitivity study of a comprehensive model describing a pf combustion system.

2.2.2 Full-Scale Sensitivity Study of Complex Models

A unique methodology was developed for the present sensitivity study. This methodology, particularly useful for studying large, complex computer codes requiring substantial computational time, was established by combining two techniques previously developed for different applications. The resulting methodology proceeds in two steps: 1) a linear sensitivity technique or screening design to screen the initial parameter set for those parameters with primary effects, and 2) a global nonlinear sensitivity technique which examines only those parameters identified in step one. The procedure used during each step of the study will be discussed in the following section.

Screening Design

Screening designs, or fractional factorial designs, are obtained by performing a fraction of a total factorial design(Daniel, 1976). The present study used a "Plackett-Burman" design to analyze the nineteen parameters shown in Table 2.1. In the absence of experimental variability, a completely saturated fractional design is capable of screening out real parameter effects. A completely saturated design consists of $n + 1$ simulations for n parameters. The main objective of the screening design was to identify those parameters exhibiting significant primary effects. Higher order effects were addressed in the final phase of the sensitivity study.

The parameters shown in Table 2.1 consist mainly of physical parameters describing the combustion process (radiation, turbulent fluid mechanics, devolatilization, etc.). One numerical parameter, thought to have a significant effect on model predictions, was also included. Parameter ranges were established from a literature search or from experts in the field. Special effort was made to select parameters completely independent from one another to avoid confounding (masking important effects by combinations of parameters dependent upon each other) during the screening design. To characterize the uncertainty in the parameters between their low and high extremes some assumptions about their probability density function were required. In the absence of any information concerning the error function, a normal distribution

is usually selected to represent the randomness of the data. Hence, parameter ranges identified from the literature or expert experience represented the most probable values for the specific parameters. For a normal distribution, the ranges indicated in Table 2.1 would represent a three-standard-deviation confidence interval (99% confident of observed value being in range). A base case, well characterized by experimental work (Asay, 1982) was identified to provide a mean input parameter set shown in Table 2.1. Again, only the low and high extremes were used in the screening design. A summary of model input describing the reactor geometry and the operating conditions for the base case is presented in Table 2.2. Parameter effects were characterized as significant by seven such model predictions as shown in Table 2.3. Care was taken to select outputs that represent the main combustion characteristics (i.e. turbulent mixing and fluid mechanics processes, homogeneous and heterogeneous reaction processes, mass and energy transport processes, etc.).

Next, input for each of the twenty separate cases was prepared by setting the parameters to their low or high value according to the design pattern. Finally, each case was converged and the values of the selected output functions were recorded. Each of these values were then analyzed to determine parameter effects.

Effects were classified as significant by a two-sided t-test with an 80% confidence interval and 19 degrees of freedom. A different subset of key parameters was identified from each model prediction. A list of the most crucial parameters was formed by combining the results from each output analysis. Table 2.4 shows the final set of nine (from the original nineteen) parameters chosen for further study. The first six parameters shown in Table 2.4 had a t-statistic greater than the critical t-statistic (significant effect) indicating a primary effect. The last three parameters had t-statistics less than but very near the critical t-value and were included to examine the possible nonlinear effects caused by higher order coupling. Together, these nine parameters formed the final parameter set for examination in the global sensitivity analysis.

Results from the screening design indicate that uncertainty in devolatilization and turbulent particle dispersion parameters have a dominant impact on model predictions as indicated by comparing the corresponding t-statistic to the critical value. Uncertainty in the radiation coefficient, char oxidation parameters and gas-turbulence parameters had a less significant (again based

Table 2.1: Input Parameters for the Screening Design.

	Parameter Name†	Description	Range
1.	VISCOS (kg/m s)	Approximate laminar viscosity for entire reaction chamber	3.90 - 5.52 (10^{-5})
2.	PRK [2,30]	Turbulent Prandtl/Schmidt number for particle dispersion	0.30 - 1.00
3.	GAMMA [28]	Particle swelling parameter	0.00 - 0.20
4.	XI [2]	Particle surface area factor	1.00 - 2.00
5.	EMJ(1,1) (J/kmol) [2]	Activation energy for first devolatilization reaction	7.36 - 10.46 (10^7)
6.	EMJ(1,2) (J/kmol) [2]	Activation energy for second devolatilization reaction	16.73 - 10.46 (10^7)
7.	YY(1,1) [2]	Stoichiometric coefficient for first devolatilization reaction	0.30 - 0.39
8.	YY(1,2) [2]	Stoichiometric coefficient for second devolatilization reaction	0.80 - 1.00
9.	EL(1,1) (J/kmol) [1,2]	Activation energy for char oxidation energy	8.35 - 9.30 (10^7)
10.	WIC(1,3) [31]	Elemental mass fraction of hydrogen in coal particles	0.049 - 0.054
11.	WIC(1,4) [31]	Elemental mass fraction of oxygen in coal particles	0.159 - 0.205
12.	WIC(1,5) [31]	Elemental mass fraction of nitrogen in coal particles	0.013 - 0.016
13.	PHIL(1)	Stoichiometric coefficient for oxidizer in char reaction	1.00 - 2.00
14.	QAB [28]	Absorption efficiency for radiation from particles	0.80 - 1.00
15.	QSC [28]	Scattering efficiency for radiation from particles	0.20 - 0.50
16.	EMW [10]	Reactor wall emittance	0.50 - 0.90
17.	URF‡	Gas velocity under-relaxation numerical parameter	0.45 - 0.55
18.	TINFLO(1) [2]	Turbulence intensity in the primary inlet stream	0.135 - 0.165
19.	TINFLO(2) [2]	Turbulence intensity in the secondary inlet stream	0.162 - 0.180

† FORTRAN variable names from PCGC-2.

‡ All gas velocity under-relaxation factors were changed together as one parameter.

Table 2.2: Summary of Base Case Data Describing Reactor Geometry and Operating Conditions.

Geometry	
Primary tube diameter (m)	0.022
Secondary tube diameter (m)	0.084
Chamber diameter (m)	0.203
Chamber length (m)	1.561
Inlet Gas Properties	
Primary swirl number	0.000
Primary turbulence intensity (%)	15.0
Primary temperature (K)	300.0
Primary mole fractions:	
AR	0.046
H_2O	0.035
N_2	0.725
O_2	0.194
Secondary swirl	2.000
Secondary turbulent intensity (%)	18.0
Secondary temperature (K)	589.0
Secondary mole fractions:	
AR	0.009
H_2O	0.000
N_2	0.781
O_2	0.210

Feed Rates	
Primary gas (kg/s)	$6.228\ (10^{-3})$
Secondary gas (kg/s)	0.019
Coal in Primary (kg/s)	$2.835\ (10^{-3})$
Reactor Parameters	
Reactor Pressure (N/m^2, m)	$8.60(10^4)$
Side wall Temperature (K)	1000.00
Particle Parameters	
Particle solid density (kg/m^3)	1340.0
High Heating Value, dmmf (J/kg)	$2.97\ (10^7)$
Mass mean particle diameter (m)	$5.025\ (10^{-5})$
Initial analysis:	
raw coal	0.931
ash	0.069
Elemental analysis (daf):	
C	0.752
H	0.051
O	0.182
N	0.015
S	0.000

Table 2.3: Screening Design Output Functions and Results.

	Output Function	Comments	Significant Parameters†	t-statistic‡
1.	Carbon conversion at reactor exit (%)	Reflects overall combustion characteristics	EMJ(1,2), PHIL(1)	-3 · 1 ·
2.	Maximum axial centerline gas temperature (K)	Represents degree of mixing and combustion	PRK, GAMMA, EMJ(1,2)	-1.54 -1.34 -2.97
3.	Maximum axial flame front gas temperature	Reflects devolatilization/ oxidation and flame structure characteristics	EMJ(1,2)	2.15
4.	Flame front axial position in reactor (cm)	Reflects flame structure characteristics	EMJ(1,2), PHIL(1)	3.53 -1.36
5.	Carbon conversion at flame front (%)	Relationship between particle reactions and gas temperature	PRK, EMJ(1,2)	1.23 -3.15
6.	Percent of total carbon conversion at flame front (%)	Relationship between particle reactions and total carbon conversion	PRK, EMJ(1,2), WIC(1,4)	-2.26 -2.56 1.45
7.	Mixing cup NO_x concentration at reactor exit (ppm)	Reflects pollutant formation characteristics	PRK, EMJ(1,2), QSC	-1.59 2.83 -1.56

† FORTRAN variable names from PCGC-2.

‡ Critical t-statistic for two-sided t-test with eighteen DOF is 1.33

on smaller t-statistics) effect on model predictions.

Global Sensitivity Analysis

After reviewing various techniques capable of performing a global sensitivity analysis of PCGC-2, Fourier Amplitude Sensitivity Test (FAST) was selected for the final step of the sensitivity study. FAST is a well proven technique that has been used in several engineering disciplines to aid in validation of mathematical models (Boni and Penner, 1977; Pierce, 1981; Pierce and Cukier, 1981; Smith, J.D., 1984; Kuntz, et al., 1976; Koda, et al., 1979; Falls, et al., 1979; Tilden, et al., 1981). A detailed description of the theoretical development of the technique is given elsewhere (Cukier, et al., 1978), and only a brief review of the salient features of the method are given here.

FAST statistically varies all parameters simultaneously over the probable parameter space in a sinusoidal fashion with a specific frequency assigned to each parameter. This method has been shown to provide a good approximation to the probable parameter space (Pierce, 1981). Results from model predictions, corresponding to unique parameter sets, are Fourier-analyzed. The number of unique parameter sets, which corresponds to the number of computer simulations (N) required to obtain the sensitivity information for n parameters is approximated as:

$$N \approx n^{2.5} \tag{2.5}$$

More specifically, the total number of simulations required in a FAST sensitivity analysis is determined by the maximum sampling frequency. This frequency is based on the Shannon Sampling Theorem (Jerri, 1965) and the order of accuracy of the frequency set (Schailby and Schuler, 1973).

The Fourier coefficients are used to determine variables that quantify sensitivity of the predictions to input uncertainty. The average prediction, total deviation of the average prediction and the individual contribution to the total deviation caused by uncertainty in each parameter are calculated. Using these sensitivity variables, the parameter uncertainty causing the greatest variance in model predictions can be determined.

The sensitivity analysis of PCGC-2 required a large amount of computer time even with a small subset of the original list of input parameters. To accomplish this portion of the study in a reasonable amount of time, the

Table 2.4: Parameters Examined in Step Two of the Sensitivity Study.

No.	Parameter	Units	Base Value	±	Uncertainty
1.	Turbulent Particle Schmidt Number	--	0.65		0.35
2.	Particle Swelling Factor	--	0.10		0.10
3.	Activation Energy for High Temperature Reaction	(10^7) J/kmol	20.90		4.20
4.	Stoichiometric Coefficient for High Temperature Devolatilization Reaction	--	0.90		0.10
5.	Activation Energy for Char Oxidation Reaction	(10^7) J/kmol	8.80		0.40
6.	Elementary Mass Fraction of Oxygen in Particle	--	0.18		0.02
7.	Stoichiometric Coefficient for the Oxidizer in the Char Oxidation Reaction	--	1.50		0.50
8.	Turbulence Intensity of Primary Gas Stream	--	0.15		0.05
9.	Scattering Efficiency for Particle Radiation	--	0.35		0.15

computer calculations were performed on the Cray computers at Los Alamos National Laboratory in New Mexico. The sensitivity analysis of input parameters listed in Table 2.4 required 323 separate simulations (based on the maximum frequency of the fourth-order frequency set) of PCGC-2 to obtain the appropriate sensitivity measurements. An analysis of this magnitude previously had not been conducted so techniques were developed to perform the analysis. In addition, to facilitate conducting the sensitivity analysis on the Cray computers certain operating procedures were established.

Because parametric variance was identified from both the literature survey and expert experience and because there was not a most probable value identified in each range, it was desired to give equal weighting to all parameter values over their ranges. Thus, the uniform distribution function shown in Equation 2.6 was used:

$$f(\alpha_i; N) = \frac{1}{N} \tag{2.6}$$

where α_i is the parameter and N is the number of simulations conducted in the analysis. In most cases, the error is assumed to have a normal distribution about some mean value. However, in this study a uniform error function was utilized to represent the knowledge or lack thereof concerning the distribution of each parameter over its range. Given the parameter ranges and the uniform pdf's, the analysis was conducted.

2.2.3 Sensitivity Analysis Results

Results of the sensitivity analysis for each output function considering the different parameters are typically characterized by three basic variables which can conveniently be established from the Fourier coefficients. The Fourier coefficients are obtained by transforming the multi-dimensional parameter space (9 dimensions in this case) into a one-dimensional search domain. The resulting function is sampled over the appropriate number of simulations (323) and the output is Fourier analyzed. The three main sensitivity variables are then calculated from the Fourier coefficients (Cukier *et al.*, 1978). In addition to the average functional value, total function deviation, and partial functional variances, a fourth sensitivity variable was developed during this study.

This sensitivity variable, *Deviation-Accounted-For* (D_a) was defined to illustrate the high-order coupling between model parameters and model pre-

dictions:

$$D_a^i = \frac{\sum_{j=1}^{n} S_j^i + \sum_{j=1}^{n} \sum_{k=1}^{n} S_{jk}^i}{\sigma_{total}^{(i)2}} \qquad (2.7)$$

This variable illustrates regions where the frequency set (fourth-order) used in the sensitivity analysis was not capable of elucidating parameter interactions.

Predicted Burnout

The average predicted burnout over the entire simulation set is shown in Figure 2.1a. Also shown is the calculated standard deviation for the predicted burnout. The calculated standard deviation corresponds to a pdf describing probable values of predicted burnout. If this pdf were normal, then the standard deviation shown in Figure 2.1b would account for about 68% of the probable values of predicted burnout. Included in Figure 2.1a are three calculated pdf's derived from frequency plots of calculated burnout for all simulations. Reactor locations corresponding to the pdf's are representative of the early reactor region (high particle heating rates), the immediate post-flame region (fuel-rich zone) and the well-mixed region (reactor exit). Deviation in predicted burnout increases from 0 to about 10% in the first region while it reaches a maximum of 15% in the next region after which it decreases to about 5% at the reactor exit. Also included in this plot is a comparison of both the predicted burnout from the base case and the experimentally measured values (Asay, 1982).

Figure 2.1 part b shows the parameters which account for over 90% of the functional deviation in the mixing cup (radially averaged) burnout along the axial length of the reactor. Uncertainty in the activation energy for the high temperature devolatilization reaction accounts for over 80% of this calculated deviation. Even though this partial variance first becomes important in the second zone of the reactor where devolatilization begins, it dominates the calculated uncertainty in burnout for the remainder of the reactor. This demonstrated sensitivity in the post-ignition region of the reactor illustrates the dominant effect that overall volatile yield has on the burnout prediction. Thus, future work should focus on obtaining accurate measures of these parameters with an emphasis on getting accurate predictions of the overall volatile yield.

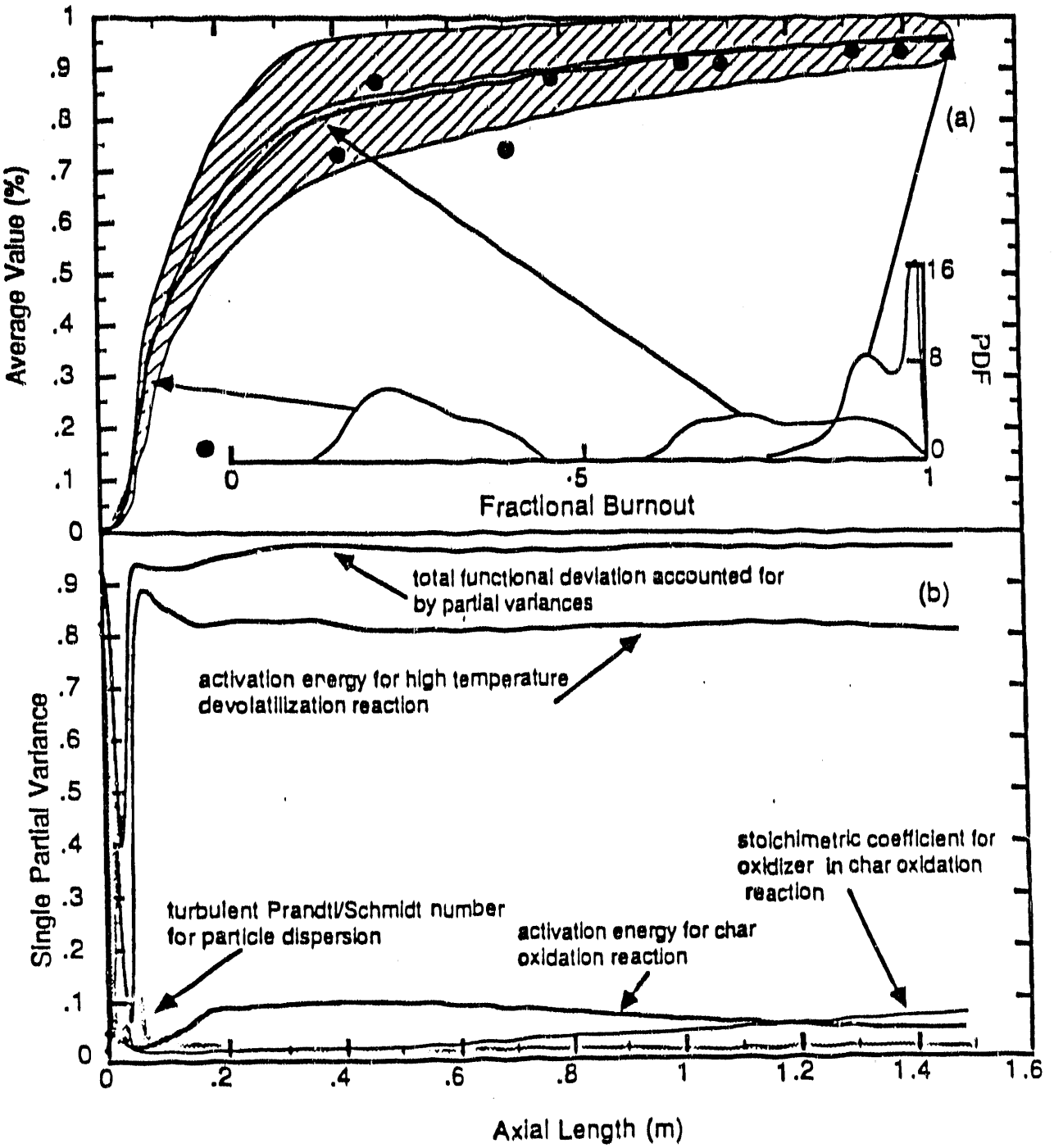

Figure 2.1: a) Sensitivity Results for Predicted Mixing cup Burnout, b) Fraction of Functional Deviation Attributed to Individual Parameters.

Both the calculated and the measured values, with the exception of two The deviation envelope represents a prediction incorporating both the experimental and inherent variance in the rate constants required by the devolatilization submodel. It is apparent that the two equation devolatilization submodel used in PCGC-2 does an admirable job of describing the devolatilization process in the reactor when considering the parameter uncertainty. The first data point is outside the deviation because PCGC-2 predicts the ignition point to be earlier in the reactor than the measured data indicate. Both a fundamental lack of understanding of the devolatilization process (which dominates the location of the ignition point) and the experimental technique used to measure this data near the ignition point may account for this disparity. Uncertainty in the devolatilization submodel parameters produces the greatest error in predicting both the ignition point and the overall carbon conversion in the early regions of the reactor.

Thus, uncertainty in the devolatilization parameters may control the prediction of ignition point location and the overall carbon conversion. However, once ignition occurs ,the particle undergoes rapid heating which leads to further devolatilization (Kobayashi, et al., 1977). This process continues until the volatiles have been expelled from the particle. Thus, the particle heating rate controls the amount of devolatilization the particle will experience. If ignition is predicted to occur too early in the reactor, combustion may be limited by the amount of oxidizer available for reaction with the volatiles. This may cause lower particle heating rates which would in turn reduce the overall volatile yield. Thus, accurate prediction of the ignition point could control the predicted volatile yield and the overall carbon conversion. Further sensitivity work may help answer the question of how predicted volatile yield is related to ignition point. Regardless of which controls, accurately predicting both the overall volatile yield and the ignition point are shown to be the dominant factors governing the overall coal burnout prediction. Thus, future development work should focus on these aspects of the submodel. Also, better predictions from the existing devolatilization submodel may be realized by obtaining more accurate kinetic data as related to overall volatile yield.

The second largest partial variance is caused by uncertainty in the activation energy for the char oxidation reaction. The magnitude of this partial variance increases as the partial variance associated with the devolatilization process decreases which shows the initiation of char oxidation. The partial

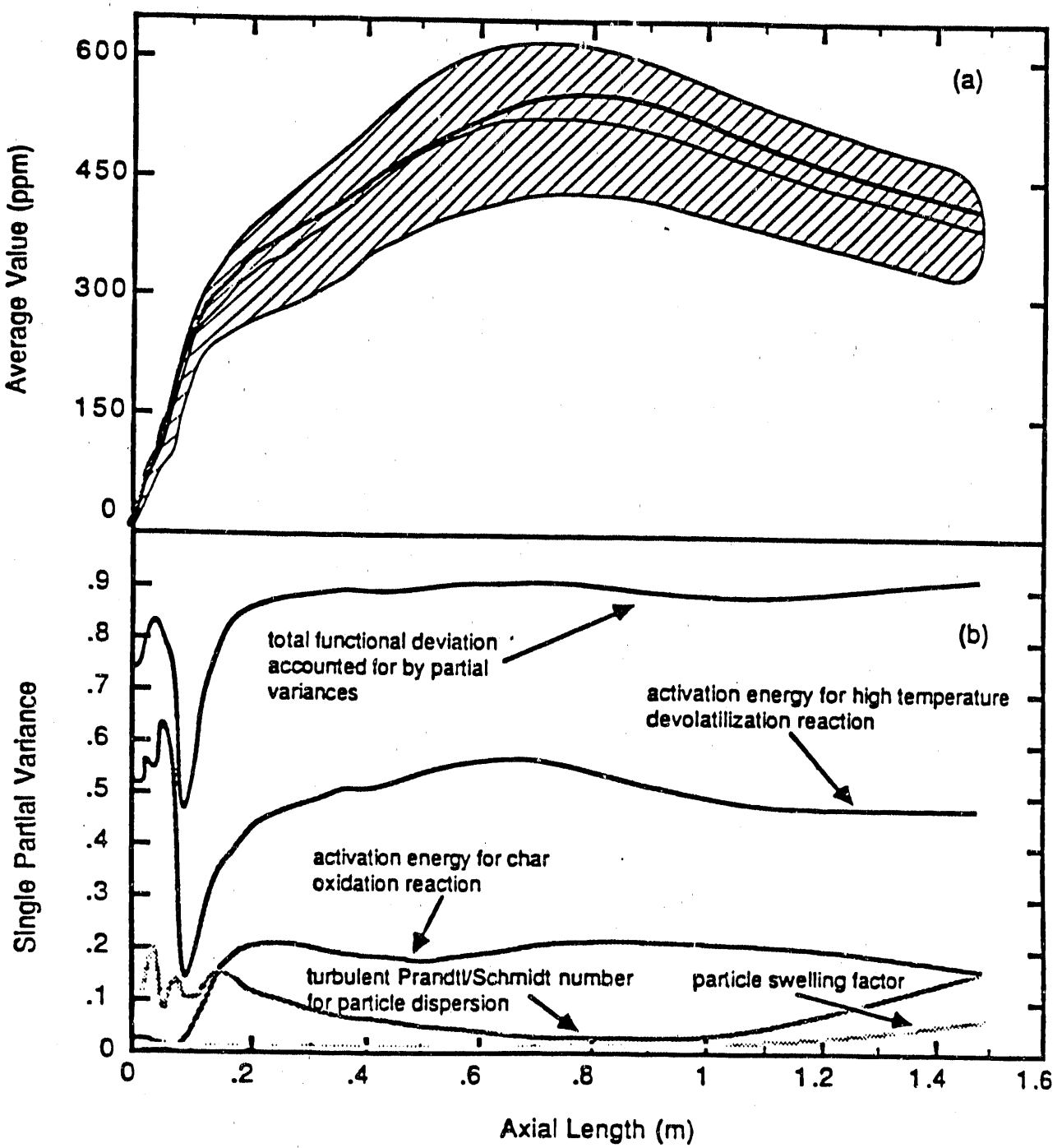

Figure 2.2: a) Sensitivity Results for Predicted Mixing cup NO_x Concentration, b) Fraction of Functional Deviation Attributed to Individual Parameters.

variance corresponding to char oxidation remains the second largest contributor to the overall variance in burnout until the last portion of the reactor. At this point, uncertainty in the stoichiometric coefficient for the char oxidation reaction becomes the second largest contributor to the overall uncertainty in predicted burnout. This suggests that the oxidation mechanism becomes important near the reactor exit. Thus, it would be beneficial to carry out a study of the char oxidation mechanism under conditions similar to those which exist in the last portion of the reactor.

The last parameter exhibiting a significant impact on the calculated deviation for predicted burnout is the turbulent Prandtl/Schmidt number. This parameter is associated with turbulent particle dispersion. The partial variance corresponding to this parameter is important very early in the reactor, prior to devolatilization. At present, PCGC-2 models the turbulent particle dispersion process through a Fickian dispersion method. Five different size classifications of particles are used to model the particle size distribution in this study. The impact of particle size distribution on calculations with PCGC-2 has previously been demonstrated (Sowa, 1986). The trajectories of the smaller particles can be influenced by the gas flow more dramatically than the large particles. The swirl component of the inlet gas stream has been shown to increase combustion efficiency via several mechanisms (Sloan, et al., 1986). One such mechanism is the effect that the swirl has on helping to mix hot active species with fresh reactants through large turbulent diffusion in recirculation zones more readily than the large ones, they would become an important factor in stabilization of the flame-front through the devolatilization process. This may explain the apparent sensitivity of the turbulent dispersion parameter. It also helps to emphasize the impact that particle size distribution has on overall predictions of coal burnout.

Another insight gained from this analysis is the fact that although devolatilization occurs early in the reactor, it is not limited to that region. Indeed, larger particles continue to devolatilize throughout the remainder of the reactor. The same is true for char oxidation. The smaller particles require less time to heat up, and thus they devolatilize first. The larger particles require more time to heat up, and will thus devolatilize further from the inlet. Therefore, devolatilization and oxidation occur concurrently with the smaller particles burning out first, followed by the larger ones. The fact that the small particles burnout more quickly can also affect the devolatilization mechanism. Enhanced burnout of small particles will increase the gas

temperature which will in turn cause the high temperature devolatilization reaction to dominate the low temperature reaction. This also explains the dominant effect of the activation energy for the high temperature reaction in the devolatilization mechanism.

The single partial variances shown in Figure 2.1b account for more than 80% of the total deviation in burnout. This indicates that there is no significant two-way or higher parameter coupling effects present. The same is indicated by the plot of D_a. Thus, the frequency set selected for the second step of the sensitivity study was capable of identifying the important parameter sensitivities.

Predicted NO_x Concentration

The predicted average value for NO concentration is compared to the predicted NO concentration from the base case in Figure 2.2a. As before, the two compare very well. However, in this instance there appears to be a disparity of about 30 ppm at the maximum average value. This region also exhibits the largest calculated functional deviation (about 200 ppm). This occurs in the oxidation zone (Zone 3) at about 0.8 meters down the reactor. At this point, the oxidizer has mixed thoroughly with the fuel and NO_x formation is at a peak. Further down the reactor, NO_x is converted to nitrogen or reacts heterogeneously with char to form some other nitrogen species. Thus, the effects of parameter uncertainty are most important in this region of the reactor.

Figure 2.2b presents the significant, calculated, partial variances caused by parameter uncertainty. As before, the main effect is caused by uncertainty in the activation energy for the high temperature devolatilization reaction. For the calculated burnout this partial variance was insignificant in the very early portion of the reactor, suddenly increased in importance at the flame-front (about 0.1 m down the reactor), and remains dominant thereafter. Conversely, for NO_x, this partial variance is initially dominant at the inlet, decreases dramatically at the flame-front (about 0.1 m down the reactor), slowly builds in importance to the region where NO_x formation is at its maximum value (0.8 m down the reactor) and remained dominant to the end of the reactor. The D_a follows much the same path as the partial variance for this parameter. There appears to be a large amount of high-order coupling at the flame-front although it is impossible to identify which parameter

uncertainties cause this coupling, because of the frequency set used in this analysis. This is not critical though, since the total calculated deviation for NO_x at this point, is only 40 ppm compared to more than 200 ppm later on. Also, immediately following the region which indicates high-order coupling, the D_a increases to and remains at more than 90% for the rest of the reactor. Thus, the partial variances provide the necessary information on the controlling processes.

Uncertainty in the Prandtl/Schmidt number is the second most important factor early in the reactor and again at the exit of the reactor. This is indicative of the importance of turbulent particle dispersion. Particle dispersion was shown to be important to coal burnout early in the reactor. This was attributed to its affect on flame-front formation due to the devolatilization of small particles. It follows that this same process would affect NO_x formation. In this instance, the NO_x formed would be from nitrogen bound in the fuel structure and released during the devolatilization process. Dispersion effects, indicated by the corresponding partial variance at the end of the reactor, may be due to the dispersion of char particles resulting in a corresponding destruction of NO_x by char oxidation. This could be quantified by examining a plot of the sine coefficients. If the coefficients are negative, then an increase in this parameter (corresponding to an increase in particle dispersion) would result in a decrease in the predicted NO_x concentration at the reactor exit.

Finally, it is interesting to note the increased effect of uncertainty in the particle swelling parameter at the end of the reactor. This indicates a link between greater char particle surface area and NO_x concentration. It may result from the formation of fuel NO_x by enhancing the release of the remaining nitrogen in the char matrix.

Local Gas Temperature

The average value of the local gas temperature in the axial direction and at five radial positions of the reactor is shown in Figure 2.3a. This function is shown in two-dimensions to illustrate the multi-dimensional effects involved in modeling pf combustion. Again, the average value, calculated during the sensitivity analysis, is compared to the base case predictions. This comparison shows no major disparities between the average temperature and the base case temperature. Also, there is relatively very little calculated functional de-

viation caused by parameter uncertainty. The greatest deviation occurs on the centerline in Zone 1 (flame-front) and represents approximately 600K. This deviation is caused primarily by the change in the predicted ignition point. Again, it illustrates both the difficulty and the importance of predicting this phenomenon. As one moves in the radial direction away from the reactor centerline, the region of greatest deviation shifts. This indicates the two-dimensional nature of the flame. In the first three radial positions, the deviation envelope persists for a short axial distance in the reactor (corresponding to the flame-front). The magnitude of the deviation (width of the envelope) becomes smaller until it is almost uniform at the fourth radial point. However, at the last radial point, the deviation envelope shows significant increase over the last two reactor zones. This indicates the impact parameter error would have on heat flux at the wall. Critical parameters for each radial position can be identified to provide insight into the controlling mechanisms in each reactor region.

Figure 2.3b presents the significant partial variances for each radial position. As expected, the parameters identified as important to burnout and NO_x concentration show up here. Specifically, the turbulent dispersion, devolatilization, and oxidation parameters (Parameters 1,3,5 and 7 from Table 2.4). However, two new parameters show importance: the stoichiometric coefficient for the high temperature devolatilization reaction (Parameter 4) and the elemental mass fraction of oxygen in the coal particle (Parameter 6). It is interesting to note that these parameters exhibited marginal importance in the screening design. At the first two radial locations (near the centerline) where the volatiles are formed, Parameter 4 accounts for a significant portion of the calculated deviation. Even though the partial variance for this parameter is overshadowed by the partial variance caused by Parameter 3, the variance caused by uncertainty in this parameter further emphasizes the importance of the devolatilization process. Since the devolatilization process occurs at the flame-front, it is not surprising that this parameter uncertainty is important near the centerline and less significant near the outer reactor wall. Partial variance caused by uncertainty in Parameter 6 becomes important as one moves from the centerline toward the reactor wall. This indicates the effect that coal rank has on combustion characteristics. According to Singer (1981), the elemental oxygen content of coal is a good guide to coal rank. Thus, the impact of this parameter on predicted gas temperature

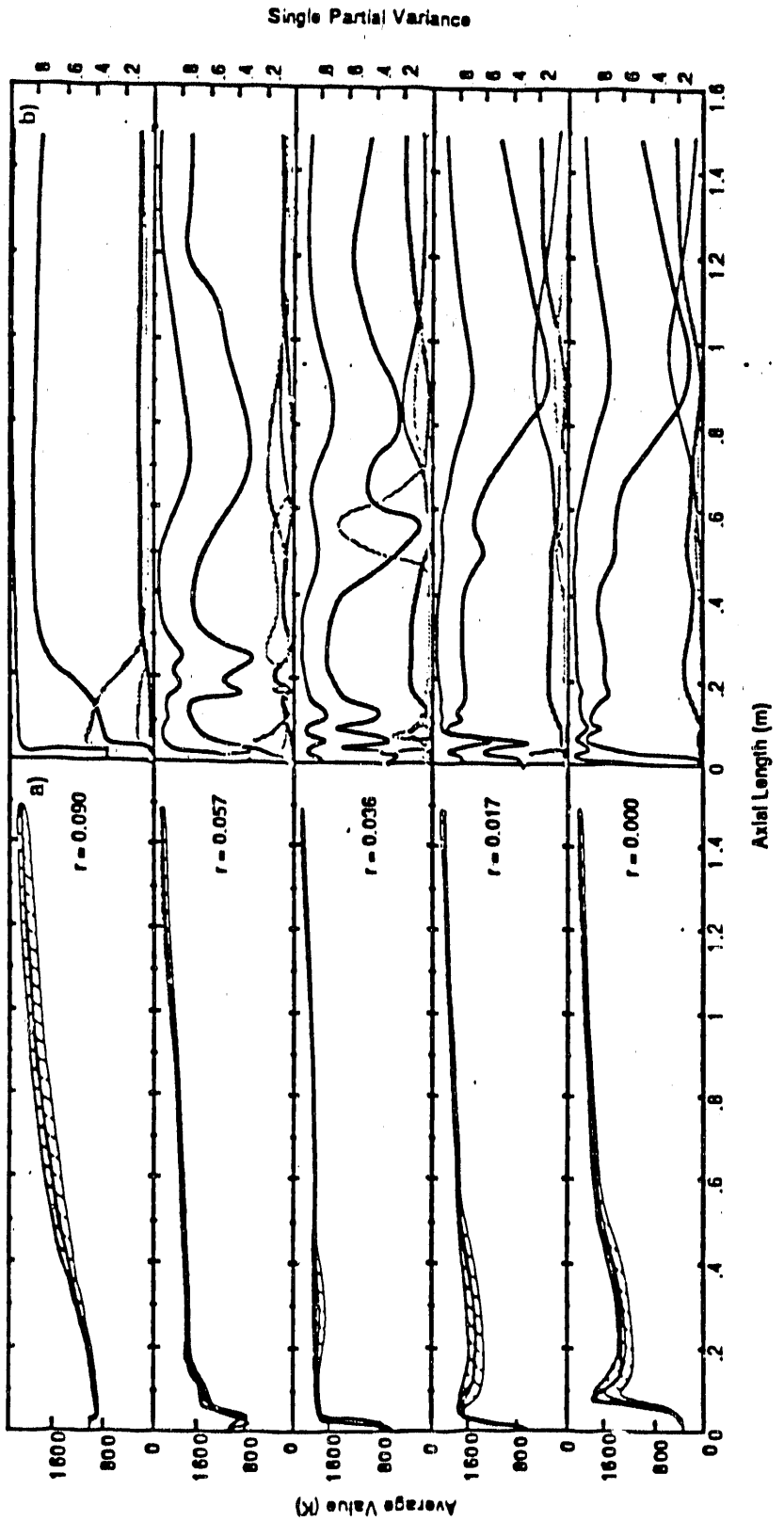

Figure 2.3: a) Sensitivity Results for Predicted Local Gas Temperature, b) Fraction of Functional Deviation Attributed to Individual Parameters.

shows this relationship. A more detailed discussion of the significance of the other partial variances shown in Figure 2.3b can be found elsewhere (Smith, J.D., 1987).

Local Coal-Gas Mixture Fraction

The average value for the local coal gas mixture fraction as a function of both the axial and radial directions in the reactor are shown in Figure 2.4a. Again, these values are compared to those from the base case calculation. Only slight differences between the two values are noticeable. These differences occur in the first reactor zone corresponding to the flame-front. Since the coal-gas mixture fraction relates both the mixing and the kinetic processes, sensitivity analysis results for this output function provide insight into the coupling of these important phenomena. This coupling can be seen by noting the large calculated functional deviation near the early regions of the reactor centerline. Here, the amount of coal-gas evolved varies greatly due to the predicted change in flame-front location. In later regions of the reactor, there is essentially no deviation in this output function which indicates no relationship to parameter uncertainty. However, as one moves away from the reactor centerline, the calculated deviation in the latter regions of the reactor becomes more significant.

This deviation is caused by uncertainty in the devolatilization parameters. As with burnout, this shows the effect of parameter uncertainty on predicting the ignition point and overall volatiles yield. The shift in the deviation envelope again illustrates the two-dimensional nature of the flame-front. This is further illustrated by examining the partial variances shown in Figure 2.4b. As before, the dominant effects are attributed to the devolatilization and oxidation parameters. However, uncertainty in the stoichiometric coefficient for the high temperature devolatilization reaction appears significant near the centerline and uncertainty in the turbulent dispersion parameter appears important near the reactor wall. These apparent significant effects occur in regions where the total deviation envelope is relatively small. Thus, these partial variances have only a small impact on the overall predictions. The observed deviation in the coal-gas mixture fraction near the wall most likely is caused by recirculating gas from farther down the reactor. This fact may be the reason for the apparent impact of the turbulent dispersion parameter on the coal-gas mixture fraction near the outer wall (as discussed earlier).

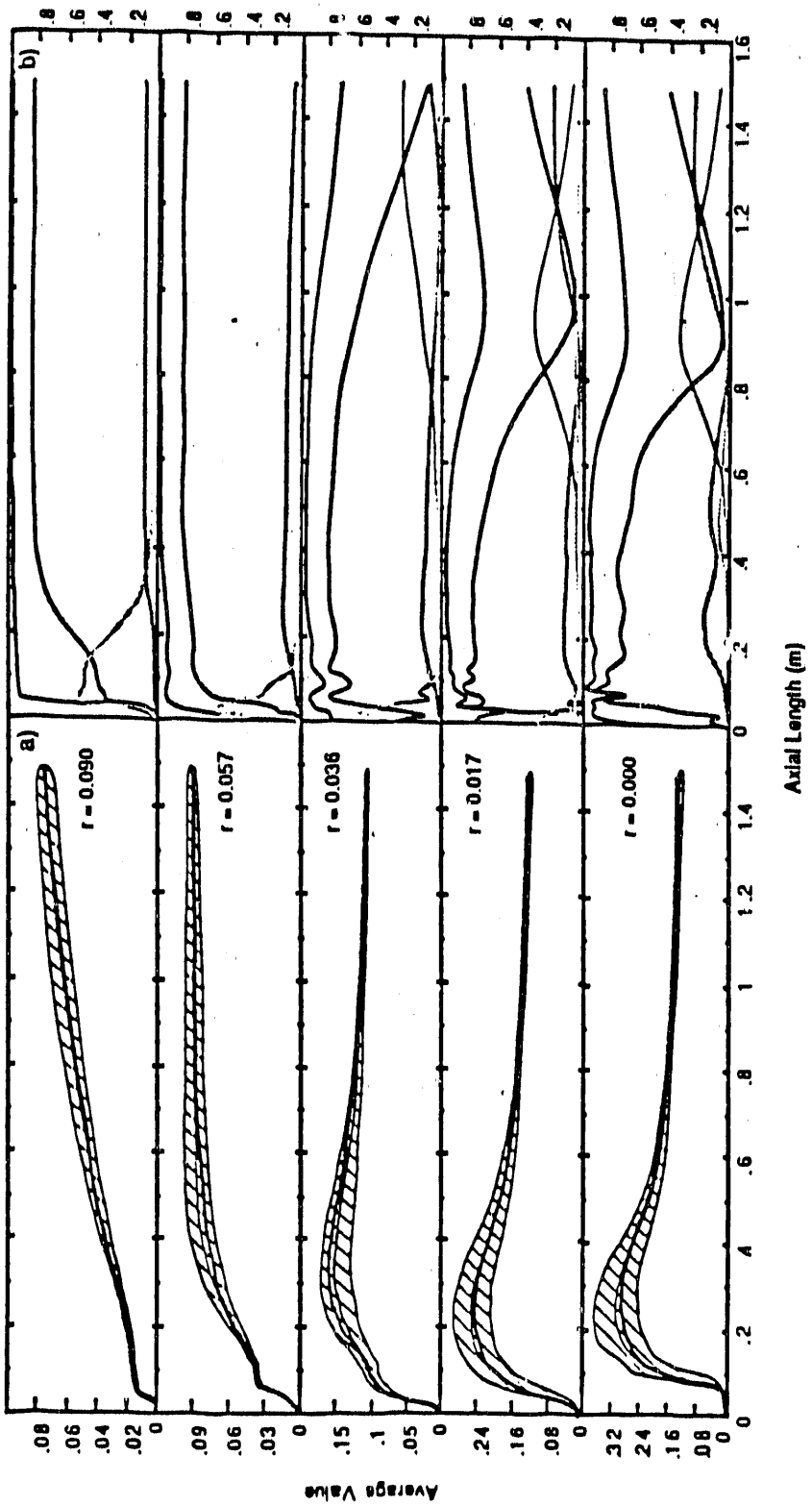

Figure 2.4: a) Sensitivity Results for Predicted Local Coal-Gas Mixture Fraction, b) Fraction of Functional Deviation Attributed to Individual Parameters.

2.2.4 Conclusions

Results of this study indicate specific parameters which have the greatest impact on model predictions. Specific model prediction for coal burnout, NO_x concentration, local gas temperature, and local coal-gas mixture fraction were used to identify critical parameters. Model parameters examined in this study represent the physical and chemical processes which occur in pf combustion. The parameters required to describe the devolatilization subprocess showed the greatest overall impact on model prediction while parameters governing char oxidation were the second most important. Char oxidation has the most impact on model prediction for NO_x concentration. Particle dispersion had a secondary effect on overall model predictions and had the greatest impact on coal burnout and coal-gas mixture fraction predictions. Also, of secondary importance was the effect of coal rank as indicated by the elemental oxygen content of the coal. This affected gas temperature predictions most dramatically. Parameter uncertainties for the radiation coefficient, turbulence intensity, and the particle swelling factor showed little or no impact on model predictions. This is attributed to the dominant influence of the uncertainty in the other parameters on the sensitivity analysis.

This study demonstrates that future modeling efforts should be focussed on a better definition of the parameters governing particle devolatilization/oxidation mechanisms. This effort should focus on providing better predictions of the ignition point and overall volatile yields. An integral part of that work must include efforts to quantify the physical parameters describing the turbulent kinetic, mass transfer, and heat transfer processes involved in the devolatilization/oxidation mechanisms. Additional work must also focus on developing a better definition of the turbulent particle dispersion mechanism. These conclusions are not unique to this discussion and work has been underway to obtain a better understanding of these mechanisms. The results presented here do conclusively demonstrate the need to incorporate the best knowledge (from the laboratory) concerning critical mechanisms into better numerical submodels which make up comprehensive computer models describing complex phenomena such as pf combustion.

Additionally, sensitivity analysis work should be conducted to examine the impact that particle size has on turbulent particle dispersion and ignition point. The relationship between ignition point and volatile yield should also be investigated to determine the controlling process according to the two equation devolatilization submodel presently used in PCGC-2.

While the results obtained in the sensitivity analysis are case-specific, they do focus attention on the critical submodels which appear to dominate the predictions. These results provide direction to future submodel development as well as experimental efforts to obtain accurate values of the physical parameters required by these submodels. This work also illustrates the role of sensitivity analysis as an engineering tool to be used to gain a deeper understanding of the physical process being modeled. In addition, the techniques used to perform this study may aid in future sensitivity studies of large computer models describing physical systems in a realistic fashion.

2.3 Numerical Evaluation

2.3.1 Numerical Diffusion

The finite differencing scheme implemented in PCGC-3 provides the accuracy of the central differencing at low Reynolds numbers with the stability of the upwind differencing at higher Reynolds numbers. This scheme introduces numerical errors in the convection terms of order $O(\Delta x_i)$ when upwind differencing is used and $O(\Delta x_i)^2$ when central differencing is used. Roache (1976) notes that when conventional upwind differencing is used, the error introduced from the finite difference approximation can be viewed as an artificial numerical diffusion.

The upwind scheme developed by Patankar (1980) and used in PCGC-2 and many CFD codes will be referred to as HUDS (Hybrid Upwind Differencing Scheme). Roache (1976) states that the diffusion terms are normally neglected since they are smaller than the error associated with the convection terms. The control volume approach utilizes cell face velocities, which are calculated from surrounding nodal values. Patankar approximates each cell face velocity by using the velocity from the closest velocity cell in the direction of interest. For example, the velocity for the east face of the cell in Figure 1.2 would be set equal to the velocity stored at the east node point. Patankar states that this approximation ($u_e = u_E$) is closer to the actual face value than a linear average of the two closest nodes ($u_e = \frac{u_E+u_P}{2}$).

Alternative differencing schemes have been proposed to improve the estimation of velocities on cell faces. These schemes usually fall into two basic

categories: skew corrections and higher-order methods. Raithby (1974, 1976) proposed a skew-upwind differencing scheme (SUDS) which significantly reduces the numerical diffusion through the consideration of velocity direction. This reduces the "skewness error", the most damaging contribution to numerical diffusion. Leonard (1975) has proposed a quadratic upwind differencing scheme (QUDS) that is free from false diffusion. The basic difference among these schemes is the determination of the cell face velocities.

Several recent reviews of upwind differencing techniques (Castro and Jones, 1987; Leschiziner and Rodi, 1981; Vanka, 1987) contain conflicting recommendations. Leschziner (19891) found Raithby's SUDS and Leonard's QUDS to be far superior to conventional HUDS formulations. Castro (1987) found that the higher-order schemes were less susceptible to non-uniform grid errors. Although the new upwind schemes are more accurate, Castro concluded that they were "increasingly inadequate" at high Reynolds number flows and have not yet been evaluated in the context of turbulent flows. Vanka experienced difficulties with convergence and the overshooting of known solutions with the higher-order methods (Vanka, 1987). For high Reynolds number flows, under-relaxation factors of 0.3 were needed for the QUDS. The common HUDS scheme was relaxed at 0.8 and converged considerably faster. Vanka concluded that "no clear benefits of using the higher-order upwind scheme are observable" (Vanka, 1987).

Due to convergence problems with QUDS and SUDS and the false diffusion found in HUDS, a nodal upwind scheme (NUDS) was formulated as part of this study. This upwind scheme involved three modifications to HUDS found in PCGC-2. The first change was the inclusion of diffusion terms with the upwind scheme. The second modification eliminated the error associated with the face velocity approximation. This was accomplished by upwinding solely between node points, eliminating the need for specifying velocities at cell faces. The new scheme relates the velocity at the cell center to the velocity of the nearest upstream neighbor. Table 2.5 compares the differencing of a first-order partial derivative term for equal spaced cells for the four upwind schemes. (See Figure 1.2 for cell label definitions).

The final modification to HUDS is the use of nodal (and not facial) differencing coefficients. This requires the convection term to be initially modeled in the non-conservative form. The advantage of this scheme is its use of nodal values and avoidance of variable interpolation onto cell faces.

Table 2.5: Comparison of Four Upwind Schemes.

HUDS	$\frac{\partial\phi}{\partial x} = (\phi_P - \phi_w)/2\delta_{ew}$
SUDS	$\frac{\partial\phi}{\partial x} = (\phi_{P+\beta} - \phi_{P-\beta})/2\delta_{p\beta}$, $\beta = f(u,v,w)$
QUDS	$\frac{\partial\phi}{\partial x} = (2\phi_E + 3\phi_P - 6\phi_W + \phi_{WW})/6\delta_{ew}$
NUDS	$\frac{\partial\phi}{\partial x} = (\phi_P - \phi_W)/\delta_{PW}$

2.3.2 Overall Convergence Criteria

Although PCGC-3 iterates on each differential equation individually, the equation coupling necessitates the simultaneous convergence of the entire equation set. Various methods have been used to measure convergence, compare the convergence of different equations, and determine the required level of convergence. Typically, the error of each Finite Difference Equation (FDE) is calculated from Equation 2.8, which is a rearrangement of Equation 1.42. This error, R^o_ϕ, can be summed over the entire computational domain to represent the degree of convergence for the ϕ equation.

$$R^o_\phi = A_E\phi_E + A_W\phi_W + A_N\phi_N + A_S\phi_S + A_T\phi_T + A_B\phi_B + S_U - A_P\phi_P \quad (2.8)$$

The comparison of errors from different equations is a more complex task. The independent variables, source terms, and difference coefficients can vary several orders of magnitude among the equations. For example, mixture fraction values are always less than unity while velocities can approach one hundred meters per second. Without being able to compare the convergence of different equations, it is difficult to ascertain when overall convergence is achieved or which equation is slowing the overall convergence process.

PCGC-2 normalized the error sums from the different equations with an inlet value which was characteristic of the variable of interest. For example, the normalization factor for the axial momentum equation was based on the total inlet axial momentum, Equation 2.9. There are two problems with this formulation. First, it is difficult to derive characteristic inlet normalization factors for certain variables. The k and ϵ equation errors are not normalized in PCGC-2 due to this problem. Second, the normalized errors are dependent on variable magnitudes and cannot be directly compared.

$$R_\phi^\psi = \frac{\sum_{n=1}^{N} R_\phi^o}{\sum_{n=1}^{N} \rho \mathcal{A}_{in} u^2} \tag{2.9}$$

PCGC-3 uses the largest term found in each variable's FDE to normalize equation errors. A truncation term, defined by Equation 2.10, is calculated from the product of A_P and ϕ_P. The requirement of diagonal dominance in the coefficient matrices and the manipulation of the source terms guarantee that the product of these terms, Equation 2.10 will exceed the magnitude of other terms in each FDE. The final equation error is calculated with Equation 2.11. This normalization allows for the comparison of the errors among the different equations and measures the closeness of computer round-off error to equation error. The total equation error, R_ϕ^ψ, ranges from approximately unity to 10^{-nd}, where nd is the number of digits of computer accuracy. When the equation error reachs 10^{-nd}, computer round-off error prevents further reductions in equation error.

$$\psi_\phi = A_P \phi_P \tag{2.10}$$

$$R_\phi^\psi = \frac{\sum_{n=1}^{N} R_\phi^o}{\sum_{n=1}^{N} \psi_\phi} \tag{2.11}$$

2.3.3 Equation Convergence Checks

Overall convergence is enhanced when all the coupled partial differential equations are converged at similar rates. A tight convergence on a single equation can slow the overall convergence process. This is due to the coupling of the equation set; the pressure-velocity coupling is especially sensitive. The procedure previously followed in PCGC-2 was to iterate several times (typically either 3 or 4) on each equation. The number of iterations was not dependent on the degree of equation convergence and no emphasis was given to the solution of any particular equation. Van Doormaal (1984) proposed establishing different convergence criteria for each equation. A slightly altered form of Van Doormaal's suggestions was implemented in PCGC-3.

The idea behind this approach is to converge each equation to preset convergence limits before proceeding to the next equation. Initially, the guessed values for the variables are far from their true values and more micro-iterations are needed during the macro-iteration (Definitions of macro- and

Table 2.6: Equation Convergence Parameters.

Equation	Maximum Sweeps	Convergence Factor
p	20	0.20
p^c	20	0.20
$\tilde{u}$	4	0.003
$\tilde{v}$	4	0.003
$\tilde{w}$	4	0.003
$\tilde{f}$	4	0.003
$\tilde{g}$	4	0.003
$\tilde{k}$	4	0.003
$\tilde{\epsilon}$	4	0.003

micro-iterations are provided in Figure 1.1). When overall convergence is almost reached, some equations may require little additional computational work.

The new approach requires the specification of two parameters per equation; these parameters are given in Table 2.6. The first parameter specifies the maximum number of equation micro-iterations. This prevents unnecessary iterations during the early stages of simulation when initial inaccurate guesses can prevent an equation from converging. Equation convergence criteria are based on the initial and current error found in the equation. Current error is defined as the equation error present after the last micro-iteration. Initial error refers to the equation error present at the start of a macro-iteration. The equation error is calculated by summing the nodal errors throughout the computational domain. This calculation is represented by the numerator of Equation 2.11. The second parameter specifies the reduction in error necessary to consider the equation converged. When the current equation error multiplied by the convergence factor is less than the initial equation error, the micro-iteration is terminated and work is begun on the next equation. This process was developed to allocate more computational effort to the solution of the pressure equations. Van Doormaal states that solving the pressure correction equation "can represent as much as 80% of the total cost of solving the fluid flow problem" (Van Doormaal and Raithby, 1984).

Table 2.7: Variable Specifications for Exact Solution Case.

Equation	$\tilde{u}$	$\tilde{v}$	$\tilde{w}$	p	$\tilde{f}$	$\tilde{g}$	$\tilde{k}$	$\tilde{\epsilon}$
Chosen Value	xyz	yz	z	xyz	xy	xz	y	x
Parameter	c_{g2}	μ_e	g_x	g_y	g_z			
Value	0	0	0	0	0			

2.3.4 Known Solution Analysis

Numerical methods are best evaluated by comparing their performance with known solutions. Unfortunately, there are very few exact solutions of the Navier-Stokes equations for flows containing regions of recirculation. Therefore, an exact case was devised to evaluate the accuracy of the finite differencing in PCGC-3. Equation source terms were altered to allow simulations which resulted in a known solution.

Exact solution values based on geometric parameters were specified for the cardinal variables in PCGC-3. For example, the solution of the mixture fraction equation was equated with the local product of the x and y distance to the origin along their respective axes. This formulation creates nonlinear solution effects and allows spatial variation of the quantities being simulated. Several model parameters were redefined to simplify the known solution source term derivations. Table 2.7 provides the variable and parameter definitions used in the exact solution case.

New source terms for each differential equation were determined based on the equation assignments. This process is demonstrated for the x-component of the momentum equation in Equations 2.12 and 2.13. A differential equation is first extracted in its expanded form from Table 1.1. After variable assignments are substituted into Equation 2.12, it can be reduced through differentiation to Equation 2.13. This equation represents a new source term and is added to the original x-momentum source term. The solution of the resulting FDE gives local values of xyz, the assigned value of $\tilde{u}$. Similar derivations were made for each differential equation solved by PCGC-3.

$$S_u^K = \frac{\partial(\bar{\rho}\tilde{u}\tilde{u})}{\partial x} + \frac{\partial(\bar{\rho}\tilde{v}\tilde{u})}{\partial y} + \frac{\partial(\bar{\rho}\tilde{w}\tilde{u})}{\partial z} -$$

Table 2.8: Errors with Exact Solution Case.

GRID	HUDS	HUDS w/WCD	NUDS
Regular	1.3	1.3	9.4×10^{-8}
Irregular	1.2	8.7×10^{-1}	8.2×10^{-8}

$$\frac{\partial}{\partial x}\left(\mu_e \frac{\partial \tilde{u}}{\partial x}\right) - \frac{\partial}{\partial y}\left(\mu_e \frac{\partial \tilde{u}}{\partial y}\right) - \frac{\partial}{\partial z}\left(\mu_e \frac{\partial \tilde{u}}{\partial z}\right) - \frac{\partial P}{\partial x} + \frac{\partial}{\partial x}\left(\mu_e \frac{\partial \tilde{u}}{\partial x}\right) + \frac{\partial}{\partial y}\left(\mu_e \frac{\partial \tilde{v}}{\partial x}\right) + \frac{\partial}{\partial z}\left(\mu_e \frac{\partial \tilde{w}}{\partial x}\right) + \rho g_x \tag{2.12}$$

$$S_u^K = \rho(2xyz)(yz + z + 1) + yz \tag{2.13}$$

Two methods can be used to evaluate exact solution simulations. If the independent variables are initialized with their exact values, the calculated error for the first iteration should be close to the computer round-off error. Alternatively, a case can be fully converged without initialization and the final variable values can then be compared to known exact values. Both procedures were used to evaluate PCGC-3 for uniform and non-uniform grids. Table 2.8 displays the magnitude of errors associated with several differencing schemes implemented in PCGC-3 on a regular and irregular grid. The error in this table represents an average error for the $\tilde{u}$, $\tilde{v}$, $\tilde{w}$, $\tilde{f}$, $\tilde{k}$, and $\tilde{\epsilon}$ equations. The symbol, WCD, in the table refers to weighted central differencing.

Two types of errors were identified and removed through the exact solution simulations. The first type of errors found were coding inconsistencies. Individual FORTRAN variables could be compared with calculations based on the known specification of the cardinal variables. Approximately a dozen previously hidden coding errors were corrected through this procedure.

The second class of errors found with the exact solution experiment were algorithmic problems. Both the weighted central differencing and the nodal upwind differencing formulations were a direct result of efforts to reduce errors in exact case simulations. Exact solution runs were verified on uniform and non-uniform grids over a wide range of Reynolds numbers. The known solution case is a valuable tool in CFD model development and remains an option in PCGC-3.

Table 2.9: Numerical Effects on Solution Time.

Numerical Option	Sudden Expansion Flow [s]	Corner-Fired Furnace [s]
HUDS	30.70	467.01
NUDS	23.35	404.96
Convergence Checks	24.83	356.96
TDMA Change	22.48	326.42
Initialization	22.60	269.41
Total Reduction	26.4%	42.3 %

2.3.5 Numerical Effects

This subsection has presented several new numerical techniques which were incorporated into PCGC-3. The motivation for many of these changes was to improve the accuracy of model predictions. Their effect on convergence time will now be examined. Some slowing of overall convergence can be attributed to inaccuracies in the numerical approximations. The removal of these problems should improve convergence. Table 2.9 compares run time for several versions of PCGC-3 to determine the effect of numerical changes on code efficiency. The initialization of velocities and turbulence variables was the last numerical change whose effect was quantified. This initialization not only reduces convergence time for many cases, but also increases robustness for large cases. Table 2.9 also lists overall simulation time reductions resulting from numerical changes listed in the table.

2.3.6 SIMPLE-Based Algorithms

PCGC-3 was coded to allow simulations with the SIMPLE, SIMPLER, SIMPLEC, and SIMPLEST algorithms. Several authors have compared the speed of SIMPLE algorithm variations (Braaten, 1985; Van Doormall and Raithby, 1984). When comparing algorithms, it is important that all other factors affecting speed remain constant. Comparisons should be made on the same computer system under similar loads running the identical problem. Optimally, the different algorithms should be incorporated into the same computer code. This prevents a single method of being penalized due to inefficient coding. PCGC-3 is capable of handling all the pressure-velocity coupling algorithms discussed in this section.

The different variations of the SIMPLE algorithm are not exclusive in their implementation. For example, it is possible to combine the correction found in SIMPLEC with the explicit treatment of the convective terms used in SIMPLEST and simulate a flow including the pressure equation proposed in SIMPLER. Such a combination of techniques will be referred in this study as a SIMPLERCT run. The eight combinations of SIMPLE-based algorithms are SIMPLE, SIMPLER, SIMPLEC, SIMPLEST, SIMPLERC, SIMPLERT, SIMPLESTC, and SIMPLERCT. PCGC-3 can employ any of the eight algorithms.

2.3.7 Algorithm Evaluation

Fletcher (1983) showed that for the simulation of the BYU Combustor with PCGC-2, the SIMPLER algorithm converged in nearly half the time required by the SIMPLE algorithm. Braaten (1985) found in a series of two-dimensional moderate Reynolds number cases that SIMPLER, SIMPLEC, and SIMPLEST were approximately equal in efficiency and were all significantly faster than SIMPLE. Fewer iterations are nearly always observed with SIMPLER, but the solution of the extra differential equation increases the time per iteration and this results in similar run times.

Van Doormaal (1984) and Braaten have compared the performance of the SIMPLE and SIMPLEC algorithms for simple laminar flows. Van Doormaal observed a 61% reduction in computational effort for a sudden expansion flow and a 76% reduction for a laminar tank flow. Braaten obtained similar results. A 66% decrease in iterations was required to converge a sudden expansion flow and a 64% decrease was observed for a driven cavity flow. Unfortunately, these large reductions in computational effort are only observed where "the predominant factor governing solution cost is the pressure-velocity coupling. In other situations, the interaction between the turbulence model and the momentum equations, or the interplay of the buoyancy forces . . . may be the factor mainly responsible for slow convergence" (Van Doormall, 1984).

Markatos (1984) found the SIMPLEST algorithm had superior convergence properties for the simulation of natural convection. Braaten (1985) found that although SIMPLEST performed very well at moderate Reynolds numbers, it reverts to Jacobi iterations at high Reynolds numbers, causing

substantially slower convergence. SIMPLEST appears to be most efficient at low Reynolds numbers.

The SIMPLE-based algorithms were evaluated by comparing their respective performance on the two test cases. The cases were run with various levels of under-relaxation factors and using different combinations of SIMPLE variations. This evaluation is based on two factors: convergence time and algorithm robustness. This study measured robustness by the width of the range of under-relaxation factors which produce converged simulations.

Several graphs have been created to display the results of this numerical experiment. Each point represents a converged solution. The different lines on the graphs represent different variations of the SIMPLE algorithm. The lower lines on the graph represent faster converging algorithms.

The specification of under-relaxation factors are very case dependent. The process of optimizing these parameters for a specific case is often more time consuming than converging the case with less-than-optimal under-relaxation factors. A secondary objective of the SIMPLE variation study is the establishment of general recommendations for specifying the value of under-relaxation factors.

Case 1

The SIMPLERT, SIMPLESTC, and SIMPLERCT variations performed poorly and will not be considered further. The SIMPLER, SIMPLEST, SIMPLEC, and SIMPLERC were all fairly robust as illustrated by the width of the respective curves in Figure 2.5. SIMPLER and SIMPLERC converged at the largest under-relaxation factors. However, both the SIMPLEC and SIMPLEST algorithms were significantly faster than SIMPLER and SIMPLERC at under-relaxation factors of 0.5 and 0.6. SIMPLE was the least robust. It diverged at under-relaxation factors exceeding 0.6.

All the algorithms produced remarkedly comparable minimum execution times. The similarity in performance at an under-relaxation factor of 0.7 is noteworthy. This suggests that perhaps the velocity/pressure coupling is not the limiting factor for overall convergence, but the turbulence modeling is slowing the convergence process. This is supported by the relative small differences between algorithm minimum execution times.

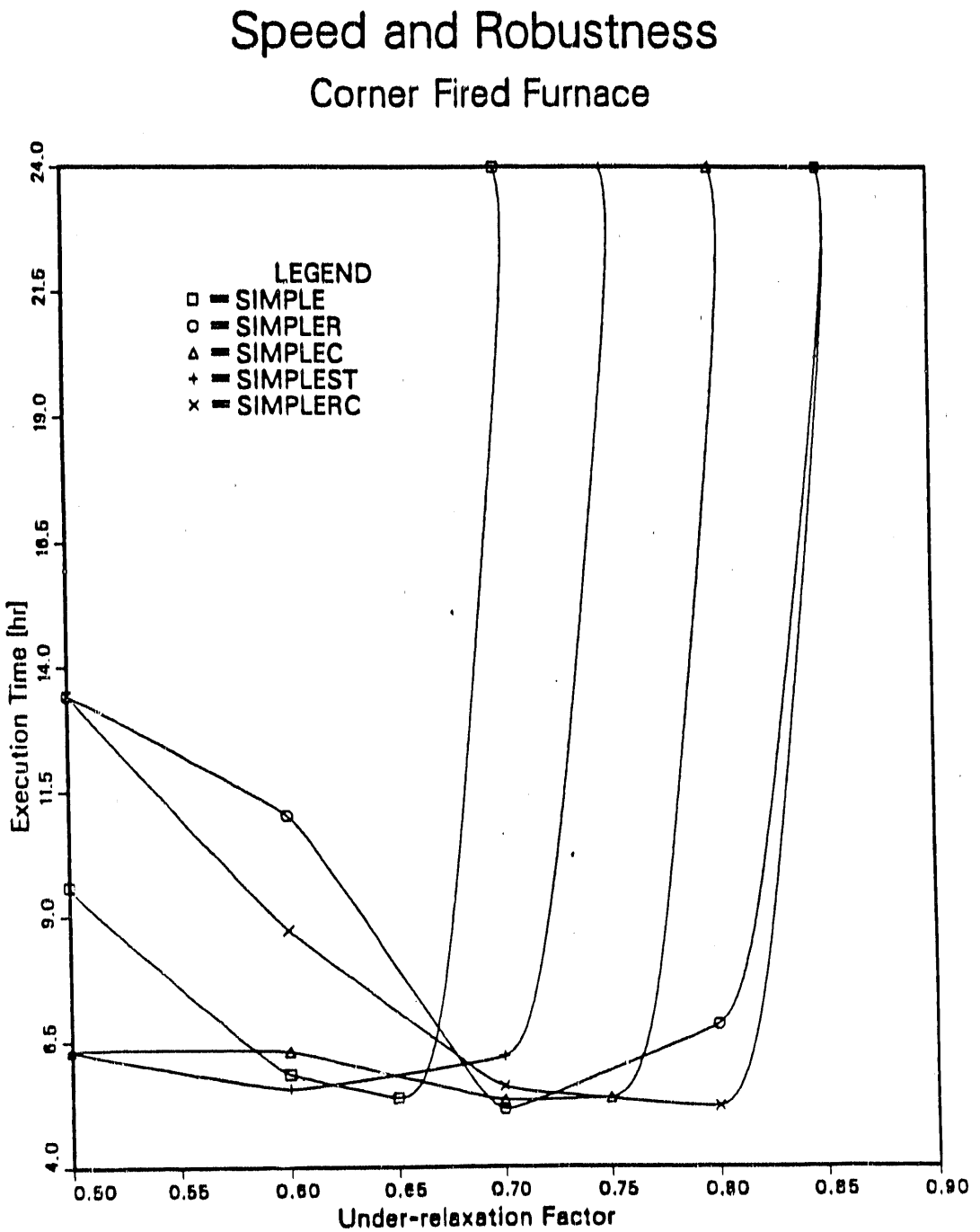

Figure 2.5: Performance Curve for Case 1.

Case 2

The SIMPLEST algorithm diverged for this case, which involved a high Reynolds number. Once again, the SIMPLE algorithm diverged above under-relaxation factors of 0.6. The SIMPLER, SIMPLEC, and SIMPLERC algorithms performed similarly, minimizing execution times around an under-relaxation factor of 0.8 as shown in Figure 2.6. The proximity in overall performance suggests the turbulence submodel is limiting algorithm efficiency.

General Recommendations

Algorithm performance and optimal under-relaxation factors are case dependent. Based upon these three cases, it is recommended to use the SIMPLERC option with under-relaxation factors of 0.8. The SIMPLER and SIMPLEC algorithms provide similar performances and could also be used.

The turbulence submodel appears to be the limiting factor for overall convergence for high Reynolds number flows. This conclusion is based on two observations. The similar performances of SIMPLE-based algorithms support this idea. The best evidence, however, is an examination of case convergence histories. These histories reveal the equation errors for the k and ϵ equations are typically much larger than the other equation errors.

2.4 2-D Comparative Evaluation

2.4.1 Introduction

In 1985, BYU amassed a set of combustion-related data from various investigators. The Data Book (Smoot, et al., 1985) provides a single reference containing detailed experimental data for use in model evaluation. All of these data are two-dimensional axi-symmetric in nature. The smaller-scale 2-D laboratory data provide a much larger and more reliable data source than do 3-D large-scale data bases (see last subsection in this chapter). Although not an exhaustive review of all related data, the Data Book supplies relevant, applicable data for pulverized coal combustion and gasification modeling. Five categories were organized to allow independent analysis of different model components (i.e. coal reaction processes, particle effects, etc.). They include: gaseous isothermal flow, particle-laden isothermal flow,

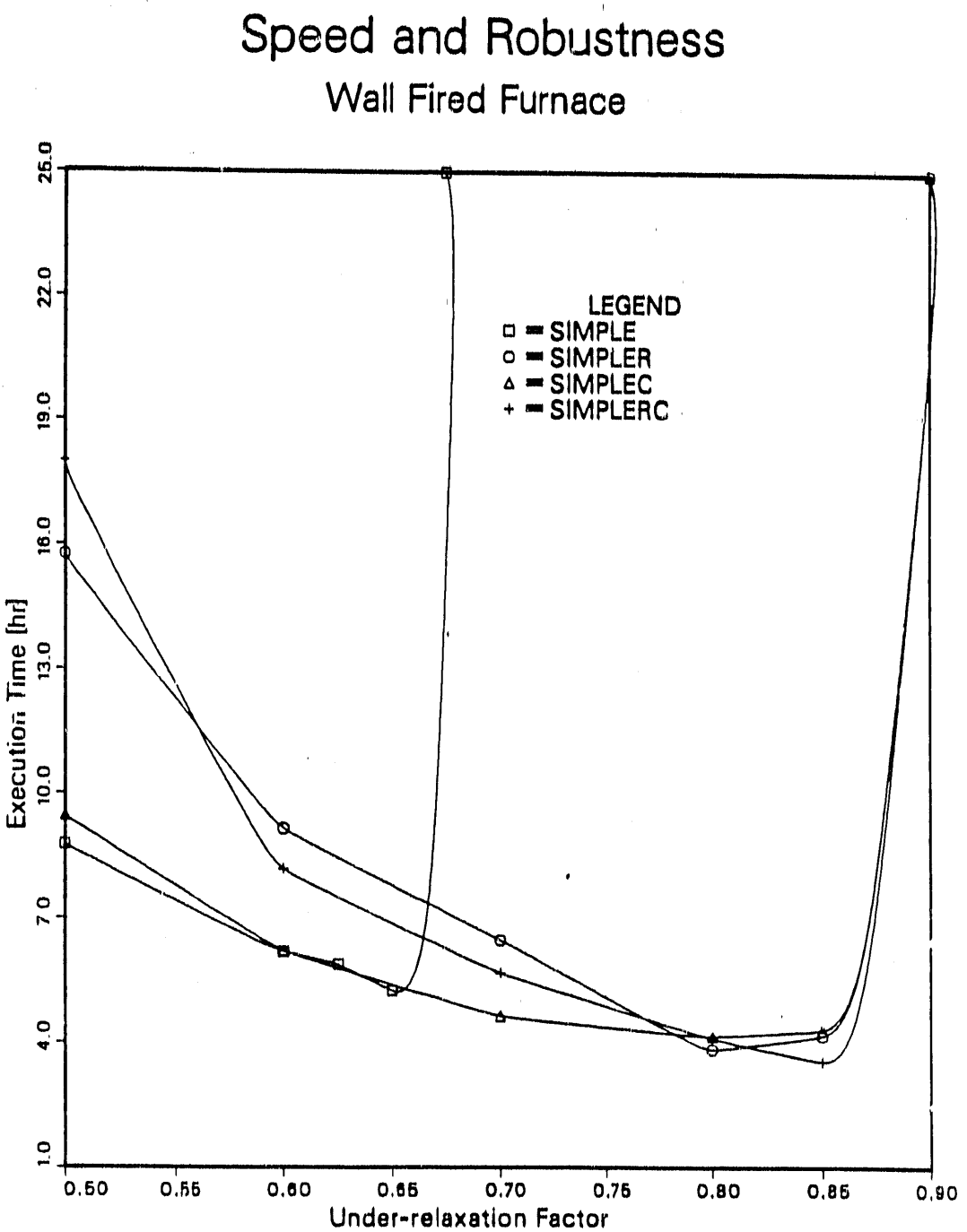

Figure 2.6: Performance Curve for Case 2.

gaseous combustion, coal combustion, and coal gasification. Each category was further subdivided into swirling and non-swirling flows. Many of these data sets have been previously compared to 2-D (PCGC-2) predictions by past investigators, but without general review purposes in mind. A more comprehensive review of model capabilities was needed. This was done as part of this study by examining the remaining data sets and by making an additional generalized study of the previous cases. Since this source of data was axi-symmetric and since the existing 2-D code (PCGC-2) has the same framework as the expected 3-D code, it provides a reasonable test bed for evaluating model capabilities and accuracy.

This project was to evaluate, in a general sense, the capabilities of PCGC-2. In order to accomplish this goal, several specific projects were undertaken. Briefly: a sound data base was established, all data sets were converged on PCGC-2, and the results were subsequently analyzed. These specific tasks are outlined below.

Establishment of Data Base

Although a complete set of data was available for comparative purposes in the form of the Data Book, it was not a thoroughly reliable source of data. Many errors were suspected throughout the book but few had been located. Thus, to validate the data, each case was compared with the original document from which it has been extracted. Transcription errors found were noted and corrected. Errors suspected due to experimental methods or due to typographical problems in the original manuscript were noted but not changed unless permission from the original investigator was received. Except where relevant (i.e., significant errors in the measurement of inlet parameters), the results of this task are not included in the main body of this report.

PCGC-2 Predictions of Data Base

Many of the sets of data contained in the Data Book had been studied previously with the aid of PCGC-2 by three different investigators: Hill (Hill, 1983), Fletcher (Fletcher, 1983), and Sloan (Sloan, 1985). However, at the commencement of this project, seventeen of the 35 cases had not yet been analyzed with PCGC-2. Consequently, these cases were run on PCGC-2 and the results were analyzed. PCGC-2 predictions performed during this study

were based as closely as possible to the physical description of each case. Predictions were not enhanced artificially by "fine-tuning" parameters, nor was the code changed or modified in any way to increase predictive accuracy. In some cases, it became necessary to estimate physical parameters if they were not reported by the original investigator. However, these estimates were based on previous experimental work and represent realistic values. These PCGC-2 predictions were compared to numerical results from other investigators, when available, and are reported by Rasband (1988). Previously studied data cases were not re-run unless significant errors were discovered in the inlet parameters used by the former investigators.

Analysis of Trends and Patterns in Predictions and Data

Once each case was converged with PCGC-2, the results were examined individually and collectively. Individual analysis entailed graphical comparison of data with numerical results (PCGC-2 and others) and evaluation of measuring techniques and apparatus. Models used by other investigators were not thoroughly examined. They were included solely as a basis for "grading" PCGC-2's performance. Inlet parameters yielding optimum results for PCGC-2 calculations of each case, as well as given inlet conditions (i.e. reactor geometry, flow rates, etc.) were also tabulated.

Whereas the individual analysis is detailed, the comprehensive analysis is general. Ideally, all aspects of combustive flow would have been examined concurrently for every case (i.e. mixture fractions, coal burnout, velocity components, etc.). Each set of data, however, did not contain such comprehensive, detailed information. Cases in similar categories did include enough similar data to effectively identify trends in numerical predictions, data, and the discrepancies between the two. A few important trends were discovered through comparisons of "unlike" data (i.e., comparison of mixture fraction with argon concentration, etc.).

2.4.2 Analysis

The complete analysis of this comparison of the Data Book cases and PCGC-2 performance is given by Rasband (1988). The analysis comprises 33 separate cases as summarized in Table 2.10. Only the following example is given in this report.

Table 2.10: Evaluation of Codes.

Category	Investigator	Chem. System	Recorded Measurements	Swirl No.	Measurement Techniques
Gaseous, Cold Flow	Owen [Aro. Inc.]	Air/Air	U, V	----	LDV
Gaseous, Cold Flow	Takagi et. al. [Osaka Univ.]	H2/Air	H2, N2, O2, U, <V>, <W>, <U>	----	LDV, stainless steel water-cooled probe
Gaseous, Cold Flow	Webb [BYU]	Air/Air	U, <U>	----	LDV (without frequency shifting)
Gaseous, Cold Flow	Samuelsen et. al. [U.C. Irvine]	CO2/Air	U, <U>, W, <W>	0.3, 0.0 0.8, 0.0	LDV
Gaseous, Cold Flow	Webb [BYU]	Air/Air	U, <U>, V, <V>	0.0, 0.49	LDV (without frequency shifting)
Gaseous, Cold Flow	Gouldin et. al. [Cornell Univ.]	Air, Air	U, <U>, V, <V>	0.5, 0.56 0.5,-0.56	LDV
Particle-Laden Cold Flow	Leavitt [BYU]	Coal/Air	Ar, PFLUX	----	Collection Probe
Part.-Laden, Cold Flow	Sharp [BYU]	Silicon/Air	Ar, PFLUX	----	Collection Probe
Part.-Laden, Cold Flow	Modarress et. al. [U.C. Irvine]	Silicon/Air	U, <U>, <V>, PURMS, PUVL	----	LDV
Part.-Laden, Cold Flow	Modarress et. al.	Silicon/Air	U, <U>, <V>, PURMS, PUVL	----	LDV
Part.-Laden, Cold Flow	Leavitt [BYU]	Coal/Air	Ar, PFLUX	0.0, 0.40	Collection Probe
Part.-Laden, Cold Flow	Leavitt [BYU]	Coal/Air	Ar, PFLUX	0.0, 0.40	Collection Probe
Part.-Laden, Cold Flow	Leavitt [BYU]	Coal/Air	Ar, PFLUX	0.0, 0.90	Collection Probe
Gaseous Combustion	Michelfelder [IFRF]	Propane/Air	O2, N2, CO2, H2, Temp.	----	Water-cooled probe, Suction pyrometer
Gaseous Combustion	Michelfelder [IFRF]	Methane/Air	O2, N2, CO2, H2, Temp.	----	Water-cooled probe, Suction pyrometer
Gaseous Combustion	Takagi et. al. [Osaka Univ.]	N2,H2/Air	O2, N2, H2O, H2, U, <U>, V, <V>	----	LDV, suction pyrometer
Gaseous Combustion	Hassan [Imperial College]	Nat. Gas/Air	O2, CO2, Temp.	----	Water-cooled probe,

Table 2:10: Evaluation of Codes (Continued).

Coal Combustion	Hein [IFRF]	Anthra./Air	O2, N2, CO2, Temp.	0.0, 1.4	Water-cooled probe, Suction pyrometer
Coal Combustion	Harding [BYU]	Anthra./Air	O2, N2, CO2, H2, Ar, CO, H2O, CH4, HCN, NH3	0.0, 2.2	Water-quenched isokinetic probe
Coal Combustion	Asay [BYU]	Anthra./Air	O2, CO, CO2, H2, Ar, N2, NO, H2O, NH3, HCN, CH4, C, H, N, O-S, ASh	0.0, 2.0	Water-quenched isokinetic probe
Coal Gasification	Snelberg [BYU]	Bitum./Air	O2, CO, CO2, H2, Ar, N, N2, NO, NH3, HCN, Ash, H, CS2, SO2, COS, H2S, C	----	Water-quenched isokinetic probe
Coal Gasification	Brown [BYU]	Subbit./Air	Ar, He, CO2, CO, CH4, S, H2, O2, C, H, O, Ash, N	----	Water-quenched isokinetic probe
Coal Gasification	Brown [BYU]	Lignite/Air	Ar, He, CO2, CO, CH4, S, H2, O2, C, H, O, Ash, N	----	Water-quenched isokinetic probe
Coal Gasification	Brown [BYU]	Bitum./Air	Ar, He, CO2, CO, CH4, S, H2, O2, C, H, O, Ash, N	----	Water-quenched isokinetic probe
Gaseous Combustion	Michelfelder [IFRF]	Methane/Air	O2, N2, CO2, H2, Temp.	0.0, 0.50	Water-couled sampling probe, suction pyrometer
Gaseous Combustion	Samuelsen [U.C. Irvine]	Propane/Air	U, W, $\langle U \rangle$, $\langle W \rangle$, U-W	0.0, 0.80	LDV
Gaseous Combustion	Gouldin et. al. [Cournell]	Nat. Gas/Air	U, $\langle U \rangle$, V, $\langle V \rangle$	0.5, 0.56 0.5,-0.56	LDV
Coal Combustion	Beer [MIT]	Anthra./Air	O2, CO2, Temp.	----	Suction pyrometer, T-suction pyrometer
Coal Combustion	Hein [IFRF]	Anthra./Air	O2, N2, CO2, Temp.	----	Water-cooled sample probe
Coal Combustion	Thurgood [BYU]	Bitum./Air	O2, CO, CO2, H2, N2, C, Ar, H, S, O	----	Water-quenched, isokinetic probe
Coal Combustion	Michel & Payne [IFRF]	Bitum./Air	O2, CO, CO2, H2, NO, N, Ash, Temp.	----	Water-cooled probe, Suction pyrometer
Coal Combustion	Rees [BYU]	Bitum./Air	O2, CO, CO2, H2	----	Water-cooled probe, Suction pyrometer
Coal Combustion	Hein [IFRF]	Anthra./Air	O2, N2, CO2, Temp.	0.0, 1.0	Water-cooled probe, Suction pyrometer

Beer reported local gas properties and mean velocity measurements of a detached anthracite-air flame in a 1.5 X 1.5 m rectangular, horizontal furnace. Gas temperatures were gathered with a suction pyrometer. PCGC-2 predictions of this case were analyzed previously by Fletcher (1983) and are summarized below. Mean velocity data were not included in the Data Book due to the unreliability of the probe measuring techniques.

Normal standard devolatilization constants of coal are recommended by Ubhayakar, et al. (1976) (these constants are based on a numerical curve fit of devolatilization rates for a variety of bituminous coals). However, because these constants were found inappropriate by Fletcher, he reduced the yield factors from recommended values of 0.39 and 0.80 (Smoot and Pratt, 1979; Smith, et al., 1981) to 0.06 and 0.12, respectively. The resulting centerline temperature, and O_2 and CO_2 concentration profiles are illustrated in Figure 2.7. Centerline predictions of temperature lag behind experimental temperatures. This pattern parallels those observed in gaseous diffusion flame predictions made in this study. One possible cause of this discrepancy between the data and predictions is the measuring technique used by Beer. His use of thermocouples is a very difficult task in coal-laden flames. Fletcher noted that the recommended devolatilization constants used in his first parametric prediction led to significantly overpredicted devolatilization. This overprediction might not have been solely the result of erroneous devolatilization parameters. Rather it was probably due to a combined result of devolatilization modeling problems, inadequate turbulence modeling, and problems associated with the assumption of mixing-limited reaction. Radiation from the chamber wall, particle effects, heat loss, and problems due to the large reactor geometry also probably contributed to these discrepancies.

Centerline predictions of O_2 concentration reflect the underprediction of centerline temperature in the forward section of the chamber where oxygen depletion is less rapid than the data indicate. Despite the discrepancies observed in the temperature and O_2 comparisons, CO_2 predictions agree quite well with the data. In the near-exit regions of the reactor, PCGC-2 shows a more complete combustion of oxygen and formation of CO_2 than is evidenced in the measurements. Radial profile comparisons were made but did not add any significant information except to show that the discrepancies along the centerline were reflected in the radial profiles.

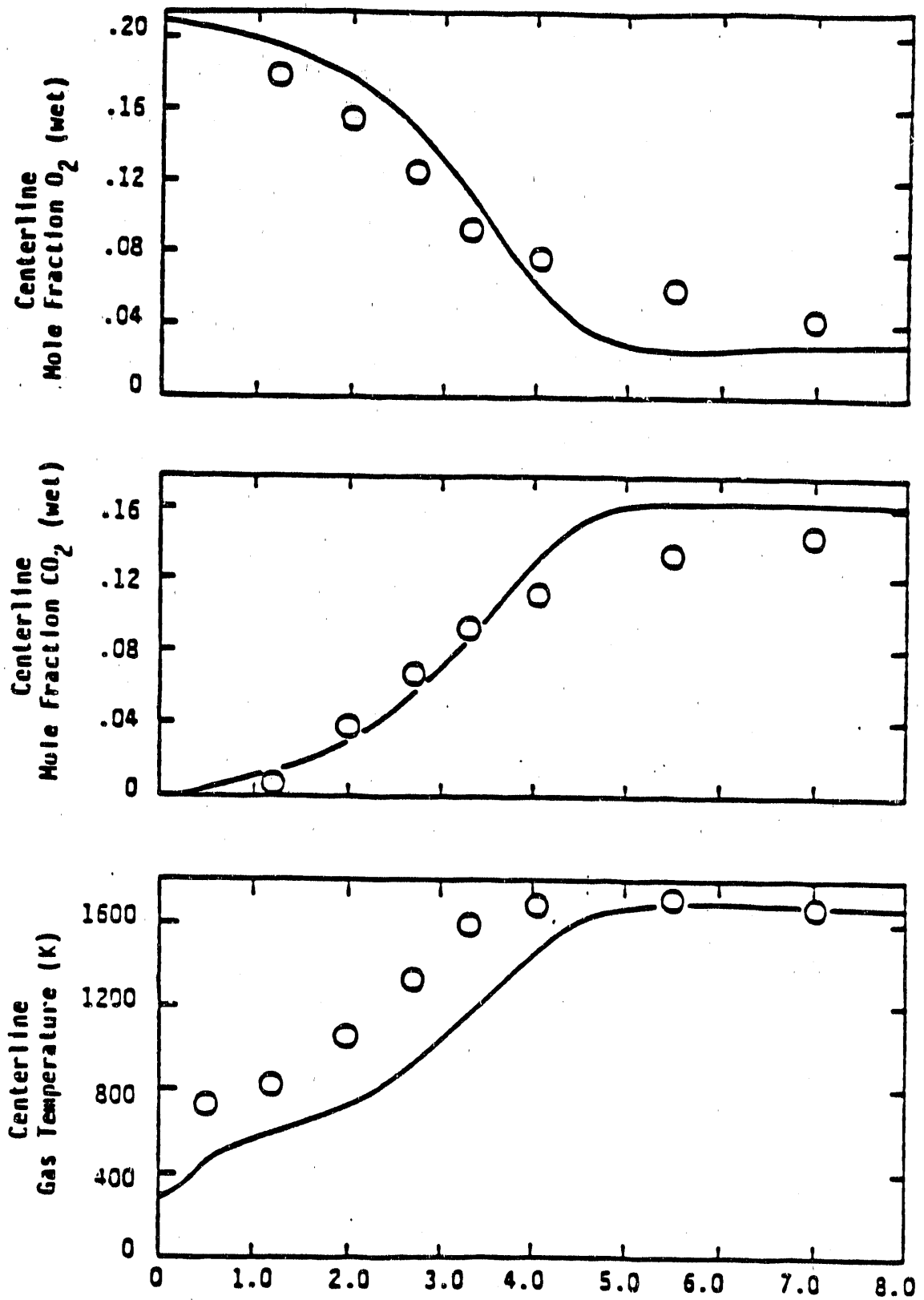

Figure 2.7: Centerline Profiles of O_2, CO_2 Concentration and Gas Temperature (O_2-data from Beer [1964], PCGC-2 Predictions from Fletcher [1983]).

It is difficult to attach too much significance to the accuracy with which PCGC-2 predicted this case for the following reasons: the reactor was not axi-symmetric; the reactor was horizontal (adding to buoyancy effects, which are not modeled by PCGC-2); and, due to the larger size of the reactor and the fixed number of allowed grid spaces, the numerical accuracy of the prediction was lessened in comparison to predictions of smaller reactors.

2.4.3 Conclusions

Data reliability was investigated during the comparison of data with PCGC-2 predictions and the results are tabulated below. Typical experimental problems (i.e. probe effects) are not discussed.

(1) Webb (1982) noted Bragg cell calibration difficulties for the gaseous cold flow data; however, the data appear to be consistent (i.e. do not show unusual or random behavior).

(2) The gaseous flow cases reported by Samuelsen and Brum (1982) appear extremely reliable; however, the lack of inlet characteristics makes these data difficult to model.

(3) Webb Case II (1982) contains data considered to be poor by Webb. Flow rates from integrated axial velocity profiles at downstream locations were 30% in error. It is suggested that these data not be used for analysis purposes.

(4) The counter-swirling case of Gouldin, et al. (1983) indicates flow asymmetry, rendering it dubious for axi-symmetric modeling.

(5) Caution should be exercised in interpreting the Gouldin, et al. (1983) data as they show evidence of flow intermittency (this intermittency does not render the data useless).

(6) Leavitt Case II, III, and IV (1980) show discrepancies in the inlet and exit argon concentrations. This data is not recommended for general modeling use.

(7) The Soelberg data (1985) seem reliable with the exception of the data gathered 0.2 m from the inlet. It is suggested that the profiles at this axial location be disregarded.

After the data were reviewed for accuracy, analysis of each case with PCGC-2 predictions was completed. Each section summarized data/prediction comparisons individually and collectively (in relation to the specific Data Book

category in which the data belonged). Despite the range of possible experimental error and the inability to quantify these errors, a comparison of a wide variety of data allows for broad analysis.

Given the complex nature of turbulent flows, PCGC-2 performs respectably in predicting such a wide variety of data as collected in the Data Book. Isothermal flows represent the simplest flow data in the Data Book and are described adequately. A cursory glance at predictions for more complex flows indicates less predictive accuracy. This inability to define more complex flows appears to set PCGC-2 at a disadvantage when compared to flow descriptions made by other investigators. However, the main thrust of this study was to determine the overall, general robustness of PCGC-2, not to determine whether PCGC-2 could generate perfect flowfield characterizations.

Models used by other investigators were adjusted (in cases where agreement between data and predictions was substantially better than that of PCGC-2) to improve their predictions. For example: Zhang, et al. (1985) imposed a small pressure gradient along the centerline of the reactor to improve predictions of the Modarress, et al. (1982) data; Lockwood, et al. (1983) changed the equilibrium rate constant for CO formation and specified detailed devolatilization profiles for the Michel and Payne (1980) case; and Fletcher (1983) improved predictions of the Soelberg case by introducing a partial equilibrium scheme into PCGC-2. It is not to be supposed that these modifications devalue the work of these investigators. Rather, predictions of that type served a different purpose. The goal in this project was to determine how PCGC-2 would perform without fine tuning parameters or modifying the code for each individual set of data. Given this objective, PCGC-2 performed admirably in many areas. Some of these areas are discussed below.

Perhaps the most impressive accomplishment of PCGC-2 was that it was able to reach a solution for 33 of the 35 cases in the Data Book. Many of these data sets were characterized quite easily. Considering the broad array of the physical characteristics of the cases, this was quite an achievement.

In most cases, despite discrepancies between predicted and measured profiles in the recirculation zone, the outer regions of the reaction chamber were described very well. Exit compositions and carbon conversions were predicted with almost complete accuracy. Areas of fully mixed flow were also characterized well.

Despite these accomplishments, some problem areas exist and are discussed in the following section.

Weaknesses in PCGC-2's ability to simulate flow and combustion behavior appear primarily in system-related (boundary specifications) and code assumptions-related (phenomenological) groups.

Obtaining reliable predictions (especially in strongly swirling, recirculating flows) is heavily dependent upon the availability of accurate and complete inlet boundary conditions. The predictions can be very sensitive to the distributions of each inlet stream and to the axial location at which computations are initiated. Many data sets contained in the Data Book did not delineate sufficient boundary conditions for adequate flow characterization.

During the analysis of PCGC-2, it became evident that three boundary conditions were essential for adequate characterization by PCGC-2. These were: inlet mean velocity and turbulence intensity profiles, heat loss and heat effects near the chamber wall, and geometry configurations consistent with PCGC-2 assumptions. (Rather than eliminating all data in which the reactor geometry does not conform to PCGC-2 configurations, the code has been improved to allow various burner and reactor configurations.)

Although insufficient or inaccurate boundary conditions contribute significantly to discrepancies between PCGC-2 predictions and experimental data, there are also many phenomenological problems associated with assumptions made by various submodels in PCGC-2. Three submodels in particular added to much of the errors in PCGC-2 predictions. These were: the turbulence model, the devolatilization model, and the submodel dealing with equilibrium kinetics. Each are summarized below:

Turbulence Submodel

Rodi (1981) evaluated the performance of the k-ϵ model for turbulent systems. He suggested that more complex turbulence models would be more accurate but would be too complex and computationally expensive for practical use. Harsha (1977) reviewed independent studies of the adequacy of the k-ϵ models were adequate for describing turbulent flow in axi-symmetric systems. Sloan (1985) also stated that the performance of the k-ϵ model was poor, especially in the vicinity of central toroidal recirculation zones. He does, however, believe the k-ϵ model performed satisfactorily for the mean axial velocity in the recovery region or at large radii from the symmetry axis. He found that turbulence intensity predictions were also adequate in

the recovery of near-exit regions. The conclusions of all three of these investigators (Rodi, Harsha, and Sloan) concurred with problems observed in data/predictions comparisons.

Perhaps the most clear evidence of k-ϵ model inadequacies appeared in the premature rate of predicted mixing centrally and radially for non-swirling flows. Mixture fraction profiles, mean axial velocity profiles and argon concentration profiles (non-reacting flow cases) and species composition profiles (reacting flow cases) illustrated PCGC-2's tendency to predict more rapid mixing than observed experimentally.

Root-mean-square (RMS) velocity comparisons yielded fair results in simple flows. However, as the flow became more complex (becoming more anisotropic in nature) predictive accuracy degenerated. An increase in system anisotropy would necessarily decrease the k-ϵ model's ability to perform well, as it assumes isotropicity among the normal stresses.

As inlet turbulence was increased (i.e., swirl number, or the addition of a quarl), the predictive accuracy decreased for the low volatiles-content coal, and profile comparisons yielded results increasingly similar to those of high-volatile coal combustion.

Most of the combusting systems showed a prematurely predicted flame-front. This was characterized by a more rapid rise in initial temperature, increase in product species, and depletion of reacting species. Product species profiles of CO_2 showed a characteristic peak along the centerline not evidenced in the data, while predicted profiles of CO showed concentration levels twice in peak magnitude and skewed upstream relative to the data profile. Many other factors may have contributed to erroneous flame-front predictions (i.e., devolatilization, "mixed is burned" theory, etc.). However, given the tendency of PCGC-2 to prematurely predict mixing in non-reacting flows, it is reasonable to assume the k-ϵ model also played an important role in combusting systems.

Devolatilization Submodel

Devolatilization parameters used in the competing, parallel devolatilization reactions represent a primary source of error in this submodel. Fletcher (1983) indicated that devolatilization parameters for one coal would not necessarily yield good results for a coal with different characteristics.

Ubhayakar, et al. (1976) evaluated devolatilization for several coals rang-

ing from volatiles content of 0.11 to 0.47. Based on a curve fit of the resulting devolatilization rates, he recommended values for devolatilization parameters. Subsequent use of these values illustrated the need for individual analysis and calculated values of rate parameters for each coal.

The actual model itself (the competing, parallel reaction model) also contributed to inaccurate devolatilization characterization. This model follows the model proposed by Kobayashi, et al. (1977). When compared to the multiple, parallel reaction proposed by Sprouse and Schuman (1981), the predictions of PCGC-2's devolatilization model showed faster devolatilization rates.

Low-volatile content coal combustion (i.e., Beer (1964), and Hein, et al. (1970)) was reasonably described by PCGC-2 when the yield parameters were specified at more appropriate (or smaller) values than those recommended by Uhbahayakar.

High-volatile content coal combustion predictions indicated a prematurely predicted flame-front. Predicted centerline temperatures rose more rapidly than the measured temperatures. Predictions of product species formation and reacting species consumption also indicated a premature flame. Predictions of centerline CO_2 concentration showed a sharp local peak in the inlet region, while CO concentration profiles were higher in peak magnitude and skewed upstream relative to the data profiles.

It is important to note that in coal combustion and gasification, probe effects are possibly significant (especially in areas of high species concentration and large temperature gradients). In many instances, probes have been found to act as a species carrier. In these instances, species were carried along the probe from one area in the reactor to another. It is possible that much of the disagreement along the centerline is directly attributable to probe effects or other physical problems.

Equilibrium Kinetics Assumption

PCGC-2 assumes that the rate of chemical reaction is governed by the rate of mixing of gaseous oxidant and reactant. This assumption is especially good when the gas-phase reactions are fast compared to the time-scale of turbulence. Gaseous properties then become functions of the turbulent mixing rate, and can be calculated from the mixture fractions using equilibrium considerations. Because some of the reactions do not reach equilibrium, and

others reach a sort of super-equilibrium state, this introduces a definite source of discrepancies in prediction/data comparisons.

The gaseous propane and methane combustion cases of Michelfelder and Lowes (1974) provided a clear example of this. The propane case exhibited more discrepancies between data and predictions than did the methane case. Propane reactions are less applicable to assumptions of local equilibrium than methane reactions and, therefore, the assumption that propane production is mixing-limited would necessarily produce a premature ignition. Coupling this with the evidence of premature mixing due to turbulence modeling problems, the resulting predictions show exaggerated peaks in product species production where methane cases show mild peaks.

Taking this one step further, a look at the coal combustion and gasification cases gives evidence of the problems associated with assuming the "mixing-burnt" theory to be valid. In the high-volatile content coal combustion and gasification cases, the prediction of volatiles is known to be premature. These volatiles include higher chain hydrocarbons and other species that are less agreeable to assumptions of equilibrium kinetics.

Combined effects of premature mixing, premature devolatilization and incorrect equilibrium exaggerate discrepancies between predicted and measured flame-front locations. Gasification and coal combustion of high-volatile content coal shows these expected discrepancies. Peaks in predicted centerline CO_2 concentrations are more exaggerated than those observed in gaseous combustion cases. Other profiles, in general, are not adequately described qualitatively or quantitatively.

2.5 3-D Comparative Evaluation

2.5.1 Turbulence Model Options

Three options were initially coded in PCGC-3 for turbulence modeling: constant eddy diffusivity, Prandlt's mixing length model, and the standard k-ϵ model. The first two options are difficult to use because they require the *a priori* specification of either the eddy diffusivity or local mixing length. Initial attempts to specify a mixing length included calculating the mixing length to be the distance between the node and the nearest wall or assigning the mixing length to a characteristic dimension of the burner and/or furnace.

These methods proved inadequate. In order to compare these options, a k-ϵ model simulation was first performed. Results from this simulation were then used to calculate parameters for simulations using the other two turbulence submodels. The average value of eddy diffusivity used in the k-ϵ predictions could be easily obtained from the k-ϵ simulation. The average mixing length was calculated from the following procedure provided by Sampath (1987).

A local length scale of turbulence, l_ϵ, can be deduced from the values of k and ϵ using the relation:

$$l_\epsilon = \frac{c_\mu k^{\frac{3}{2}}}{\epsilon} \tag{2.14}$$

This length scale represents the macro scale of turbulence and is related to Prandtl's mixing length, l_m, through the relation:

$$l_\epsilon = c_\mu^{\frac{1}{4}} l_m \tag{2.15}$$

The same configuration and flow rates were used for all three simulations. The following sections compare and contrast the predictions for these three turbulence options. The case simulated was a corner fired furnace operated by Combustion Engineering, Inc. Details of this case have been presented in the numerical evaluation section.

Velocity Vector Plots

Before model predictions are presented, a brief explanation of the velocity plots appearing in this report is given. Each plot represents a plane within the computational volume. The shaded areas in the figures represent reactor walls and the arrows signify velocity vectors constructed from the two components of velocity parallel to the designated plane. The length and direction of each vector represents predicted velocity magnitude and direction for the location specified by the vector tail. In order to reduce congestion, only a fraction of the computational nodes are represented with vectors. There are two sizes of unfilled arrowheads and their ratio along with the scale for both the small vectors and reactor dimensions is given near the top of each figure. Filled arrowheads represent experimental data.

Constant Eddy Diffusivity Model

The velocity predictions found in Figure 2.8a were calculated using a constant eddy diffusivity. The constant value used in the simulation was 0.0155 $kg\ m^{-1}\ s^{-1}$. Several geometric features of the furnace are seen in Figure 2.8. The end of the furnace nose is visible at a height of about 3.8 meters and the three panels (platens) attached to the furnace ceiling are shown. The overall agreement between predictions and data is reasonable. Experimental velocities are larger near the furnace bottom (height of about 1.0 m) than the calculated values. The model fails to predict the complex flow interactions in the platen region.

Mixing Length Model

The predictions for the mixing length simulation are very similar to the constant eddy diffusivity calculations. The average mixing length was specified at 0.0248 meters for the case represented by Figure 2.8b. The predictions in the platen region were again poor. The model predicted the flow passing directly past the down-hanging panels with little interaction. Velocity predictions in the lower regions were again low, but some predicted velocity directions were slightly improved compared to the constant eddy diffusivity simulation.

k-ϵ Model

The results from the k-ϵ simulation are given in Figure 2.9. A close inspection of this figure reveals several subtle improvements over the previous predictions. The calculated velocities at a height of about 1.0 m are much closer in magnitude and direction than the simpler turbulence submodels. The simulated velocities at a height of about 3.0 m contains a larger horizontal component than found in Figure 2.8. The experimental data shows an even greater horizontal velocity component. The k-ϵ model predicts some swirling flows near the furnace ceiling. This option provided the best prediction of velocity magnitudes. The similarity among the predictions is due mainly to the simpler turbulence option simulations being based on values calculated with the k-ϵ simulation.

An earlier study of a complex wall-fired furnace flow (Gillis and Smith, 1988; Gillis and Smith, 1988) produced greater differences in predictions for

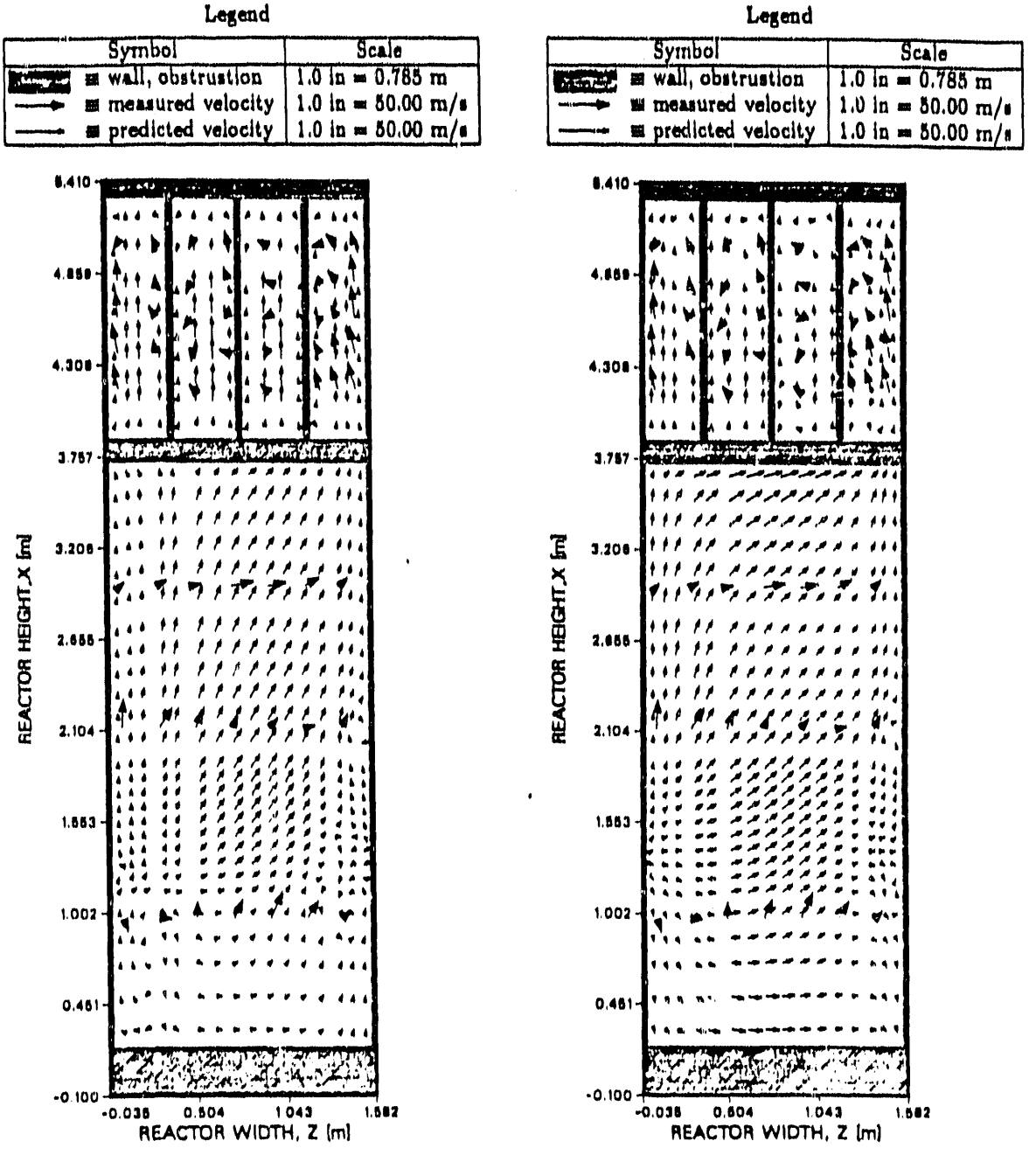

Figure 2.8: a) Constant Eddy Viscosity and b) Mixing Length Predictions of the Velocity Field in a Corner-Fired Pilot-Scale Furnace.

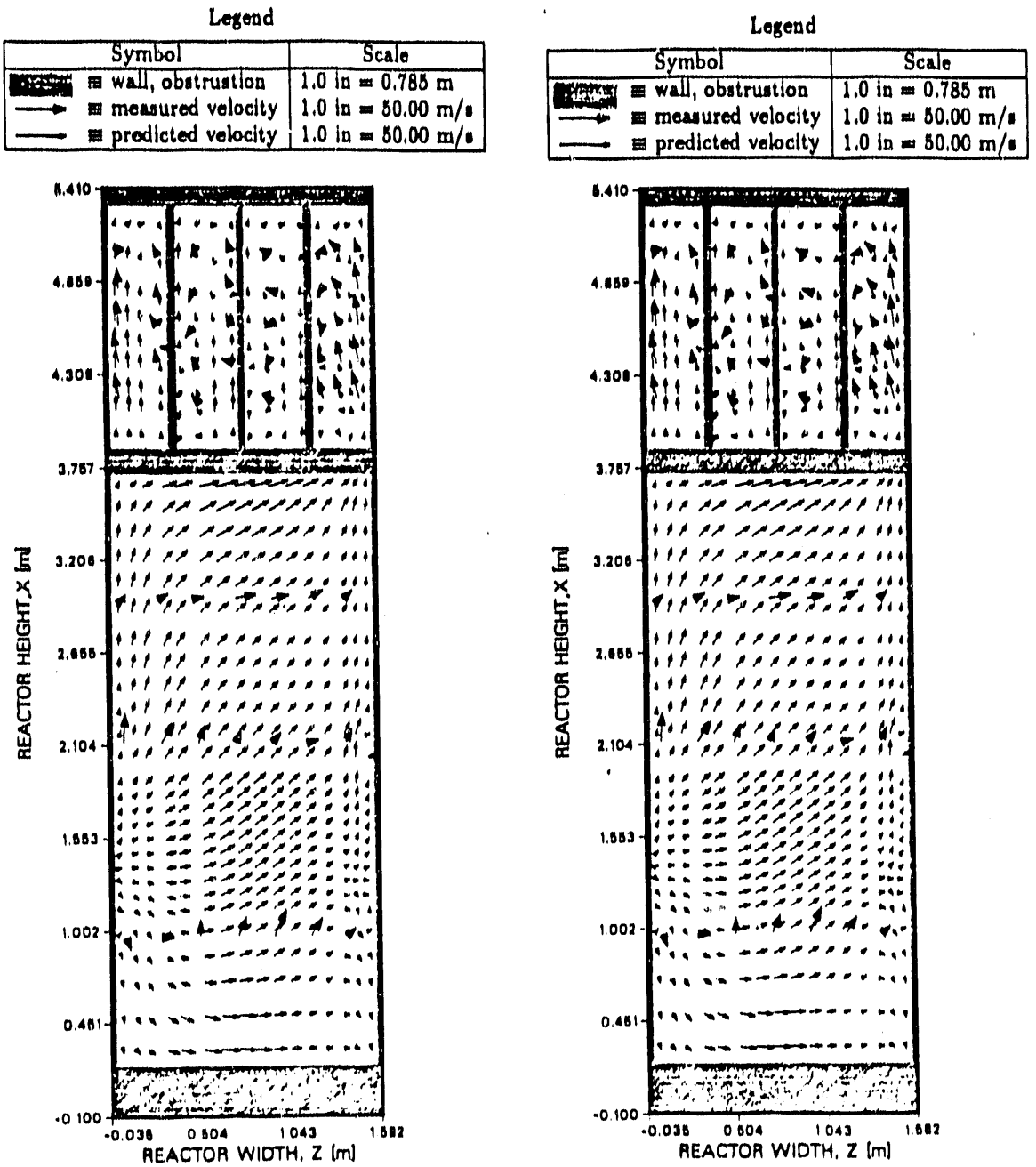

Figure 2.9: k-ϵ and Relaminarization Predictions.

the turbulence options. These differences were due to the added complexity of the flow and the use of best estimates for the mixing length and eddy diffusivity. The superiority of the k-ϵ model in this earlier study was quite pronounced. This suggests the similarity of Figures 2.8 and 2.9 is due primarily to the accurate specification of the eddy diffusivity and average mixing length.

Relaminarization Predictions

The relaminarization model of Jones and Launder (1972, 1973) was implemented as an option in PCGC-3. This model was initially tested by comparing simulations performed with the relaminarization model, the standard k-ϵ model and with a constant eddy diffusivity model, which was set equal to the laminar viscosity. These options were used to simulate a laminar pipe flow. Both the laminar and relaminarization simulations give the correct velocity profile in the pipe. The standard k-ϵ model fails to predict a parabolic profile.

A second evaluation of relaminarization was conducted by modeling a fully turbulent pipe flow. These simulations were made with the same conditions as the previous test, except the velocity was increased. The relaminarization and k-ϵ model produced similar profiles, which were close to the theoretical turbulent profile. This demonstrates the ability of the relaminarization model to correctly predict negligible eddy diffusivity at low Reynolds numbers, but then revert to normal k-ϵ predictions at high Reynolds numbers.

The k-ϵ model with relaminarization was then used to simulate the tangentially-fired furnace modeled earlier in this section. The results, presented in Figure 2.9, can be compared to the other models in Figures 2.8 and 2.9. The relaminarization simulation required additional under-relaxation in comparison to the standard k-ϵ run. The predicted velocities in Figure 2.9 are similar to earlier predictions with the other turbulence options.

2.5.2 Turbulence Conclusions

The four turbulence options in PCGC-3 all produced fairly similar predictions for the corner-fired furnace geometry. However, in the case of the mixing length and constant eddy diffusivity models, key parameters were obtained

based on a k-ϵ simulation. The requirement to specify *a priori* the eddy diffusivity or average mixing length greatly lessens the usefulness of those two turbulence options.

The relaminarization model correctly simulated laminar and turbulent pipe flows. The added complexity of this model reduced overall robustness. It is recommended that the relaminarization model should be used judiciously in transitional flows. The standard k-ϵ model will be employed in all further simulations presented in this study. This decision is based on its wide acceptance and its predictive superiority.

2.5.3 Case Dependency

The evaluation of computational fluid dynamics methods is hampered by the complex coupling of partial differential equations that often leads to case-dependent results. This phenomenon can preclude the formulation of general numerical conclusions. The effect of the turbulence submodels on the overall solution method can also complicate analysis. Most numerical evaluations are conducted with simple flows and are not applicable to complex industrial processes. CFD codes should be evaluated using the geometries and flow systems of their specific application. Therefore, the numerical evaluations in this study are based on turbulent flow simulations in industrial furnace configurations. It is also important to validate simulations with experimental data and perform quantitative velocity comparisons. Due to computational costs and data unavailability, many furnace models lack adequate evaluation.

Two cases have been chosen to initially evaluate PCGC-3. These cases were included in the 3-D data book of cases, which is documented in the next section. They were chosen to represent the two major classes of furnaces used in industrial boilers: a tangential or corner-fired system and a wall-fired swirled burner furnace. Corner-fired furnaces typically have less complex flow fields due to the interactions of burners resulting in the formation of a single large vortex. This is contrasted to wall-fired systems where the interaction among closely spaced swirled burners can create a complex vortex structure. The cases will be presented in order of increasing complexity.

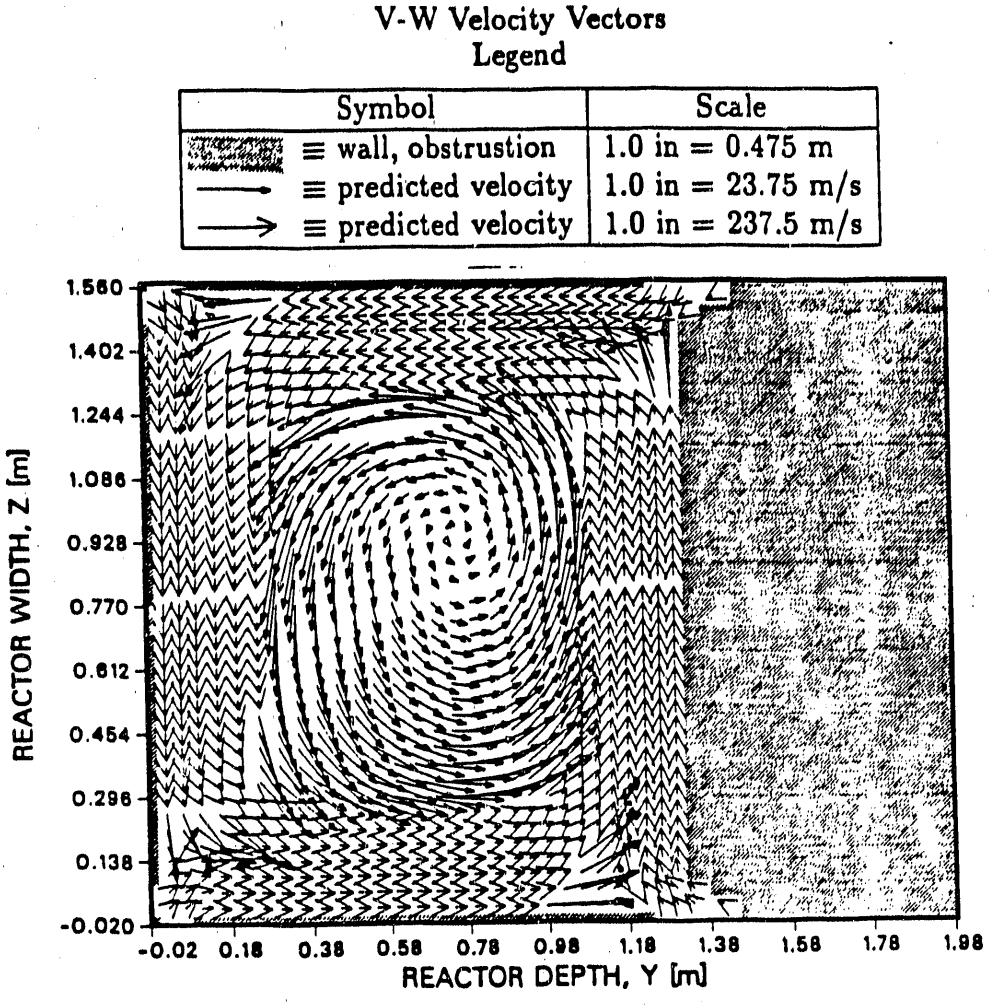

Figure 2.10: Burner Plane of LSFATF Facility.

2.5.4 LSFATF

The next case is the Large-Scale Furnace Aerodynamics Test Facility (LSFATF) operated by Combustion Engineering in Windsor, Connecticut. The facility is a 0.46 scale model of the C.E. Boiler Simulation Facility used in combustion tests. The furnace is tangentially-fired and contains a nose as well as three rectangular flow obstructions hanging from the furnace ceiling which represents the superheater and reheater platens and panels. Ambient air was blown into the furnace at an equal velocity in both the fuel and air ports of all four corner burners. Some details of the geometry can be seen in Figures 2.8-2.10. Figure 2.10 shows velocity vectors in a horizontal plane passing through all four burners. A strong counter-clockwise swirling flow is predicted. Figure 2.13 gives additional geometric detail of the nose and ash pit.

Data Set

Experimental velocity data were obtained for the LSFATF facility via a calibrated five-hole pitot tube coupled to a computer-controlled traversing data acquisition system. Approximately 100 data points were obtained on each of seven different test planes. Additional information concerning the furnace, operating conditions and data acquisition can be found elsewhere (Koucky, *et al.*, 1987).

Predictions

The filled arrowheads in Figure 2.9 signify experimental velocity vectors. Figure 2.9 shows reasonable agreement between predictions and data in the central area of the furnace. The predicted velocities at a height of about 1 meter compare favorably with overall data trends, but magnitudes are predicted in excess of experimental values. Less favorable agreement is found in the platen region due to inadequate local grid resolution. Good agreement is found in Figure 2.13.

2.5.5 Consol Case

The final case was a pilot-scale furnace operated by Consolidation Coal Corporation in Liberty, Pennsylvania. The furnace has approximately a 1 megawatt firing rate feed from four swirled burners. The furnace geometry is similar in design to large industrial boilers and contains an ash bin, furnace nose, and several clipped corners. Figure 2.11 depicts the reactor geometry in a horizontal plane passing through two burners. Clipped corners and some burner details, including the quarl region and the walls separating inlet streams, are shown. The burners are located on a single wall in a diamond configuration and are all swirled in the same direction. The outlet is located above the burners on the east wall. Further details of the furnace configuration can be seen in Figure 2.15.

Data Set

Experimental data were collected with air flowing in both the primary and secondary inlet streams. The air temperature (and therefore density) in the primary streams differed from the air temperature of the secondary stream.

Velocity measurements in the Consol furnace were made with a $\frac{1}{4}$ inch pitot tube connected to an electro-manometer. Experimental data for the x- and z-components of velocity were obtained for 50 locations. These data points are contained in four horizontal planes situated above the burners. The filled arrowheads in Figures 2.14-2.15 represent these experimental velocity measurements.

Predictions

The burner plane calculation, Figure 2.11, illustrates the complex interactions between swirled burners. The burners are swirled to lower the pressure downstream from the burners and to create a recirculating flow in the near-burner region, which can be seen in Figure 2.11. Difficulties in correctly predicting flow structure in this region can lead to problems in the flow modeling throughout the furnace.

Although not always exact in magnitude, some general flow field features are predicted by PCGC-3. Larger left (versus right) velocities at a normalized height of about 0.4 m are seen in both the experimental and predicted velocities. An earlier study of two-dimensional swirling flows faulted the k-ϵ model with predicting excessive recirculation zone lengths (Sloan, *et al.*, 1986). The data reveal a central downward recirculation region surrounded by large upward velocities. The poor predictions could be due to grid resolution problems or turbulence model inaccuracies. The swirl numbers reported for the burners are uncertain. The calibration used to quantify the swirl was performed several years earlier than the time of data acquisition.

The measurement of turbulent velocities is a formidable task. The transient nature of turbulence creates difficulties in correctly determining direction and magnitude of gas velocity in recirculation zones. The steady-state velocities predicted by PCGC-3 are difficult to experimentally verify in regions where transient turbulent eddies are constantly passing. Some turbulent flows possess observable large-scale, time-dependent behavior (Lindsay, 1986) which will not be predicted with a steady-state model. More precise inlet conditions could also aid in isolating the cause of these discrepancies.

V-W Velocity Vectors
Legend

Symbol	Scale
⟶ ≡ predicted velocity	1.0 in = 1.11 m/s
⟶ ≡ predicted velocity	1.0 in = 11.1 m/s

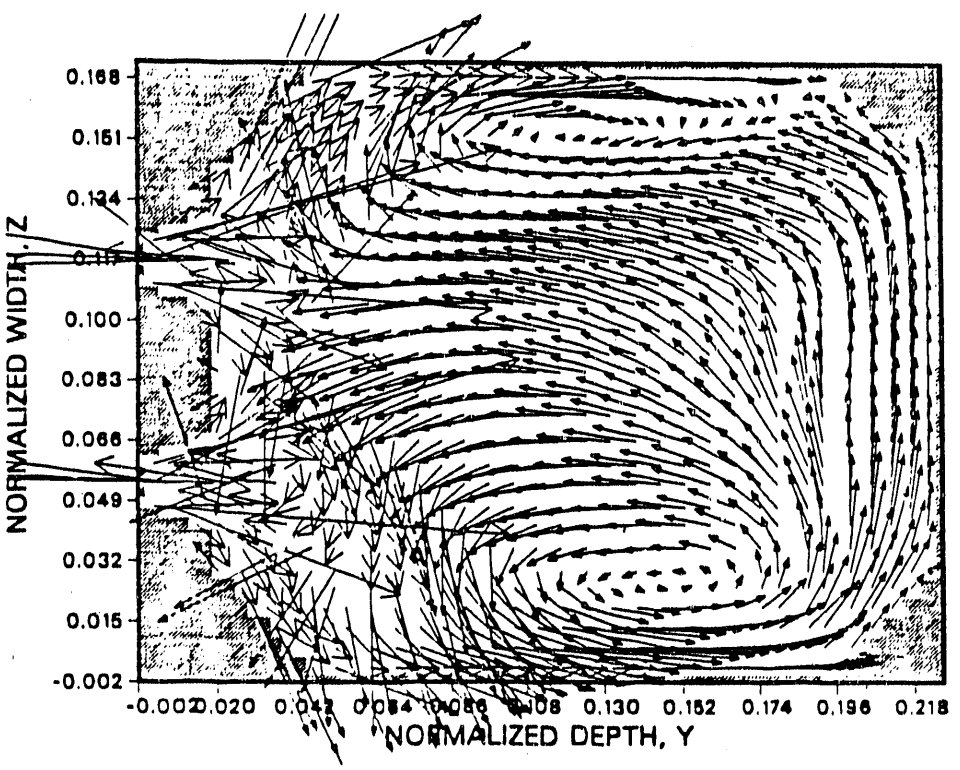

Figure 2.11: Burner Plane in Consol Pilot-Scale Furnace.

2.5.6 Grid Independence

In complex flows, such as observed in the Consol furnace (see Figure 2.10), a fine grid structure is essential to correctly predict velocities. When coarse grid structures are employed in complex flow simulations, important features of the flow can be lost. The grid density required to accurately resolve flow fields can easily be found by employing successively finer grid structures until velocity predictions remain relatively constant.

There are two major reasons why fine grid resolution is needed to accurately model complex flows. The finite different approximations are only valid if the variable of interest behaves smoothly between node points. It is incumbent upon the computational scientist to demonstrate mesh independent solutions. A fine mesh is also needed to sufficiently describe complex geometries. The increased ability to resolve boundaries can be seen in Figures 2.12-2.15.

LSFATF

To facilitate the study of the effect of grid resolution on flow field predictions, flow within the LSFATF furnace was simulated with grid structures consisting of 6,750, 16,800, 68,820, and 121,360 computational nodes. Velocity predictions for these four cases can be found in Figure 2.12 and 2.13. The coarsest grid predictions differed vastly from the velocity data and the predictions for the finer grids. Poor agreement was observed throughout the furnace for the 6,750 node case. Overall agreement was reasonable for the 16,800 node case and all finer simulations. Agreement continued to be improved as more computational nodes were added. Around and below the furnace nose, the finest grid simulation followed experimental data very closely. None of the simulations properly resolve the velocities near the reactor top where flow interactions with the pendant panels was significant. Although the finest grid resolved additional details, reasonable flow predictions were obtained with the 16,800 node case except between the platens.

Consol Furnace

The Consol furnace was simulated with grid structure consisting of 17,500, 48,125, 102,375, and 222,750 nodes. Figure 2.14 and 2.15 present velocity predictions for these cases and show the flow field to be strongly influenced

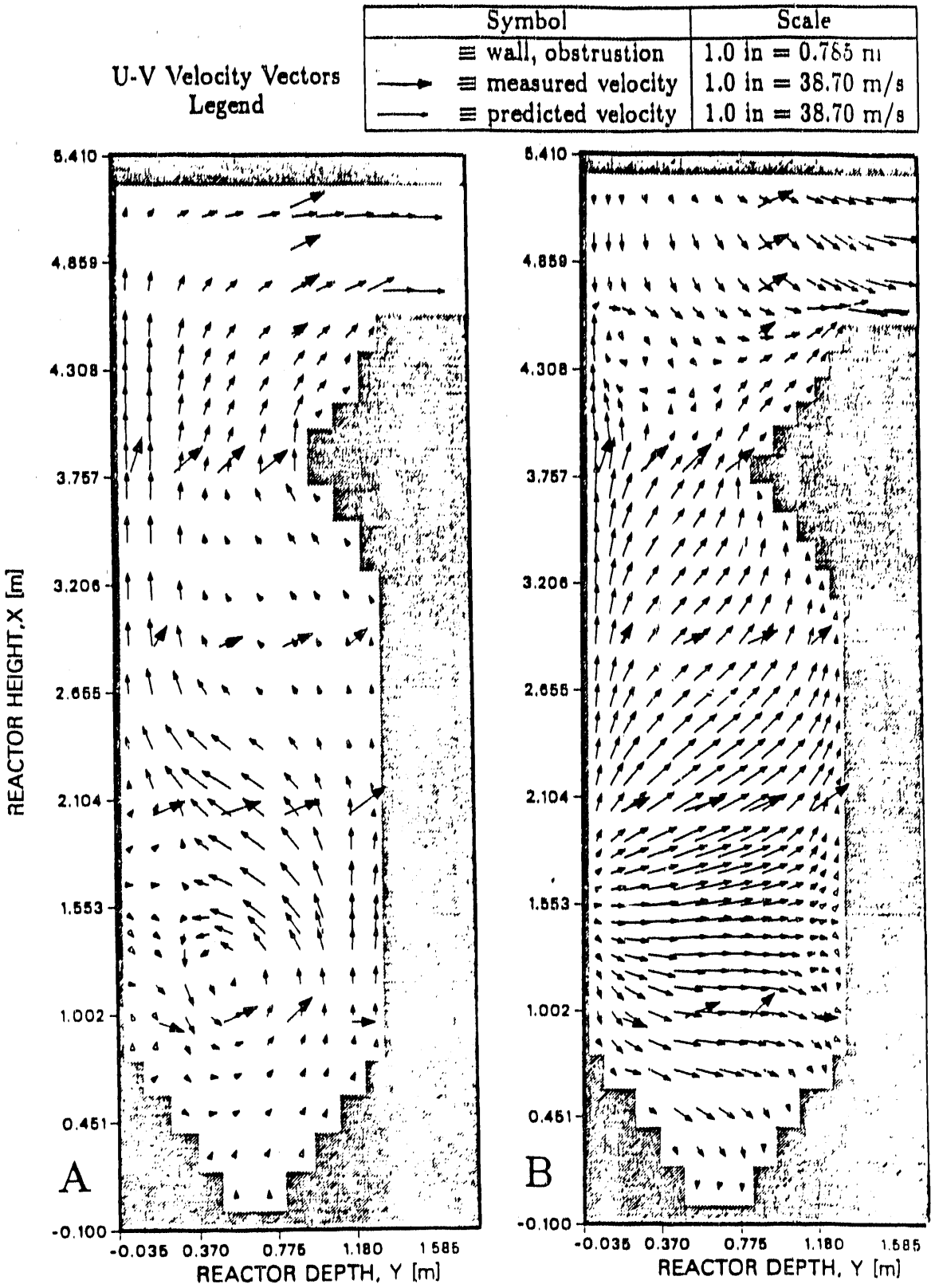

Figure 2.12: a) 6750 and b) 16800 Node Simulations of LSFATF.

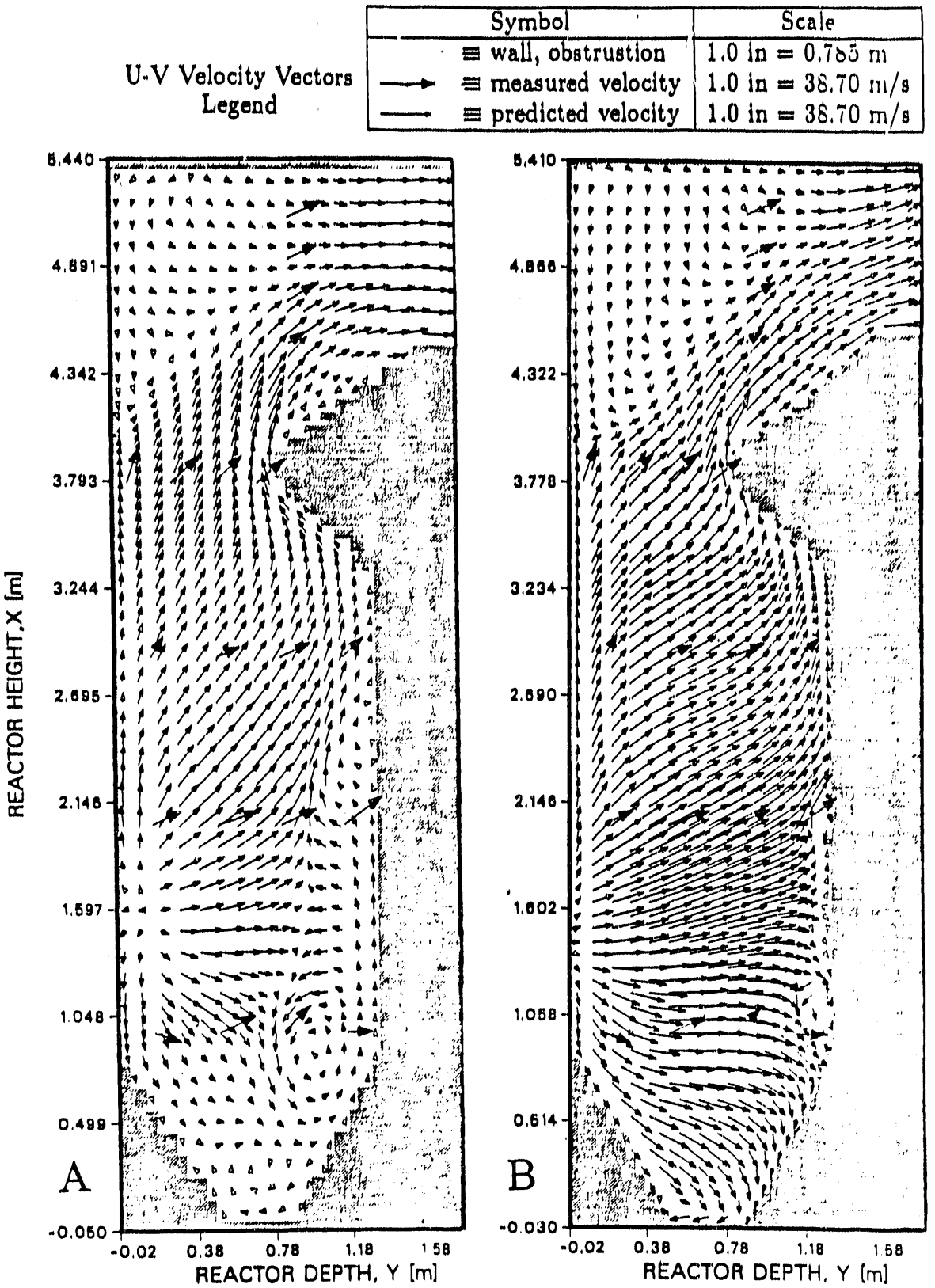

Figure 2.13: a) 68820 and b) 121360 Node Simulations of LSFATF.

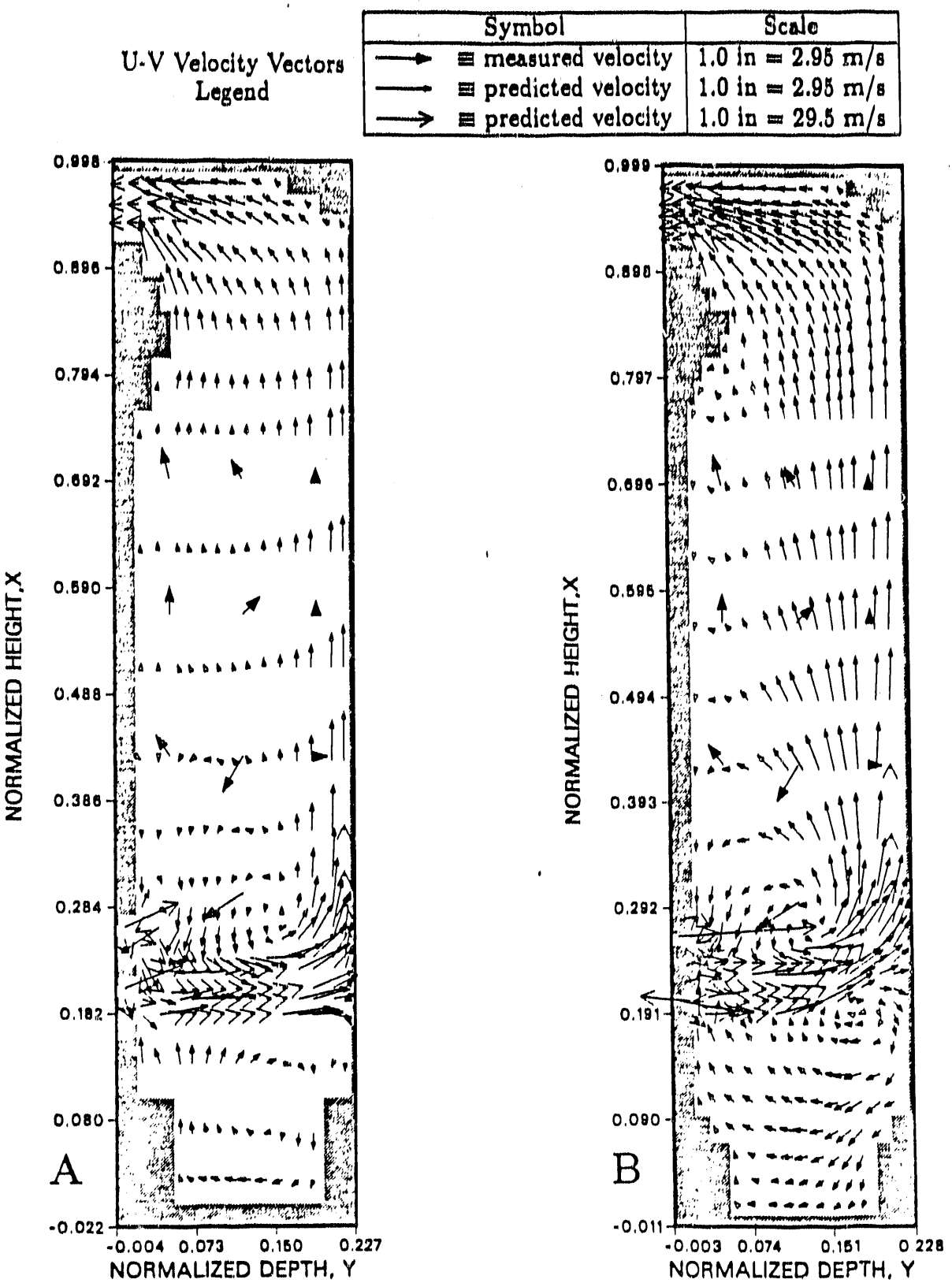

Figure 2.14: a) 17500 and b) 48125 Node Simulations of Consol Case.

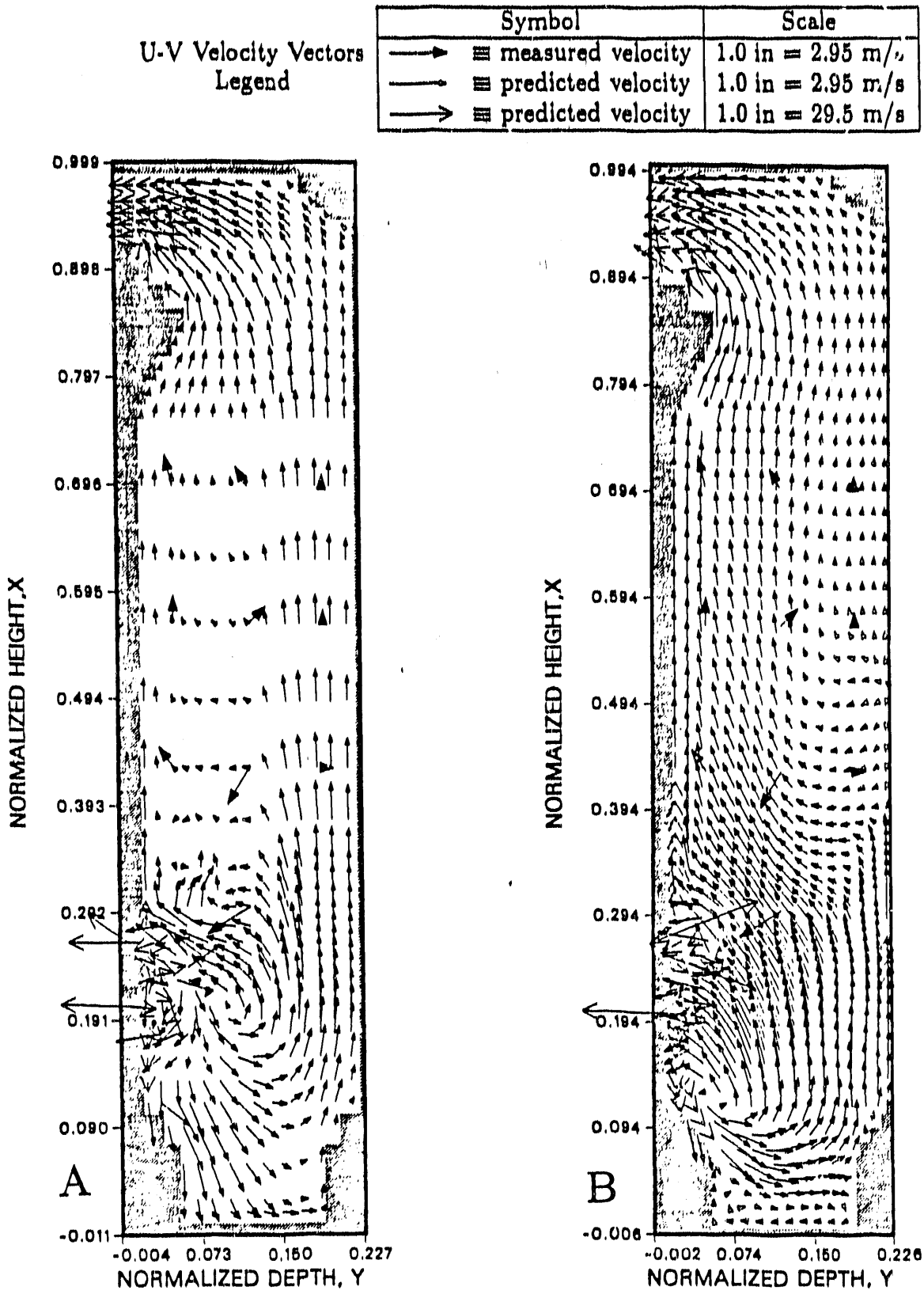

Figure 2.15: a) 102375 and b) 222750 Node Simulations of Consol Case.

by grid resolution. The overall flow structure is sensitive to the near-burner recirculation regions, which appear to be poorly predicted. The finest grid case predicts higher upward burner wall (versus opposite wall) velocities. This trend is found in the data but is not predicted by the three other simulations. The overall agreement for all grid resolutions is not good. The lack of data in the near-burner region makes the evaluation of contributing factors difficult.

If the Consol furnace with four burners can barely be simulated with 222,750 node points, then a full-scale, wall-fired furnace with 40 burners could require several million grid points. It should be pointed out that the inability of the code to accurately predict Consol furnace data could be partially attributed to the inability of the k-ϵ model to handle strongly swirling flows.

2.6 Three-Dimensional Data for Combustion Model Evaluation

2.6.1 Introduction

According to Smoot and Smith (1985), various methods can be used to provide increased confidence in comprehensive combustion codes. Of the various methods, four methods were recommended as being essential to any rigorous model evaluation: (1) numerical evaluation, (2) sensitivity analysis, (3) trend analysis, and (4) comparison with comprehensive data. Three of these methods (but not numerical evaluation) rely, at least in part, on the ability to obtain relevant and reliable experimental data. Sensitivity analysis, which evaluates the sensitivity of code predictions to changes in important model parameters, in the strictest sense, does not require experimental data.

Trend analysis is used to compare changes (or trends) in model predictions (such as NO_x concentration at various locations in the furnace) when a test parameter is systematically varied over a range of conditions (such as firing rate or stoichiometric ratio). The ability of a model to correctly predict the magnitude and direction of change in trend analysis helps establish confidence in its use.

Two types of data are available for evaluating combustion models. Effluent (stack or chimney outlet) data are useful for providing some idea of model validity, but fall short in their ability to evaluate the three-dimensional

processes occurring within the furnace. Profile data, which are spatially resolved inside a computer, give a more definitive evaluation of model accuracy, especially when several properties (species concentration, temperature, velocity, etc.) are "simultaneously" measured (Smoot, 1984). Not only does this provide the magnitude of the properties, but also information concerning the relationship between the various species and processes occurring in combustion.

Developers of the earlier two-dimensional combustion models, such as PCGC-2, found it useful to have a single, compiled source of experimental data with which to evaluate the model. A compilation of two-dimensional, axi-symmetric data (Smoot and Christensen, 1985) was used to evaluate PCGC-2 over a period of several years (Rasband, 1988). However, this data compilation is not applicable to evaluation of 3-D combustion codes since the data deal strictly with axi-symmetric experiments.

There was no known compilation of 3-D data available, and a review of the available data has not been done. A compilation of such relevant data provides a data base for evaluating 3-D combustion models. As partial fulfillment of Task 2, three-dimensional combustion data have been located, collected, evaluated, and compiled into a data book for combustion code evaluation. This data book is published as Volume 3 of this final report. A summary of Volume 3 is given below.

2.6.2 Main Objectives

The main objectives of the 3-D data book are (1) to assess the availability and suitability of 3-D data for model evaluation, and (2) to provide a single source of detailed 3-D combustion and combustion-related data suitable for comprehensive combustion model evaluation. Four related sub-objectives are: (1) to establish suitable criteria for selecting data to include in the data book and to identify and document all available 3-D combustion data, even if it is unsuitable for use in the data book; (2) to select acceptable 3-D data cases, to document them thoroughly, and to publish them in a 3-D data book; (3) to assess the current state of three-dimensional combustion data and identify areas where more and/or better data are needed for 3-D model evaluation; and (4) to identify problems with obtaining existing (published and unpublished) quality experimental data and make recommendations for methods to improve the dissemination of information. Selected cases from this data

Table 2.11: Classes of Combustion Data for Model Evaluation.

1.	Non-Reacting Gaseous Flow (Cold Flow)
2.	Non-Reacting Gaseous Flow (Particle Laden)
3.	Reacting Gases
4.	Pulverized Coal Combustion
5.	Entrained Coal Gasification

book have been compared with 3-D model predictions as documented in this report.

2.6.3 Data Search

The desired data types were selected f om five categories based on the complexity of the flow in a combustor. Table 2.11 lists the five categories from the most simple flow (cold gaseous flow) to more complex combusting flows (Smoot and Christensen, 1985). The use of five categories corresponds well to model development and permits independent evaluation of major model components such as gas-fluid mechanics, particle dispersion, reacting gases, and pulverized coal combustion. Gasification, which is essentially fuel-rich combustion, is added as a separate category for convenience. Data from any size furnace were acceptable.

A set of criteria for evaluating the completeness of the data sets was established (Table 2.12). Each data set was evaluated and scored using a weighting scale to assign points to the data sets based on the extent that the selection criteria were met. The "best" sets were included in the data book (Table 2.13). The data sets that were of sufficient quality and scope were compiled into the data book and evaluated to estimate the accuracy and reliability of the combustion data. The evaluation identified key data needs, important trends in the data, key variables, and estimates of accuracy.

Five computer-assisted literature searches were conducted to find references to three-dimensional data in the five categories listed above. Three major technical data bases specializing in technical literature were searched: National Technical Information Service (NTIS), Engineering Information (EI),

Table 2.12: Criteria for Evaluation and Selecting Three-Dimensional Combustion Data for Model Evaluation.

A. Required
   1. Three-dimensional Geometry
   and
   2. Detailed Profile Data
      a. Temperature
      b. Wall Temperature
      c. Compositions
      d. Velocities
   or
   3. Systematic Parametric Variation

B. Desired
   1. Complete Boundary Conditions
   2. Several Measured Properties
   3. Complete Data Set
   5. Data Accuracy Information
      a. Material Balances
      b. Estimation of Errors
   5. Data in Tabular Form

and Department of Energy (DOE) Energy Data Base. Two-hundred, eighty-one abstracts of potential interest were initially extracted from the data bases. By examining the abstract content, the 281 articles were reduced to those most likely to have 3-D experimental data. The criterion at this point of the data selection was for the article to potentially have three-dimensional data.

Most available experimental data of interest to the three-dimensional data book, if they existed, were expected to be found in the "sub-literature" of government reports and unpublished reports created for internal use by energy-related companies. Thus, a survey of major combustion facilities was also conducted by mailing a questionnaire to individuals at 67 combustion-related

Table 2.13: Description of Facilities for Cases Included in Data Book.

Case	Location	Capacity (MWe)	Firing Configuration	No. of Burners	Width, Depth, Height (m)	Heat Release/ Volume, (MW/m^3)	Inlet Flow Type	
							primary	secondary
A1. CE/EPA (Koucky, 1988)	Windsor, CT	NA	tangential corner fired	4	1.55, 1.32, 5.40	NA	air	air
A2. Consolidation Coal Company (Havekotte, 1987)	Library, PA	NA	wall fired	4	restricted	NA	air/CO/CO_2	air
C1. Institute of Gas Technology (Abassi, 1983)	Chicago, IL	0.6 thermal	end fired	1	1.37, 4.27 0.914	0.207	natural gas	air
D1. Consolidation Coal Company (Havekotte, 1987)	Library, PA	0.44 thermal	wall fired	4	restricted	.12613	Northern West VA. bitum. coal	air
D2. Conevilie (Cetegen, 1985)	Coshocton, OH	420	tangential corner fired	20 - 5 levels per corner	15.8, 13.4, 51.2	0.167	High volatility bitum.	air
D3. Duck Creek (Cetegen, 1985)	Canton, IL	420	wall fired	24 4 rows of 6 burners each	16.8, 11.6, 50.4	apprx. 0.27	Crown II mine bitum. coal	air

companies or facilities. Approximately 15% of the questionnaire recipients responded. However, most responses indicated that no data were available. Three cases of interest for the data book were located through the survey.

2.6.4 Available 3-D Data

After identifying potential sources of 3-D data, the data in digital format were requested from the various sources. Data referenced in journal articles were requested from the authors of the articles. Many known, potential sources of data were not obtainable for the data book.

None of the data in journal articles of the proceedings of conferences and seminars found from the literature searches were complete enough to use in the data book. Requests to the authors of these reports were not answered, except for one case in which data were borrowed from another individual.

Once data were collected from their original source documents, each case required screening and evaluation to determine which data were suitable for 3-D model evaluation.

Each of the data sets listed in Table 2.14 were rated on a scoring system of zero to three, with three being the best, for each of the selection criteria of Table 2.12. Table 2.15 gives brief comments about each data set in Table 2.14. Sets that were deficient of key information were identified and eliminated from inclusion in the data book. Further details regarding data selection are found in Volume 3.

Table 2.14: Detailed Evaluation of Data Using Data Selection Criteria.

Case	Size	Completeness							Composite Score
		B.C.	I.C.	detailed 3-D dimens.	T.C.	prof. data	effl. data	param. data	
Cold Flow									
*CE/EPA (Koucky, 1988)	pilot	3	3	3	3	3	2	0	17
*Consolidation Coal Company (Havekotte, 1988)	pilot	3	3	3	3	3	0	0	15
Reacting Gas									
*Institute of Gas Technology (Abbasi, 1983)	pilot	2	2	2	3	1	3	2	15
Youssef (Youssef, 1967)	lab	1	2	1	2	1	0	0	7
Shoffstall (Shoffstall, 1976)	lab	1	2	1	2	0	0	1	7
Robinson (Robinson, 1985)	full	1	1	1	1	1	0	2	7

Table 2.14: Detailed Evaluation of Data Using Data Selection Criteria. (Continued).

Case	Size	Completeness							Composite Score
		B.C.	I.C.	detailed 3-D dimens.	T.C.	prof. data	effl. data	param. data	
Pulverized Coal Combustion									
†Institute of Gas Technology (Briceland, 1983)	pilot	3	3	3	3	1	3	2	18
*Consolidation Coal Company (Havekotte, 1987)	pilot	3	3	3	3	3	2	0	17
Sakai, et al. (Sakai, 1984)	Full	1	1	1	2	1	0	1	7
Homer City (Anaki, 1980) (Hunter, 1987)	Full	2	1	1	2	0	3	3	12
*Coneville (Cetegen, 1987)	Full	2	2	3	2	3	2	1	15
*Duck Creek (Cetegen, 1987)	Full	2	2	3	2	3	2	1	15

* - data set included in data book
† - data set not included because furnace is axially fired and flow is symmetric.

Table 2.15: Comments on Data Selection.

	Comments
Cold Flow	
CE/EPA (Koucky, 1988)	extensive profile data at seven test planes in the model.
Consolidation Coal Company (Havekotte, 1988)	dimensions of furnace restricted. operational conditions carefully monitored.
Reacting Gas	
Institute of Gas Technology (Abbasi, 1983)	boundary and inlet conditions fairly well described. parametric effluent data. several parameters varied.
Youssef (Youssef, 1967)	geometry is not fully three dimensional. measurements show no three dimensional characteristics. measurement taken too far down stream.
Shoffstall (Shoffstall, 1976)	furnace has square geometry but is axially fired. data are symmetrical.
Robinson (Robinson, 1985)	insufficient information given about furnace dimensions and burner locations.

Table 2.15: Comments on Data Selection. (Continued).

	Comments
Pulverized Coal Combustion	
Institute of Gas Technology (Briceland, 1983)	furnace geometry is rectangular but axially fired with one burner. profile data limited to centerline. emphasis placed on effluent response to coal particle size at inlet. flow is essentially 2-D because of firing method.
Consolidation Coal Company (Havekotte, 1987)	dimensions of furnace restricted.
Sakai, et al. (Sakai, 1984)	inadequate inlet conditions given for modeling. only data are heat flux.
Homer City (Anaki, 1980) (Bhat, 1987)	lacks details about operating conditions. includes information about devolatization rates. data consist of effluent pollutants and wall temperatures.
Coneville (Cetegen, 1987)	extensive report. many operational details difficult to determine from report and must be estimated.
Duck Creek (Cetegen, 1987)	extensive report. many operational details difficult to determine from report and must be estimated.

When selecting the data, engineering judgment was used to maintain a balance between choosing the best data available and not eliminating all the data because of incompleteness or a lack of indicators of accuracy. This approach was necessary since none of the data sets presented complete information on data accuracy. Because of the great expense and time to obtain large-scale 3-D data, few measurements were ever repeated during the course of an experiment. Energy and material balances were not complete or not considered in any of the data sets obtained. Accuracy was not a major factor in selecting the data sets, since questions regarding accuracy were applicable to all of the data considered.

Six data sets were chosen for use in the data book. These sets had acceptable scores based on the data selection criteria discussed previously. Table 2.13 summarized the types of data included by furnace type, rated capacity, firing method, etc. Table 2.16 summarizes the operating conditions represented in the data book. Each of these sets is described in Volume 3.

2.6.5 Data Assessment

An overall evaluation of the data was conducted to characterize the scope and quality of the included data. Included in this analysis were the types of facilities, the measurements, and the operating conditions for which data were included. A case-by-case general characterization of the physical and chemical aspects of the data includes key observations and trends in the data, ranges of temperatures, velocities and other general information. The accuracy of the data based on analyses performed as part of this project, such as material and energy balances, are presented and their significance to the quality of the data book is discussed. Limitations of the data are indicated.

Furnace Characteristics

Two cold-flow cases, one reacting gas case, and three pulverized coal combustion cases were included in the data book. Both the cold flow and the reacting gas cases are from pilot-scale facilities. The coal combustion cases are from one pilot-scale furnace and two commercial-size furnaces. Firing methods include wall-fired (cold flow and coal combustion), tangentially-fired (cold flow and coal combustion), and end-fired (reacting gas case).

Table 2.16: Summary of Test Operating Conditions.

Case	Load (MWe)	Stoich. Ratio	Fuel Flowrate (kg/s)	Primary Air Flowrate (kg/s)	Secondary Air Flowrate (kg/s)	Windbox Air Temp. (°C)	Theoretical Swirl Number
A1. CE/EPA (Koucky, 1988)	NA	NA	NA	9.5	NA	24	0
A2. Consolidation Coal Company (Havekotte, 1987)	NA	NA	NA	0.0301	0.192	100	5.9
C1. Institute of Gas Technology (Abassi, 1983)							
D1. Consolidation Coal Company (Havekotte, 1987)	0.60	1.41	0.0104	0.0228	0.134	344	5.9
D2. Coneville (Cetegen, 1987)	405	1.21	42.1	78.36	334.5	320	NA
D3. Duck Creek (Cetegen, 1987)	385	1.18	42.8	57.46	367.8	314	1.0

Furnace design is a major impedance to obtaining data over a wide range of positions. Considering the size of a typical large-scale furnace (2000 square feet cross section), it is obvious that probes must be very long to access the middle of the furnace. A long probe is very heavy and requires chains and other supports, as well as several people, to maneuver. A limited number of access ports limit the number of locations where a probe can be inserted. Impact and suction probes are inherently poor devices for measuring velocities, temperatures and other properties. The problems with the various types of probes make use of nonintrusive methods, such as Laser Doppler Anemometry for velocities and Ramen Scattering techniques for species concentrations, more attractive except for their high capital and operating costs, and high level of expertise needed for proper operation and data analysis.

None of the data sets in the data book are as complete as desired. The most complete data sets are the two cold flow cases. The relative ease of collecting cold flow data in a pilot-scale facility made extensive data collection more feasible compared to pulverized coal combustion in a large furnace. However, the two cold flow cases are limited in that they are each for a single operating condition. A parametric study varying the flow rates, the number of inlets being used, or the swirl number would enhance the value of the data for evaluating the cold flow capability of combustion computer codes over a range of conditions.

Data Accuracy

The accuracy of the data was estimated using information from the original report on the data set and through the independent calculations performed as part of this study based on the experimental data and the specified inlet conditions. This method worked well for the cold flow data cases but was subject to considerable estimation error in the combustion cases because of the limited number of measurements taken in a single test plane. The estimated accuracy of each data set is presented in Volume 3 using information from original reports as well as calculations performed for this work. The detailed calculations of data accuracy are shown in the Volume 3 appendices.

One of the major problems with obtaining quality combustion data is proper control of the operating conditions over long periods during which data are taken. The inherent nature of large combustion facilities is to incur variations in operating conditions over time. Because of the long time

required to take combustion measurements, the testing must usually be conducted over a period of days, even for small-scale facilities. Establishing steady-state conditions is a problem as is determining how the data measurements change because of process variations.

2.6.6 Data Needs and Recommendations

Reviewing the state of combustion data in the literature and project reports have lead to definite perceptions regarding three-dimensional data needs in combustion facilities for evaluating comprehensive, three-dimensional combustion models. The most important qualities that have been identified to be missing in data for both cold (non-reacting) flows and reacting flows are accuracy and completeness. There are two areas where complete information is lacking and yet of utmost importance: 1) profiles of velocity, concentrations, and temperature in the lowest part of the furnace (fire box), especially near the burners, and 2) detailed geometric data describing the furnace dimensions (walls, nose, intrusions, etc.) and burners (quarls, angle of tilt, etc.).

Most test matrices that were reviewed appear to distribute the measurement locations throughout the furnace, starting at some point above their burners and moving up until the outlet is reached. Often, the distance between elevations is quite large such that a large proportion of measurements are taken in the upper half of the furnace. However, much of the combustion process takes place in the lower half of the furnace. In the upper portions of the furnace, velocity, concentration, and temperature profiles are often relatively flat, and in the case of velocity, parallel to the furnace walls. In the lower portions of the furnace, there are recirculation zones, swirling inlets, vigorous combustion, mixing, and large changes in species concentrations, temperatures, and velocities.

Incomplete furnace details reduce the confidence from comparisons of prediction and measurement. It is preferable to have complete, accurate data taken at one or two operating conditions rather than to have incomplete data taken at several conditions.

It is recommended that the majority of the measurements be taken in the lower half of the furnace. The location and number of measurements taken on a given horizontal plane in the lower portion of the furnace should be closer together and more numerous than in the upper part. Velocity profiles taken

as near as possible to the burner outlets traversing the width of the furnace would be very useful in verifying the inlet conditions. Detailed information about the furnace geometry and burner settings, are needed to properly set the boundary and inlet conditions in the computer model of the furnace. Most of this can be provided from working plans used during design and construction of the furnace.

A long list of possible data measurements can be assembled. Table 2.17 lists three classes of data that would be useful for evaluating the three-dimensional combustion model. Under each class of data (i.e. cold flow, gas combustion, pulverized coal combustion) are listed the types of data that are needed. Each data type has been ranked as to importance by the numbers 1,2,3 (1 being most important and 3 least important) to help prioritize the measurements included in the test matrix. Quality data in all of the three classes are needed.

Data quality is also questionable. Measurement techniques are typically with probes and therefore limited to the accuracy of the method, with estimated error often as high as 30%. The spatial resolution within furnaces is also poor, leaving many parts of the furnace with little or no data to characterize the test plane sufficiently. The access to the inside of the furnace through ports is extremely limited. Another problem with obtaining data are the insufficient resources made available to extract data from computer tapes or paper archives. For-profit companies cannot easily afford to take an engineer off current projects to search for an old report, especially if the report is of questionable quality or completeness. Also, most data are proprietary, owned by either the consulting engineering firm that took the data or the industrial company that paid for obtaining it. For economic reasons, it is not usually feasible to give away expensive data to competitors. Alliances of industry and government are needed so that cost sharing and data sharing can be made possible.

2.7 Summary of Model Evaluation

In this section, we have explored evaluation of the overall 3-D model with its integrated submodels. Separate submodel evaluation (independent of other submodels) is presented in the sections discussing the specific submodels (see Section 3 for example). In evaluating coupled components of the modeling

Table 2.17: Types of Data Needed for Data Book for Evaluation of Three-Dimensional Combustion Model.

The following types of data are needed for evaluation of the 3-D data book. The data types listed apply to both single operating condition data sets as well as data sets taken for several operating conditions with one or more variables varied in a systematic manner.

A. Non-reacting Flow

1. Velocity Profiles
2. Concentration Profile (this requires that a known concentration and flowrate of some inert tracer such as CO2 or CO be injected along with the gas).
3. Temperature Profiles (this measurement requires that inlet streams at widely different temperatures, one hot and one cold, be injected into the furnace).

B. Gas Combustion

1. Velocity Profiles
1. Temperature Profiles
1. Wall Radiative (& Convective) Heat Flux
1. Concentration Profiles
2. Wall Temperatures
2. Effluent Temperature
2. Effluent Species Concentration

C. Pulverized Coal Combustion

1. Velocity Profiles
1. Temperature Profiles
1. Concentration Profiles
1. Detailed Fuel (Coal) Analysis (particle size distribution, etc.)
1. Wall Temperatures
1. Wall Heat Flux
2. Effluent Temperature
2. Effluent Species Concentration
2. Particle Properties Profile
2. Effluent Particle Properties
3. Ash Analysis
3. Slag Deposition Rates, Composition of Slag, Temperature through Deposit

strategy we have made extensive use of both the 2-D and 3-D versions of the model. The 2-D code has been a useful and complimentary test bed for evaluation of certain aspects of the final 3-D product.

The evaluation included a nonlinear sensitivity analysis of an axi-symmetric laboratory coal-fired furnace, numerical analysis of the 3-D code using several approaches including identification of mesh-size independent solutions for several cases, comparisons with known exact solutions, extensive 2- and 3-D comparative evaluations with experimental data, and an evaluation of available 3-D data. Major observations and conclusions from this evaluation are:

1. A global nonlinear sensitivity analysis of a laboratory coal-fired furnace was used to identify specific parameters which have the greatest impact on model predictions. Model prediction for coal burnout, NO_x concentration, local gas temperature, and local coal-gas mixture fraction were used to identify critical parameters. Model parameters examined in this study represent the physical and chemical processes which occur in coal combustion.

2. The parameters required to describe the devolatilization subprocess showed the greatest overall impact from the sensitivity analysis while parameters governing char oxidation were the second most important. Char oxidation has the most impact on model prediction for NO_x concentration. Particle dispersion had a secondary effect on overall model predictions and had the greatest impact on coal burnout and coal-gas mixture fraction predictions. Also, of secondary importance was the effect of coal rank as indicated by the element oxygen content of the coal. This affected gas temperature predictions most dramatically.

3. Parameter uncertainties from the sensitivity analysis for the radiation coefficient, turbulence intensity, and the particle swelling factor showed little or no impact on model prediction. This is attributed to the dominant influence of the uncertainty in the other parameters on the sensitivity analysis.

4. While the results obtained in the sensitivity analysis are case-specific, they do focus attention on the critical submodels which appear to dominate the predictions. These results provide direction to future submodel development as well as experimental efforts to obtain accurate values of the physical parameters required by these submodels. This work also illustrates the role of sensitivity analysis as an engineering tool to be used to gain a deeper understanding of the physical process being modeled. In addition, the techniques used to perform this study may aid in future sensitivity studies of large computer models describing physical systems in a realistic fashion.

5. Various differencing schemes were implemented into the 3-D code for evaluation. A nodal upwind scheme coupled with a weighted central difference scheme was selected, as the most accurate for arbitrary mesh. The evaluation included comparison with exact solutions for coupled linear functions.

6. An exact solution evaluation was conducted to identify algorithmic and coding errors in the 3-D code. Such errors were removed and the exact solution reproduced to within the accuracy of truncation error.

7. Residual error within individual equations has been quantified and compared with truncation error. This analysis is used to track convergence in the 3-D code.

8. An evaluation of various 3-D momentum-continuity coupling schemes has been conducted. The schemes explored have included SIMPLE, SIMPLER, SIMPLEC, SIMPLEST, and all combinations and pernutations of the above schemes. SIMPLERC with under-relaxation of 0.8 resulted in the most efficient and robust combination.

9. A comprehensive, comparative evaluation of the 2-D version of the reacting coal code was completed. This analysis included cases from non-reacting cold flow with and without particles to reacting hot flow with and without coal particles. The analysis was comprised of 33 separate cases all with detailed profile data. The analysis included an evaluation of the experimental data reliability.

10. In the 2-D evaluation discrepencies between predicted and measured profiles were most apparent in the recirculation zone. The outer regions of the reaction chamber were described very well. Exit compositions and carbon conversions were predicted with almost complete accuracy. Areas of fully mixed flow were also characterized well.

11. The 2-D comparative evaluation revealed the sensitivity of the calculation to inlet and boundary conditions particularly in inlet mean velocities, turbulence intensity profiles, and heat effects near walls.

12. The 2-D comparative evaluation showed the weakest phenomenological submodels to be the turbulence model, the devolatilization model and the reaction and heat effects model.

13. A full 3-D comparative evaluation was conducted on four simple turbulence models, constant eddy diffusivity, Prandtl mixing length, a k-ϵ model, and a k-ϵ model with relaminarization.

14. The relaminarization model correctly simulated laminar and turbulent pipe flows. The added complexity of this model reduced overall robustness. It is recommended that the relaminarization model should be used judiciously in transitional flows.

15. Two cases have been chosen to evaluate PCGC-3. These cases were chosen to represent the two major classes of furnaces used in industrial boilers: a tangential- or corner-fired system and a wall-fired, swirled-burner furnace. This evaluation provided confidence to incorporate reacting gaseous and particulate systems. Geometric spatial scales and fluid-dynamic temporal scales can be resolved at least for pilot scale furnaces.

16. Finer mesh calculations than previously demonstrated in computational combustion are needed to resolve physical processes in practical 3-D furnace geometries. One quarter of a million nodes were needed for four burner wall-fired, swirl-flow pilot furnace simulation.

17. A study was conducted to collect available 3-D furnace data for model evaluation. Data were documented from six large-scale tests. Recommendations were made for data collection.

Section 3

Research Task 3 - Submodel Development

3.1 Introduction

During the course of this project, eight submodels received particular emphasis. Seven of these submodels had some previous framework already established in 2-D codes and are discussed in this chapter. The fourth submodel on mineral matter fouling and slagging was developed as a first generation "straw-man" for this study and is discussed separately in Section 4. The seven submodels in this section are in the following order: radiation, char oxidation, turbulent dispersion of particles, nitrogen oxide formation, carbon monoxide partial equilibrium, coal devolatilization, and turbulence modeling. The rationale and need for research is discussed by introducing each of the separate submodels. In addition, the state of development, independent evaluation, conclusions and recommendations of each submodel are also given separately. At the end of this chapter, a summary of all seven submodels is presented.

The turbulence submodeling was performed exclusively in the 3-D code. It has been incorporated in a coupled fashion and evaluated in the 3-D code. None of the other six submodels have been evaluated in the 3-D code. All were implemented first in a 2-D version of the code. The radiation model has been extended to 3-D in a stand-alone mode and is presented and evaluated in this section in its 3-D form. The intention is to incorporate all of these revised submodels into the 3-D code in the future.

3.2 Radiation

3.2.1 Introduction

The success in predicting the complex combustion process in axi-symmetric cylindrical furnaces (Smoot and Smith, 1985; Truelove, 1986; Lockwood, et al., 1985) has created interest in applying the modeling techniques to three-dimensional systems (Abbas and Lockwood, 1986; Boyd and Kent, 1986). A major part of this effort is directed toward modeling combustion in industrial boilers, which are most often rectangular in configuration. In large systems, experimental determination of the effect of changes in operating conditions or fuel characteristics is very expensive and highly time-intensive, and errors can cause costly shut-downs. Therefore, an appropriate mathematical description of the combustion and related processes inside the boiler would be highly desirable. Radiative heat transfer to the water-tubes and water-cooled panels on the walls of the combustion chamber is often the main consideration in such large-scale systems.

Early boiler models (Lowe, et al., 1974; Bueters, et al., 1974) had simple or empirical bases for flow characteristics and heat release rates with the major emphasis on radiative heat transfer calculations. In modern-day comprehensive codes, these quantities are computed rather than treated as inputs. Consequently, for the sake of efficiency, the treatment for radiation has to be amenable to the numerical methods for fluid mechanics and reaction kinetics. This requirement has given rise to the flux models (Gosman and Lockwood, 1973; Lowes, et al., 1973; Varma, 1979). Conceptually, the discrete ordinates method (Carlson and Lathrop, 1968; Truelove, 1978; Fiveland, 1984; Jamaluddin and Smith, 1978), belongs to the family of flux models, but corrects the lack of coupling between the directional intensities present in some of the conventional flux models.

In the discrete ordinates method, the integral-differential radiation transport equation is solved in a number of directions. The angular integral is discretized through the assumption of non-variance of radiative intensities in prescribed solid angles surrounding representative directions. This results in a number of coupled partial differential equations of intensity transport. the

number depends on the order of the discrete ordinates approximation, which are then solved by suitable numerical methods.

3.2.2 Formulation

Radiation calculations are based on solving the radiation transport equation which is an energy balance for radiation intensity passing through a volume element (see Figure 3.1) containing an absorbing-emitting-scattering medium. In a rectangular coordinate system this can be written as

$$\xi_m \frac{\partial I_m}{\partial x} + \mu_m \frac{\partial I_m}{\partial y} + \eta_m \frac{\partial I_m}{\partial x} = -(k_a + k_s) I_m + k_a I_b + \frac{k_s}{4_\pi} \int 4_\pi P(\Omega, \Omega') I d\Omega' \qquad (3.1)$$

The left side of Equation 3.1 represents the gradient of intensity in the direction of propagation, while the right hand side represents, respectively, the attenuation of intensity due to absorption and out-scattering, and the contribution to the directional intensity due to emission by the medium and in-scattering. $P(\Omega, \Omega')$ is a probability density function, formally known as the phase function, which determines the distribution of the scattered intensity. μ_m, η_m and ξ_m represent the direction cosines for the discrete direction Ω (Figure 3.2). In two-dimensional rectangular enclosures, only the first two terms on the left side of the equation are required.

Equation 3.1 is solved in a number of directions spanning the total solid angle of 4π steradians. The number of directions depends on the order of the discrete ordinates approximation through the relationship $N_m = n(n+2)$ (Carlson and Lathrop, 1968), where n represents the order of the discrete ordinates approximation (the number of values for the direction cosines considered within the range ± 1.0). In a two-dimensional enclosure, Equation 3.1 needs to be solved in half as many directions. The angular integral is evaluated using numerical quadrature.

The solution of Equation 3.1 requires the boundary conditions (T_w and ε_w) as well as the temperature of the medium. Considering the surrounding surfaces to be diffusely emitting-reflecting, the boundary conditions for the above equation are

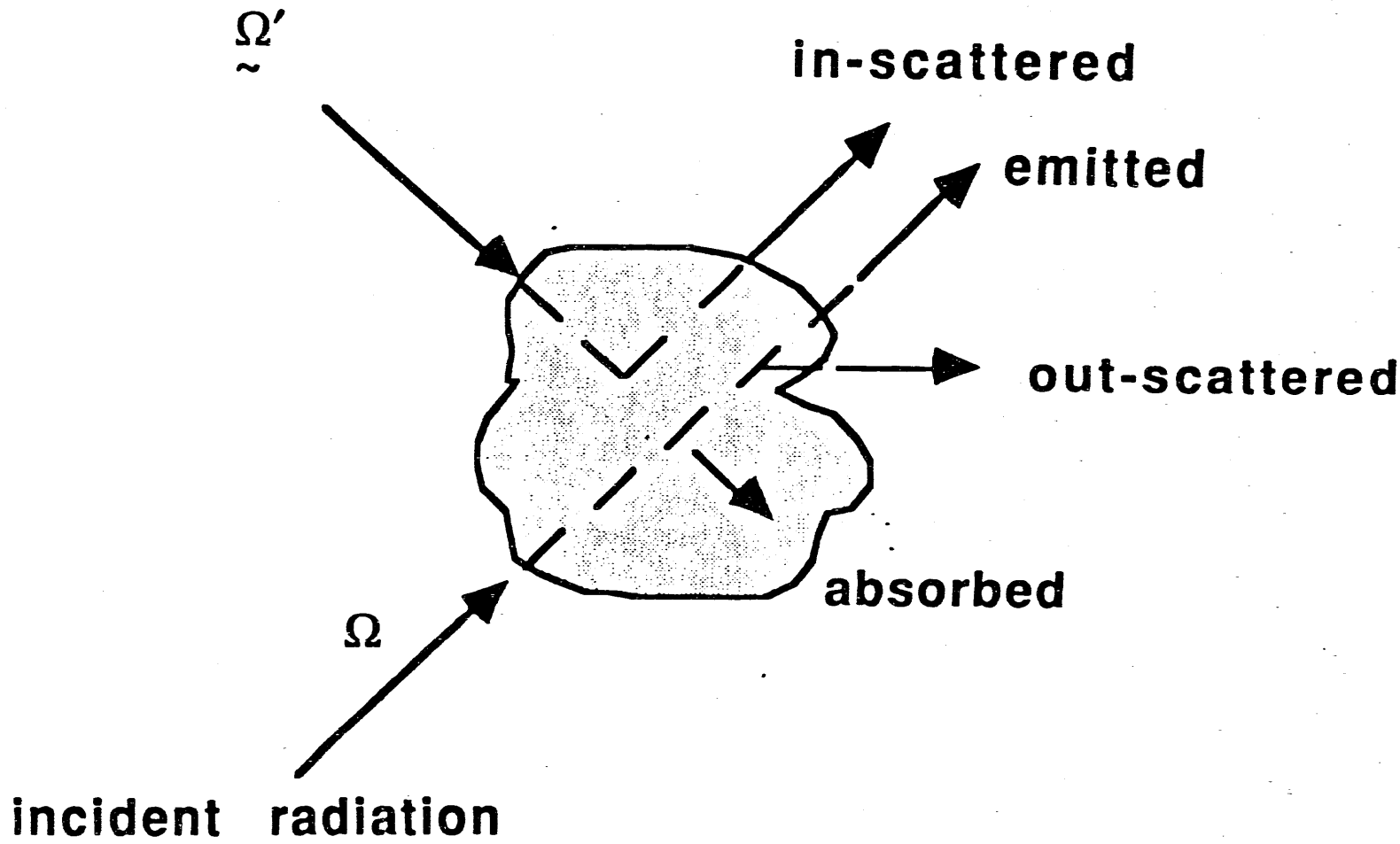

Figure 3.1: Pictorial Representation of the Radiation Transport Equation.

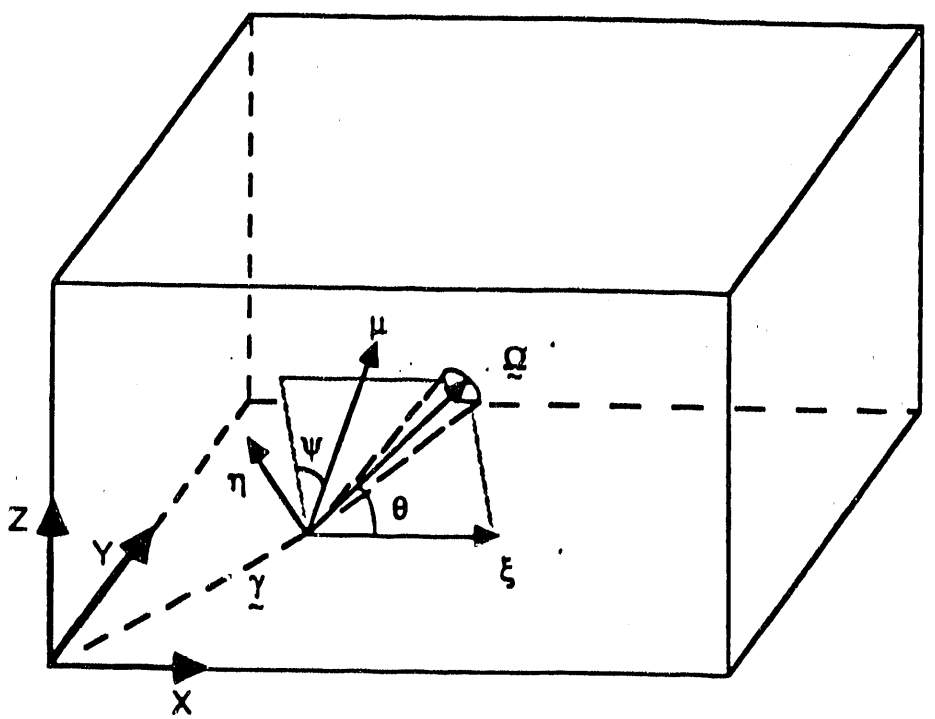

Figure 3.2: The Direction Cosines.

$$\text{at } x = 0 \quad : \quad I_m = \varepsilon_w I_{bw} + (1 - \varepsilon_w)\frac{q_x^-}{\pi} \quad ; \quad \xi_m > 0$$

$$\text{at } x = L \quad : \quad I_m = \varepsilon_w I_{bw} + (1 - \varepsilon_w)\frac{q_x^+}{\pi} \quad ; \quad \xi_m < 0$$

$$\text{at } y = 0 \quad : \quad I_m = \varepsilon_w I_{bw} + (1 - \varepsilon_w)\frac{q_y^-}{\pi} \quad ; \quad \mu_m > 0$$

$$\text{at } y = W \quad : \quad I_m = \varepsilon_w I_{bw} + (1 - \varepsilon_w)\frac{q_y^+}{\pi} \quad ; \quad \mu_m < 0$$

$$\text{at } z = 0 \quad : \quad I_m = \varepsilon_w I_{bw} + (1 - \varepsilon_w)\frac{q_z^-}{\pi} \quad ; \quad \eta_m > 0$$

$$\text{at } z = H \quad : \quad I_m = \varepsilon_w I_{bw} + (1 - \varepsilon_w)\frac{q_z^+}{\pi} \quad ; \quad \eta_m < 0$$

the hemispherical fluxes ($q_d^{\pm}$) are obtained as

$$q_d^{\pm} = \int_{2\pi} (\mathbf{n} \bullet \mathbf{\Omega}') I d\mathbf{\Omega}' \tag{3.2}$$

by use of the appropriate direction cosines.

In some practical situation, the temperature profile in the enclosed medium may not be known. In such situations, an additional relation involving the temperature of the medium is necessary. This additional relation is obtained by writing an energy balance on the volume element.

$$S_{nr} = 4\pi k_a I_b - k_a \int_{4\pi} I d\mathbf{\Omega}' \tag{3.3}$$

In the above equation, the first term on the right hand side represents the radiation emitted by the volume element; the second term represents the incident radiation on the volume. Therefore, S_{nr} is the rate of energy generated within the volume element by means other than radiation. Expressing the emission term ($k_a I_b$) in Equation 3.1 as S_{nr}, the equation can be rewritten as

$$\xi_m(A_{i+1}I_{i+1} - A_i I_i) + \mu_m(B_{j+1}I_{j+1} - B_j I_j) + \eta_m(C_{i+1}I_{i+1} - C_k I_k) = -(k_a + k_s)V_p I_m + d_a V_p I_b + \frac{k_s V_p}{4\pi} \sum_m P(\mathbf{\Omega}, \mathbf{\Omega}') I_m w_m \tag{3.4}$$

Assuming scatter to be linearly anisotropic, the phase function may be represented by

$$P(\mathbf{\Omega}, \mathbf{\Omega}') = 1 + a_o cos\phi \tag{3.5}$$

where ϕ is the angle between the incident and the scattered intensities, and a_o is an asymmetry factor which attains a value of +1.0 for strongly forward-directed scatter (−1.0 for strongly backward directed scatter, and 0.0 if the scattering is isotropic). In terms of the direction cosines, $P(\Omega, \Omega')$ can be written as

$$P(\Omega, \Omega') = 1 + a_o(\mu_m \mu_{m'} + \eta_m \eta_{m'} + \xi_m \xi_{m'}) \tag{3.6}$$

The intensities I_{i+1}, I_{j+1} and I_{k+1} can be expressed in terms of the discrete intensities I_i, I_j and I_k using weighted diamond-differencing

$$I_{i+1} + fI_i = I_{j+1} + fI_j = I_{k+1} + fI_k = (1+f)I_m \tag{3.7}$$

I_m, the intensity at the center of the volume element may be evaluated as

$$I_m = \frac{\xi_m A I_i + \mu_m B I_j + \eta_m C I_k + V_p(k_a I_b + k_s I_s)}{\xi_m A + \mu_m B + \eta_m C + V_p(k_a + k_s)} \tag{3.8}$$

Equation 3.1 or Equation 3.4 is strictly applicable to the case where μ_m, η_m and ξ_m are positive. For other combinations, the equation changes slightly.

3.2.3 Solution Procedure

The solution procedure involves solving Equation 3.1 (or Equation 3.4) in each of the ordinates directions, and forming a set of $N_m(N_m/2$ in case of a two-dimensional enclosure) coupled partial differential equations. The calculation is started at the top, right-hand corner of the back wall using the boundary conditions. The directions of traverse are so chosen that the values of the direction cosines gradually increase; a change in the sign of the direction cosine signifies a reversal in the direction of integration. The radial (y-) traverses are first, followed by the vertical (z-) traverses. Finally, the axial (x-) traverses complete the computations. The solution has to be obtained iteratively, because the calculated intensities enter the boundary conditions as well as the in-scattering (and the incident radiation) terms (see Equation 3.2). When the temperature of the medium is unknown, the recursive solution is initiated with an assumed temperature profile for the medium. Otherwise Equation 3.4 is solved first without the incident radiation term, and then including the incident radiation as a perturbation on the approximate solution in order to obtain the final, converged solution to the radiation

transport equation. In the case of a scattering medium, likewise, an approximate solution is first obtained without the in- and out-scattering terms. The scattering terms are then included as a perturbation on the approximate solution.

When symmetries exist, the computational domain can be narrowed down to account for the symmetry (in one or more directions), and the computational time requirement reduces proportionately. With total symmetry, the radiation transport equation needs to be solved for one octant only. The boundary condition on the symmetry axis is based on the consideration of conservation of flux (i.e., reflective boundary).

Calculation is initiated with $f = 1.0$, which represents central differencing. If negative intensity is encountered during extrapolation, (using Equation 3.7) the value of f is reduced globally, and systematically, until negative intensities are removed. An alternative approach would be to set $f = 0.0$, in which case the intensities are always nonnegative. However, upwind differencing ($f = 0.0$) may provide slightly less accurate predictions.

3.2.4 Evaluation

The accuracy of the discrete ordinates solutions depends on the choice of the quadrature scheme. Although this choice is, in principle, arbitrary, completely symmetric quadrature is preferred in order to preserve geometric invariance of the solutions. The quadrature schemes used in the present work are based on the "moment-matching" technique of Carlson and Lathrop (1968), whereby the ordinates are chosen to integrate as many moments of intensity distribution as possible. Also, the ordinate values for the S_2 and the S_4 approximations have been take from Truelove (1976, 1978), and those for S_6 and S_8 from Fiveland (1987). The quadrature scheme for one octant (one quadrant in case of a two-dimensional system) are presented in Table 3.1.

Two-Dimensional Rectangular Enclosures

The discrete ordinates solutions for two-dimensional rectangular enclosures are evaluated against exact analytical and Zone model predictions. The zone model predictions were made for an absorbing-emitting, isotropically

Table 3.1: The S_2, S_4, S_6 and S_8 Quadratures for Rectangular Enclosures [one quadrant (2-D/Octant (3-D))].

Designation	μ_m	η_m	ξ_m	w_m
S_2 (2-D)	0.50000	0.70711	0.50000	3.14159
S_2 (3-D)	0.57735	0.57735	0.57735	1.57080
S_4 (2-D, 3-D)	0.29588	0.90825	0.29588	0.52360
	0.90825	0.29588	0.29588	0.52360
	0.29588	0.29588	0.90825	0.52360
S_6 (2-D, 3-D)	0.18387	0.96560	0.18387	0.16095
	0.69505	0.69505	0.18387	0.36265
	0.96560	0.18387	0.18387	0.16095
	0.18387	0.69505	0.69505	0.36265
	0.69505	0.18387	0.69505	0.36265
	0.18387	0.18387	0.96560	0.16095
S_8 (2-D, 3-D)	0.14226	0.97955	0.14226	0.17124
	0.57735	0.80401	0.14226	0.09923
	0.80401	0.57735	0.14226	0.09923
	0.97955	0.14226	0.14226	0.17124
	0.14226	0.80401	0.57735	0.09923
	0.57735	0.57735	0.57735	0.46172
	0.80401	0.14226	0.57735	0.09923
	0.14226	0.57735	0.80401	0.09923
	0.57735	0.14226	0.80401	0.09923
	0.14226	0.14226	0.97955	0.17124

scattering medium, for which Fiveland (1984) had made discrete ordinates predictions.

Figure 3.3 compares the predictions of the S_2, S_4 and S_6 discrete ordinates approximations with the exact analytical solution (Lockwood and Shah, 1981) for an infinitely long square cavity of which all four walls are black with zero emissive powers. The medium is assigned an emissive power of unity. Three different values of the optical thickness, viz., 0.1, 1.0, and 10.0 are used. All of the discrete ordinates approximations provide acceptable predictions for the wall heat fluxes, compared with the exact solution. Little improvement in predictions is achieved by using higher (than S_4) order approximations.

Emitting-Scattering Medium

In the case of the scattering medium (Ratzel and Howell, 1982), the enclosure is again assumed to be an infinitely long square cavity. One of the walls is assigned an emissive power of unity, while the other three walls have zero emissive powers. The enclosed medium is assigned an optical thickness of unity and is assumed to be in radiative equilibrium ($S_{nr} = 0.0$). The wall emissivities are assigned values of 0.1, 0.5 and 1.0. The predictions of the S_2, S_4 and S_6 discrete ordinates approximations are compared with those of the Zone model in Figure 3.4. All the predictions are in good agreement with the predictions of the Zone model, signifying that either S_2 or S_4 approximation is sufficiently accurate for predicting radiative transfer in two-dimensional rectangular enclosures.

Three-Dimensional Rectangular Enclosures

Evaluation of the discrete ordinates approximation in absorbing-emitting medium is compared with the Zone model predictions for one of the M3 trial cases (Flame 10) from the International Flame Research Foundation (IFRF). The relevant data on the furnace are presented in Table 3.2, and the measured gas temperature profiles (taken from Hyde and Truelove, 1977) are shown in Figure 3.5. Figure 3.6 shows that S_4, S_6 and S_8 discrete ordinates predictions are in good agreement with the prediction of the Zone model (Hyde and Truelove, 1977), while the S_2-predictions are in error by up to 30%. The inadequacy of the S_2 approximation in three-dimensional systems is expected

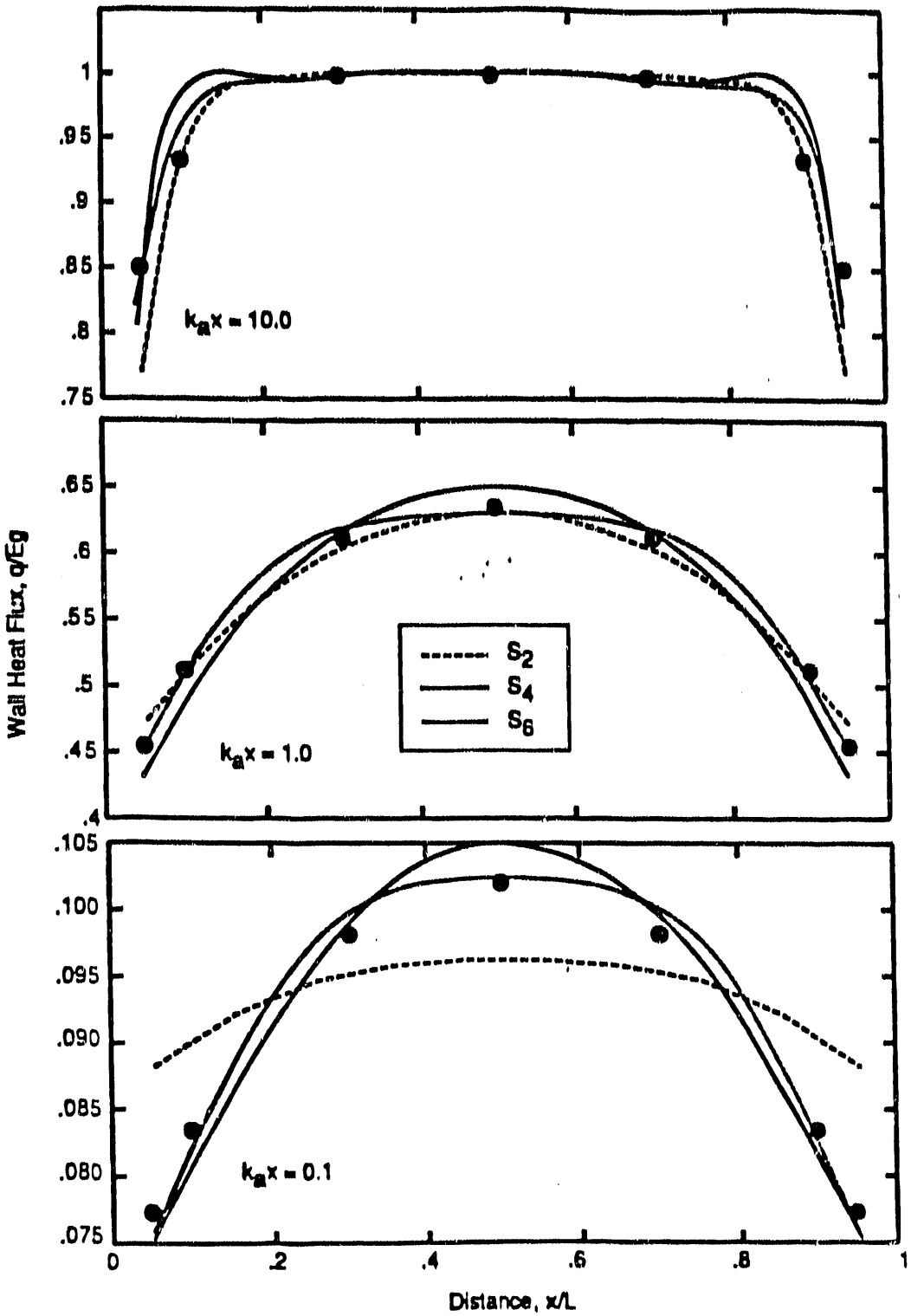

Figure 3.3: Predicted Net Radiative Fluxes at the Walls of a Square Cavity Containing Absorbing-Emitting Medium.

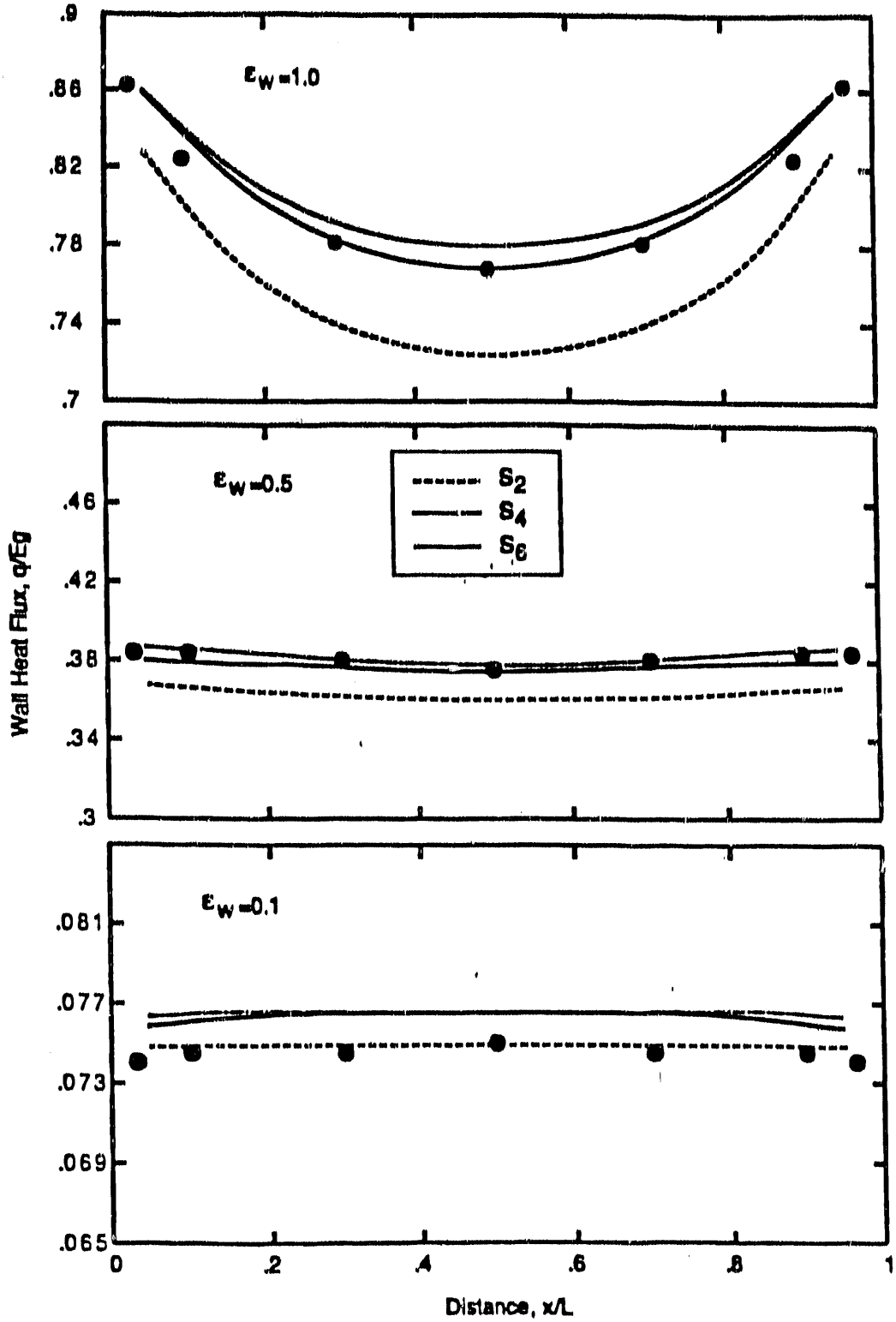

Figure 3.4: Predicted Net Radiative Fluxes at the Hot Wall of a Square Cavity Containing Emitting-Scattering Medium.

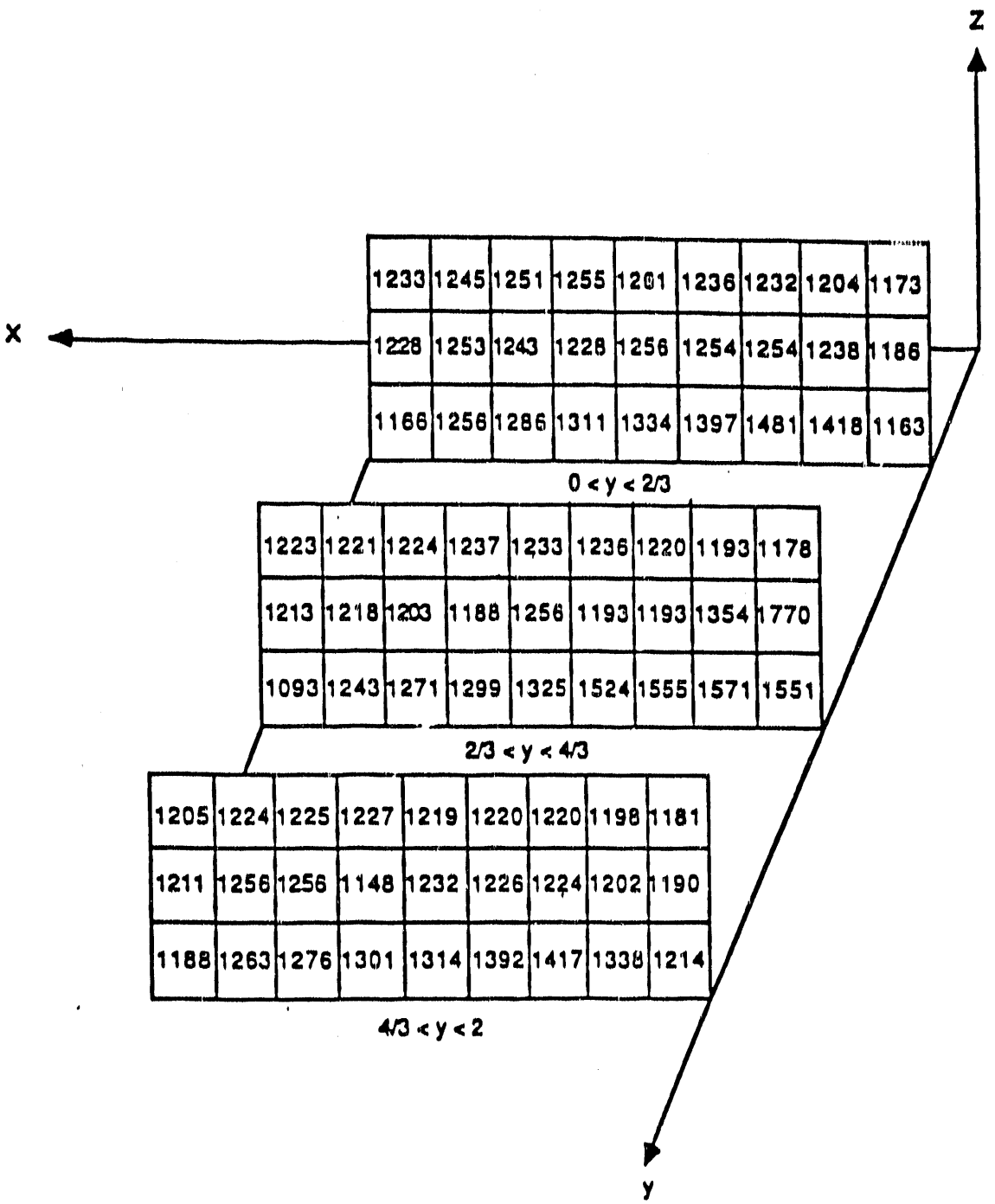

Figure 3.5: Measured Gas Temperatures for the IFRF-M3 Trial (Flame 10).

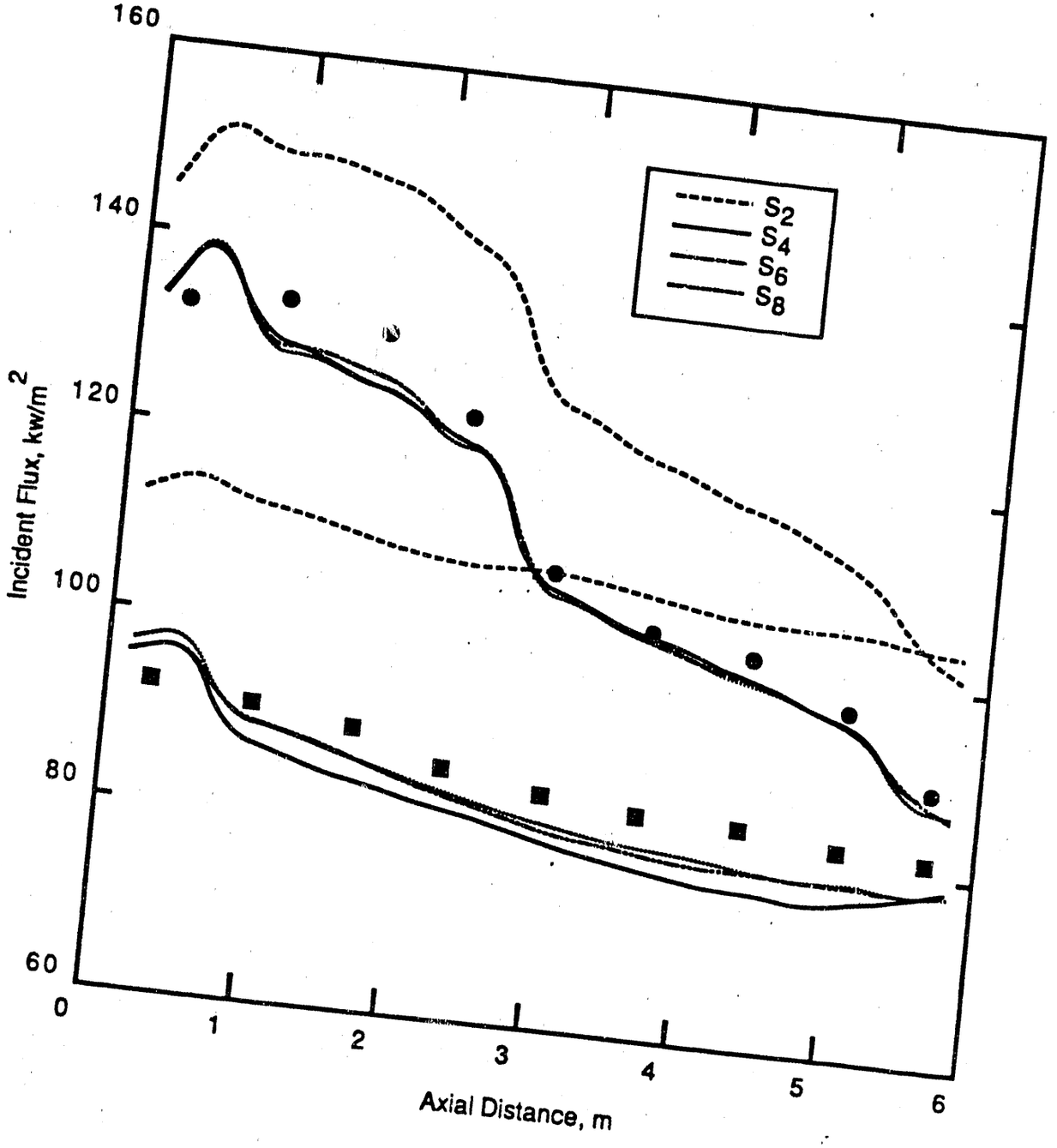

Figure 3.6: Predicted Incident Radiant Fluxes to the Floor and the Roof.

on theoretical grounds. The S_2 quadrature does not accurately integrate the half-range, first-order moment of intensity distribution. No measurable advantage is obtained by using the S_6 or S_8 approximation as compared to the S_4 predictions, but the computational time required increases by a factor of about two (in the case of S_6) to three (in the case of S_8). This is not entirely unexpected, since the refinement in angular quadrature may not necessarily yield more accurate results unless accompanied by corresponding refinement in spatial discretization (Carlson and Lathrop, 1968). The S_4 calculation took about 23 seconds cpu time on a VAX 11/750 computer using a 18 x 6 x 6 grid resolution.

This categorical system is studied earlier by Menguc and Viskanta (1985). Table 3.3 describes the furnace and the boundary conditions. Once again, discrete ordinates predictions have been made using S_2, S_4, S_6 and S_8 approximations. Figure 3.7 shows that the S_2 approximation does not provide good predictions for the wall heat fluxes; while the other approximations predict the fluxes in close agreement with the zone model prediction. The predicted temperatures of the medium at three axial locations (Figure 3.8) also bear out this fact. Considering the significant differences in computational time, the S_4 approximation is again considered adequate.

The absorbing-emitting-scattering case studied is a variation of the Menguc and the Viskanta system, where the medium is assigned a scattering albedo of 0.7. The zone model predictions for the wall heat fluxes and the temperatures of the medium are taken from Truelove (1987). Figure 3.9 shows that the predicted wall heat fluxes are almost unaffected by the isotropic scatter. However, the predicted temperatures of the medium (see Figure 3.10) show measurable increase due to the enhancement of the medium's effective emissive power in the presence of the scatter. Of the four discrete-ordinates approximations, S_4 turns out to be the best, considering the accuracy of the predictions and computer time requirements.

3.2.5 Sensitivity Study

A sensitivity study of the S_4 discrete ordinates approximation to uncertainties in radiative properties and other relevant system parameters (i.e., temperatures, furnace dimensions, etc.) was undertaken using Fourier amplitude sensitivity technique (FAST) (Cukier, et al., 1978; Smith and Smith, 1987).

Table 3.2: Description of the 3-D Furnace used in the IFRF M3 Trials.

Furnace dimensions	:	6.0m x 2.0m x 2.0m
Wall temperatures and emissivities	:	Floor, T_w = 320 K, ε_w = 0.86 Others, T_w = 1090 K, ε_w = 0.70
Properties of the medium	:	k_a = 0.2 m^{-1}, T_g = measured (see Fig. 5)

Table 3.3: Description of the 3-D Furnace of Menguc and Viskanta (1985).

Furnace dimensions	:	4.0m x 2.0m x 2.0m
Wall temperatures and emissivities	:	Firing end, T_w = 1200 K, ε_w = 0.85
		Exit end, T_w = 400 K, ε_w = 0.70
		Others, T_w = 900 K, ε_w = 0.70
Properties of the medium	:	k_a = 0.5 m^{-1}, S_{lir} = 5.0 kW/m^3

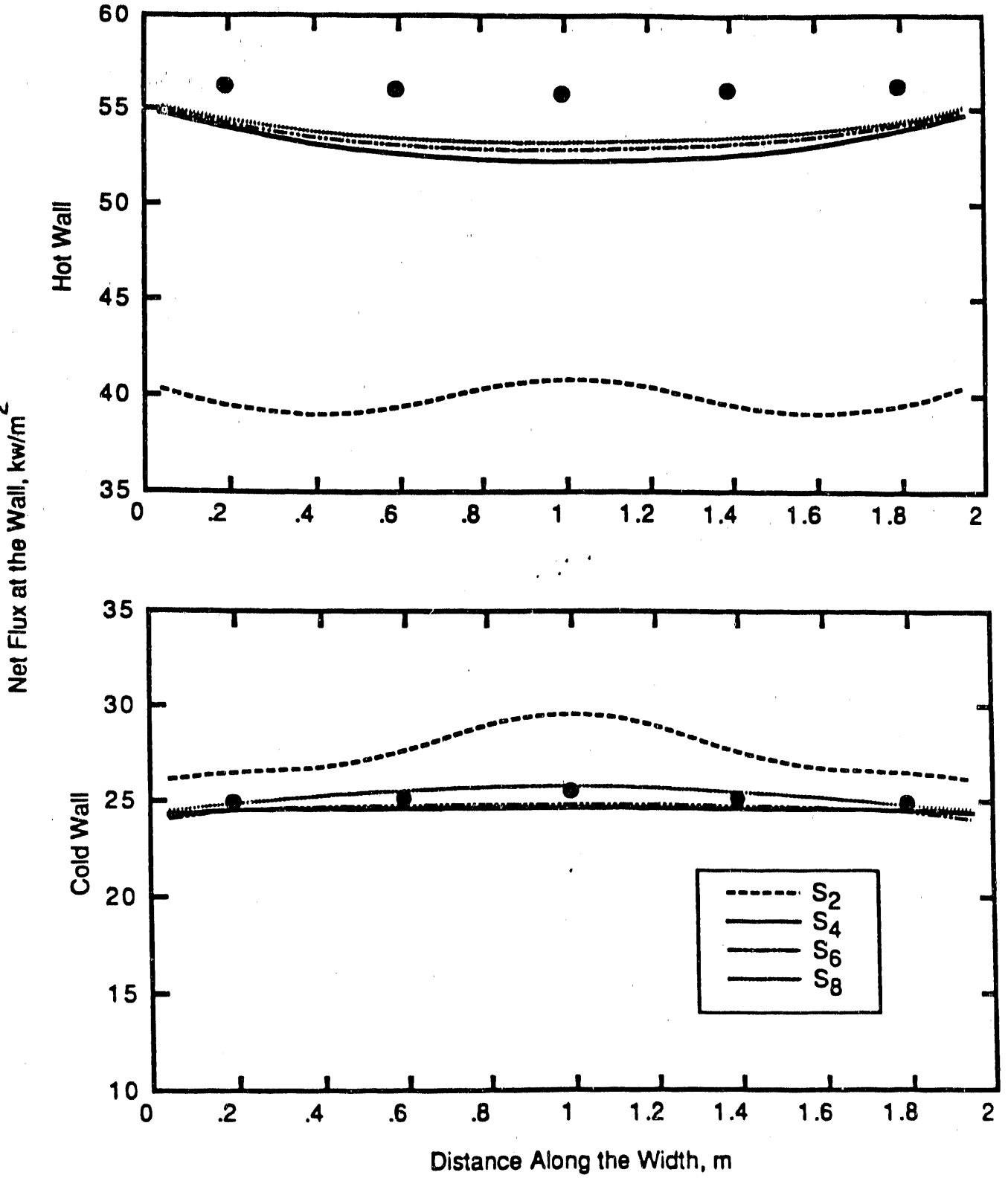

Figure 3.7: Predicted Net Radiative Fluxes at the Hot and Cold Walls of a Rectangular Enclosure Containing Absorbing-Emitting Medium with Finite Source Term.

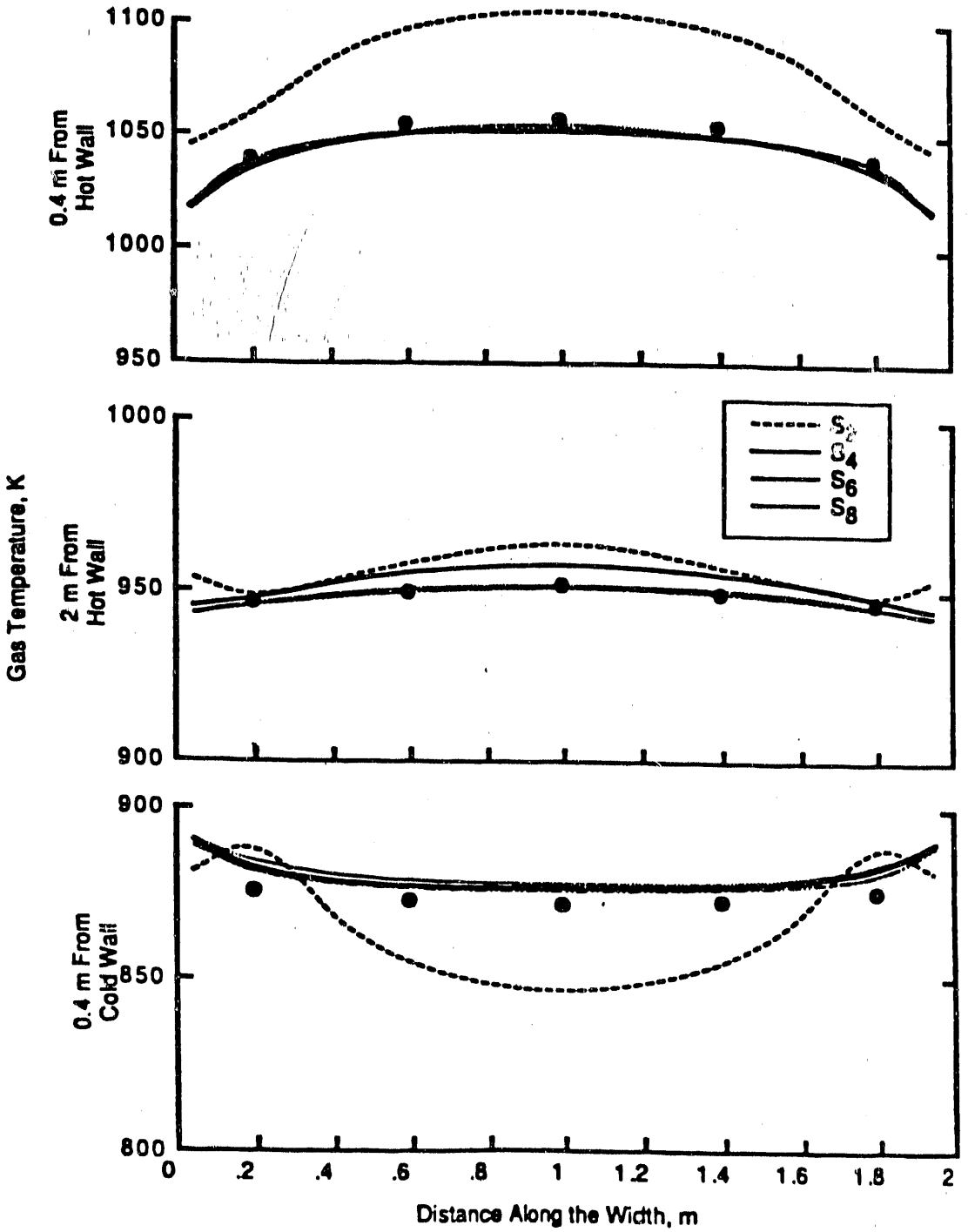

Figure 3.8: Predicted Temperatures of the Medium at Three Axial Locations (Absorbing-Emitting Medium).

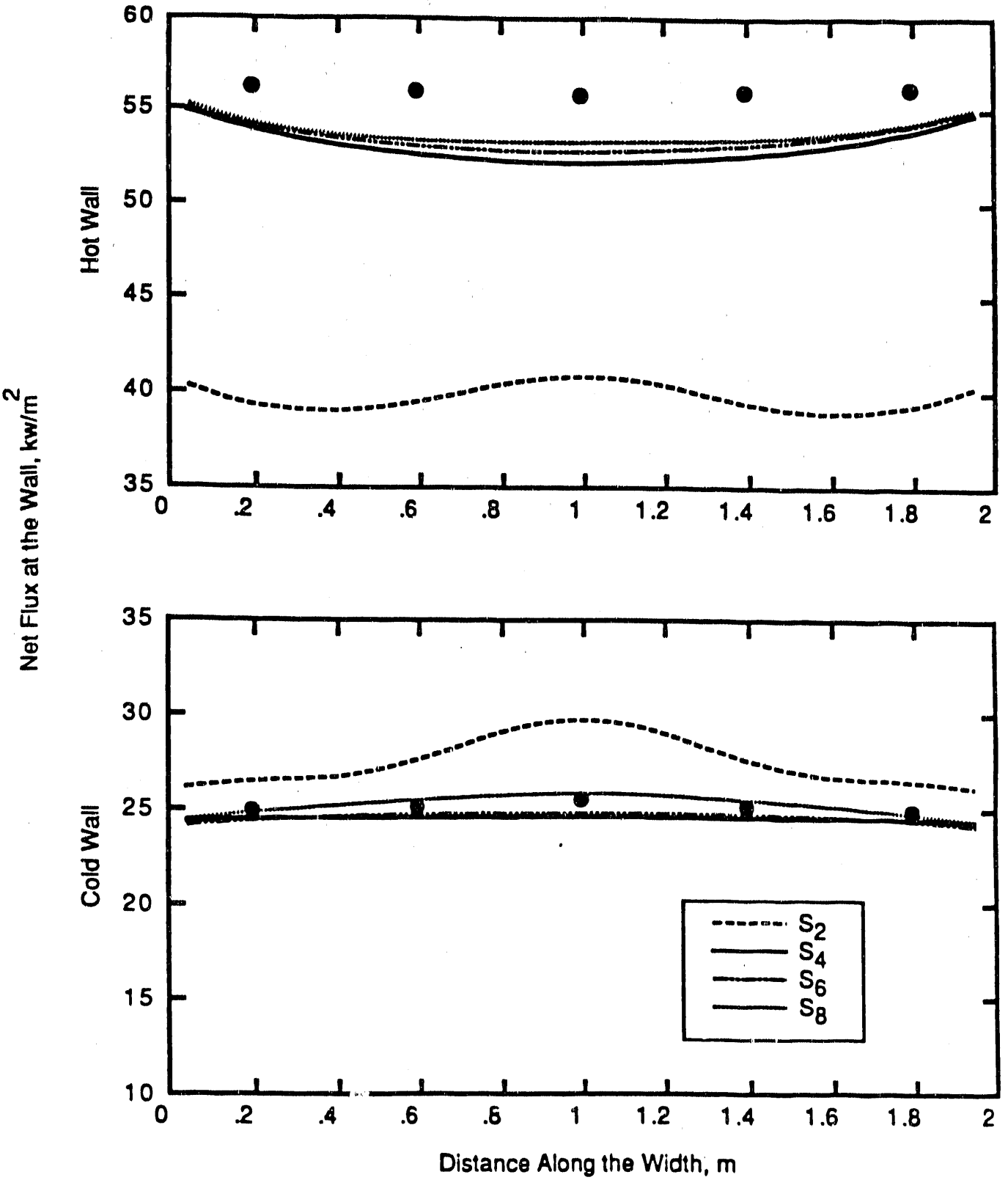

Figure 3.9: Predicted Net Radiative Fluxes at the Hot and Cold Walls of a Rectangular Enclosure Containing Absorbing-Emitting-Scattering Medium with Finite Source Term.

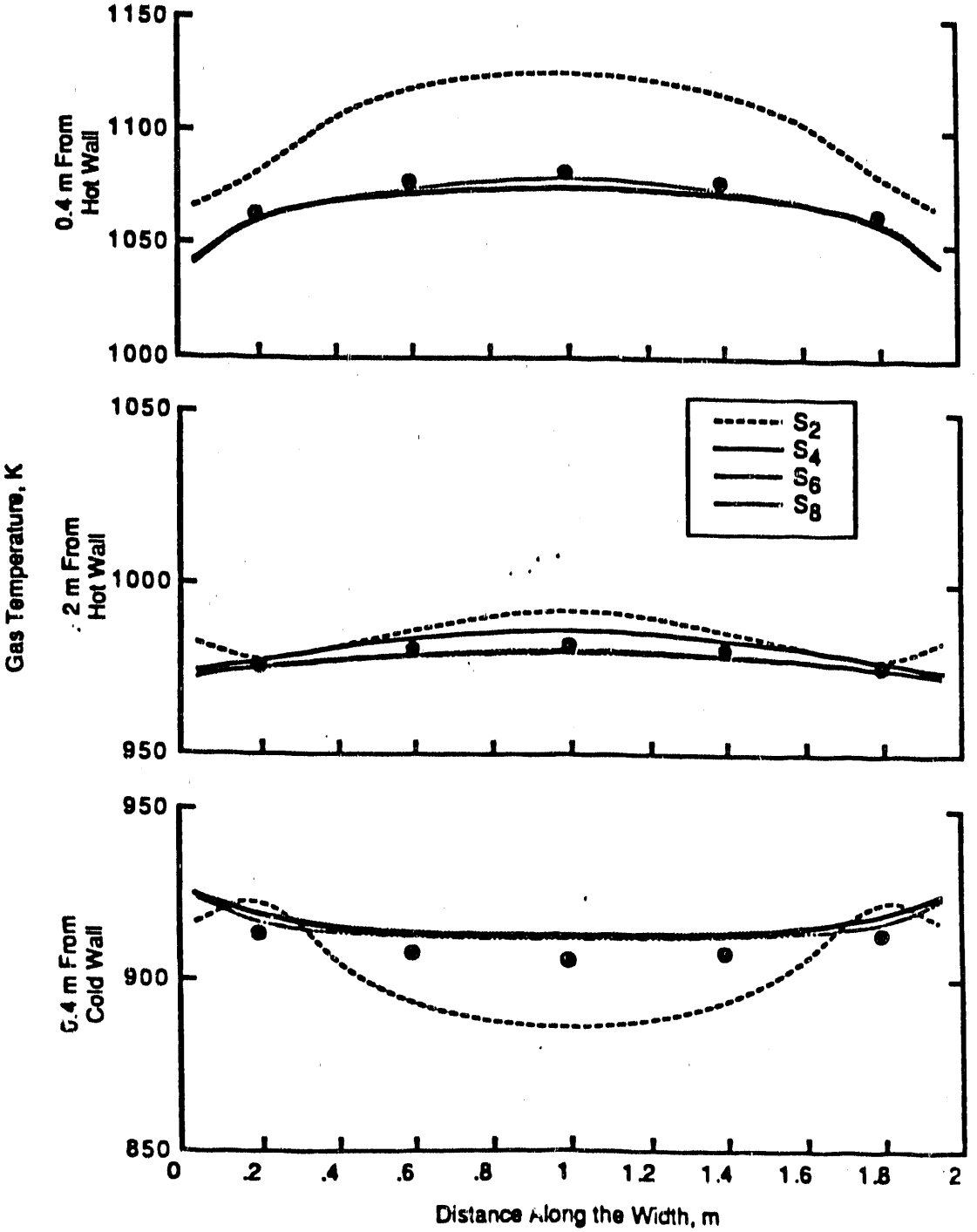

Figure 3.10: Predicted Temperatures of the Medium at Three Axial Locations (Absorbing-Emitting-Scattering Medium).

The input parameters and their ranges of variability for this study are presented in Table 3.4. The parameters are varied simultaneously following a statistical approach. The n-dimensional parameter space is transformed into one-dimensional parameter space by the introduction of a search variable, s, and a transformation function, G:

$$p_\ell = G_\ell[sin(w_\ell s)] \tag{3.9}$$

The w_ℓ is a set of nonequal frequencies, one assigned to each parameter p_ℓ. As s varies from $-\infty$ to $+\infty$, the combinations of w_ℓ and s carries all the parameters through their ranges of variation. The frequencies are chosen so the output variables at any fixed time become periodic in s, and can therefore be Fourier-analyzed.

The partial variance for parameter p_ℓ, defined as the fraction of the total variance of the output function due to uncertainty in p_ℓ while the output function is averaged over the uncertainties and coupling of uncertainties of all other parameters, serves as an excellent measure of the sensitivity of the output to the uncertainty of the l'th parameter.

$$S_l^{(m)} = \frac{[\sigma_{\ell,w_\ell}^{(m)}]^2}{[\sigma^{(m)}]^2} = \frac{\sum_{p=\ell}([A_{\ell,w_\ell}^{(m)}]^2 + [B_{\ell,w_\ell}^{(m)}]^2)}{\sum_k([A_k^{(m)}]^2 + [B_k^{(m)}]^2)} \tag{3.10}$$

A total of 99 simulations were required in the sensitivity study reported in this work. A sensitivity code developed by Pierce (1981) was used.

The single partial variances of radiant fluxes incident on the side wall of the three-dimensional rectangular enclosure for the six parameters considered in the study are presented in Figure 3.11. The wall temperature and the grid resolution were fixed at 500K and 20 nodes x 20 nodes x 20nodes, respectively, in this study as a preliminary sensitivity study showed the wall fluxes were not sensitive to these parameters. All inputs were assumed to be uniformly distributed, so the radiation transport equation had to be solved for one octant only. Radiation from the gas phase was neglected. Scatter was assumed to be isotropic.

The wall heat flux predictions (at the center of the wall, measured from the center of the furnace to the exit end) are most sensitive to the temperature of the medium, (Figure 3.11) with significant dependence on the extinction coefficient and the scattering albedo. Still, the predictions are

Table 3.4: The Parameters and Their Range of Values Considered in the Sensitivity Study.

	Parameter	Range	Mean
①	Furnace length, m	2.0 - 10.0	6.0
②	Furnace width/height, m	1.0 - 4.0	2.5
③	Extinction coefficient, m^{-1}	0.0 - 1.0	0.5
④	Albedo of scatter	0.0 - 1.0	0.5
⑤	Wall emissivity	0.6 - 1.0	0.8
⑥	temperature of medium, K	1200.0 - 2000.0	1600.0

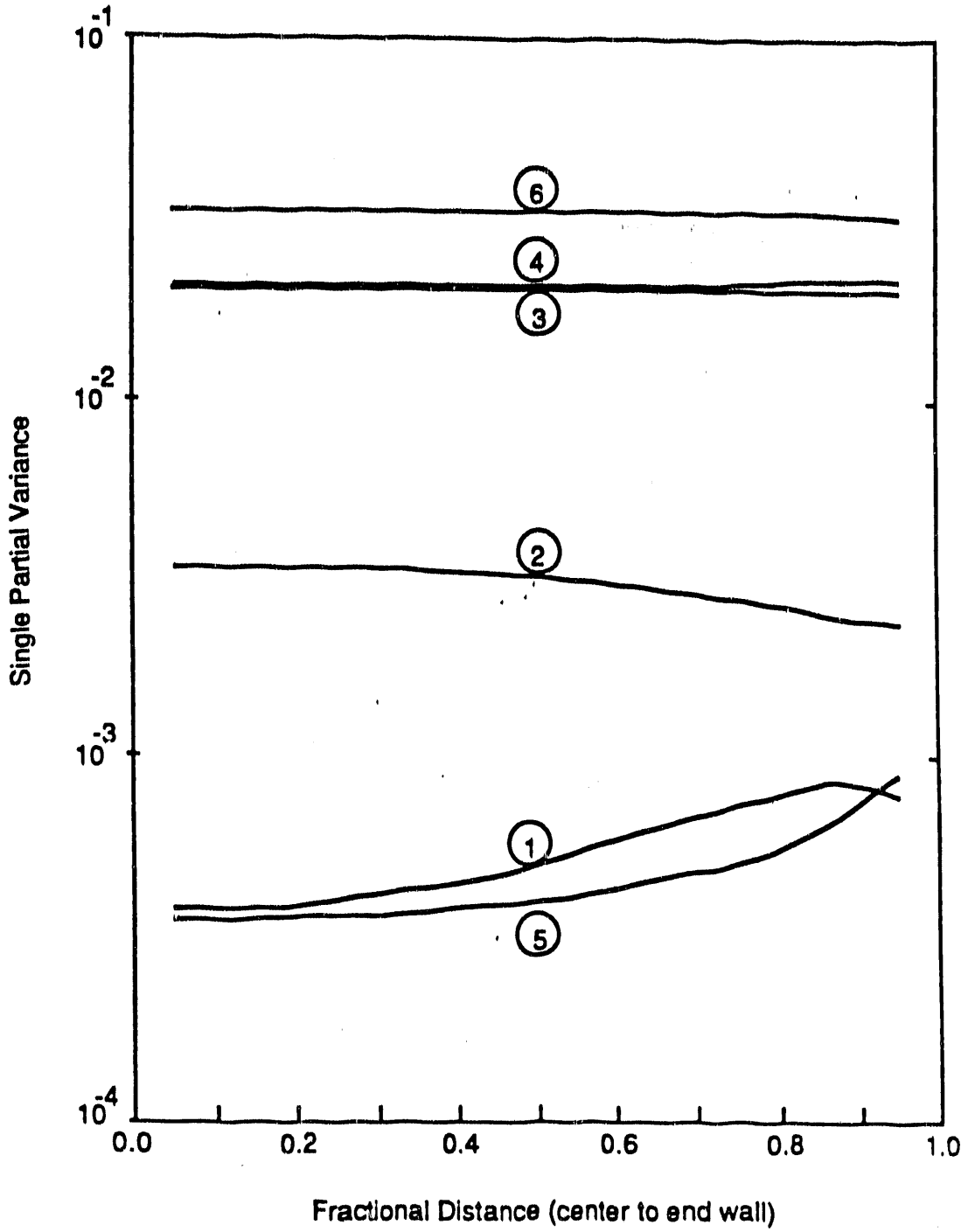

Figure 3.11: The Single Partial Variances of the Incident Radiation Flux Due to Uncertainties in the Parameters within the Prescribed Range (see Table 3.4).

rather insensitive to variations in the furnace length and the wall emissivity. The apparent contradiction between this finding and the findings of Figure 3.9 may owe to the fact that the effect of scattering is more pronounced in systems where the temperature of the medium is specified.

3.2.6 Conclusions

All discrete ordinates approximations (S_2, S_4, S_6 and S_8) predict radiative transfer in two-dimensional rectangular enclosures containing absorbing-emitting-scattering media with acceptable accuracy. However, S_2 and S_4 are more acceptable in two-dimensional enclosures because they consume considerably less computer time with little loss in accuracy.

In three-dimensional rectangular enclosures, the S_2 predictions are grossly in error. However, acceptable prediction accuracy is obtained using S_4, S_6 and S_8 approximations. The S_4 predictions are again considered adequate.

Radiative transfer in a three-dimensional rectangular enclosure is highly sensitive to uncertainties in the temperature of the medium, significantly sensitive to the extinction coefficient and the scattering albedo, but rather insensitive to the furnace length and wall emissivity.

3.3 Char Oxidation

This subsection deals with the process of heterogeneous oxidation, by which the organic matter remaining after devolatilization reacts and, by which nearly all of an anthracitic coal combusts. The accurate physical description of coal and char oxidation is complicated by evolving pore structures, temperature gradients, mass and heat transfer effects both inside and outside the particle, and unknown but probably changing surface chemistry. Catalytic effects of inorganic matter and the age and history of the coal also play roles in its oxidation behavior. Many of these matters have been reviewed and are current areas of research. Laurendeau (1978) offers an excellent review of these issues. However, global oxidation rates based on external surface area and simple Arrhenius expressions for reaction rate coefficients are the most common descriptions of oxidation processes. Because of these complications, scientists and engineers represent this process in both comprehensive codes and focused experiments.

The work in this section deals with the analysis of data intended to be fit to nonlinear equations. The Arrhenius equation is used as the example throughout. The discussion applies, with appropriate modification, to all nonlinear equations and the data thereof. All Arrhenius data needs no modification, whether it describes heterogeneous oxidation or some other process. The statistical and mathematical development is fundamental. As discussed below, many previous conclusions about the quality, agreement, and interpretation of Arrhenius data will be altered or even reversed when a more rigorous approach is applied.

Although this approach to analyzing Arrhenius data closely follows established statistical theory, it is rarely used by either engineers or scientists. Of the several authors who have considered some aspect of the problem, none have offered a comprehensive derivation or discussion of this approach (Cvetanovič, et al., 1975; Cvetanovič, et al., 1979; Jeong, et al., 1984; Lopez, et al., 1981; Shmel'ev, et al., 1981; Schuhler, 1982; and Héberger, et al., 1987). The latter three references include illustrations of the correlation of the pre-exponential factors and activation energies of these results. However, these are approximations to the more fundamental approach discussed in this chapter.

This subsection examines the classical technique of data linearization to determine parameters for Arrhenius expressions and finds it to be inadequate. The statistical theory with results of a more rigorous technique are presented and compared to the classical technique. Both the values of the parameters and the conclusions about the data/correlation change substantially when the more rigorous technique is used. Even when such errors are correlated, the more rigorous technique indicates confidence contours for the data, treat data with nonconstant precision, and treat data with errors in both measured reactivity and in temperature. A computer program, to treat Arrhenius data according to this more rigorous theory, has been written and the results are presented as illustrations of the several issues discussed below. The theory is used to reevaluate the parameters for coal, char oxidation and gasification reaction rate coefficients.

A rigorous method of parameter estimation for Arrhenius data differs substantially from the classical approach. Differences between these methods of data analysis relate to the assumptions about the data and the intended use of the correlating expressions. A sensible assumption is that the data follow an Arrhenius form of an equation, with errors in measured reactivity

which are normally distributed with a mean of zero and constant variance. Under these assumptions, the reaction rate coefficient is expected to be given by

$$k_i = Ae^{-E/RT_i} + \epsilon_i \tag{3.11}$$

where ϵ_i is the error term. It is a normally distributed random variable with a mean of zero and a constant variance for all the data.

Equation 3.11 is not the same as the implicitly assumed form of the error term when the linearized form of the equation is used. The latter equation is shown as equation 3.12.

$$\ln k_i = \ln A' - \frac{E'}{RT_i} + \epsilon'_i \tag{3.12}$$

where ϵ'_i has the same definition as ϵ_i. The two equations are not equivalent unless the values of the error terms are always 0.0. Several principles of statistical theory indicate that Equation 3.11, or some generalization of it, is the appropriate equation to use in the analysis of reactivity data.

3.3.1 Maximum Likelihood Estimation, Least Squares, and Arrhenius Data

The most common criterion for determining the best parameters for a model is least squares analysis, which is the minimization of the sum of the squares of the data from the correlating function. Least squares analysis of a linear function in its parameters, yields estimates of these parameters which are unbiased and have minimum variance (Canavos, 1984). These properties are independent of the assumed distribution properties of the errors (Draper and Smith, 1981). If the errors are assumed to be normally distributed, the least squares and maximum likelihood estimates of the parameters are equivalent. The maximum likelihood estimates of the parameters are consistent estimates of the parameters (in all cases of practical interest) and are invariant. They also yield the efficient estimates (and thus sufficient estimates) of the parameters, if they exist.

Not all the theoretical advantages of least squares analysis for linear models extend to models that are nonlinear in their parameters. However, if the errors are assumed to be normally distributed, the least squares and maximum likelihood estimates are still equivalent and will not vary. The Ar-

rhenius equation is also unique. The properties of the maximum likelihood estimates of parameters do not depend on the linearity of the model.

The use of the maximum likelihood estimation technique requires some knowledge of the distribution of the errors in the data. The assumption made here is that the data are normally distributed about a mean which is given by an Arrhenius expression (Equation 3.11 is assumed to be the appropriate equation for the data). The errors are also assumed to be only in the measurement of reactivity, as opposed to temperature, and to have the same variance for each data point. The assumption of a normal distribution is sensible in many practical cases. The central limit theorem indicates, with notable generality, that data which include the results of many small and independent errors is normally distributed about its mean (Montgomery, 1984). Many well executed combustion experiments fall into this category, where data are often averages of results for many thousands of small particles collected from the experiment. In the absence of overriding evidence, this assumption seems sensible. It provides a useful illustration of the method in any case. The assumptions of errors in the measurement of the reaction rate coefficient and of constant variance are only for convenience and illustration, and will be relaxed in the general approach described later in this section.

The likelihood function represents the probability that a given set of parameters in a model would have generated the observed data. This function is not a probability density function by a strict definition, but has many similar properties. With the assumptions discussed above, the likelihood function is given by

$$L = \Pi_{i=1}^{n} \frac{1}{\sigma(2\pi)^{1/2}} e^{-\epsilon_i^2/2\sigma^2} \tag{3.13}$$

where (for this application),

$$\epsilon_i = k_i - Ae^{-E/RT_i} = k_i - \hat{k}_i \ . \tag{3.14}$$

The maximum likelihood estimate for a parameter maximizes the likelihood function with respect to the data. In other words, the most probable value of the parameter which would have yielded the observed results. The maximum in the likelihood function is also the maximum in its logarithm. Differentiating the logarithm of the likelihood function with respect to A and E and setting the result to zero produces the least squares criterion for the best parameters of the model. That is, the most likely parameters A and E for a given set of data are those which satisfy the minimization:

$$min_{A,E} \sum_{i=1}^{n} [k_i - Ae^{-E/RT_i}]^2 = \sum_{i=1}^{n} [k_i - \hat{k}_i]^2 \ . \tag{3.15}$$

Equation 3.15 illustrates the connection between maximum likelihood and least squares estimations. However, the appropriate function is the nonlinear least squares estimator of A and E, not the logarithmic transformation. Equation 3.15 is the appropriate approach to determining the best parameters A and E (even if the Arrhenius expression is being used as a simple correlation, with little or no belief in a corresponding underlying physical or chemical mechanism). For example, it is used to correlate heterogeneous global reaction rates on surfaces experiencing complicated surface chemistry. In situations where the Arrhenius expression is believed to be an accurate expression by virtue of physical or chemical mechanisms, Equation 3.15 has a stronger advantage over its linearized counterpart. In any case, this approach is superior to that of the linearized expression under the assumptions discussed at the beginning of this section. Methods of relaxing these assumptions while maintaining the desirable statistical properties are discussed next.

The derivation of Equation 3.15 assumed that only the error in reactivity is significant and that no correlations of error in reactivity and error in temperature exist. Equation 3.15 was also derived by assuming that the precision of the data is the same for each data point collected. In many practical applications, all these assumptions are incomplete.

A generalization of this approach is used to relax several of the assumptions required to derive Equation 3.15. If one assumes that the errors in reactivity and temperature are bivariate-normally distributed, with known correlation coefficient and variance in reactivity and temperature at each point, the likelihood function is

$$L = \Pi_{i=1}^{n} \frac{1}{\sigma_{T_i} \sigma_{k_i} 2\pi (1 - \rho_i^2)^{1/2}} e^{-q_i} \tag{3.16}$$

where

$$q_i = \frac{1}{2(1-\rho_i^2)} \left\{ \left(\frac{k_i - \hat{k}_i}{\sigma_{k_i}} \right)^2 - \rho_i \left[\frac{(k_i - \hat{k}_i)}{\sigma_{k_i}} \right] \left[\frac{(T_i - \hat{T}_i)}{\sigma_{T_i}} \right] + \left(\frac{T_i - \hat{T}_i}{\sigma_{T_i}} \right)^2 \right\} . \tag{3.17}$$

From this likelihood function, the following criteria for determining the coefficients results:

$$min_{A,E} \sum_{i=1}^{n} q_i \tag{3.18}$$

which is equivalent (but not equal) to

$$min_{A,E} \sum_{i=1}^{n} \frac{1}{1-\rho_i^2} \left\{ \left(\frac{k_i - \hat{k}_i}{\sigma_{k_i}} \right)^2 - \rho_i \left[\frac{(k_i - \hat{k}_i)}{\sigma_{k_i}} \right] \left[\frac{(T_i - \hat{T}_i)}{\sigma_{T_i}} \right] + \left(\frac{T_i - \hat{T}_i}{\sigma_{T_i}} \right)^2 \right\}. \tag{3.19}$$

The parameters $\hat{k}_i$ and $\hat{T}_i$ can be determined from the pointwise minimization of

$$min_{\hat{k}_i, \hat{T}_i} \frac{1}{(1-\rho^2)} \left\{ \left(\frac{k_i - \hat{k}_i}{\sigma_{k_i}} \right)^2 - \rho_i \left[\frac{(k_i - \hat{k}_i)}{\sigma_{k_i}} \right] \left[\frac{(T_i - \hat{T}_i)}{\sigma_{T_i}} \right] + \left(\frac{T_i - \hat{T}_i}{\sigma_{T_i}} \right)^2 \right\} \tag{3.20}$$

where

$$\hat{k}_i \equiv A e^{-E/R\hat{T}_i} \tag{3.21}$$

(with no error term).

The terms σ_{T_i} and σ_{k_i} represent the variance in the measurement of the temperature and reactivity, respectively. The term ρ_i represents the correlation coefficient between errors in temperature and reactivity measurements. In general, each of these terms can vary from point to point.

Equation 3.20 assumes that A and E are known whereas Equation 3.19 assumes that $\hat{k}_i$ and $\hat{T}_i$ are known. The approach to solving both equations is iterative. For example, starting with an estimate of A and E, $\hat{k}_i$ and $\hat{T}_i$ estimates are generated for each data point by application of Equation 3.20. These estimates are then used to generate new estimates of $\hat{k}_i$ and $\hat{T}_i$ by using Equation 3.19. The iterations continue until estimates of all $2n + 2$ parameters $\hat{k}_i$, $\hat{T}_i$, A, and E are obtained within a desired precision. The results (discussed later in this chapter) also required mathematical shepherding, such as underrelaxation and several perturbation techniques that capitalize on the structure of the problem.

Satisfying Equations 3.19 and 3.20 will determine the best estimates of A, E, $\hat{k}_i$ and $\hat{T}_i$ under the assumption of bivariate-normally distributed errors. The quantities $\hat{k}_i$ and $\hat{T}_i$, defined by Equation 3.20, represent the coordinates of the closest point on the Arrhenius correlation curve, in a nondimensional, statistical sense, to the measured data point (k_i, T_i).

3.3.2 Application of Rigorous Analysis of Arrhenius Data

The improved fit of the rigorous nonlinear technique appears both in the statistics and visual comparison of the data with the correlation lines. The data and correlations in Figure 3.12 illustrate these points. The linear technique comes closer to the lowest temperature data point but fits the rest of the data more poorly than the nonlinear technique. One of the undesirable characteristics of the parameters determined by linearizing the data is that they weight the low temperature data too heavily. The data in this figure are for oxidation of a Texas lignite char by carbon dioxide and were collected by Combustion Engineering [Goetz et al., 1982].

A statistical comparison of the fit of the two lines shown in Figure 3.12 shows, with 90% confidence, that the improvement in the fit is significant. Indeed, a statistical analysis of the less rigorous correlation concludes, with over 90% confidence, that the Arrhenius equation does not correlate this data within its inherent error. This would indicate (unjustifiably) that some more sophisticated model (Langmuir-Hinshelwood for example) is required to correlate the data. The same test applied to the rigorous correlation indicates that the lack of fit is not significantly greater than the inherent error in the data. These opposed findings illustrate the erroneous conclusions which can be drawn from the less rigorous fitting technique. The confidence levels cited here and elsewhere in this section should be regarded as approximate because the lack of fit statistic may not follow a chi-square distribution exactly (Draper and Smith, 1981). However, the tests and methods themselves are exact.

The gasification rate of chars by CO_2 is practically important at temperatures higher than the highest data indicated in Figure 3.12. The inset in Figure 3.12 illustrates the difference in the extrapolated gasification rate for these chars. A lack of data at such high temperatures often gives rise to extrapolation of low temperature data in predicting gasification efficiency, etc. The difference in the extrapolated reaction rate is substantial and, while extrapolation is prone to error under any circumstance, the extrapolation using the rigorously determined parameters is the most sound from a statistical standpoint. A practical illustration of this point is discussed in the final subsection of this chapter.

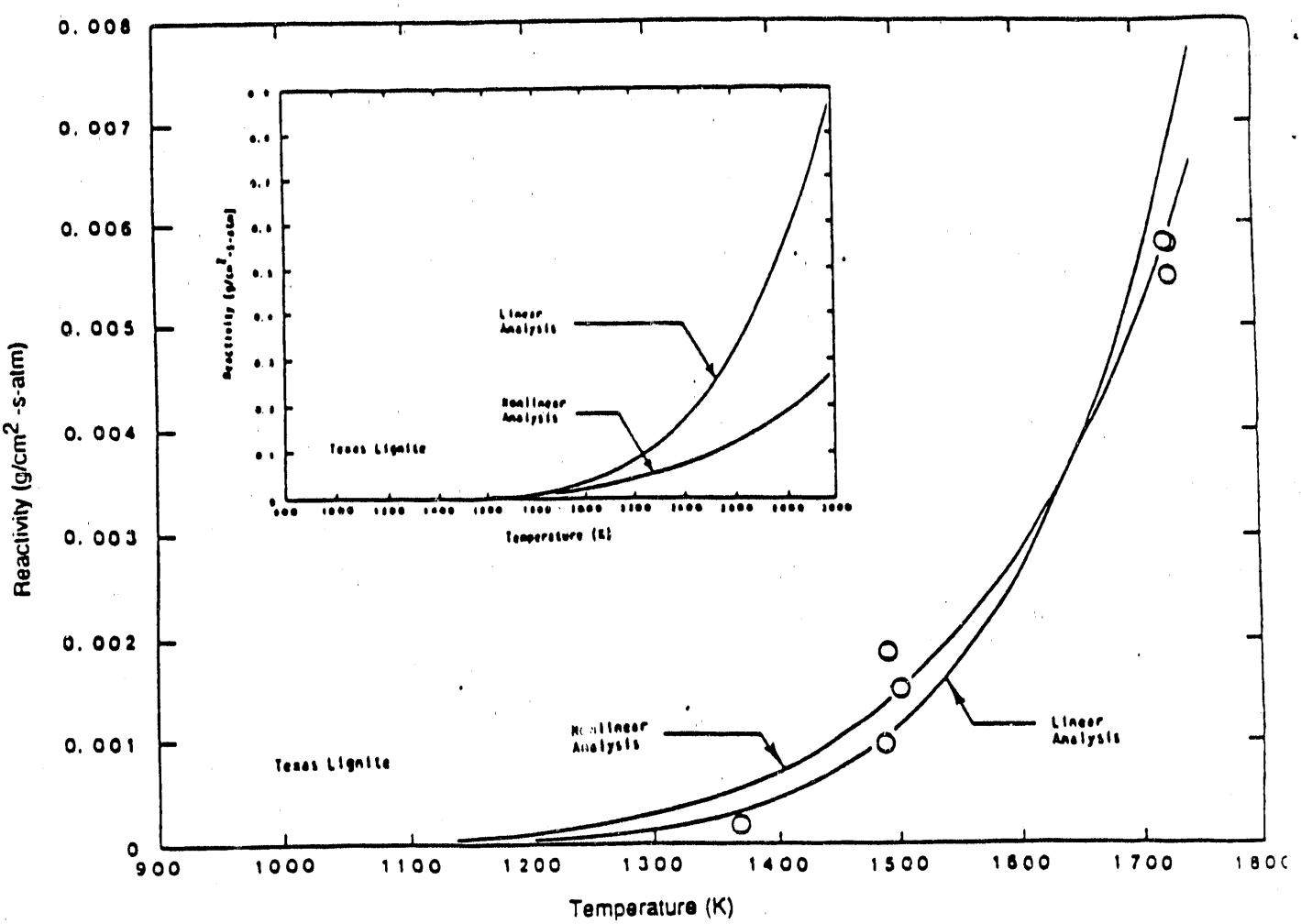

Figure 3.12: Illustration of the Difference of the Nonlinear and Linear Data Analyses for Typical Heterogeneous Oxidation Data. Data from Goetz, et al. (1982).

3.3.3 Confidence Contours for the Parameters

Confidence contours can also be calculated for the parameters of the model based on the above theory. A common but misleading approach to calculating such contours yields elliptical contours based on the covariance matrix evaluated with the best estimates of the parameters [Héberger, et al., 1986]. An exact approach is used in this section to evaluate the confidence contours (intervals) of the parameters of the Arrhenius expression [Beck and Arnold, 1977]. Such calculations require that the correlating expression is the proper expression for the data.

Confidence regions for the values of the pre-exponential factor and activation energy can be constructed by plotting contours of constant $S(\theta)$ where

$$S(\theta) = S(\hat{\theta})[1 + \frac{p}{n-p}F(p, n-p, 1-\alpha)] \tag{3.22}$$

and $S(\hat{\theta})$ is the value of the minimization shown in Equation 3.19 evaluated with the best estimates of the coefficients, p is the number of parameters estimated in the model, n is the number of data points, and F is a standard F-statistic with p and $n-p$ degrees of freedom at a nominal confidence level of $100(1.0-\alpha)\%$ (Draper and Smith, 1981). This is a ***nominal*** confidence level because $S(\hat{\theta})$ does not necessarily follow the standard F-distribution exactly. The contour itself is exact. It is the confidence level which is approximate.

Char oxidation data reviewed by Field (Field, et al., 1974) are used here to provide an example of the results. These data also play a role in the following subsection of the report. However, identical techniques have been applied to gasification and oxidation data from many sources with similar results.

Field reviewed the work of a large number of investigators and selected data from six of them which provided information on oxidation rates which were free of diffusion limitations and otherwise useful. All of the data were for the consumption of carbon in oxygen. He tabulated much of this data in his report. At the conclusion of Field's report, parameters were suggested for use in Arrhenius expressions for char oxidation. These parameters were determined by the nearly universally applied linearization of the data.

Using the more rigorous data analysis and confidence contour techniques outlined and referenced above, the data tabulated by Field was reanalyzed. Figure 3.13 illustrates the results of this analysis. The point indicated by the

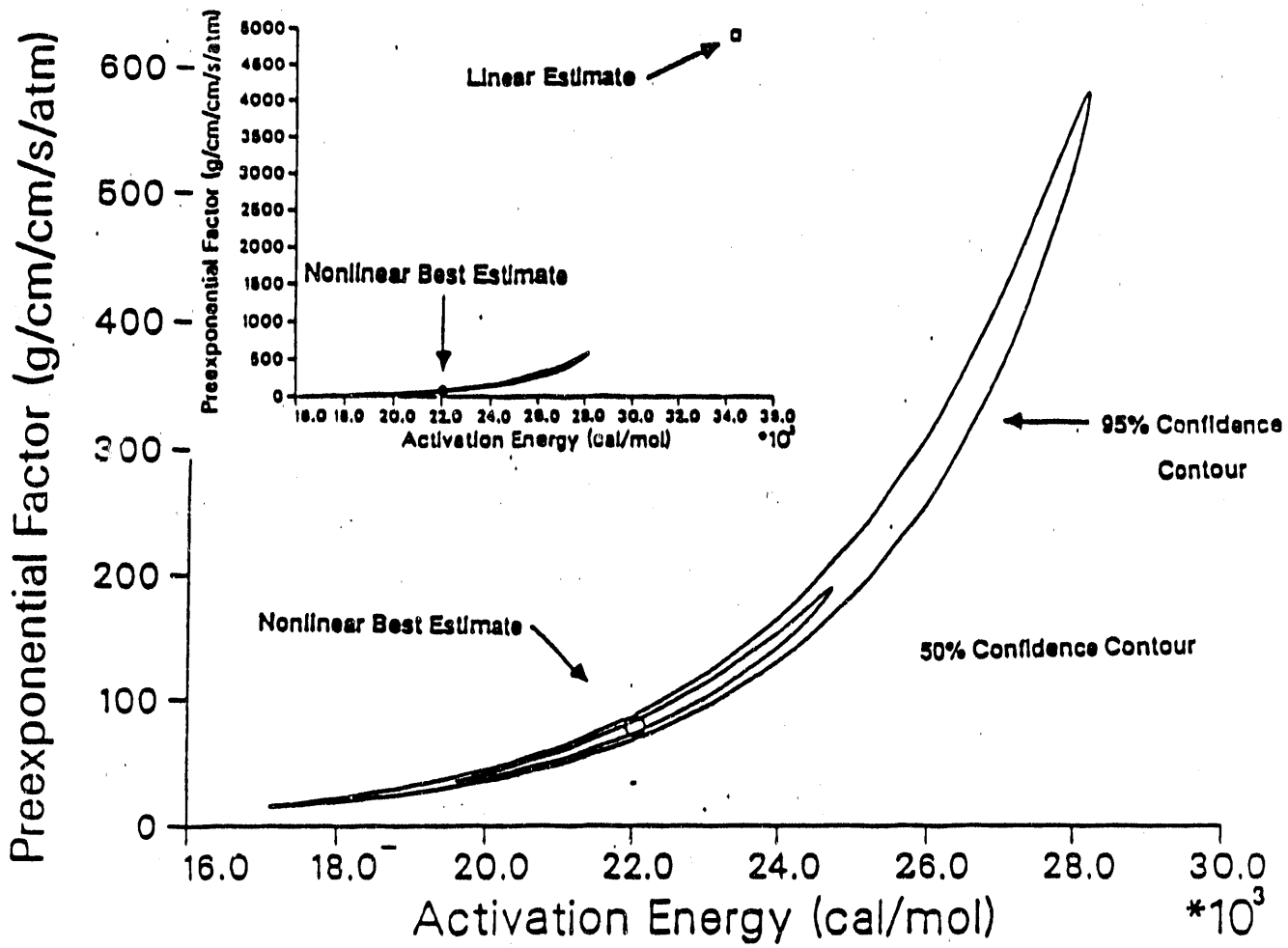

Figure 3.13: Illustration of the Confidence Contours for the Data Reviewed by Field, et al. (1974) for Heterogeneous Char Reaction with Oxygen.

circle in the figure is the best estimate of the parameters of the model. The loops in the figure are contours of 50% and 95% confidence for the parameters of the model. That is, if the entire population of chars could be collected and analyzed, the confidence level of the contour represents the probability of the predicted parameters A and E from these data falling within the loop. The confidence contour for the pre-exponential factor varies over a much larger interval than that for the activation energy, as would be expected.

The shape of the loops in Figure 3.13 indicates that specifying only the endpoints of the confidence contours is a misrepresentation of the actual uncertainty in the parameters. That is, while the 95% confidence interval is 17 to 28 kcal/mol for the activation energy and 20 and 600 g/cm^2-s-atm for the pre-exponential factor, there is a vanishingly small probability that one of these parameters would be at its upper bound while the other is at its lower. This has significant implications when confidence intervals are used in sensitivity analyses, comparisons of coefficients from different sets of data, etc. The contours illustrate the structure of the confidence regions accurately.

The slender loops in Figure 3.13 illustrate the correlation and compensation which the activation energy and pre-exponential factor can have with each other. This effect, which is considered controversial to some [Héberger, et al., 1987], is manifest in the ability of two substantially different activation energies correlating a set of data if the pre-exponential factors are allowed to be adjusted. In this specific case, no significant difference would be seen in the degree of correlation of the data if the activation energy were 20.0 kcal/mol and the pre-exponential factor were 30 g/(cm^2 s atm) as compared to an activation energy of 25 kcal/mol and a pre-exponential factor of 180 g/(cm^2-s-atm). That is, both results lie within the fifty% confidence contour.

It is also clear that the range of reasonable variation for the pre-exponential factor is much broader than that for the activation energy. It is not correct, however, to conclude that the correlation is insensitive to the value of the pre-exponential factor. Arbitrary changes in the pre-exponential factor without compensating (but relatively smaller) changes in the activation energy significantly decrease the extent of agreement between the data and the predictions. The specific example just used illustrated that the pre-exponential factor can vary within a factor of six without significantly compromising the ability of the Arrhenius equation to fit the data. However, changing the pre-exponential factor by a factor of just three *without simultaneously changing the activation energy* produces a result which is well outside of even a 99.9%

confidence contour for the results. The conclusion is that activation energies alone are not good measures of reactivity and that account must be taken of the structure of the areas of correlation of these parameters to do meaningful comparison of kinetic results from different sets of data.

It is useful to compare the results of this analysis with the results of a linear analysis of the same data. The inset in Figure 3.13 provides such a comparison. This figure illustrates the same points on a scale which includes the best estimate of the parameters from the less rigorous linear analysis. This point lies well outside of the 95% or even 99.9% confidence contour, indicating that it is a poor approximation to the actual values of the parameters.

The parameters generated by the linearization of the data are shown to not only be poor estimates of the actual best estimates, but can be concluded to be wrong with a confidence level in excess of 99.9%. Just as in the previous section, where an analysis of the fit of the Arrhenius expression not only improved but actually reversed the conclusion of the statistical test, here the conclusions about the parameters are reversed. The predicted confidence contours also reasonably represent the range of parameters typically measured for char oxidation.

The general shape of the contours is a property of the Arrhenius expression. However, the size and detailed shape of the contours depends on the accuracy and number of data. With fewer and less accurate data over a narrower temperature range, the importance of performing a proper confidence contour analysis becomes more pronounced.

3.3.4 Practical Usefulness of Rigorous Analysis

Data and conclusions which Field published after his above-cited review will be used to illustrate the practical usefulness of rigorous data analysis [Field, 1974]. Figure 3.14 illustrates data collected by Field of the results of other investigators. These data span a greater temperature range than the data in Field's review. Both lines in the plot are predictions based on the data in the review, *not* the data illustrated in the figure. The predictions based on the linearization analysis are poor. Low temperature reactivities are slightly underpredicted and high temperature reactivities are greatly overpredicted. Field observed this same result and chose to fit his data with a reactivity which is linear in temperature even though negative reactivities were predicted at temperatures below about 1300 K.

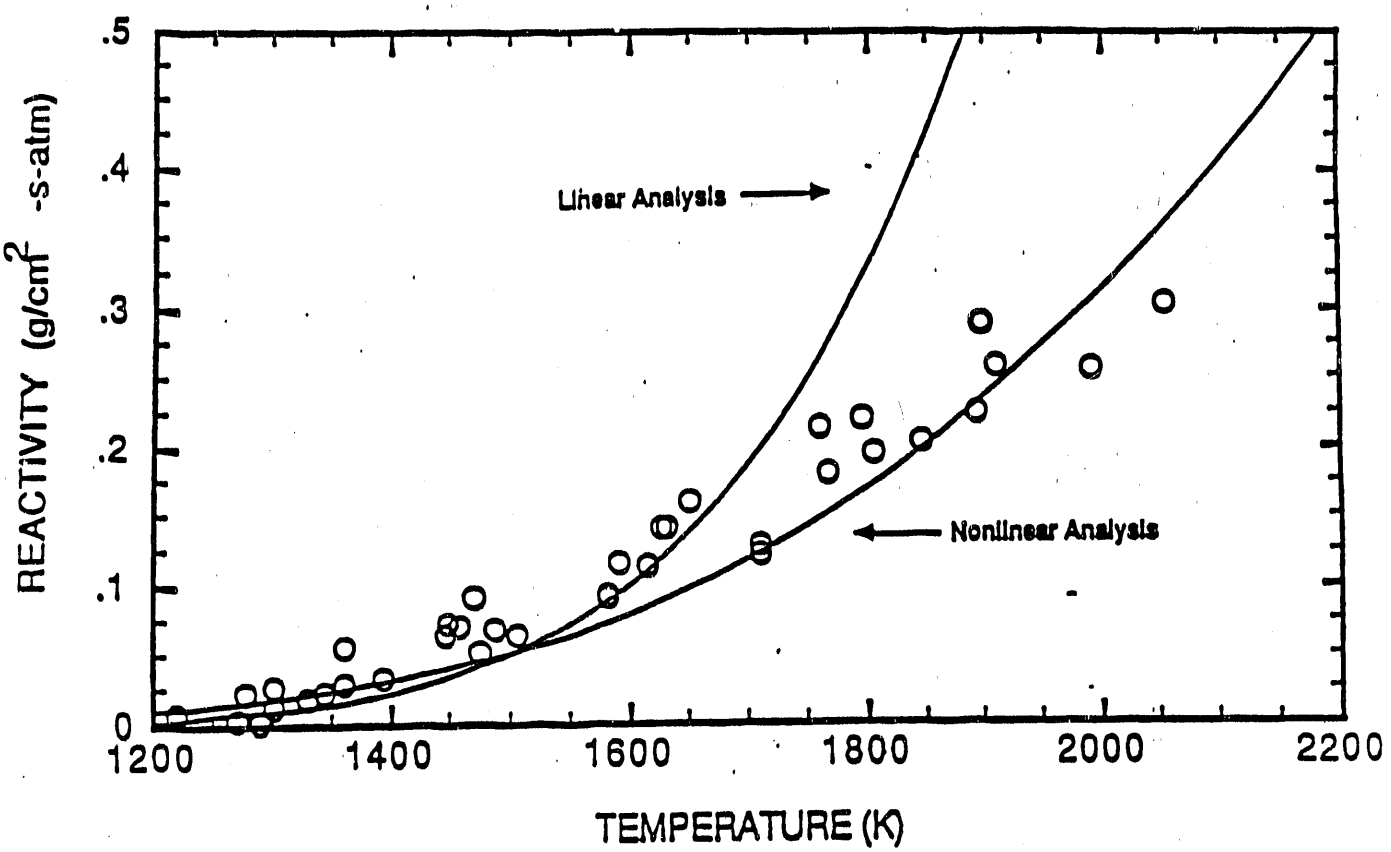

Figure 3.14: Comparison of the Prediction of Independently Gathered Data Based on the Linear and Nonlinear Analysis Techniques.

The apparent decline in char reactivity at the high temperture region, as compared to the predictions from the linearization technique shown in this figure, is often cited as evidence of changing activation energies during char oxidation. In principle, there is no reason to expect the Arrhenius law to correlate data over a broad temperature range. The complicated surface chemistry involved in char oxidation involves adsorption, surface reaction, and desorption of species. The controlling mechanisms in this complicated sequence are sensitive to temperature, reactant and product concentration, and changing morphology of the coal particle. Additionally, the results here pertain to global reactivities, which ignore the processes involved with pore diffusion and oxygen penetration. For these reasons, one should not necessarily expect an Arrhenius expression to correlate reactivity data over a broad temperature or composition range.

However, a careful analysis of the data shows that the apparent decrease in reactivity at high temperatures is not a feature of coal reactivities but rather an artifact of the data analysis used to determine the reaction rate coefficients used in the Arrhenius expression. There is no support for applying an Arrhenius expression over all temperature and composition ranges. There is equally no support from these data for the contention that the apparent, global char reactivity parameters change at high temperatures. The second line in the figure illustrates this point. It represents a prediction using parameters from a correlation of the data reviewed by Field, again *not* a correlation of the data illustrated in the figure. The agreement between these independently measured sets of data over many years time and a broad temperature regime is impressive. The predictions at high temperature represent a significant extrapolation of the Arrhenius law from the range of temperatures in the data used to calculate its coefficients, making this agreement more impressive still and underscoring the importance of careful data analysis when dealing with nonlinear equations.

These results show how the classical linearization procedure can lead to several poor results. The Arrhenius form of the equation is unjustifiably rejected, the parameters are not justified by the data, and the extrapolation is poor. However, a proper statistical analysis indicates a great deal more consistency and accuracy in the data than has previously been reported.

3.3.5 Coal Gasification and Oxidation Data

The techniques above apply to any type of correlating expression for data. However, current research seldom extends beyond Arrhenius expressions for either global or intrinsic reactivity. Several authors have suggested that Langmuir-Hinshelwood expressions, which account for effects of adsorbed species, are more appropriate (see Smoot and Pratt, 1979). However, the coefficients which are required for these expressions are ill defined and will require more fundamental research before the expressions are useful. Coefficients for global kinetics were gathered in this study.

Data for the oxidation rate of coal are plentiful but disparate. The coefficients listed in Table 3.5 represent reasonable values based on data viewed to be reliable. Wherever possible, the data were reanalyzed according to the preceeding methods. Therefore, the coefficients in Table 3.5 often differ substantially from those suggested in the respective references. The results reported by the original investigators are also listed. In each case they were found to be the results obtained by linear analysis.

Data for the gasification rate of coal are rare. None were found which were of the same quality as most of the oxidation data. Nevertheless, coefficients based on the scarce existing data are listed in Table 3.5 with no comment, either positively or negatively, about the quality of the data from which they were derived.

3.3.6 Conclusions

The nonlinear nature of the Arrhenius law has been shown to have significant implications on the method of correlating the Arrhenius parameters to data. A derivation has been presented which traces a rigorous data analysis technique to fundamental features of the data being correlated while preserving as many desirable statistical properties as possible. The resulting method of data analysis differs substantially from that most commonly used to correlate data with the Arrhenius law.

The common approach to correlating data with the Arrhenius law compromises both the fit of the data within the temperature range over which it is measured and the extrapolation of the results outside of this range. In general, the more common approach overemphasizes the low temperature data in determining the parameters for the Arrhenius expression. This biasing

Table 3.5: Arrhenius Parameters for Predicting the Heterogeneous Reaction Rates of Various Ranks of Coal with Various Oxidizers.

$$\frac{dq_n}{dt} = AT^n_{exp}(-E/RT)\ [oxidizer]$$

Oxidizer	Rank	Reference	n	A ($m/K^n s$)	E (J/kmol)
O_2 *	all ranks	This Study	1.0	2.30	9.29×10^7
	all ranks	Field, et. al., 1967	1.0	0.30	1.49×10^8
	hv Bituminous A	This Study	1.0	1.03	7.49×10^7
	hv Bituminous C	"	1.0	0.479	5.25×10^7
	Subbituminous C	"	1.0	10.4	9.31×10^7
	hv Bituminous A	Goetz, et. al., 1982	1.0	2.25	8.52×10^7
	hv Bituminous C	"	1.0	2.02	7.18×10^7
	Subbituminous C	"	1.0	4.96	8.36×10^7
CO_2	Lignite	This Study	1.0	3.419	1.30×10^8
	hv Bituminous A	"	1.0	1160.0	$2.59. \times 10^8$
	hv Bituminous C	"	1.0	4890.0	2.60×10^8
	Subbituminous C	"	1.0	6188.0	2.40×10^8
	Lignite	Goetz, et al., 1982	1.0	45.0	1.65×10^8
	hv Bituminous A	"	1.0	95.14	2.25×10^8
	hv Bituminous C	"	1.0	88.5	2.36×10^8
	Subbituminous C	"	1.0	70.95	1.78×10^8
	Graphite	Mayers, 1934	1.0	4.40	1.62×10^8
H_2O	Graphite	Mayers, 1934	1.0	1.33	1.47×10^8
	Lignite	Otto, et al., 1979	1.0	4.26×10^4	3.16×10^8
	Lignite	"	1.0	208	2.40×10^8

*Recommended good estimate if no data are available.

toward the low temperature data and the inability of the common approach to produce parameters with desirable statistical properties has the potential of producing correlations so poor that the Arrhenius law would incorrectly be rejected as the proper fit of the data. This poor correlation of the data is amplified when the Arrhenius law is extrapolated beyond the range of the data on which its parameters are based.

The parameters determined from the common approach can lie well outside of high-confidence contours for the true (population) parameters. A rigorous analysis of these contours shows that they are not simple rectangles, as implied by stating their extreme values. They also are not elliptical, as would be predicted from an extension of techniques used in analyzing linear equations. They are slender loops which illustrate both the nonlinearity of the equation and the correlation of the parameters with each other.

A reexamination of many sets of heterogeneous reaction rate data shows that features of past comparisons of trends have been inappropriately interpreted as decreases in char reactivity at high temperatures when, in fact, they are artifacts of data analysis. Reanalysis of several sets of data have been completed with the more rigorous approach.

3.4 Turbulent Dispersion of Particles

3.4.1 Introduction

Many practical combustion processes which use solid particles, liquid droplets, or slurries as fuels introduce these fuels into turbulent environments. Examples include spray combustion, pulverized coal and coal slurry combustion, fluidized beds, sorbent injection, and hazardous waste incineration. The interactions of the condensed phases with the turbulent environment have not been well described. Such a description is complicated by the difficulty of describing turbulence in general, even in the absence of particles or droplets. But the complications in describing the dispersion and reaction of the condensed phases in turbulent environments do not stem entirely or even primarily from the uncertainties in the description of the turbulence. Theoretical descriptions of the turbulent dispersion of particles and droplets are not well established, even when the characteristics of the turbulence are known.

Several reviews of turbulent particle dispersion document the progress in this area of research to date. Faeth(1983) provides a review of mixing and transport in turbulent spray environments. Other discussions of some of the aspects of turbulent dispersion of particles are developed by Kuo(1986), Hinze(1975), Goldschmidt, et al. (1972), Lumley(1978), Chigier(1976), Lilly(1973), Crowe(1982), and Smith and Baxter(1986). In terms of an analytical and comprehensive description of turbulent dispersion, Shuen, et al. (1983) have shown modifications of a model originally proposed by Gosman and Ioannides(1981) which yields reasonably good predictions in a variety of flows and may be the most rigorous technique currently available. The approach, called a stochastic separated flow (SSF) model, is essentially a Monte-Carlo simulation of the particle flowfield. Several thousand trajectories are typically used to compute the overall particle or droplet behavior. The success of this approach is also strongly dependent on a rather arbitrary choice of methods of evaluating its parameters (Shuen, et al. (1983). Other approaches, which are both less computationally intensive and less rigorous, are discussed by Smith and Baxter(1986) and Fletcher(1980) The success of these models also depends on the accuracy of modeled terms. A truly fundamental description of turbulent dispersion cast in a computationally efficient form has not yet been documented in the literature.

The following discussion of this task presents a different description of the turbulent dispersion of particles than those mentioned above which is both fundamental and computationally efficient. Although the approach is different, many aspects of the underlying theory are not new, being founded in the works of Taylor(1922), Langevin(1908), and Chandrasekhar(1943). It is essentially a first principles description of the turbulent dispersion of particles. If the turbulent flow field is well characterized, the model predicts such elusive phenomena as counter gradient diffusion and time dependent diffusivities, both of which have been experimentally observed. It is also computationally efficient. The model has been incorporated into a comprehensive code and has reduced the time involved to obtain overall convergence. The general approach can also be applied to other challenging issues, such as turbulence and chemistry interactions and dispersion in fluidized beds.

The following discussion of this task derives the turbulent dispersion model, compares its predictions with exact solutions, alternative models, and experimental data, and illustrates the incorporation of the model into a comprehensive computer code.

3.4.2 Theoretical Derivation

The description of turbulent disperion of particles given here is to model the evolution of a probability density function(pdf) for particle position in a Lagrangian reference frame. The parameters used to describe the evolution of this pdf are calculated from inherent properties of the turbulence and the particles and are independent of the specific method of determining or predicting the turbulence.

The terms in the equations used to describe this model generally are first and second order tensors. The tensorial nature of the equations follows directly from a scalar derivation. To avoid confusing nomenclature, most of the derivation will deal only with these scalar quantities.

The customary decomposition of particle position and velocity into their mean and fluctuating components is used here, with the fluctuating components designated with primes and the mean values designated with angled brackets. The decompositions are ensemble decompositions, as opposed to conventional time (Reynolds) or mass-weighted (Favre) decompositions.

The rate at which an initially concentrated group of fluid particles disperses in a homogeneous turbulent flow field, with no gradient in mean or turbulent properties, was first developed in a series of articles by Taylor(1921,1932,1935,1938), which have since been cited and generalized by several authors, Hinze(1975), Tennekes and Lumley(1972), Kampe de Feriet(1939,1948), Batchelor(1957), Monin and Yaglom(1971), and Csanady(1973), giving particularly relevant discussions. The method, sometimes called Taylor's theorem, plays a central role in this model and the key results are presented here.

The path of an individual particle is given by

$$x_p(t) = \int_0^t u_p(t_1)\, dt_1 + x_p(0)\ , \tag{3.23}$$

where x and u are the the scalar components of the instantaneous particle position and velocity in an arbitrary coordinate direction.

An ensemble average of Equation 3.23 yields a method of predicting the time evolution of the expected value, $\langle x(t) \rangle$, of the pdf for the position of the particle ensemble in a Lagrangian reference frame in terms of the average

particle velocity, $\langle u(t) \rangle$. This averaging process is an arithmetic procedure which commutes with integration. Here it operates on the integrand to yield

$$\langle x_p(t) \rangle = \int_0^t \langle u_p(t_1) \rangle \, dt_1 + \langle x_p(0) \rangle = \mu_x \, . \tag{3.24}$$

In the application to turbulent particle dispersion, the mean particle velocity, $\langle u_p(t) \rangle$, must be related to the mean gas velocity. If the particle Reynolds number is in the Stokes regime, this relationship can be derived from ensemble averaging the particle equation of motion. The formal development would include the virtual-mass, Bassett, jetting, and static pressure gradient terms. Baxter(1989) shows that these terms could be rigorously included and related to ensemble average velocities. These terms rarely have a significant impact on the results, however, and will be neglected in the following equations. Therefore, the scalar equation of motion for particles becomes

$$\frac{d \langle u_p \rangle}{dt} = \beta \Delta \langle u \rangle + g \, , \tag{3.25}$$

where $\Delta \langle u \rangle$ represents the difference between the ensemble mean gas and particle velocities and g is the component of the acceleration of gravity in this coordinate direction. If the particle Reynolds number is not in the Stokes regime, an analytical function could still be formulated for the relationship between the mean particle and gas velocities. In the practical applications illustrated in this paper, the particles are small and well within the Stokes regime.

Equation 3.25 predicts the relationship between the mean particle and gas velocities, which is used in Equation 3.24 to predict the expected value of the pdf for the particle ensemble position. Neither equation is appropriate for describing individual particle ballistics.

The second moment, or variance, of the pdf for particle position can be similarly derived. The variance primarily describes the dispersion of the particle ensemble, whereas the mean value primarily describes the bulk transport.

The time derivative of the mean-square displacement of an ensemble of particles with respect to their mean position is found by squaring Equation 3.23 and differentiating the result with respect to time.

$$\frac{dx'^2_p}{dt} = 2x'_p \frac{dx'_p}{dt} = 2 \int_0^t u'_p(t) u'_p(t_1) \, dt_1 \, . \tag{3.26}$$

The velocity $u'_p(t)$ can be taken inside the integral because the integration is with respect to the variable t_1 rather than t. Only the limits of integration refer to t. Ensemble averaging Equation 3.26 yields

$$\frac{d\left\langle x'^2_p\right\rangle}{dt} \equiv \frac{d\sigma_x^2}{dt} = 2\int_0^t \left\langle u'_p(t)u'_p(t_1)\right\rangle dt_1 \tag{3.27}$$

where σ_x^2 is the variance. This result can be cast in terms of more classical turbulence properties by defining a generalization of the Lagrangian autocorrelation function for the particles as

$$R_p^L(t,\tau) \equiv \frac{\left\langle u'_p(t)u'_p(t+\tau)\right\rangle}{\left\langle u'^2_p(t)\right\rangle} . \tag{3.28}$$

This definition simplifies to the classical definition of the Lagrangian autocorrelation function and R_p^L becomes a function of τ only if the flow is stationary and homogenous. The functional form of the autocorrelation coefficient will be discussed later.

Substituting Equation 3.28 into Equation 3.27 and integrating with respect to time yields

$$\sigma_x^2(t) = 2\int_0^t \int_0^{t_1} \left\langle u'^2(t_1)\right\rangle R_p^L(t_1,\tau)\, dt_1\, d\tau \tag{3.29}$$

or, an equivalent form which follows by partial integration if all variables are stationary and was first derived by Kampe de Feriet (1939,1948)

$$\sigma_x^2 = 2\left\langle u'^2_p\right\rangle \int_0^t (t-\tau) R_p^L(\tau)\, d\tau . \tag{3.30}$$

The tensorial derivation of these relationships is analogous to the above derivation in every respect. The results of the derivation are given here in standard indicial notation. The tensorial Lagrangian autocorrelation function for the particle ensemble is defined by

$$R_{ij}^L(t_1,t_2) \equiv \frac{\langle u'_i(t_1)u'_j(t_2)\rangle}{\left[\left\langle u'^2_i(t_1)\right\rangle \left\langle u'^2_j(t_2)\right\rangle\right]^{1/2}} \tag{3.31}$$

where the subscript p is implied but has been dropped and the covariance tensor (matrix) is

$$\sigma_{ij}(t) = \int_0^t \int_0^{t_2} \left[\left\langle u_i'^2(t_1)\right\rangle \left\langle u_j'^2(t_2)\right\rangle\right]^{1/2} \left[R_{ij}^L(t_1,t_2) + R_{ji}^L(t_1,t_2)\right] dt_1\, dt_2 \quad (3.32)$$

Equation 3.32 can be rewritten, through partial integration and by assuming all variables are stationary, as

$$\sigma_{ij}(t) = 2\left[\left\langle u_i'^2\right\rangle \left\langle u_j'^2\right\rangle\right]^{1/2} \int_0^t (t-\tau) R_{ij}^L(\tau) d\tau \ . \quad (3.33)$$

These general forms of the equations were first derived from Batchelor(1957).

The mean-square fluctuations of the particle velocity, $\left\langle u_p'^2\right\rangle$, are required to compute the variances in the specific application of the turbulent dispersion of particles. When the particle concentration is small, the particle velocity fluctuations are driven by the gas velocity fluctuations. Under these assumptions, an approximate relationship between the fluctuations is

$$\left\langle u_p'^2\right\rangle = \left\langle u_g'^2\right\rangle (1 - e^{-\beta\tau_g}) \ , \quad (3.34)$$

where β is related to the particle drag coefficient, as shown in Equation 3.25, and τ_g is a characteristic time scale of the gas turbulence, as discussed later.

Higher order moments of the pdf for particle position could similarly be calculated. In the limit of stationary, homogeneous flows, a first principles analysis shows that these moments describe a multivariate normal distribution (Baxter,1989). These normal distributions have long been verified experimentally in flows, even when the flow has some gradient in mean or turbulent properties (Kalinske and Pien,1944). If the flow has some gradient in mean or turbulent properties, the distributions can become skewed. The direction of skewness in passive turbulent diffusion is somewhat dubious, having been both predicted and measured to be both toward the high and low velocity regions, depending on detailed properties of the turbulence (Hinze,1975; Okubo, and Karweit,1969). The data typically lie midway between the predictions including skewness and a normal approximation and the necessary detailed turbulence properties to make such predictions are rarely available.

These results apply only to the instantaneous pdf for the position of an ensemble of particles in a Lagrangian reference frame. The total distribution in a steady flow is obtained by integrating the results of the instantaneous

distributions with respect to time in the Eulerian computational domain. The overall flow field affects the prediction for total mean particle number density and other particle properties such that they may bear little resemblance to the instantaneous pdfs or to each other.

The description of particle dispersion in turbulent environments is now complete, with the exception of the necessary description of the turbulence itself. Evaluations of this model will be illustrated in which it has been compared with exact solutions, results of other stochastic models, experimental data, and by incorporation into a full combustor simulation. In the cases of the exact solutions and comparisons with other stochastic models, the turbulence properties were predetermined. In the comparison with experimental results, most of the necessary turbulence properties were measured with the particle dispersion data. The functional form of the autocorrelation functions was derived from the Markovian approximation in the general theory of stochastic processes (Ethier and Kurtz,1986), as given below. In the full combustor simulations, the turbulence properties were predicted from the results of a k-ϵ turbulence model combined with this Markovian approximation. The Markovian approximation and k-ϵ parameters used in these simulations are described below.

The Markovian approximation to stochastic processes assumes that the fluctuations of the random variables are independent and instantaneous. In this approximation, the Lagrangian autocorrelation function becomes

$$R_p^L(\tau) = e^{-\tau/\mathcal{L}_\tau}, \tag{3.35}$$

where $\mathcal{L}_\tau$ is the Lagrangian integral time constant. This time constant can be approximated from k-ϵ parameters and particle properties as

$$\mathcal{L}_\tau = max(\tau_g, \beta), \tag{3.36}$$

where β is given in Eq. 14 and τ_g is calculated from k-ϵ parameters as

$$\tau_g = \frac{C_\mu^{3/4} k^{3/2}}{\epsilon(2/3k)^{1/2}} \tag{3.37}$$

The above relationship for τ_g is based on three independent results: a theoretical analysis by Corrsin(1963) and two modeling calibrations (Shuen, et al., 1938; Gosman and Ioannides,1981). The results from the $k-\varepsilon$ model were

used to calculate mean-square velocity fluctuations, which were assumed to be isotropic, according to

$$u_i'^2 = (2/3)k. \tag{3.38}$$

This mean-square velocity, which is a Favre-averaged property in most implementations of the k-ϵ turbulence model, is assumed to be the same as the ensemble averaged mean-square velocity. This assumption of ergodicity is a strict formality, since the accuracy of the turbulence model falls short of being able to distinguish between Favre, Reynolds, and ensemble averages.

The largest errors in this approach to predicting the turbulent dispersion of particles come from the inaccuracies in the turbulence properties available from current turbulence models. Although the above approximations have some theoretical and empirical foundation, they clearly are inadequate in many ways as full descriptions. Nevertheless, they have performed quite well in the evaluations of the model.

3.4.3 Results

This approach to describing the turbulent dispersion of particles has been compared to exact solutions for hypothetical systems. These exact results are invariably for highly simplified systems which neglect many important and interesting effects of real systems. The most common exact solution used for comparison is that of one-dimensional, homogeneous, steady flow with dispersion characterized by a constant effective diffusivity. In terms of the fundamental equations derived above, this corresponds to assuming that the Lagrangian autocorrelation function is a delta function with an area of $\mathcal{L}_\tau$ and that the mean-square velocity is given by

$$\overline{u_p'^2} = D/\mathcal{L}_\tau, \tag{3.39}$$

where D is the specified effective turbulent diffusivity.

This approach to turbulent particle dispersion reproduces the original exact solution. That is, the concentration profile in the cross-stream direction is normally distributed with a variance which increases proportional to time or distance and is identical in every detail to the solution of the classical one-dimensional diffusion equation. In a numerical simulation, the numerical solution is obtained with a single time integration of Equations 3.24 and 3.33.

This exact solution has also been used to evaluate other dispersion models. The models chosen for comparison here are two different implementations of the SSF model discussed in the introduction. The exact solution just discussed was used to calibrate the models. The computations for the two SSF models were performed and reported by others (Shuen, et al., 1938; Gosman and Ioannides,1981). As discussed, these two models differ only in the choice of the time constant used in the simulation. The SSF model produces results close to the exact solution when the parameters are appropriately calibrated. Between 2000 and 5000 individual particle simulations were required to generate the results illustrated.

By comparison, the approach described here reproduces the exact result precisely, requires no calibration, and is much more efficient. The numerical effort in this pdf simulation is roughly equivalent to that involved in a single particle trajectory simulation in the SSF model. Similar improvements in efficiency with respect to other dispersion models will be discussed later in this paper in conjunction with the comprehensive reactor simulations.

The simplifications required to obtain the exact solution shown above neglect many important aspects of turbulent dispersion of particles. Specifically, the early portion of the dispersion process of an initially concentrated group of particles cannot be characterized with a constant effective diffusivity. The diffusivity must show an explicit time dependence, varying from zero to an ultimate constant value. In turbulent systems, the variation is not necessarily monotonic and the diffusivity may become negative. All of these trends are predicted in this approach to turbulent dispersion of particles and are discussed by Baxter(1989). A set of data which illustrate some of these trends is used to further evaluate this approach to describing the turbulent particle dispersion.

Figure 3.15 illustrates an experimentally measured time dependence of effective turbulent diffusivity in terms of a pdf variance. The experiment involved dispersion of chlorinated hydrocarbons in water. Data were collected under nine different geometric and flow conditions. Each data point in the figure is calculated by measuring the radial profile of concentration and characterizing the profile, which was normal, with a variance. The figure illustrates how this variance increases, the derivative of the increase varying from zero to a constant value. The data have been normalized such that all nine cases fall on the same line.

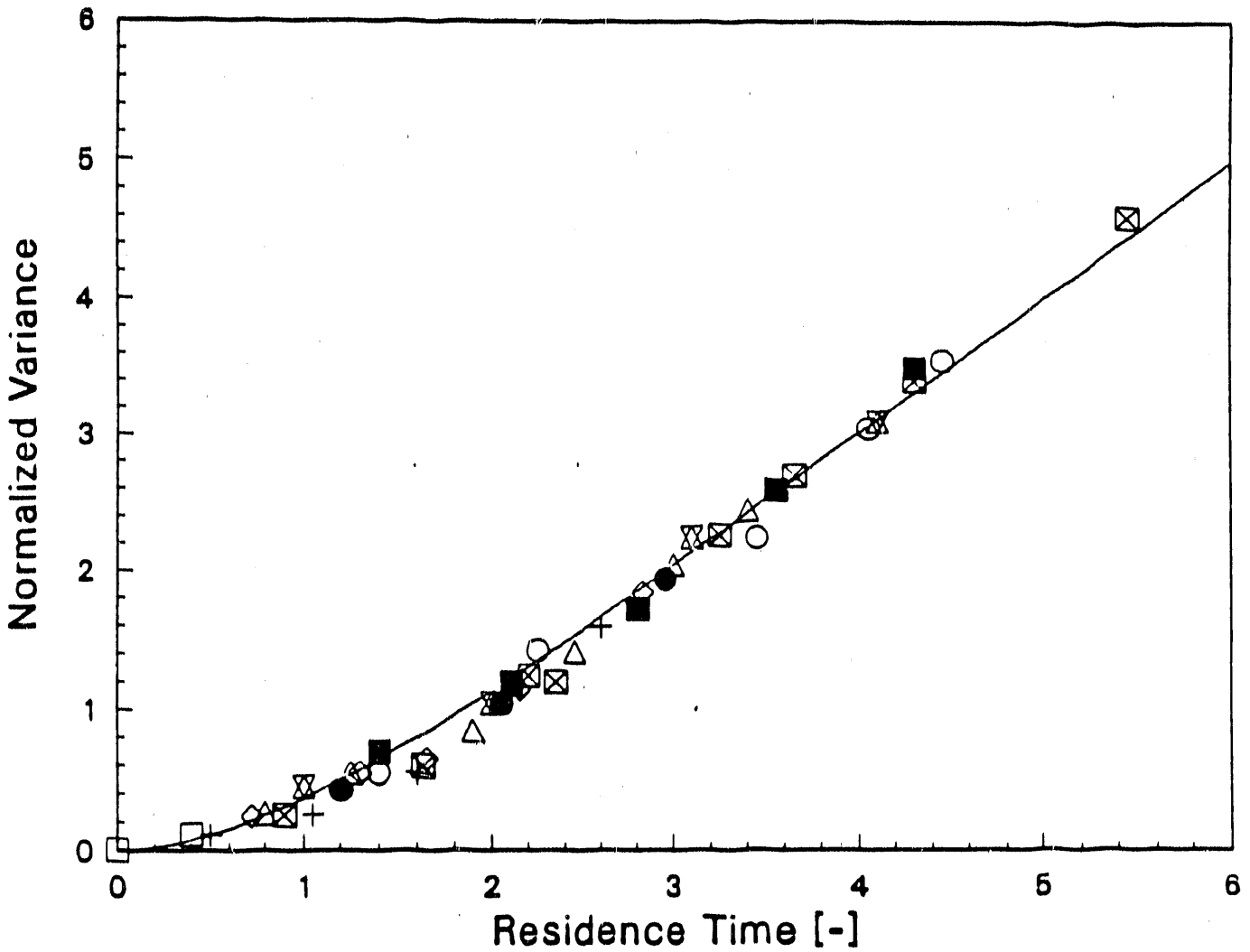

Figure 3.15: Comparison of the Turbulent Dispersion Model with Experimental Data. The Data are Derived from a Paper by Kalinske and Pien (1944).

The method of predicting particle dispersion discussed above does not involve either turbulent diffusivities or concentration gradients. Diffusivities can be calculated from the results of the method, however, by computing the predicted concentration gradients and fluxes and calculating the diffusion coefficient necessary to relate them through Fick's law. These diffusivities are proportional to the time derivative of the variance. The equations involved can be dedimensionalized and, if the autocorrelation function is known, the time dependence of the diffusivity can be computed numerically or, in this and some other cases, analytically. None of these analyses requires introduction of arbitrary parameters. The line in Figure 3.15 represents the results of the predictions. It falls within the inherent error of the data and precisely predicts the time dependent portion of the curve.

The Markovian autocorrelation function was used to make these predictions. This autocorrelation function was derived from the theory of stochastic processes, independently of the dispersion model. Several alternative and arbitrary autocorrelation functions were also investigated and none performed as well, even when they were augmented with tunable parameters. The Markovian autocorrelation function included no tunable parameters. The autocorrelation function is, in general, a property of the turbulence and independent of the dispersion process. An *a priori* specification of the autocorrelation function is not available in general. The Markovian approximation is least subject to error in strong turbulence with no coherent structures but should not be expected to apply to all turbulent flows.

This dispersion model has also been incorporated in and used as the framework for the particle calculations in the comprehensive, axi-symmetric combustion code (Smoot and Smith, 1985). By way of evaluation, the results of comprehensive predictions from PCGC-2, using the original particle dispersion model and this particle dispersion model are illustrated here. Figure 3.16 illustrates the previous solution of the reacting flow environment in an axi-symmetric pulverized coal combustor. The flow field is complex, including swirl, recirculation zones, large gradient in properties, etc. In general, the flow is from left to right in the contour plot, with the top, bottom, and right side of the contour plot representing the reactor wall, centerline, and exit, respectively. The left side of the contour plot includes the coal injection point in a primary duct at the centerline, a secondary air injection annulus, and a quarl extending from the edge of the secondary stream to the wall. Two views of the temperature field are also shown as three-dimensional projections. The projection on the left is in the direction of the flow from a point

upstream of the reactor. The reactor quarl and the primary, and secondary injection points are seen in the nearest edge of this projection. The right, left, and far sides of the projection represent the reactor centerline, wall, and exit, respectively. The projection on the right corresponds to a 180 degree rotation of the projection on the left in the plane of the coordinate axes. The reactor exit, centerline, wall, and inlets are found on the near, right, left and far sides of the view on the right.

The turbulent dispersion model used in this prediction is based on the concept of a turbulent particle diffusivity. The parameters of the model have been calibrated by comparison to data and the model yields reasonable results in most cases. The model is discussed in more detail by Fletcher(1980) and Smith and Baxter(1986). A total of 150 particle trajectories were used to obtain the temperature field shown in the figure.

The details of the temperature field include a fuel-rich region near the front and centerline of the reactor, fuel-lean regions near the walls, and a roughly stoichiometric region separating the two. Within each of these regions, details of gradients appear as a result of the mixing and combustion of the coal and coal gases. The flame is slightly lifted off the burner and forms a long, high temperature ridge which reaches deep into the reactor. The ignition point is characterized by a particularly complex temperature pattern, including a rapid temperature rise followed by a rapid temperature decrease due to the fuel-rich cloud effect of the burning particles.

Figure 3.17 illustrates the predictions of the same case using this turbulent dispersion model. The orientation of the contour plot and projections is the same as in Figure 3.16. The ignition point, fuel-rich and fuel-lean regions of the reactor, flame structure, and small details of the temperature profiles within these regions, are predicted with remarkable similarity to the previous case. The jagged temperature profile at the ignition point of the previous prediction has been smoothed to a more plausible shape in this prediction.

The temperature field illustrated in Figure 3.16 required 150 particle simulations, whereas the temperature field illustrated in Figure 3.17 required one. The 150 particle simulations used in the previous figure included a total of 15 different initial particle sizes. The temperature field illustrated in Figure 3.17 was calculated with a single particle pdf simulation and was less sensitive to initial particle size. This explains most of the differences seen in the two figures. Specifically, some of the largest particles did not fully

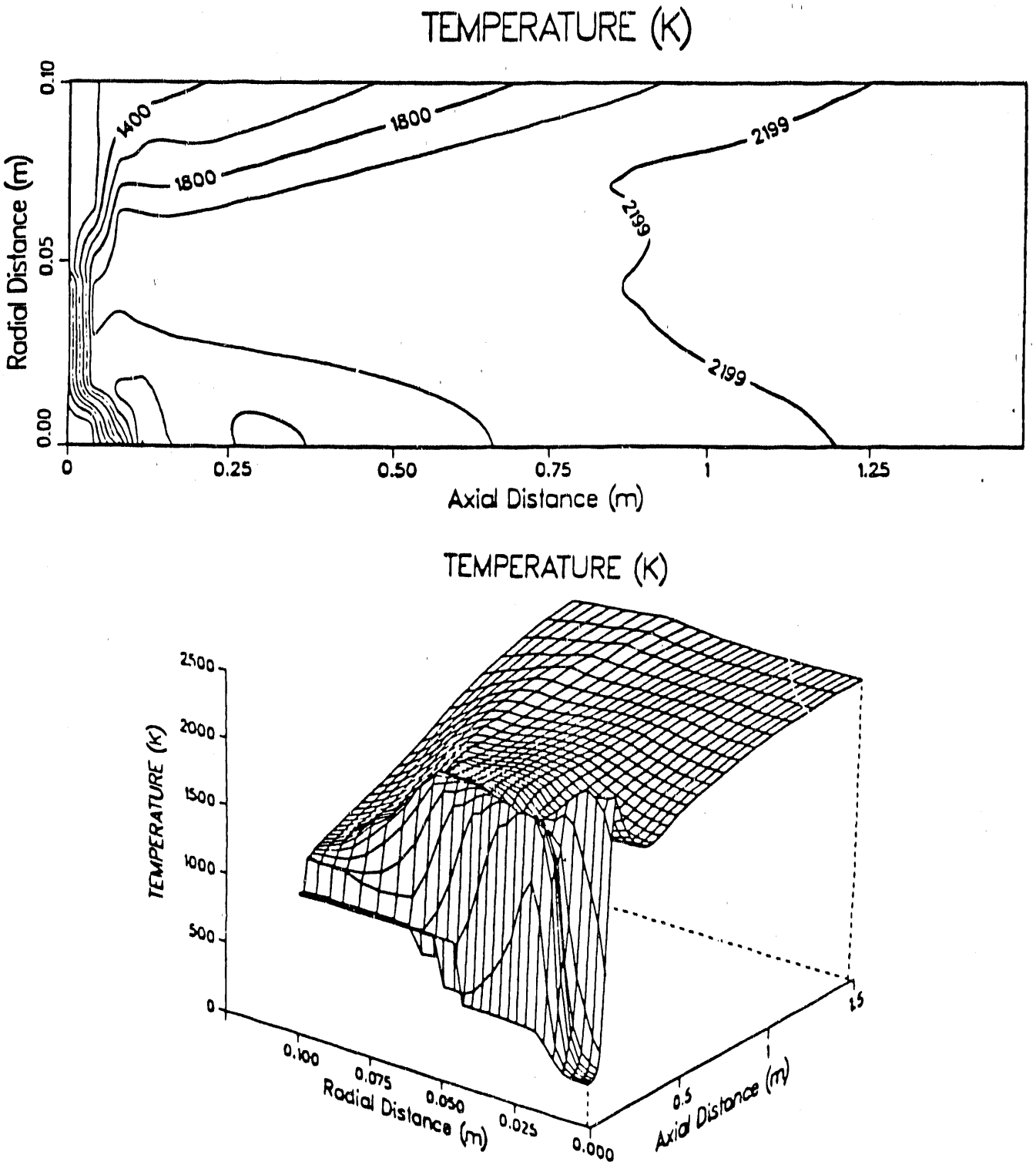

Figure 3.16: A Predicted Temperature Field in a Pulverized Coal Combustor Using the Previous Particle Dispersion Model in PCGC-2.

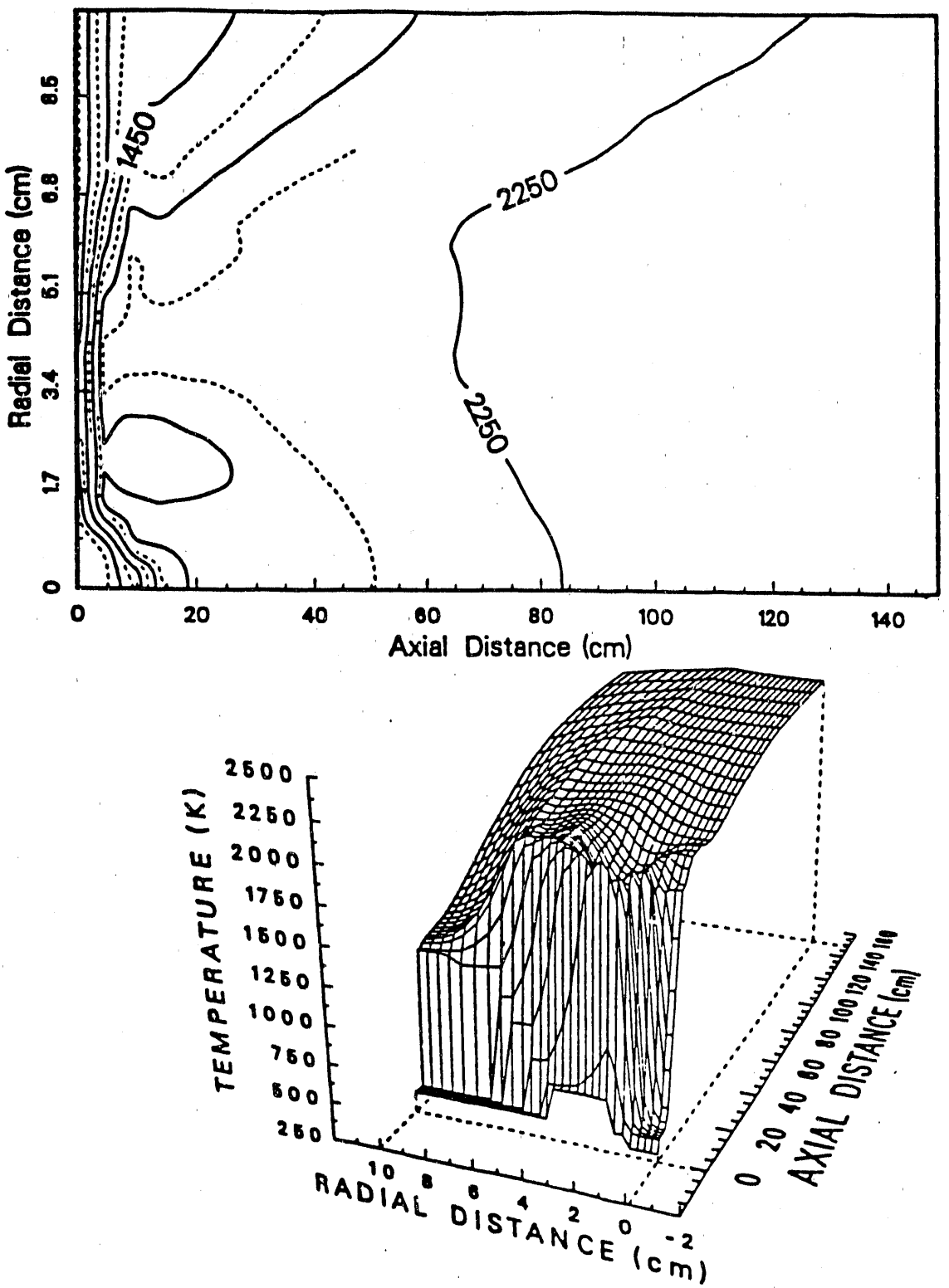

Figure 3.17: A Predicted Temperature Field in a Pulverized Coal Combustor Using the Turbulent Dispersion Model.

burnout in the earlier simulation. The total carbon conversion was higher in the latter simulation, explaining the slightly higher exit temperatures. Also, the smallest particles disperse more quickly than the larger particles, raising the gas temperature in the corner of the reactor near the quarl in the previous simulation. This effect of small particles is also not as pronounced in the latter simulation. Most simulations would be performed with multiple particle pdf simulations; however, far fewer simulations are required with this model than other methods to obtain the same detail in the results.

3.4.4 Conclusions

A first-principles approach to describing particle dispersion is available as an extension of stochastic process modeling and turbulence theory. The model requires no adjustable parameters and is independent of any particular turbulence model. The model does require a description of the turbulent flow field in terms of the mean-square velocities and Lagrangian autocorrelation functions. Approximations for these in terms of parameters from the k-ε model have yielded reasonable results.

This approach has been rigorously evaluated by comparison to exact solutions, the most accurate alternative models, and experimental data. In all cases, the model was both an accurate and efficient method of describing turbulent dispersion. This approach can reproduce the exact solutions either as analytical functions or numerically. Without invoking adjustable parameters, the model yielded more accurate solutions with orders-of-magnitude less computational effort than alternative models. The model predicted the experimental data within its inherent error over a wide range of flow conditions.

The turbulent dispersion model forms a useful framework for comprehensive computer codes. Adjustable parameters need not be used in these formulations. Side by side comparisons of the model performance allows us to conclude that the new approach increases the computational efficiency and robustness of the simulations while decreasing the total number of required particle simulations.

This approach to describing the turbulent transport of particles is fundamental, accurate, and efficient and represents a promising method of both predicting and gaining further insight into the intricacies of the phenomenon.

3.5 Evaluation of the Nitric Oxide Model

3.5.1 Background and Objectives

In order to achieve National Ambient Air Quality Standards set by the Clean Air Act of 1977, much research is currently being done to determine the best technology for reducing nitrogen oxide (NO_x) emissions. Comprehensive theory about the formation, destruction, and modeling of NO is given by Smith, Hill and Smoot (Smith, et al., 1982; Smith, et al., 1986; and Hill, et al., 1984). The work of Hill, et al., included the comparison of measurements with predicted results for pulverized coal combustion. Among other parameters, the effects of swirl, stoichiometric ratio, particle size, and wall temperature were investigated with the average difference for combined predictions of 30 cases being only 24%. However, effects of several variables were not evaluated.

The scope of this subtask was directed toward configurations including coal gasification, coal-water mixture combustion, fuel and air-staging, combustion of coal in other oxidants such as O_2/CO_2 or $O_2/CO_2/Ar$ mixtures, and char combustion. The ability of the code to predict concentrations of NO both at the reactor exit and at local points throughout the combustor, in addition to the trends in NO formation with variation in selected test variables, has been used as criteria for evaluating the model results.

The key objective of this task was to evaluate the potential for use of the submodel to aid in designing and optimizing strategies to minimize nitric oxide emissions in coal furnaces and gasifiers.

3.5.2 Comparison Data

A comprehensive review was conducted to obtain data sources from the open literature for various combustion configurations. Experimental data sources for model comparisons were selected for axi-symmetric combustion experiments that provided adequate information about the reaction geometry and operating conditions and that included the variation of lay test variables (e.g., pressure or stoichiometric ratio, S.R.). Table 3.6 lists the combustion configurations, reactor dimensions, coal types, firing rates, and other parameters for the selected data.

Comparisons of predicted NO concentrations with experimental measurements were made after acceptable agreement for the main stream variables

Table 3.6: Experimental Cases Selected for Model Evaluation. (From Boardman and Smoot [1988]).

Combust. Config.*	Data Sources	No. Cases	Fig. Nos.	Coal Feed Rate kg/h	Reported NO Conc.	Parameters Investigated	Coal
Gasification L = 1.89 m D = 0.2 m	Brown et al. (1986); Nichols et al. (1987); Azuhata et al. (1986)	4	1, 2	35	2-D profile	Press (1–5 atm); temp.	Utah bit.; Ill subbit.; N.D. lig.
Nonstaged	Wendt et al. (1978)	3	3, 4	5	1-D profile	Stoich. ratio (0.8–1.2)	Ken. bit.
Air-staged L = 2.2 m D = 0.15 m	Wendt et al. (1978)	4	5	5	1-D profile	Secondary-air stage location (0.52–0.90 s)	Ken. bit.
CO_2-O_2 Oxidizer L = 2.74 m D = 0.6 m	Berry et al. (1986)	4	6	30–35	Effluent	CO_2-O_2 ratio	Colo. subbit.
Entrained-flow	Pershing (1977)	4	7	5	Effluent	Fuel NO temp. dependence	Colo. subbit.

*L = Reactor length; D = reactor diameter.

was demonstrated. Details regarding accurate prediction of the major species and temperature throughout the reacting flow domain were discussed extensively in the First and Second Annual Progress Reports (Smith and Smoot, 1986, 1987) and will not be reproduced here.

3.5.3 Comparison of NO Predictions with Measurements

Entrained-Flow Gasification

Four simulations of three coal types were completed. Figures 3.18 and 3.19 compare the experimental and theoretical NO concentration profiles for atmospheric and high-pressure (5 atm) gasification of Utah bituminous coal, respectively. Predicted and measured peak NO concentrations are similar in magnitude and location. Predicted concentration contours closely match the experimental maps for the atmospheric case throughout the entire reactor, while the high-pressure case also matches the peak NO value but decays somewhat more slowly. A predicted exit concentration of 100 ppm is approximately 30% below the measured value for the atmospheric pressure case, while the predicted exit value of 4 ppm differs by only 2 ppm from the measured value for the high-pressure case.

These simulations illustrate the capability of the NO_x model to predict NO concentrations for extremely fuel-rich combustion of bituminous coal. The effect of operating pressure is also correctly predicted.

Results for the simulations of Illinois bituminous coal were similar to the Utah bituminous coal. However, for North Dakota lignite, although the major species and flame structure were predicted adequately, Figure 3.20 shows that both the location and magnitude of peak NO concentration were incorrectly predicted. Instead, the predictions resemble those of the bituminous coals. It has been observed that lignites, relative to bituminous coals, produce larger quantities of NH_3 during gasification (Friehaut, et al., 1987). It was also observed in this study that NH_3 concentration measurements for the North Dakota lignite were 200-300% higher than for the Utah and Illinois bituminous coals. Evidence suggests that the initial release of NH_3 and HCN collectively provide an estimate of the amount of nitrogen reduction occuring in the vicinity of the reacting particles (Kramlich, et al., 1987). Available data suggests that the gas-phase fuel-nitrogen reaction sequence is inititated by a rapid and nearly quantitative conversion of the parent fuel nitrogen com-

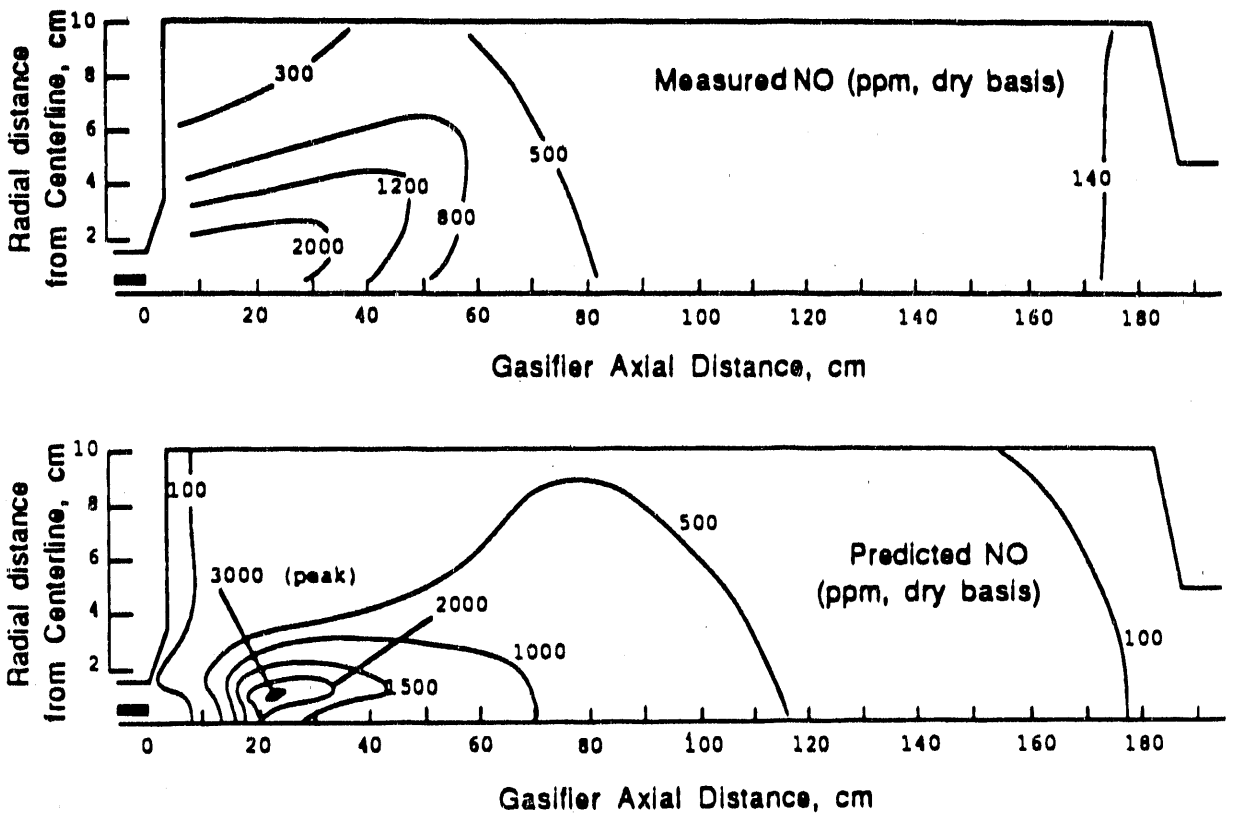

Figure 3.18: NO Concentrations During Atmospheric Gasification of Utah Bituminous Coal. Measured Data of Brown (1986).

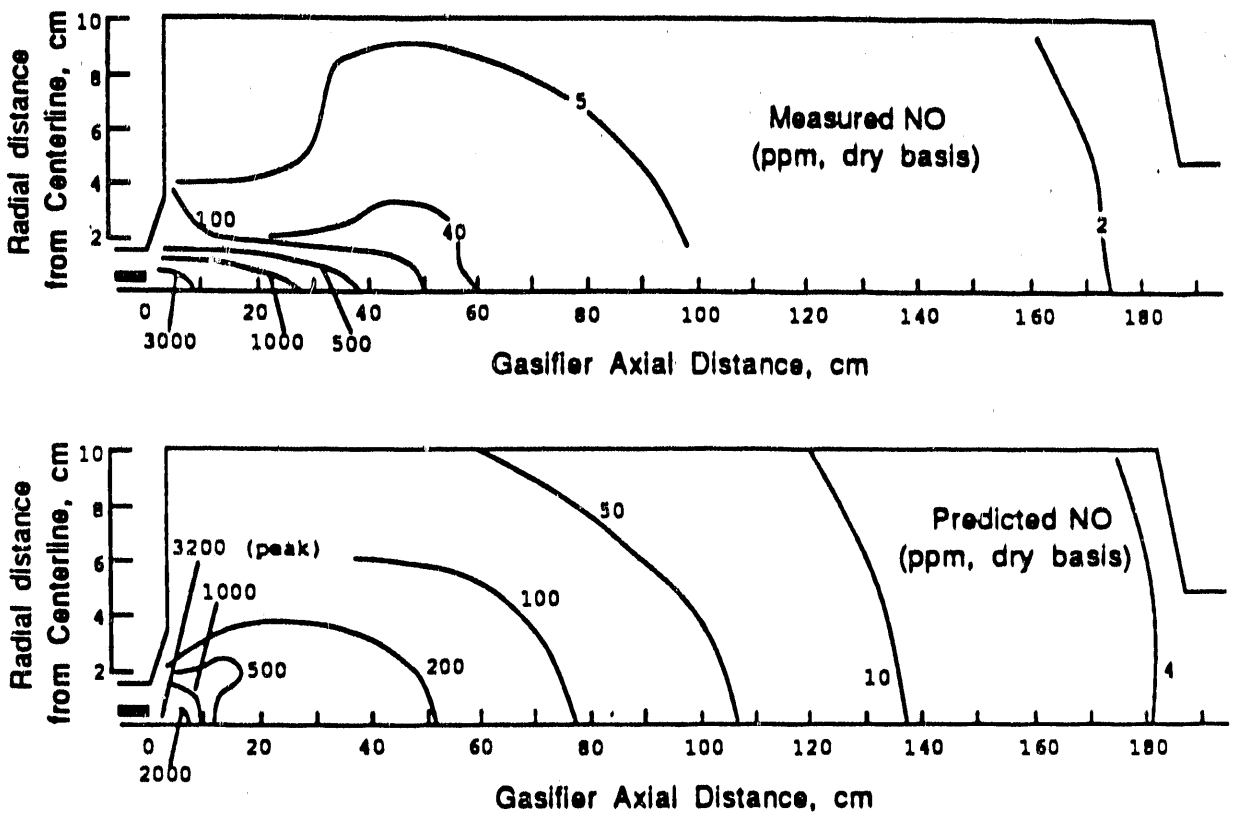

Figure 3.19: NO Concentrations during Pressurized (5 atm) Gasification of Utah Bituminous Coal. Measured Data of Nichols, et al. (1987).

pounds to hydrogen cyanide and ammonia. HCN appears to be the principal product when the fuel nitrogen is bound in an aromatic ring while NH_3 is the principal product when the fuel nitrogen is bound with amines (Axworthy and Dayan, 1977). As coal rank decreases, the number of rings also decreases leading to the conversion of fuel nitrogen to NH_3 rather than HCN. Additionally, the rate of nitrogen release from lignite coal likely does not occur at a rate proportional to total coal mass loss. Since the existing NO_x model mechanism considers only HCN, NO, and O_2 species, the inclusion of NH_3 in the global rate expressions as well as an advanced devolatilization model to predict nitrogen species devolatilization may improve the model for low rank coals simulations. This work is being pursued under independent funding (Boardman, 1989).

Nonstaged, Air-Coal Combustion

Cases were simulated for nonstaged combustion at fuel-lean (SR=1.20), near stoichiometric ratio (SR=0.95), and fuel-rich (SR=0.80) conditions. The measured data and predicted profiles are compared in Figure 3.21 for each case. For the fuel-lean case, a high peak NO concentration is predicted initially but the profile rapidly decays to approximately 8% above the experimental profile. A similar trend is predicted for the SR=0.95 case except that the NO profile decays to a level 10-15% below the measured data. The predicted NO concentrations also follow this trend for the SR=0.80 case but are consistently lower by 15-30% along the entire profile. The discrepancies between the measured and predicted NO concentrations in the early region of the reactor may be due to nonisokinetic sampling. The model predictions showed steep radial gradients in the early subsection of the reactor. In fact, the NO concentration profile predicted near the wall closely matched the experimental data throughout the entire reactor, including the early reactor region. A separate explanation for this discrepancy may be a result of assuming that fuel nitrogen is evolved at a rate proportional to the total coal mass loss.

Wendt (1980) found that at low temperature the early volatiles are nitrogen free. If the rate of nitrogen release is lower than the rate of total coal mass loss, then the model would overpredict the formation of NO in the near-burner region. Figure 3.22 compares the theoretical and experimental effluent NO concentrations over the range of stoichiometric ratios

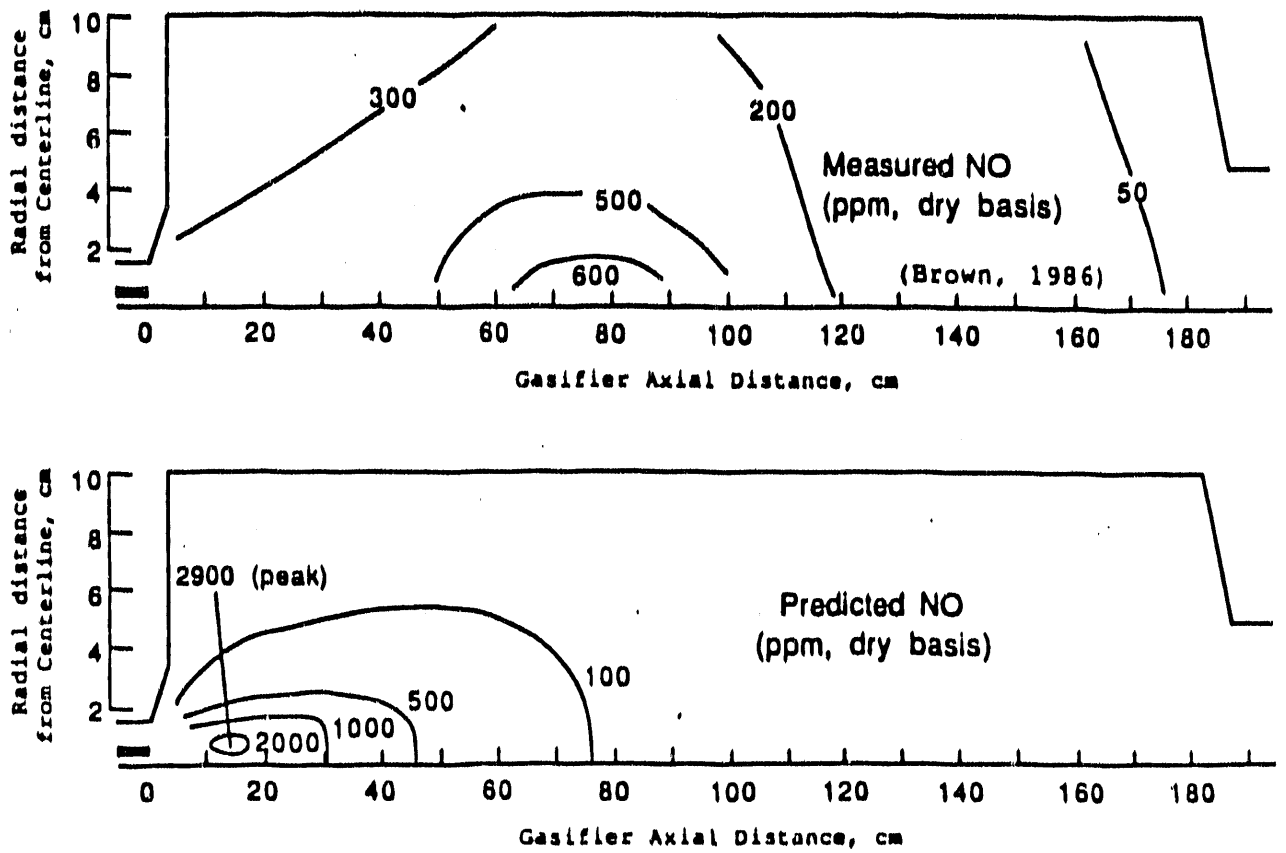

Figure 3.20: Comparison of Predicted and Measured NO Concentrations during Atmospheric Gasification of North Dakota Lignite. Measured Data of Brown (1986).

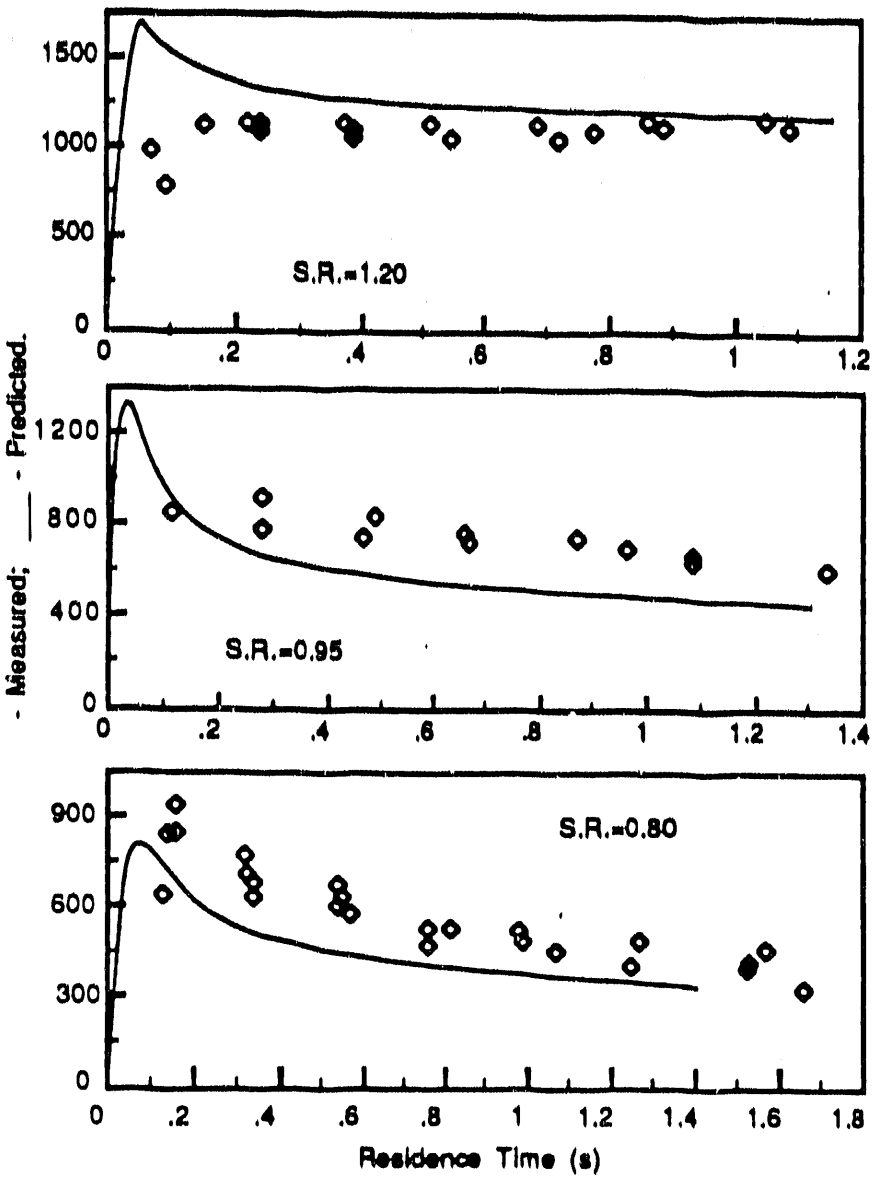

Figure 3.21: NO Centerline Profiles for Three Reactor Stoichiometric Ratios. Measured Data of Wendt, et al. (1978).

shown. The model closely predicts the measured effluent values, suggesting that thermal nitrogen fixation is insignificant in this reactor. Experimentally, it was also determined that thermal NO was neglible for the system (Wendt, et al., 1978). Predictions were also examined to determine the relative difference between the homogeneous and heterogeneous NO reduction. In most fuel-rich locations, where concentration of HCN were appreciable, the heterogeneous decay was found to be insignificant compared to the magnitude of homogeneous NO decay. This result is consistent with the experimental observation (Dannecker and Wendt, 1984) that gas-phase destruction of NO is the dominant NO reduction path in fuel-rich coal combustion.

Air-Staged Combustion

Staged combustion cases were accomplished by injecting additional air downstream from the fuel-rich primary zones. Two simulations each were completed for primary zone SR values of 0.95 and 0.80. The secondary-zone air was injected at axial locations corresponding to residence times of 0.52 and 0.90s, bringing the overall reactor SR to 1.20. It was observed that second-stage NO concentrations were independent of primay zone NO levels (Wendt, et al., 1978); however, effluent NO concentrations were decreased as the first stage was lengthened because of the fast rate of NO decline in the fuel-rich, high-temperature primary zone. Figure 3.23 shows the incremental reduction in NO at the exit for both primary-zone stoichiometric ratios. A difference of about 200 ppm NO was measured between the secondary air stage locations of 0.52 and 0.90 seconds for each case. The predicted difference in NO concentration at the exit closely matches the measured trend.

CO_2-O_2 Oxidizer

A study was conducted to determine the feasibility of producing CO_2 for enhanced oil recovery from combustion of pulverized coal in mixtures of CO_2-O_2 (Berry, et al., 1986). Three cases of pulverized coal combustion in different ratios of CO_2-O_2 oxidizer were compared to an air-combustion case of similar feed rate and heat release. On a common gas volume basis, measured NO concentrations first modestly increase and then decrease as shown in Figure 3.24 . The predictions show little change with CO_2-O_2 mixtures, suggesting that substitution of N_2 with CO_2 in the air would have little impact on

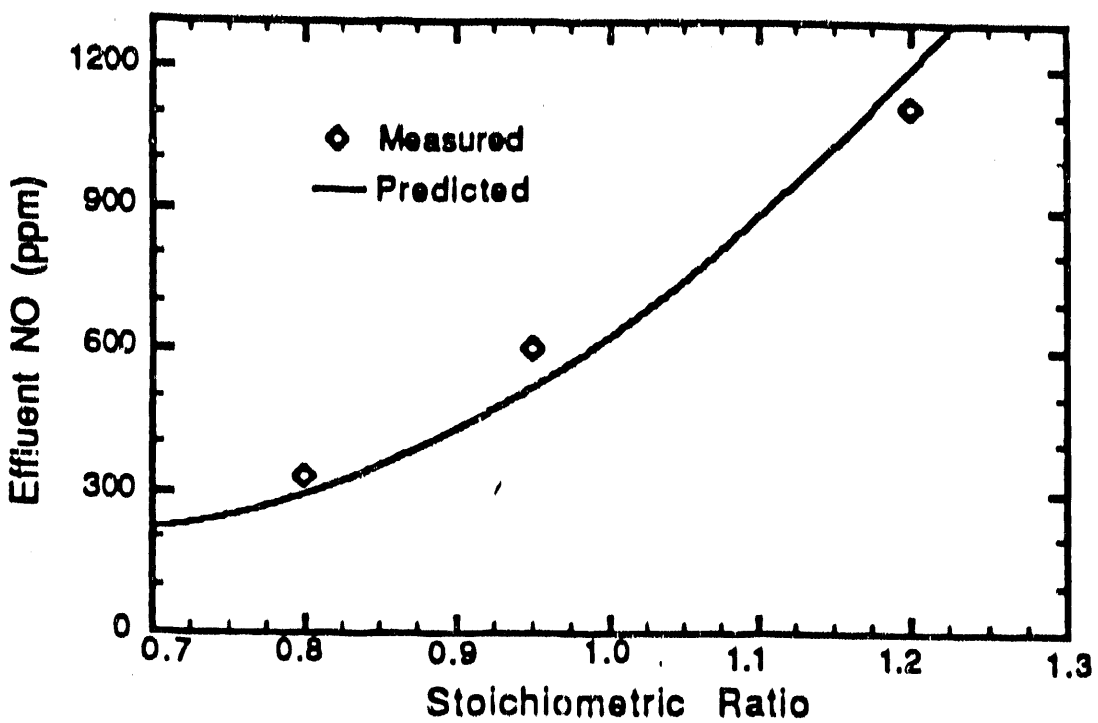

Figure 3.22: Effluent NO Concentrations for Various Reactor Stoichiometric Ratios. Measured Data of Wendt, et al. (1978).

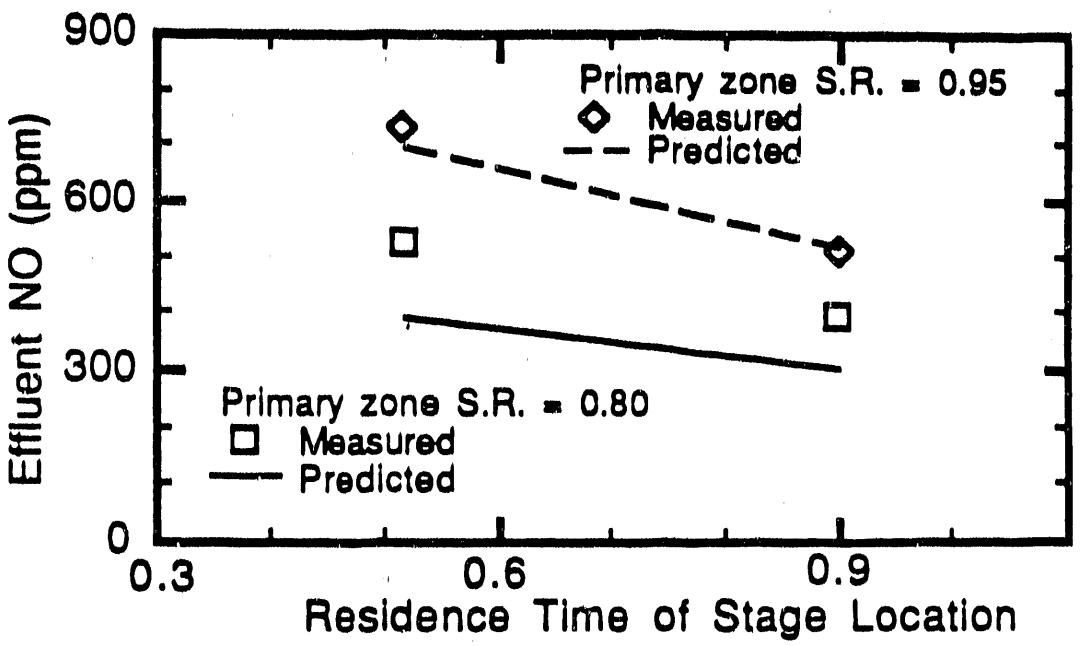

Figure 3.23: Effluent NO Concentrations for Air-Staged Combustion. Measured Data of Wendt, et al. (1978).

fuel-NO concentrations beyond dilution effects. The difference of predicted NO and measured NO is less than 2% for the air-combustion case, while an average of 20% difference was calculated for the three CO_2-O_2 oxidizer ratios.

Fuel-Rich Char Combustion

Simulations for the fuel-rich char combustion of Utah bituminous coal char were completed for stoichiometric ratios of 0.80 and 0.40. Only the last case will be shown here (see Boardman 1987). The experimental combustor used for this work (Glass and Wendt, 1981) is similar in design to the reactor operated by Wendt (1978) for the staged-combustion tests. The central combustor tube has an internal diameter of 0.152 m and a length of 2.15 m. A premixing burner and diverging quarl provide gradual expansion of the air-entrained char particles to approximate one-dimensional flow in the axial direction. Three concentric layers of Zicar vacuum-formed fibrous refractory were added to reduce the heat loss. Thus, the wall and gas phase temperatures are 200-400K hotter than the staged combustor. A char feed rate of approximately 2 kg/hr is consistent with the fuel-rich and staged-combustion feed rates.

Char oxidation represents a unique test for the NO_x submodel because the principal fuel contains only a small volatiles content. The Utah bituminous char was determined to have 6.9% (dry-basis) proximate volatiles (Glass and Wendt, 1981). This leads to a significant reduction in volatile nitrogenous species prior to and during combustion. In the absence of appreciable HCN, significant destruction of NO would be due to heterogeneous reduction of NO by the char surface.

The predicted NO profile shown in Figure 3.25 is lower than the measured data. One possibility of this incorrect result may be attributed to the effects of too high a predicted temperature causing too large a rate of decay. But it should also be noted that in the current NO_x submodel theory, NO is formed only after the nitrogen is released from the char particle and is taken to be proportional to the rate of char devolatilization or oxidation. It has since been shown that NO could also be formed on the char surface by oxidation kinetics and this may contribute to higher NO concentrations within the entire reactor. From FMC char data, Wendt (1979) assumed that nitrogen conversion occured by heterogeneous oxidation. He then fitted correlations to experimental data and suggested that NO is formed more slowly that O_2

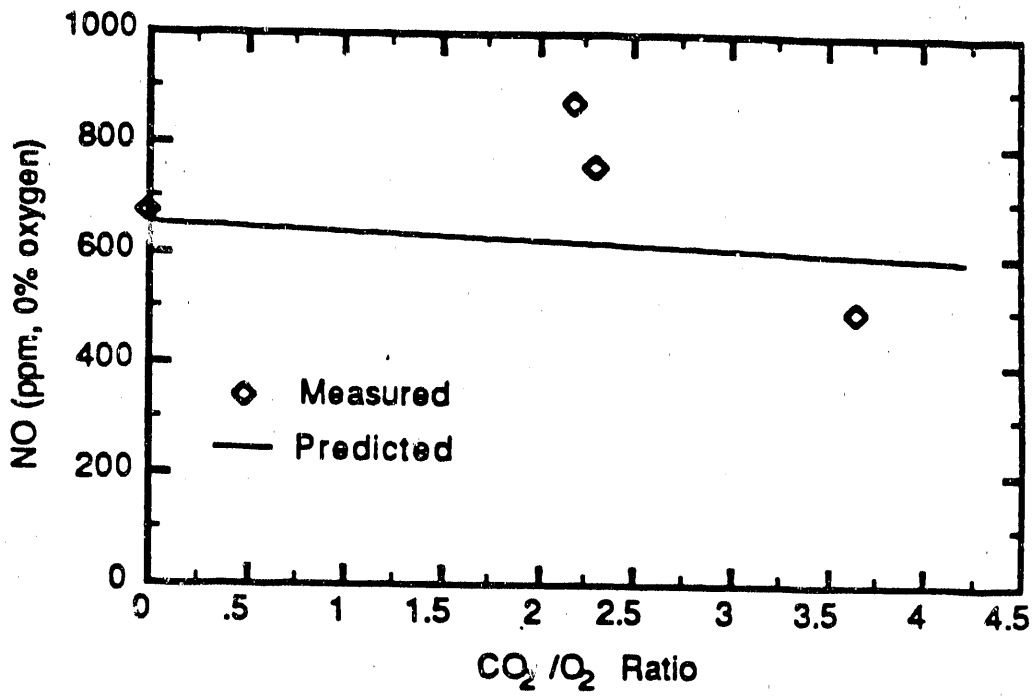

Figure 3.24: Effluent NO Concentrations for Combustion of Pulverized Colorado Bituminous Coal. Measured Data of Berry, et al. (1986).

is consumed. In either case, future work to improve, and possibly extend, the NO_x submodel to predict char-NO production should be undertaken.

Fuel-Staged Combustion

Fuel staging has become a viable NO control stragety. Unfortunately, the simplified mechanism of Smith, et al. (1982) does not adequately account for the recycle of NO and HCN via reaction with hydrocarbons and nitrogen intermediates as postulated by Kramlich, et al. (1987). Thus, no full-staged cases were considered in this study.

Coal-Water Slurry Combustion

During the period that the NO_x submodel was evaluated, PCGC-2 predictions for coal-water slurry combustion were not compatible with the NO_x submodel routine. Consequently, no comparisons were completed to evaluate NO_x submodel performance for this combustion configuration.

Temperature Dependence

From data of fuel-lean (15% excess air) pulverized-coal diffusion flames, fuel NO was observed to be essentially constant over a temperature range up to 2,550 K (Pershing and Wendt, 1977). The NO model predictd similar temperature insensitivity for diffusion-type fuel-lean (15% excess air) pulverized coal combustion, Figure 3.26. The weak dependence of fuel NO on temperature in fuel-lean regions is due to similarities in fuel nitrogen evolution for moderate heating rate conditions for a wide variety of coals (Freihaut, et al., 1987; Blair and Wendt, 1981). In fuel-rich environments, the influence of flame temperature on fuel NO is greater. NO decay can be accelerated by char/NO and fuel-rich species interactions occuring at increased temperature.

Role of Heterogeneous NO Decay

Predictions were examined to determine the relative differences between the homogeneous and heterogeneous NO reduction processes. In most fuel-rich locations, where concentration of HCN were appreciable, the heterogeneous decay was found to be insignificant compared to the magnitude of homogeneous NO decay. This result is consistent with the experimental observation

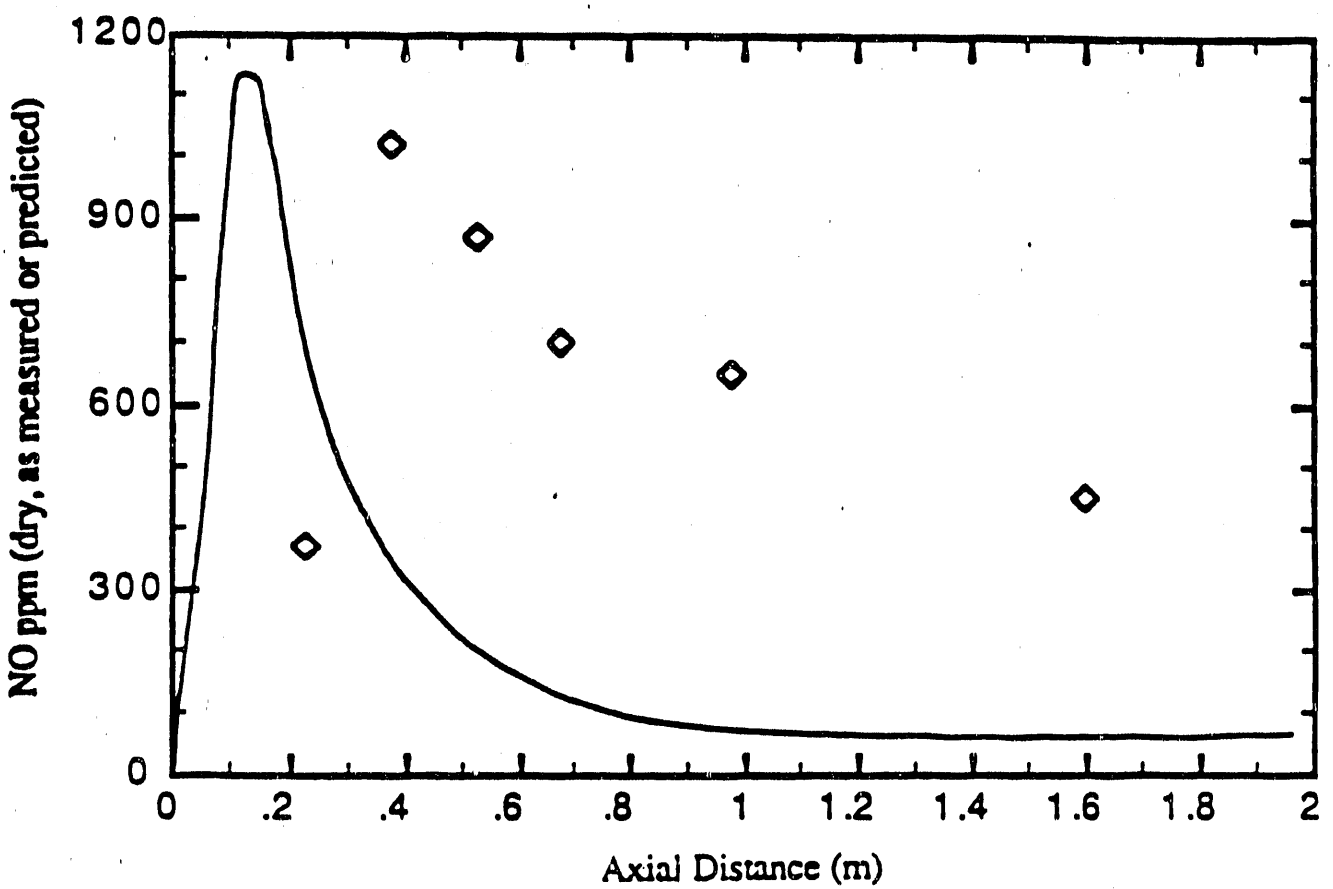

Figure 3.25: Comparison of Predicted NO Profile with Experimental Data of Glass (1981) for the Fuel-Rich Combustion of Pulverized Utah Bituminous Coal Char.

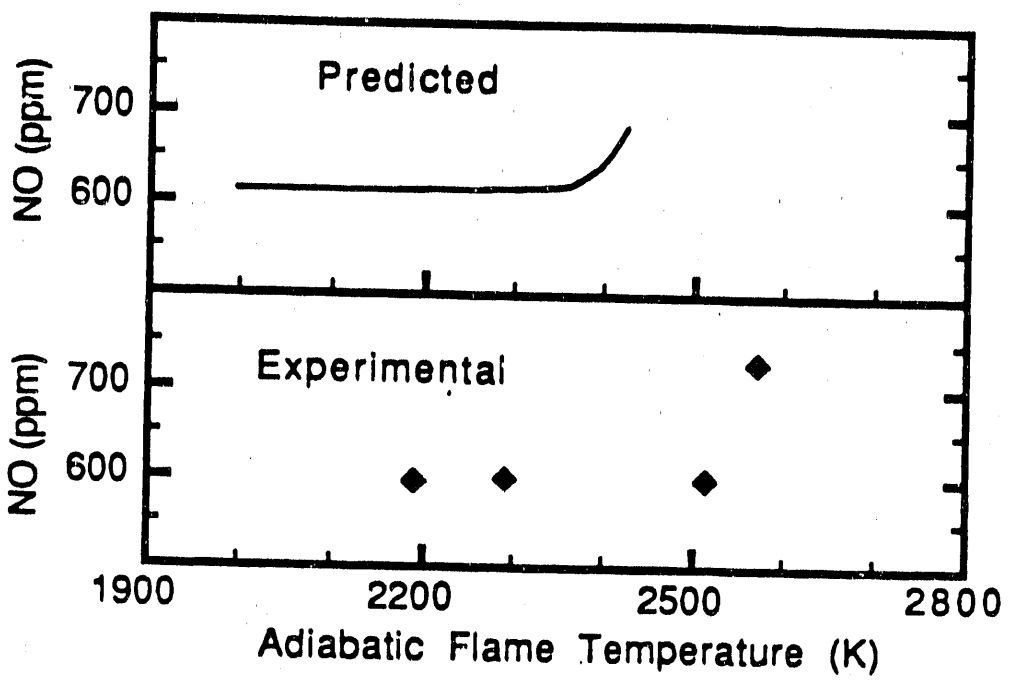

Figure 3.26: Temperature Insensitivity of Effluent NO Concentrations for Fuel-Lean Combustion of Colorado Bituminous Coal. Measured Data of Pershing and Wendt (1977).

(Danneka and Wendt, 1984) that gas-phase destruction of NO is the dominant NO reduction path in fuel-rich coal combustion. Homogeneous decay was far more significant for the gasifier predictions because of the high concentration of fuel-rich species. However, for the non-staged combustion cases, homogeneous decay was only inititally more significant but became relatively less important as the fuel-rich species were consumed. Thus, in the aft section of the combustor, heterogeneous NO decay also became important.

3.5.4 Conclusions

The simulation of these cases, in addition to the extensive predictions made by Hill (1984) provide a further evaluation of the NO_x submodel. In general, it has been shown that the model gives useful results for non-staged pulverized coal combustion under a range of reactor conditions. The success of the NO_x submodel predictions is attributed to the ability of PCGC-2 to model the overall flame structure, an adequate global NO mechanism and kinetic rate expressions, and the coupling of the chemistry reactions with turbulence in the reactor.

Favorable results had earlier been demonstrated for variation of stoichiometric ratio, coal moisture percentage, particle size, swirl number (Hill, 1984), and the substitution of CO_2 for N_2 in the combustion air (Smoot and Smith, 1985). Within the accuracy of the predicted temperature and major species and the range of experimental error, the NO_x submodel provided reliable predictions for pulverized fuel gasification and combustion of bituminous and subbituminous coals at moderate and extreme fuel-rich conditions. The impact of pressure was properly predicted for the gasification of Utah bituminous coal. In separate cases, the location and magnitude of peak NO concentration, iso-concentration locations, and effluent NO level are favorably predicted.

Fuel-rich char oxidation predictions were found to differ substantially from observed effluent concentrations. An investigation suggested that this difference resulted from the effects of temperature and the low volatiles content of the char. Reasonable agreement was demonstrated for variation in primary zone stoichiometric ratio and secondary air staging location for staged-combustion cases in a sub-scale reactor, although the model predicted higher NO concentrations in the early region of the reactor, and lower values at the exit.

The role of temperature in NO decay was found to be significant. This is expected because the kinetic expressions for homogeneous and heterogeneous decay are exponential in temperature. For the gasification cases, the rate and extent of NO decay was highest in the fuel-rich regions where appreciable concentrations of HCN exist. According to the model predictions for these systems, homogeneous NO decay is more significant then heterogeneous decay.

Although predictions could not be made for fuel-reburning in this study because of NO_x submodel limitations, it is expected that the simplified mechanism of the NO_x submodel will not adequately account for the recycle of NO to HCN and NH_i via reaction with hydrocarbons and nitrogen intermediates as postulated by Bartok and Folsom (1987) and Kramlich, et al. (1987). It is also recognized that incorporation of thermal NO formulation would further improve the usefulness of the NO_x submodel for natural gas and fuel oil combustion. This effort has been initiated in an independent investigation.

3.6 Carbon Monoxide Partial Equilibrium Model for Turbulent Coal Combustion

3.6.1 Background

Predicted values from coal combustion codes for carbon monoxide and carbon dioxide contain significant error when compared with values measured experimentally. The concentration of carbon monoxide is used by boiler manufacturers as a measure of the efficiency of the combustion process occurring in the boiler. Accurate CO concentration predictions are therefore especially desirable. Several reasons for this discrepancy have been suggested. These include: incorrect modeling of gaseous mixing, inadequate treatment of energy considerations, poor prediction of heterogeneous reactions such as devolatilization and char oxidation, and the assumption that all major gas species are in equilibrium throughout the reactor. Resolution of this error will help combustion simulations provide better predictions for use in the experimental design of new combustion systems and in determining the most efficient, least polluting operating conditions for existing systems. While the true cause of the error is likely a combination of all of these problems, evaluation of the assumption of complete equilibrium is the focus of this task.

This task was accomplished through the creation of a non-equilibrium chemistry model that specifically addresses carbon monoxide and carbon dioxide formation and destruction in coal combustion.

Gas phase reactions account for a major portion of the total reaction process in coal combustion and gasification. In modeling these reactions, the interaction between chemical reaction kinetics and turbulent fluid mechanics is crucial. The effect of such interactions depends on the relative magnitude of the reaction time scale and the turbulence time scale (Smoot and Smith, 1985). The reaction time scale is defined at the typical time necessary for the reacting species to reach equilibrium. The turbulent time scale is defined as the time required for mixing to proceed to the molecular level.

When the reaction time scale is much greater than the turbulence time scale, the chemical process occurs so slowly that the reaction is essentially independent of the turbulent fluctuations. Therefore, mean reaction rates can be calculated from the mean properties of the reactant species. This is the case for some heterogeneous reactions, but is very rarely the case for homogeneous reactions.

When the turbulence time scale is much greater than the reaction time scale, the chemical process occurs so rapidly that it proceeds essentially instantaneously to equilibrium upon mixing. This allows calculations of the mean chemical composition based only on equilibrium and the degree of mixing. This is the case for some homogeneous gaseous reactions and is the assumption used in many of the current combustion codes including all major species predictions in the current version of PCGC-2.

When both time scales are of the same order-of-magnitude then both chemical kinetics and turbulent fluctuations must be considered. This is the case for most of the reactions in gaseous combustion (Smoot and Smith, 1981).

Modeling of these interactions requires numerical representations of both the turbulence and the chemical kinetics. PCGC-2 tracks the degree of mixing due to turbulence through two progress variables, mixture fractions f and η, and their relative probability density functions. The f mixture fraction indicates the relative amount of material from the primary and secondary streams. The η mixture fraction measures the amount of material introduced into the gas phase from the coal. A similar scheme of progress variables can be used to track the state of the reaction kinetics.

Computer modeling of the coupling of the turbulent fluid mechanics with

each kinetic progress variable requires large amounts of computational time. Each additional kinetic progress variable can more than double the time required to reach a converged solution. Use of the 30-200+ separate rate equations and accompanying progress variables found in common gaseous combustion modeling schemes would rapidly expand the computational time requirements past the capability of even the most current supercomputers. It is therefore important to keep the number of modeled kinetic steps small to be able to reach a solution in a reasonable amount of time. It will be shown that a single progress variable can provide all the necessary kinetic information while optimizing computational time considerations.

The model presented in this study has been evaluated on several levels using the existing PCGC-2 combustion code. Stand alone evaluation was not possible due to the extensive input required by the new chemistry model.

Initial evaluation insured that programming changes made during incorporation of the non-equilibrium CO model into PCGC-2 still allowed the overall program to be executed unaltered with the original subroutines. Second, the results obtained with the new method of treating chemistry/turbulence interactions were compared to the old method for several cases. These results also were compared to experimental data when available. Finally, predictions for these cases were made with and without the new chemistry model using various options available for mass evolution from the pulverized fuel and intra- and inter-reactor energy transfer. These last predictions helped establish the possible causes of PCGC-2's inability to accurately predict carbon monoxide and carbon dioxide concentrations. They also were useful in judging the level of accuracy sacrificed when assuming complete local equilibrium throughout the reactor.

3.6.2 Chemical Reaction Kinetics Approximations

Based on the results of the literature search (see Colson 1989), the following assumptions have been used in the construction of the CO kinetic reaction scheme.

Devolatilization

Lignite coals should be assumed to produce volatiles containing equal weights of CO_2, CO, and hydrocarbons. The hydrocarbons have then been assumed

to instantaneously react to CO, limited only by the amount of oxygen present. The CO_2 found in the devolatilization products of lignite coal is likely, at least in part, formed through CO as an intermediary. This assumption allows a simplification to be made in the treatment of the devolatilization products of lignite coals by considering the formation of CO_2 through the kinetic model. This carbon can now be treated as through it were all either CO or hydrocarbons that react quickly with CO. Any excess oxygen from the coal is added to the pool of available oxygen.

Bituminous coals have been assumed to produce 10% CO by weight and the rest hydrocarbons but again these hydrocarbons will be treated as though they instantaneously react to form CO.

Anthracite is assumed to produce only hydrocarbons which will immediately be converted to CO.

CO Formation Kinetics

Because CO is formed so quickly and is not appreciably consumed until all hydrocarbons species are effectively eliminated, CO creation can be treated without a formal discussion of the initial fuel oxidation process. These observations allow all the hydrocarbons which leave the coal during devolatilization to be treated as if they instantaneously reacted to form CO, given sufficient oxygen, which greatly simplifies the model.

Chars are known to be oxidized primarily to CO but at rates which are orders of magnitude slower than the oxidation rate of CO (Smith, 1982), and therefore should not be ignored in the reaction scheme. The present devolatilization model calculates a rate for this oxidation and adds the resultant gaseous mass to the mass of evolved coal gas.

CO Destruction/CO_2 Formation Kinetics

The oxidation of CO to CO_2 can proceed along several different pathways; however, at atmospheric pressure and in the presence of as little as 20 ppm H_2O (Brokaw, 1966), the dominant reaction is (Peeters and Mahnen, 1972; Howard, et al., 1972; and Cherian et al., 1981):

$$CO + OH \rightarrow CO_2 + H. \tag{3.40}$$

This reaction has been studied under a wide range of conditions by many researchers. A widely accepted (Bockhorn and Lutz, 1984; Dutta, et al., 1984;

Moor and Heywood, 1974) global equation (Dryer and Glassman, 1972), shown in Equation 3.41, was selected for use in the kinetic scheme to model the oxidation of CO,

$$-d[CO]/dt = k_o[CO][H_2O]^{0.5}[0_2]^{0.25}exp(-E/RT)mole/cm^3 - sec \quad (3.41)$$

where $K_o = 10^{14.6\pm0.25}$ $(cm^3/mole)^{0.75}/sec$ and E=-40 $\pm$ 1.2 kcal/mole.

A second global kinetic equation, (Howard, et al., 1972) shown in Equation 3.42, was selected to evaluate the effect of the choice of equation,

$$-d[CO]/dt = k_o[CO][O_2]^{0.5}[H_2O]^{0.5}exp(-E/RT)mole/ml - sec \quad (3.42)$$

where $k_o = 1.3x10^{14}$ ml/mole sec and E = 30 kcal/mole.

Several studies (Dryer and Glassman, 1972 and Dutta, et al., 1984) have noted a reduction in the rate of CO oxidation when hydrocarbons, char, or both are introduced. It has been suggested (Dutta, et al., 1984) that Equation 3.41 could be corrected to account for the effect of lower OH radical concentrations from the O_2, H_2O, O, and OH thermal equilibrium value due to reactions between OH and char and hydrocarbons.

3.6.3 Turbulent Fluid Dynamics and Finite Rate Chemistry Coupling

Incorporation of the CO solution scheme into a turbulent combustion model is complicated by coupling with the overall model. For example, a change in mass of the particle phase in a coal-fired boiler affects the mass and composition of the gas phase, which in turn affects the momentum and temperature of the gas phase. A change in temperature of the gas phase changes the temperature and rate of devolatilization of the particle phase which, once again causes a change in the mass of the particle phase. In a comprehensive computer model, separate processes are normally modeled by different subroutines which are connected together to account for the interactions of the processes. Coupling is especially important when considering the effect of CO oxidation on gas temperature. This effect is large because CO and CO_2 are the major carbon containing gaseous species in most regions of a coal-fired boiler, and a comparatively large amount of energy is released during the oxidation of CO to CO_2

The need to couple the CO model to the overall model eliminates a decoupled, post-processor scheme from consideration in implementing the non-equilibrium CO model. Similarly, a fully developed kinetic scheme would be difficult to use because of the enormous increase in computer time required to obtain a solution. It is estimated, that a complete kinetic treatment of all chemical reactions in a coal-fired boiler would increase the required computer time by several orders of magnitude over the simple equilibrium model being used. Fortunately, such a scheme is neither necessary nor desirable since a partial equilibrium scheme can account for most aspects of coal combustion kinetics. A partial equilibrium scheme also requires little sacrifice of accuracy over a complete kinetic scheme, since a fully kinetic scheme can only be as accurate as the conditions it receives from a devolatilization model. At the present time, devolatilization models are only able to provide reliable predictions for overall mass loss and not volatiles composition. For these reasons, the partial equilibrium method was chosen for implementing the CO model.

Extent of Reaction

An important concept in the derivation of the partial equilibrium scheme used in this study is the extent of reaction. The extent of reaction measures how far the reaction has proceeded towards completion. The extent of the CO to CO_2 reaction is defined by:

$$\pi = (Y_{CO} - Y^0_{CO})/(Y^1_{CO} - Y^0_{CO}), \tag{3.43}$$

where π is the extent of reaction, Y_{CO} is the local mass fraction of CO, Y^0_{CO} is the initial or unreacted local mass fraction of CO, (ie., when π is 0) and Y^1_{CO} is the fully reacted local mass fraction of CO (ie., when π is 1). π equals 0 under completely unreacted conditions and equals 1 when the reaction has proceeded to completion. In this study, the reaction is assumed to proceed until all of one or more of the reactants is completely depleted. With these definitions for $\pi = 0$ and $\pi = 1$, Y^0_{CO} becomes equivalent to the partial equilibrium mass fraction of CO. Because the reaction could reach completion by depleting the supply of CO or of O_2, Y^1_{CO} is either 0 if CO controls (ie. if CO is depleted first) or is the mass fraction of CO left when all the O_2 is depleted if O_2 controls.

The equation for π can be simplified by writing it in terms of a new mass fraction, $Y_{CO,C}$. CO,C is the amount of partial equilibrium CO converted to

CO_2, a measure of the amount of CO_2 excluding any CO_2 that was input to the furnace. Rewriting π in terms of $Y_{CO,C}$ yields:

$$\pi = (Y_{CO,C} - Y^0_{CO,C})/(Y^1_{CO,C} - Y^0_{CO,C}) \tag{3.44}$$

where $Y^0_{CO,C}$ is the partial equilibrium mass fraction of CO converted to CO_2, which is always 0, and $Y^1_{CO,C}$ is equivalent to Y^0_{CO} - Y^1_{CO}. These definitions reduce π to:

$$\pi = Y_{CO,C}/Y^1_{CO,C}. \tag{3.45}$$

Incorporation

The submodel was incorporated into PCGC-2 in the following, completely coupled manner.

The present equilibrium model creates a table of equilibrium solutions as a function of the mixture fractions, f and η, and the system enthalpy, h. This table is used by the main code to interpolate equilibrium solutions for instantaneous vales of f, η, and h. Interpolating in the table instead of calling the equilibrium code every time a solution is needed saves a significant amount of computational time. This submodel was incorporated into PCGC-2 using the extent of reaction as another progress variable similar to the gas and coal gas mixture fractions.

The equilibrium code has been modified to calculate a partial equilibrium by eliminating CO_2 as a possible product, treating any CO_2 that entered the reactor in an inlet stream as an inert species. This has the effect of assuming that all of the propagation and termination reactions which do not involve CO_2 are modeled kinetically through Equation 3.40. Using this data and a complete range of values for the extent of the CO to CO_2 reaction, a different table is set up. The concentrations of CO, CO_2, and O_2 are adjusted as a function of π through the following mass balances:

$$X_{CO} = X^0_{CO} - \pi X^1_{CO,C} \tag{3.46}$$

$$X_{CO_2} = \pi X^1_{CO,C} \tag{3.47}$$

$$X_{O_2} = X^0_{O_2} - \pi X^{1/2}_{CO,C} \tag{3.48}$$

where X_{CO} is the molar concentration of CO, X^0_{CO} is the partial equilibrium molar concentration of CO, π is the extent of the CO to CO_2 reaction, $X^1_{CO,C}$

is the molar concentration of CO converted to CO_2 when $\pi = 1$, X_{CO_2} is the molar concentration of CO_2, X_{O2} is the molar concentration of O_2, and X^0_{O2} is the partial equilibrium molar concentration of O_2. A different table is created by storing the non-equilibrium values as functions of f, η, h, and π.

The existing main routine has been modified to find mean values for all these properties using interpolated values from the new table. The main routine obtains mean values by integrating instantaneous values for each property over a joint probability density function (pdf) for f and η, as shown in Equation 3.49, which accounts for fluctuations in each property caused by turbulence.

$$\overline{W}_{Y_{CO,C}} = \overline{\rho} \int_{\eta} \int_{f} [W_{Y_{CO,C}}(\eta, f, \pi)/\rho(\eta, f, \pi)] \tilde{P}(\eta, f) df \, d\eta \qquad (3.49)$$

Since the system properties are mainly a function of stoichiometry and turbulence, convoluting over the pdf's for f and η accounts for most of the fluctuations in the properties. In this initial work, the probability density function of π is assumed to be a delta function at the mean. This has the effect of considering the value of π to be independent of turbulent fluctuations and ignores the effects of time differences between eddies.

Equation 3.50 is a steady-state, partial differential species continuity transport equation on the mass fraction of CO converted to CO_2, $Y_{CO,C}$, for an axi-symmetric reactor (Smoot and Smith, 1985).

$$\frac{\partial(\bar{\rho}\tilde{u}Y_{CO,C})}{\partial x} + \frac{1}{r}\frac{\partial(r\bar{\rho}\tilde{v}Y_{CO,C})}{\partial r} - \frac{\partial}{\partial x}(D_{Y_{CO,C}}\frac{\partial Y_{CO,C}}{\partial x}) - \frac{1}{r}\frac{\partial}{\partial r}(rD_{Y_{CO,C}}\frac{\partial Y_{CO,C}}{\partial r}) = \bar{W}_{Y_{CO,C}} \qquad (3.50)$$

where $\overline{\rho}$ is the Reynolds averaged density, $\tilde{u}$ is the Favre-average axial velocity, $\tilde{v}$ is the Favre-averaged radial velocity, $D_{Y_{CO,C}}$, is the turbulent eddy diffusion coefficient, and $\overline{W}_{Y_{CO,C}}$ is the time mean rate of disappearance of CO, creating CO_2. The first term considers the amount of $Y_{CO,C}$ transported by convection in the axial direction. The second term deals with convective transport in the radial direction. The third and fourth terms account for diffusion in the axial and radial directions, respectively. $\overline{W}_{Y_{CO,C}}$ is the time-averaged local source of $Y_{CO,C}$ as calculated by the main convolution routine. The main convolution routine calculates $\overline{W}_{Y_{CO,C}}$, using Equation 3.49, from instantaneous non-equilibrium values stored in the table for the CO to CO_2

reaction rate. The boundary conditions for this equation are zero at all boundaries since no "CO,C" is transported in the reactor.

The flow field for $Y_{CO,C}$ resulting from the solution of the transport equation allows the calculation of a flow field for π from Equation 3.45 for use in the convolution routine by the next iteration. After convergence of the gas phase, the temperature and species concentrations data are stored for use by the particle model.

3.6.4 Conclusions

During incorporation, an effort was made to insure compatibility between the CO model and as many existing submodels as possible. A substantial portion of the debugging effort was devoted to ensuring there were no unintentional side effects on the other submodels. These submodels included both the normal fluctuating and the non-fluctuating turbulence options, three different radiation options, a compatible and a non-compatible existing non-equilibrium chemistry option, the NO_x post-processor option, and the coal-water slurry option. The original complete equilibrium model was also left intact as an option. This testing entailed making approximately 15 computer runs of the same case. The compatible options were run with and without the CO model to insure the continued operation of the option alone and to debug the combination of options. The few options whose theoretical assumptions rendered them incompatible with the CO model were tested alone. Messages were placed in the program to warn the user against trying to use the CO model with incompatible options. The cases were evaluated by comparing the results of the newly modified program with the results obtained from an archive version of the program using the exact same input conditions. Output differences greater in magnitude than those due to the accuracy of the computer were investigated and the causes corrected.

The Asay case (Smoot and Christensen, 1985) was used for all debugging runs except the coal-water slurry runs. This is a slightly fuel-lean coal combustion case which has become a standard debug test case for PCGC-2. It provides extensive experimental data for comparison with the model predictions including CO, CO_2, H_2O, and O_2 species concentrations. The coal-water slurry debug runs were made with an in-house version of the Rawlins case (Rawlins, 1984).

The inability of coal combustion models to accurately predict species

concentrations for CO and CO_2 was thought to be partly caused by ignoring the kinetic considerations of the reaction chemistry. A complete kinetic treatment of all the chemical processes occurring in the reactor was found to require too great an increase in computational time to be practical with the current generation of computer technology. Using a partial equilibrium method to consider the phenomenon was found to account for most of the effects of kinetics, including the issue of coupling, while requiring an acceptable increase in computation time to reach a solution.

Inclusion of the CO non-equilibrium submodel into PCGC-2 made a noticeable difference in the predictions obtained for all evaluation cases modeled. However, the difference has not always appeared to be an improvement. In general, reactor temperature and species concentrations of CO, O_2, and CO_2, were most affected by use of the non-equilibrium CO model instead of the complete equilibrium model. Water concentrations were also affected to a lesser degree. Other model predictions such as gas velocities and mixture fractions were only slightly affected. The most common effect was to delay the oxidation of CO to CO_2 until later in the reactor causing a larger flame zone and accompanying changes in the consumption of O_2. Temperature was strongly affected by the delay of energy release due to CO oxidation showing lower peaks and a general lowering of the early reactor temperatures with higher values nearer the reactor exit. Larger regions of complete oxygen or carbon monoxide depletion were also seen with the use of the non-equilibrium model. These observations are general trends, all of which were not seen in every case modeled.

Use of the non-equilibrium model also had a significant effect on the usability of PCGC-2. Large increases in computational time were sometimes seen as a result of the CO model. In addition to the time increase, many cases were more difficult to converge, resulting in greater sensitivity to the underrelaxation factors used in PCGC-2. Some cases did not converge when using the new chemistry option. This was especially true when the non-adiabatic energy model also was used. Use of the non-adiabatic energy model with the complete equilibrium model also noticeably slowed convergence.

Choice of rate parameters for use with the non-equilibrium chemistry model had a secondary effect on the predictions and convergence times. Use of the different rate equations studied in this work did not have a noticeable effect on the model predictions, but they were rarely significant in comparison to the differences between chemistry options. The differences also did not

show one equation to give consistently better results than the other. One equation often showed better agreement with experimental data in parts of the reactor while the other equation was superior in other areas. There was, however, a relatively consistent difference in convergence characteristics between the two equations. In general the Howard equation (3.40) gave faster and more easily converged solutions than did the equation suggested by Dryer (3.41). This ease of convergence may be due to the greater linearity of the Howard equation compared to the Dryer equation.

Interpretation of the usefulness and reliability of the new chemistry model has been hampered by inadequacies in many other models that provide necessary information to the non-equilibrium model. These models, such as the devolatilization and energy models which were specifically considered in this work, have been shown to have uncertainties that affect final predictions by at least the same order-of-magnitude as the effect of the CO non-equilibrium model and usually by an order-of-magnitude greater.

Table 3.7 lists a summary of the relative effects of the different model choices for each case. The percentages given are fractions of the difference between the experimental data and the adiabatic equilibrium predictions.

3.7 Coal Devolatilization

3.7.1 Particle Thermal Properties

The conditions within a typical combustor during particle devolatilization often are characterized with steep gradients in gas temperature and composition and rapidly changing particle properties. The particle temperature is of particular importance in describing devolatilization processes, both experimentally and theoretically. A proportionate share of this discussion is dedicated to analyzing uncertainties in predicting particle temperature.

Comparisons of rates of devolatilization suggested by various authors reveals about seven orders of magnitude discrepancy between the slowest suggested rates (Kobayashi, et al., 1977) and the most rapid (Serio, et al., 1986). When viewed in this way, the large discrepancy can be quite misleading. The rapid rates of temperature rise and the typically first-order nature of devolatilization reactions are coupled with the kinetic rates such that the predicted rates of mass loss in practical reactors are much more similar than the kinetic

Table 3.7: Accuracy of Various Model Combinations as a Percentage Reduction of the Error Apparent in the Adiabatic/Equilibrium/Ubhayakar Prediction (Ubhayakar, 1979).

	CASES					
	1	2	3	4	5	6
UBHAYAKAR DEVOLATILIZATION						
ADIABATIC/NON-EQUILIBRIUM						
Temperature	—	-5%	—	-10%	0%	—
O_2	5%	0%	-20%	-40%	0%	20%
CO	0%	-5%	40%	5%	0%	-10%
CO_2	15%	0%	-35%	-40%	0%	0%
NON-ADIABATIC/EQUILIBRIUM						
Temperature	—	50%		75%	30%	
O_2	10%	10%		-50%	0%	
CO	30%	50%		40%	50%	
CO_2	75%	20%		-75%	0%	
NON-ADIABATIC/NON-EQUILIBRIUM						
Temperature	—	45%			35%	
O_2	25%	10%			0%	
CO	40%	55%			75%	
CO_2	85%	30%			0%	
KOBAYASHI DEVOLATILIZATION						
ADIABATIC/EQUILIBRIUM						
O_2	20%					
CO	25%					
CO_2	10%					
ADIABATIC/NON-EQUILIBRIUM						
O_2	30%					
CO	15%					
CO_2	15%					

rate coefficients might suggest. The major differences are in the temperature and residence times at which the particles are predicted to react. The seven orders of magnitude difference in reaction rates translates to factors of up to about five difference in the residence time required for the particle to begin to devolatilize in earnest and temperatures at which this devolatilization reaction occurs which differ by several hundred degrees.

In this study we have shown that the particle heat capacity impacts its temperature history significantly. Many correlations of particle heat capacity have been suggested. The approach used in the following calculations is based on the theoretical description of the heat capacities originally presented by Einstein (Berry, et al., 1980), and the correlations of Merrick (1983). Einstein suggested a function which predicts the composition and temperature dependence of the heat capacity of solids based on quantum theory and a simplified model of vibrations within a lattice.

Merrick suggested that two vibrational constants, θ_1 and θ_2, be used to characterize the lattice vibrations of coal and graphite. The parameters were used to represent vibrations in and perpendicular to the planar structure of the lattice, respectively. By empirically fitting the parameters to experimental heat capacity data from graphite and a variety of coals ranging in volatile content from 15 to 35%, Merrick was able to predict the coal data within 10% over the available temperature range of the data (300-600 K). The graphite data were predicted within five% between 300 and 1100 K. The final correlation was

$$c_v = \frac{R}{a}[g_1(380/T) + 2g_1(1800/T)] \tag{3.51}$$

where the units are (J kg^{-1} K^{-1}). An expression for the enthalpy of the material can be derived by integration

$$h = \frac{R}{a}[380g_0(380/T) + 3600g_0(1800/T)] \tag{3.52}$$

where the units are (J kg^{-1}) and the function g_0 is given by

$$g_1(z) = \frac{1}{e^z - 1}. \tag{3.53}$$

The implied reference for the enthalpy in the above equation is zero at absolute zero.

These correlations predict c_v, the constant volume heat capacity. The constant pressure heat capacity, c_p, is usually of interest in coal combustion:

$$c_p \equiv (\frac{dq}{dT})_p = c_v + T(\frac{\partial p}{\partial T})_V(\frac{\partial V}{\partial T})_p = c_v + \frac{\alpha^2 VT}{\kappa_T} \tag{3.54}$$

Figure 3.27 illustrates two particle temperature histories which differ only in the functional form assumed for the heat capacity. The solid line illustrates the results assuming the particle has a constant heat capacity of 1250 J/kg. The dashed line illustrates the results of using the model of Merrick in which average atomic weight was calculated from the ultimate analysis of the coal to be 8.18 g/mole for the coal and was assumed to be 12.0 g/mole for the char. The heat capacity of the ash was calculated from a correlation also suggested by Merrick given by

$$c_{v,a} = c_{p,a} = 593.3 + 0.586T \tag{3.55}$$

where T is in degrees Kelvin. As illustrated, the temperature of the coal particle differs by a maximum of about 500 K, depending on the correlation used for heat capacity. The calculations illustrated in Figure 3.27 are based on an assumed initial particle diameter of 100 μm. Particles with initial diameters of 40 μm showed similar discrepancies in predicted temperature, although the overall time required for heat up was considerably shorter. This maximum difference occurs near the temperature at which the particles are predicted to devolatilize most rapidly. This discrepancy can lead to large differences in the results of data analysis, as illustrated later, and in the predicted behavior of particles. These results combine with uncertainties in gas temperatures, heat transfer coefficients, and radiative conditions to underscore the importance of careful and thoughtful evaluation when using predicted particle temperatures during coal devolatilization studies.

3.7.2 Devolatilization Modeling

Devolatilization models of varying states of sophistication have been proposed by a variety of authors. These have been classified and reviewed by Baxter and Smith (1989). In this task, we tried to formulate a generalized approach to incorporating most of the exact devolatilization models or others that may be proposed into the same computer model.

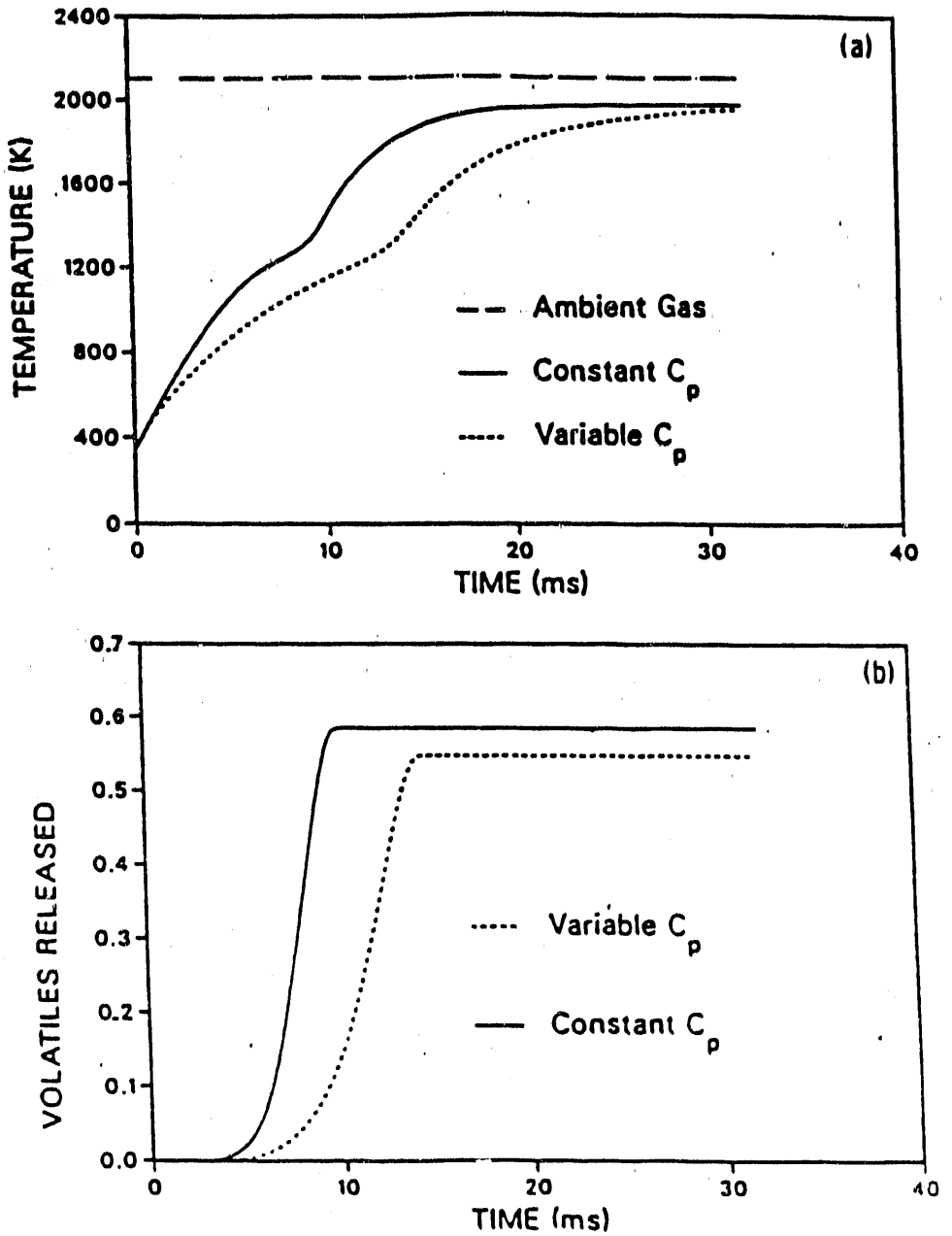

Figure 3.27: Typical Temperature and Mass-Loss Histories for Coal Particles with Constant Heat Capacities and with Variable Heat Capacities.

3.7.3 A Generalized Framework for Devolatilization Models

This subsection develops a common framework in which a large number of devolatilization models can be cast and which is useful for analyzing some of the most important properties of devolatilization models. The overall framework has not been previously presented. It is presented in its general form, with published devolatilization models from many investigators serving as specific examples of its application. The framework is based on kinetic expressions and coal composition. There are several devolatilization models which are predominately expressions of either heat or mass transfer limitations in coal particles (Oh, 1985; Freihaut, et al., 1987). Kinetic expressions play a minor role in these and they are not discussed in this section. A few terms must be defined at the onset.

A characteristic of the kinetic expressions for devolatilization models is the independence or lack thereof of their driving forces. The driving forces of the kinetic expressions used in this subsection are characterized either in terms of volatile matter, V, or coal, c, or both. A driving force for a kinetic expression is called independent if that kinetic expression is the only devolatilization mechanism by which the mass represented by the driving force is depleted. All other driving forces are considered dependent.

An overall devolatilization model can be composed of many kinetic expressions, each one of which can be driven by either dependent or independent components of coal mass. As will be discussed and illustrated later, certain experimental observations of devolatilization can only be captured by models with at least two kinetic expressions, at least one of which is dependent.

The framework in which the devolatilization models are cast is unique to this discussion. It is intended to be useful both in the analysis and computer coding of devolatilization models. Much of this discussion strictly applies only to devolatilization models with kinetic coefficients which are parametric constants. That is, the coefficients may vary with coal type, but within a given application, are considered constants. A large number of models fall within this framework, as will be shown later.

A Chemical Description of Coal

This generalized framework requires as input some description of the coal. Ideally, this description would be in terms of quantities which actually react

during devolatilization and whose kinetics are independent of the actual coal type. The description should be the result of an analysis which is or could become standardized. Several classifications have been mentioned above or are available as standard chemical procedures which approach this idealization. These include maceral groups, functional groups measurable with FTIR, NMR determinations of carbon bonding, ICP spectroscopy measurements, species extractable from coal, and hypothetical descriptions based on data from any of the previous measurements.

One critical feature of this description is that its components be related, both physically and mathematically, to devolatilization. The mathematical relationship is discussed in the next subsection. The immense body of coal science literature and current research should lend valuable insight into the physical relationship. The analyses done on coal which have been useful in characterizing its chemical composition include solvent extraction, NMR and FTIR spectroscopy, ICP atomic emission spectroscopy, laser spark spectroscopy, and classical petrographic classification according to maceral groups. In practice, these fundamental measurements are rarely related to parameters in devolatilization models such as coal composition. Establishing an accurate and convenient relationship between these coal science measurements and parameters used in describing devolatilization in coal combustion systems is seen as a critical need in this field. Figure 3.28 schematically illustrates this division of a coal particle into its several fractions.

In the figure, the fractions are identified by the products for which they are precursors similar to the divisions in the functional group model which will be further discussed. The basic building blocks may be more useful when described in terms of aromatic clusters, bridges, side chains, etc. Such a model is currently under development by Grant, et al. (1988) on the basis of NMR measurements. Yet another model based on reaction order, cross-linking, and reaction rate in an inductively-coupled plasma reactor is being developed by Muezzalar (see Windig, et al. (1987) for example). Such fundamental coal structure studies can be used to establish a foundation on which to build devolatilization models.

In this context, the detail in the simple models described in Baxter and Smith (1989) is insufficient to distinguish between the overall coal composition and the composition of individual chemical components. This does not preclude, in either case, the overall atomic composition of the particle

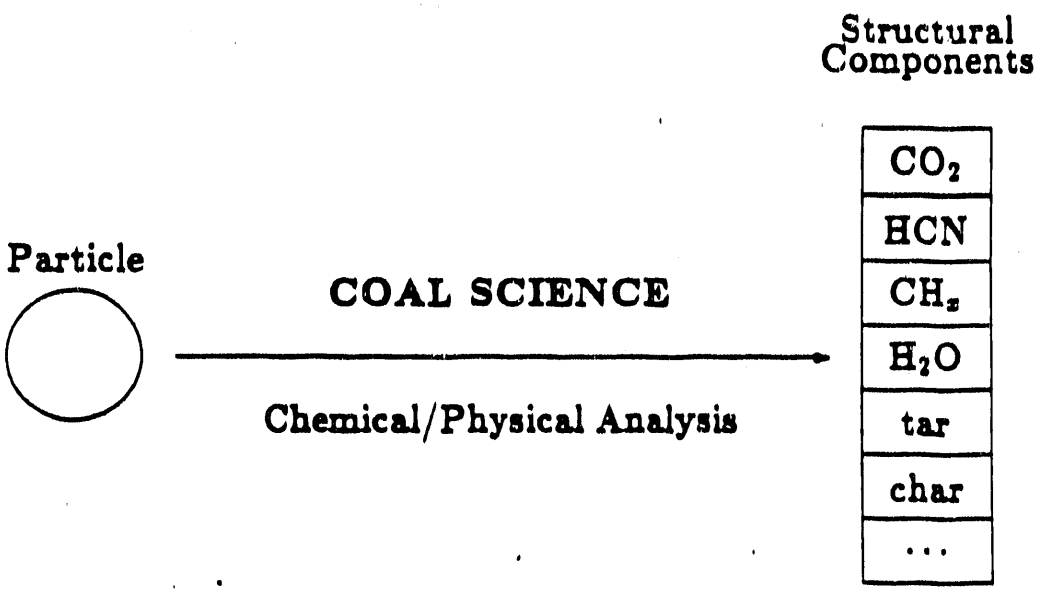

Figure 3.28: Schematic Diagram of a Coal-Science-Based Description of a Coal Particle.

changing with time. Such a feature has not been used in these simple models, but could be by methods discussed in the next subsection. Nevertheless, the opportunity for incorporating chemical structural information of the form illustrated in Figure 3.28 in these simple models is limited.

The multiple reaction model, discussed in the next subsection, has the potential of incorporating such information in a useful way. The early formulation of the model was based on precisely such an idea. In the practical applications of the model, no use has been made of this potential. The manner of doing so is not complicated. The model already requires dividing the potential yield into several fractions, each fraction being assigned a unique activation energy and reacting independently of all others. Consistent with this philosophy would be the additional assignment of a chemical composition with each fraction. To be consistent with experimental observations, the low activation energy fractions would typically be comparatively higher in hydrogen content and lower in heating value than the high activation energy components.

The models distinguishing the components of coal in their formulations include the functional group model and those models with reactive intermediate compounds. In the functional group model, this distinction is in terms of precursors of classical gases and tar. The heating value of these components is implied by their chemical composition.

A Mathematical Description of Reaction Kinetics

After establishing the composition of the coal, the next task is expression of the kinetic rates of reaction of each component. Figure 3.29 schematically illustrates many of the possible reaction mechanisms by which coal can devolatilize. The figure illustrates the production and destruction of intermediate species, labeled RI's (reactive intermediates), the competitive formation of gaseous and solid products, and the concept of char as a product through a specified yield.

In the specific implementation of this framework, the driving force for each reaction is composed of the sum of any number of the individual components. The order of reaction of these components and the instantaneous yield of the gases/tars are arbitrary for each kinetic expression. Each expression may be either of classical Arrhenius type or the distributed type. The major limitations of the current approach, include the exclusion of intermediate

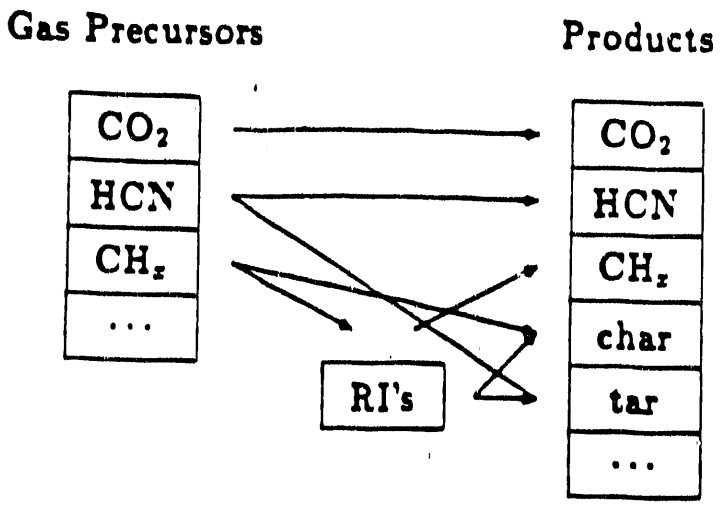

Figure 3.29: Illustration of a Reaction Network with Competition, Yield, and Reactive Intermediate Species.

species and the requirement that all coefficients in the kinetic expression be constant.

A strong symbiotic relationship arises naturally between the concepts of coal structure and description of the reaction kinetics during devolatilization. For example, a significant percent of the organic portion of some coals is extractable with the use of solvents without breaking covalent bonds. Most of this extract would either boil or have a subtantial vapor pressure at temperatures characteristic of devolatilization (800-1300 °C). Many of these compounds are aromatic, enhancing their temperature stability. It would be reasonable to expect such compounds to vaporize rather than pyrolyze during devolatilization. Vaporization could be characterized as a zero-order, low activation energy process. [Additional experimental evidence for such a scenario is offered by Windig, et al. (1987)].

One of the few undisputed experimental observations of devolatilization is the increased yield with increasing particle temperature or heating rate. The only devolatilization model which rigorously predicts such behavior is the two-step model. As illustrated previously, it can be made to predict the behavior rigorously. An analysis of the kinetic mechanisms illustrated in Figure 3.29 lends insight into the means by which this happens. The key factors in predicting such a trend are: 1)at least two kinetic mechanisms with different activation energies compete for the same coal component, and 2)the char yield of the reaction with the highest activation energy be smaller than the yield of the reaction with the lower activation energy. A similar sensitivity to particle temperature history could be incorporated into most devolatilization models by using similar kinetic mechanisms.

3.7.4 Application of this Generalized Framework for Devolatilization

The functional group model of Solomon and coworkers (Serio, et al., 1986) exercises many features of this generalized framework and will be used to illustrate its performance. Figure 3.30 shows the predicted overall mass loss on a dry ash-free (daf) basis from the functional group model in cases where the gas temperature was considered constant at 1740, 1940, and 2100 K. These computations use the initial mass fractions given by Solomon for a Wyoming subbituminous coal. All three temperatures produce the same

mass loss at residence times of 100ms and larger. The rates of mass loss are quite rapid. The rates of mass loss from some of the individual components of the coal will be illustrated later. They are evident in Figure 3.30 from the non-smooth features of the total mass loss curve.

Figure 3.31 shows the predicted temperature histories for the particles shown in Figure 3.30. These predictions are based on both temperature and composition dependent values of heat capacity. The final temperatures are all slightly less than the gas temperatures due to radiative losses. There is a subtle increase in the rate of temperature increase.

Figure 3.32 illustrates the yields of two gases and the tar included in the functional group model. These computations were done at 1740 Kelvin. The predictions are done for gas yields rather than consumption of the original fractions of coal. Tar yield is the sum of tar from approximately 30 coal fractions used in this model. It amounts to about 16% of the original coal mass. The sum of the aliphatic components and methane is also illustrated. They begin coming off the coal particle slightly after the tar, but parallel the tar results in an essentially monotonic rise. The carbon dioxide yield represents the total from different types of carbon dioxide specified in the functional group model (loose, tight, etc.). This curve is not smooth because of the evolution of each of these subgroups. The extra loose CO_2 comes off earlier than the tar. These predictions illustrate the amount of this component reacted in the coal particle, which is different than the amount produced as a gas. The initial amount of these fractions sums to about 24% of the original particle mass. The final gas yield was seen in Figure 3.32 to be about 16%. The balance formed tar. Figure 3.33 also shows how a small amount of many of the components remains in the particle, accounting for the differences in overall mass yield seen in Figure 3.30.

The impact of these computations on the overall CPU time requirements has also been examined. In the cases considered thus far, the CPU time required to converge an entire case increased by about 15% when the detailed devolatilization kinetics were used as compared with the two-step model. This increase is small considering the amount of computational effort in the detailed model. These figures and a similar discussion have been reviewed by Solomon, who agrees that this is a proper implementation of his model. This new framework offers an accurate and useful method of including various devolatilization models in comprehensive combustion models.

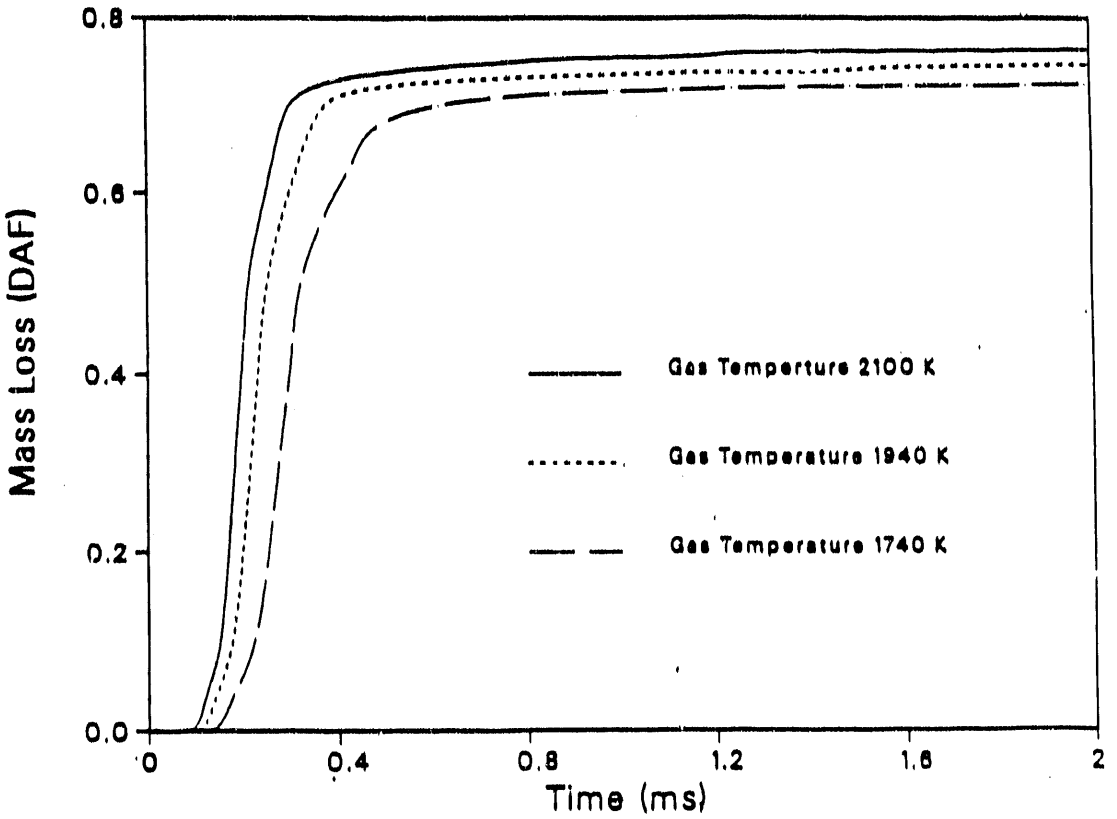

Figure 3.30: Predicted Overall Mass Loss from the Functional Group Model.

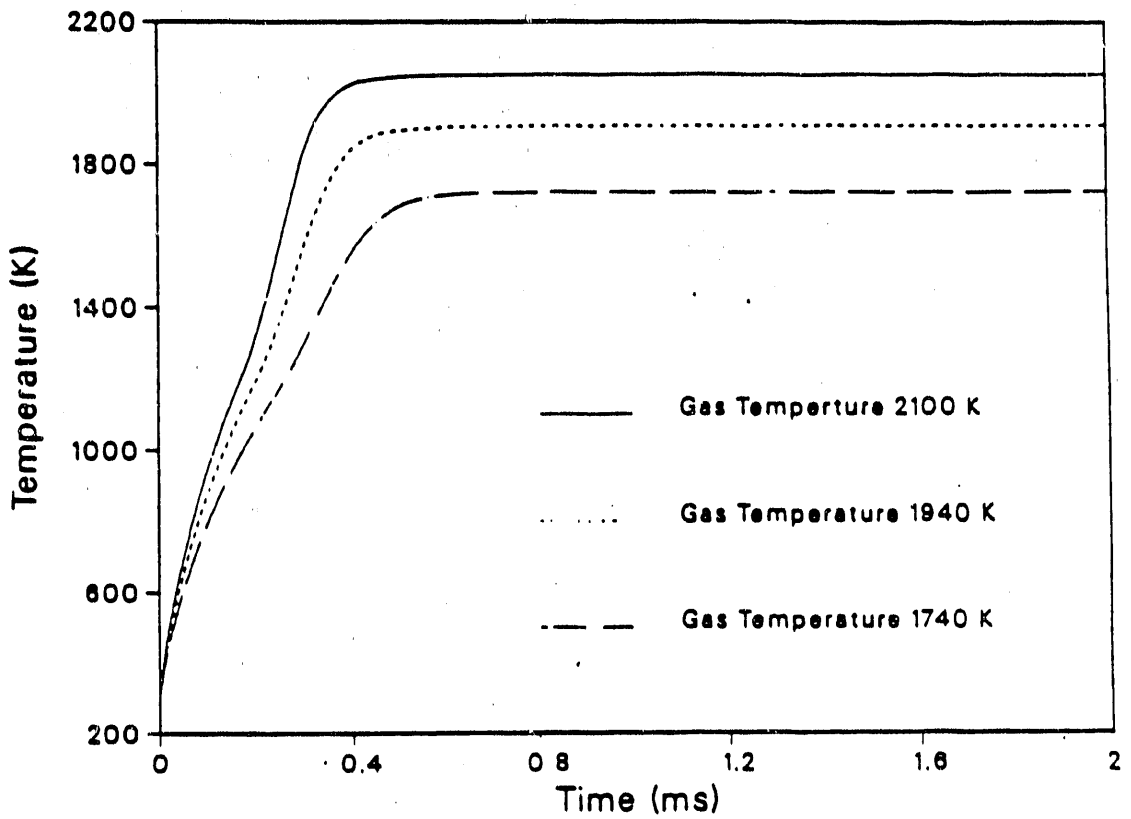

Figure 3.31: Predicted Temperature Histories for the Particles also Illustrated in Figures 3.30 - 3.33.

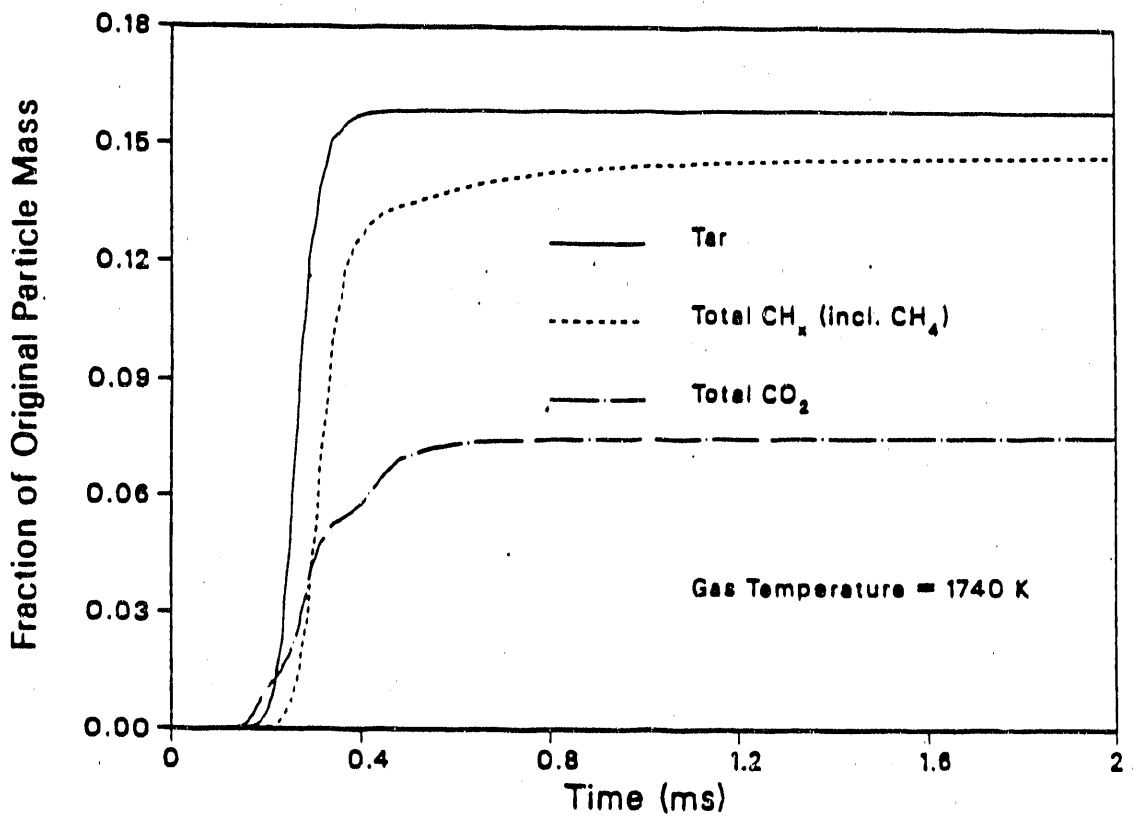

Figure 3.32: Predicted Gas and Tar Yields for the Particles also Illustrated in Figures 3.30 - 3.33.

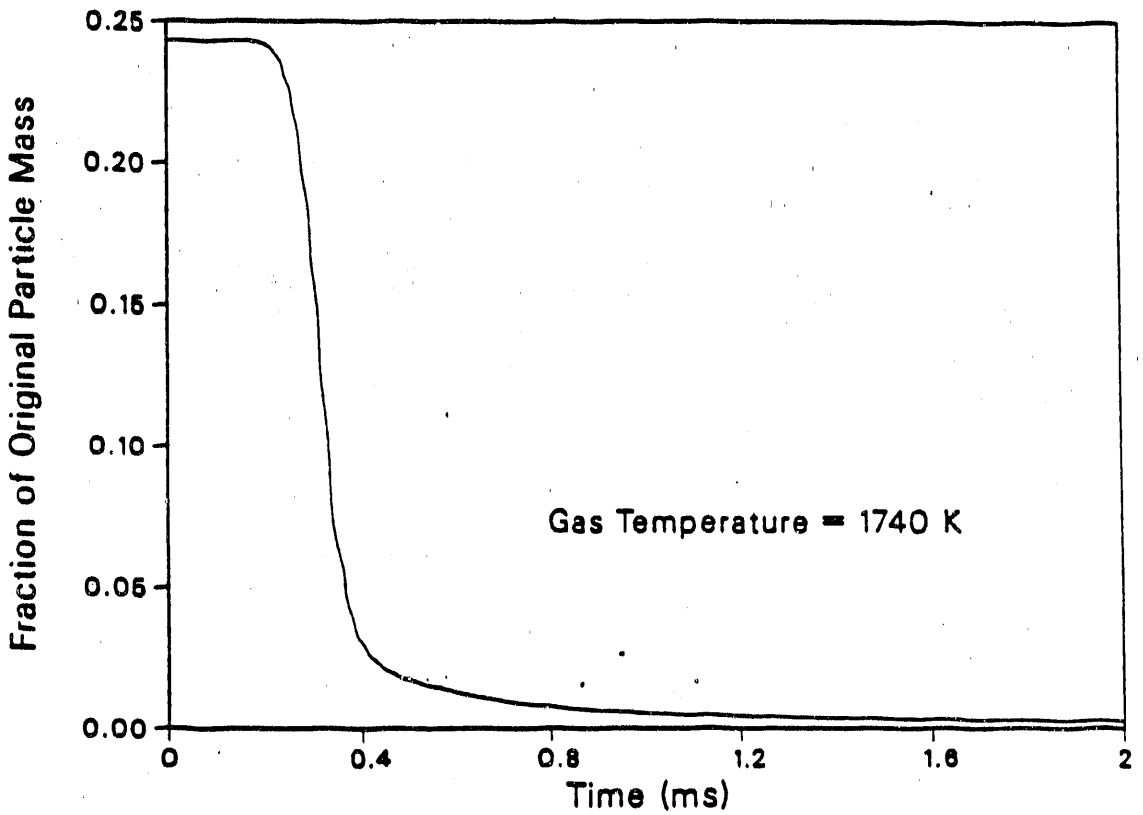

Figure 3.33: Predicted Component Mass Losses of Methane and Aliphatic Groups for the Particles.

Finally, this framework can be used to enhance the capabilities of the most sophisticated models. Discussion of this point will deal with the functional group model as it is the most complicated and sophisticated model implemented into the code thus far. The extensions to other models are obvious.

The most arbitrary portion of the functional group model is its treatment of tar. The potential mass fraction of tar formed from each component is commonly used as a parameter by those who apply this model. Furthermore, such chemical components of the coal as *nonvolatile* carbon react to form tar, and there is no concept of char formation in the model. An alternative approach to modeling devolatilization which takes advantage of the gas kinetic expressions in the functional group model, includes a more physically realistic treatment of tar and char, and can predict a temperature history dependence of ultimate mass loss, is available within this generalized framework. The model would be cast in a form similar to the functional group model so far as the light gases are concerned. Those light gases which devolatilize early, such as the loose CO_2, would be unchanged. Those which react later react to form some fraction of char and some fraction of gas/tar. The very heavy components and the 'nonvolatile' carbon would be classified as tar precursors, also producing a fraction of char. The current formulation of the tar reaction would no longer be necessary.

This formulation of the model would predict a temperature history dependent on the ultimate mass yield such as that illustrated in Figure 3.34. The variation of ultimate mass shown in this figure is a significant enhancement of the capabilities of the functional group model. In terms of comprehensive combustion modeling, the ultimate mass loss is among the most important variables to accurately predict. State-of-the-art turbulence and chemistry modeling does not even allow for the the variation in volatile composition which is implicit in the functional group model.

There are a host of other models which could be proposed, both inside and outside of the framework discussed here. However, this framework provides a commonality and flexibility among the most widely used models which has heretofore not been available. The framework also provides a useful tool with which to incorporate basic coal science measurements into practical combustion applications in a fundamental yet efficient manner.

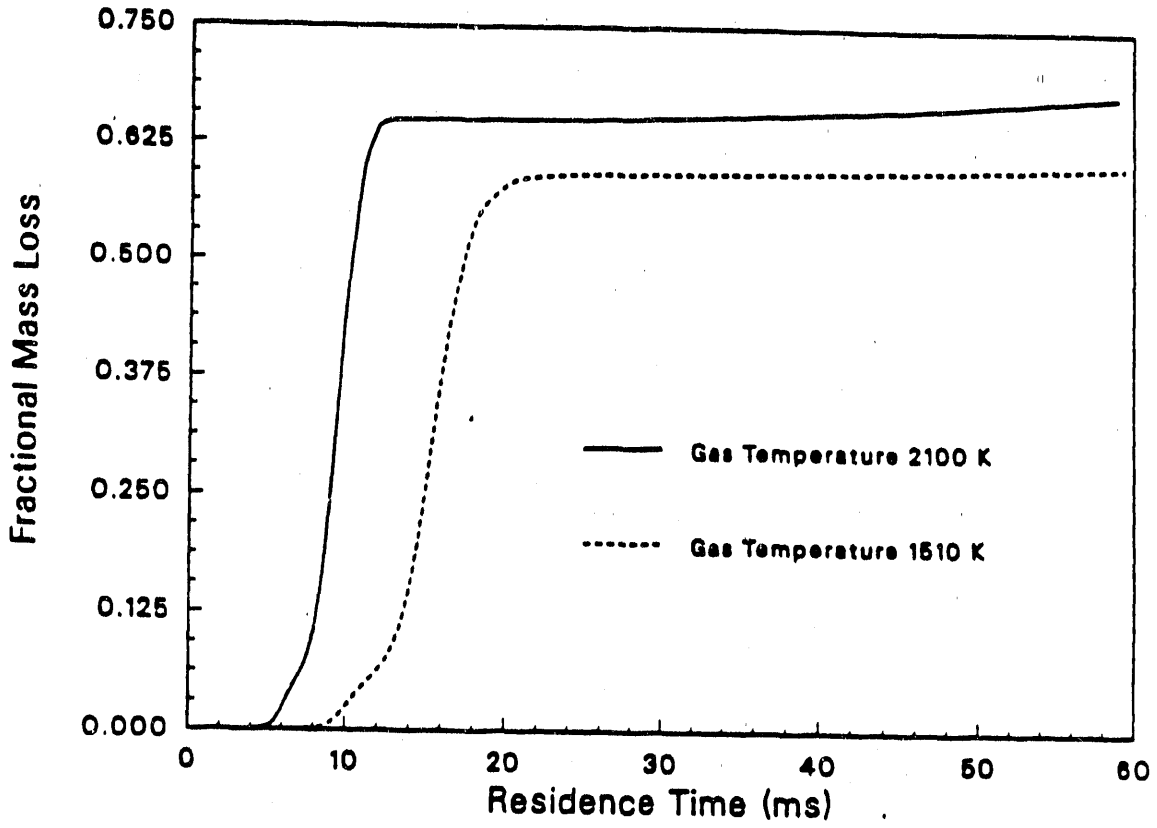

Figure 3.34: Predicted Total Mass Loss for Several Reactor Conditions with a Modified Version of the Functional Group Model.

Table 3.8: Devolatilization Coefficients Applicable for Several of the Simple Coal Devolatilization Models.

Single Step Reactions

$$\text{raw coal} \xrightarrow{k_1} Y \text{ (volatiles)} + (1-Y) \text{ char}$$

Rank	Reference	α_1^0 (DAF)*	α_2^0 (DAF)*	Y	A (s^{-1})	E (J/kmol)
Lignite	Solomon, et al., 1986	(0.4)	$1-\alpha_1^0$	1.0	4.3×10^{14}	2.29×10^{8}
	Kobayashi, et al., 1977	(0.7)	"	"	6.6×10^{4}	1.05×10^{8}
	Anthony, et al., 1976	(0.4)	"	"	2.83×10^{2}	4.64×10^{7}
	Truelove & Jamaluddin, 1986	(0.4)	"	"	6.2×10^{3}	4.64×10^{7}
Bituminous	Solomon, et al., 1986	(0.4)	$1-\alpha_1^0$	1.0	4.3×10^{14}	2.29×10^{8}
	Kobayashi, et al., 1977	(0.7)	"	"	6.6×10^{4}	1.05×10^{8}
	Anthony, et al., 1976	(0.4)	"	"	7.1×10^{2}	4.94×10^{7}
	Truelove & Jamaluddin, 1986	(0.4)	"	"	2.0×10^{4}	4.94×10^{7}
	Wiser, et al., 1964	(0.5)	"	"	4.8×10^{1}	6.27×10^{7}
	Badzioch & Hawksley, 1970	(0.4)	"	"	1.14×10^{5}	7.45×10^{7}
	Badzioch & Hawksley, 1970	(0.4)	"	"	3.12×10^{5}	7.45×10^{7}

Two Step Model

$$\text{raw coal} \begin{cases} \xrightarrow{k_1} Y_1 \text{ (volatiles)} + (1-Y_1) \text{ (char)} \\ \xrightarrow{k_2} Y_2 \text{ (volatiles)} + (1-Y_2) \text{ (char)} \end{cases}$$

Rank	Reference	Reaction	α_1^0 (DAF)	α_2^0 (DAF)	Y_i	A_i (s^{-1})	E_i (J/kmol)
Lignite	Kobayashi, et al., 1977	1	1.0	$1-\alpha_1^0$	0.3	2.0×10^{5}	1.05×10^{8}
		2	"	"	1.0	1.3×10^{7}	1.67×10^{8}
Bituminous	Kobayashi, et al., 1977	1	"	"	0.3	2.0×10^{5}	1.05×10^{8}
		2	"	"	1.0	1.3×10^{7}	1.67×10^{8}
	*Ubhayakar, et al., 1977	1	"	"	0.4	3.7×10^{5}	7.36×10^{7}
		2	"	"	0.8	1.5×10^{13}	2.51×10^{8}

*Most commonly used parameters if no data are available.
*These parameters are expected to vary with heat-up rate and/or temperature.

Table 3.8 lists several sets of coefficients which have been suggested for devolatilization models. As has been previously noted, there are differences between the coefficients. Those shown in the table are a representative, but not exhaustive list of those available. The parameters suggested by Ubhayakar, et al. (1977) have given reasonable results in many situations. However, there is no definitive evidence as to which rate parameters to use.

3.7.5 Conclusions

A generalized framework for coal devolatilization has been developed which includes most of the presently suggested devolatilization models, and incorporates fundamental descriptions of coal into a kinetic reaction scheme to predict the product distributions. This framework has been included, with the exception of the reactive intermediates, in a comprehensive combustion code. Most of the classical approaches to modeling coal devolatilization have been reviewed and many have been set on a more useful and concise philosophical, mathematical, or correlative foundation.

3.8 Turbulence Modeling

3.8.1 Introduction

This investigation was initiated with the purpose of improving the first generation, comprehensive, three-dimensional code for coal combustion and gasification processes. Important features of this code include: the ability to handle complex geometries and boundary conditions, advanced and efficient numerical techniques, and several turbulence submodel options.

This project is a concerted effort to update the various capabilities of the code. The code in its present form has three different turbulence models. These models are: 1) constant eddy diffusivity, 2) Prandtl mixing-length, and 3) the k-ϵ model. It is observed that the velocity field predicted using the k-ϵ model for industrial-scale combustors is quite realistic and agrees with experimental observations in most regions of the combustor. However, it is also observed that in some regions, agreement between the simulation and the measured data is not satisfactory. This may be due to inadequacies of the turbulence model or errors in the measurement, since the measured quantities are inherently stochastic in nature. To investigate these discrep-

ancies, a detailed review process was initiated to evaluate the current status of advanced turbulence closure methods, and select a suitable turbulence model.

3.8.2 Turbulence Models

In the last two decades, several sophisticated turbulence models have been developed namely, Reynolds stress transport (Lauder et. al., 1975; Rodi, 1982; Sloan, et al., 1986), nonlinear k-ϵ model (Speziale, 1987), direct numerical simulation (Grotzbach, 1983; Schumann and Friedrich, 1985), and large eddy simulation (Grotzback, 1983; Schumann and Friedrich, 1985). These models have proven their worth in realistically simulating idealized flows, and providing better insight to the physics of turbulence.

Reynolds Stress Transport

In this turbulence model, transport equations are solved for the individual Reynolds stresses together with the conservation equations for mass, linear momentum etc. (Launder, et al., 1975; Rodi, 1982; Sloan et al., 1986). This method is a departure from the traditional eddy viscosity concept. The major advantage of this model over more traditional approaches is that it does not assume isotropy. It recognizes that individual Reynolds stresses ,$\overline{u_i' u_j'}$'s, may have different scales and may develop differently in a particular flow. The transport equations are derived in exact form, but they contain higher order correlations which must be modeled. The advantage of these exact equations is that terms accounting for buoyancy, rotation, streamline curvature, etc. are introduced automatically. Although the need to model the Reynolds stresses has been eliminated in this approach, the task of modeling the different terms in the transport equations has increased significantly. Also, there is no unanimity among various investigators regarding the structure of the different modeled terms.

At the present time, this is the most comprehensive turbulence model which has been used with reasonable success for turbulence flows in practical engineering applications. However, it still requires formidable computational effort as a transport equation for each Reynolds stress component is required, and the basic field equations must be solved.

Direct Numerical Simulation (DNS)

In the last fifteen years, with the rapid progress in supercomputer technology, a new methodology has emerged in the study and description of turbulent flows (Grotzbach, 1983; Schumann and Friedrich, 1985). This method is "Direct Numerical Simulation," and it involves solving the exact governing equations for the detailed time development of the flow field. The technique does not use any closure modeling, and no assumptions are made concerning the turbulent behavior of the flow. This approach allows one to simulate and study the fundamental physics of turbulent flows by resolving all relevant length and time scales. However, currently the possibility of using this method to solve practical engineering problems is remote. Aside from potential numerical difficulties, the wide range of time and space scales that must be resolved is presently and for the near future, well beyond the capabilities of any existing computer system. The resolution of this wide range of time and space scales, currently restricts the use of DNS to very idealized flows at low Reynolds number. Nevertheless, this is a novel research tool which has provided a wealth of information regarding the structure of turbulence.

Large Eddy Simulation (LES)

This approach is similar to DNS but appears to have better potential for treating higher Reynolds number flows (Grotzbach, 1983; Schumann and Friedrich, 1985). It involves "prefiltering" the flow field variables into a "large scale" component and a "subgrid" component. This technique was first used in meterological sciences to describe the effects of small-scale turbulence on the larger flow patterns.

In a LES, the large-scale structure, which is unique to a specific flow, is computed explicitly from the governing equations and only the remaining unresolvable subgrid dynamics are modeled. This is the major difference of LES over the traditional moment methods. In a typical moment method, all the information regarding the structure of the flow is lost through the global averaging process. Therefore, it is expected that LES, which resolves the large-scale motion and contains subgrid models to account for the small-scale motion, would prove to be more reliable and more universally applicable as compared to the traditional moment methods. The LES has been used in numerous, nonreacting, constant-density flow simulations, (Clark, et al.,

1979; Deardorf, 1970) but a rigorous application to reacting flows has not been reported. Also, use of this approach to solve practical problems is very expensive.

Nonlinear k-ϵ and k-l models

The turbulence models described in the previous paragraphs are numerically complex and expensive to use. Moreover, these models are untested in solving practical engineering problems. In this respect, the turbulence model which may prove to be a logical compromise between the k-ϵ model and the methods discussed above is the nonlinear k-ϵ model (Speziale, 1987).

This turbulence model was proposed to update the traditional linear k-ϵ and k-l models, while maintaining the same level of mathematical complexity. The model in essence adds nonlinear terms to the expression for the Reynolds stress tensor. These nonlinear terms are quadratic in the mean-sqare velocity gradient. The functional form of the Reynolds stress tensor may be described as (Speziale, 1987);

$$\tau = \tau[\nabla\overline{v},\ \frac{D(\nabla\overline{v}}{Dt},\ k,\ l,\ \overline{\rho}] \tag{3.56}$$

This model satisfies the principles of 1) general coordinate and dimensional invariance, 2) realiability, and 3) the material frame indifference in the limit of two-dimensional turbulence.

The simplest mathematical structure of the nonlinear model which satisfies all these constraints may be written as,

$$\tau_{ij} = -\frac{2}{3}\overline{\rho}k\delta_{ij} + \overline{\rho}k^{1/2}k\overline{D}_{ij} + C_D\overline{\rho}^2[\overline{D}_{im}\overline{D}_{mj} - \frac{1}{3}\overline{D}_{mn}\overline{D}_{mn}\delta_{ij}] \tag{3.57}$$
$$+C_E\overline{\rho}l^2[\dot{\overline{D}}_{ij} - \frac{1}{3}\dot{\overline{D}}_{mm}\delta_{ij}]$$

where, C_D and C_E are dimensionless constants, $l = C[(k^{3/2})/\epsilon]$, $\overline{D}_{ij}$ = time-averaged deformation tensor and $\dot{\overline{D}}_{ij}$ = convected derivative of $\overline{D}_{ij}$.

The nonlinear k-ϵ model differs from the linear version by the addition of the two nonlinear terms on the right hand side of the equations of motion as shown in Equations 3.58-3.60.

x-component:

$$\frac{\partial}{\partial x}(\overline{\rho u u}) + \frac{\partial}{\partial y}(\overline{\rho v u}) + \frac{\partial}{\partial z}(\overline{\rho w u}) \frac{\partial}{\partial x}(\mu_e \frac{\partial \overline{u}}{\partial x} - \frac{\partial}{\partial y}(\mu_e \frac{\partial \overline{u}}{\partial y}) - \frac{\partial}{\partial z}(\mu_e \frac{\partial \overline{u}}{\partial z})$$
$$= -\frac{\partial \overline{p}}{\partial x} - \frac{2}{3}\overline{\rho}k + \frac{\partial}{\partial x}(\mu_e \frac{\partial \overline{u}}{\partial x} + \frac{\partial}{\partial y}(\mu_e \frac{\partial \overline{v}}{\partial x}) + \frac{\partial}{\partial z}(\mu_e \frac{\partial \overline{w}}{\partial x})$$
$$-1.68\frac{\partial}{\partial x}\{\frac{\mu_e^2}{\overline{\rho}k}[(\frac{\partial \overline{w}}{\partial x})^2 + 2(\frac{\partial \overline{w}}{\partial y})^2]\} + 1.68\frac{\partial}{\partial y}[\frac{\mu_e^2}{\overline{\rho}k}(\frac{\partial \overline{w}}{\partial x})(\frac{\partial \overline{w}}{\partial y})] \quad (3.58)$$

y-component:

$$\frac{\partial}{\partial x}(\overline{\rho u v}) + \frac{\partial}{\partial y}(\overline{\rho v v}) + \frac{\partial}{\partial z}(\overline{\rho w v}) - \frac{\partial}{\partial x}(\mu_e \frac{\partial \overline{v}}{\partial x} - \frac{\partial}{\partial y}(\mu_e \frac{\partial \overline{v}}{\partial y}) \quad (3.59)$$
$$-\frac{\partial}{\partial z}(\mu_e \frac{\partial \overline{v}}{\partial z}) = -\frac{\partial \overline{p}}{\partial y} - \frac{2}{3}\overline{\rho}k + \frac{\partial}{\partial x}(\mu_e \frac{\partial \overline{u}}{\partial y} + \frac{\partial}{\partial y}(\mu_e \frac{\partial \overline{v}}{\partial y}) + \frac{\partial}{\partial z}(\mu_e \frac{\partial \overline{w}}{\partial y})$$
$$+1.68\frac{\partial}{\partial x}[\frac{\mu_e^2}{\overline{\rho}k}(\frac{\partial \overline{w}}{\partial x})(\frac{\partial \overline{w}}{\partial y})] - 1.68\frac{\partial}{\partial y}\{\frac{\mu_e^2}{\overline{\rho}k}[(\frac{\partial \overline{w}}{\partial y})^2 + 2(\frac{\partial \overline{w}}{\partial x})^2]\}$$

z-component:

$$\frac{\partial}{\partial x}(\overline{\rho u w}) + \frac{\partial}{\partial y}(\overline{\rho v w}) + \frac{\partial}{\partial z}(\overline{\rho w w}) - \frac{\partial}{\partial x}(\mu_e \frac{\partial \overline{w}}{\partial x}) - \frac{\partial}{\partial y}(\mu_e \frac{\partial \overline{w}}{\partial y})$$
$$-\frac{\partial}{\partial z}(\mu_e \frac{\partial \overline{w}}{\partial z}) = -\frac{\partial \overline{p}}{\partial z} - \frac{2}{3}\overline{\rho}k + \frac{\partial}{\partial x}(\mu_e \frac{\partial \overline{u}}{\partial z} + \frac{\partial}{\partial y}(\mu_e \frac{\partial \overline{v}}{\partial z}) + \frac{\partial}{\partial z}(\mu_e \frac{\partial \overline{w}}{\partial z}) \quad (3.60)$$

It is shown by Speziale (1987), that inclusion of the nonlinear terms results in more accurate prediction of normal Reynolds stress effects. One example is that the model predicts secondary flow in non-circular ducts, a physical phenomenon which is observed experimentally. This is an important advancement over the linear model. The linear model is inherently incapable of simulating the secondary flow, as it considers the normal stresses, τ_{ii}, to be identical. On the other hand, the normal stresses calculated using the nonlinear model have different magnitudes.

It is also demonstrated that the nonlinear model more accurately predicts separated turbulent flows. Prediction of the reattachment point for turbulent flow over a backward-facing step is more realistic using this model compared to the standard linear model (Speziale, 1987).

3.8.3 Incorporation of Non-linear k-ϵ Model in the 3-D Code

The process of incorporating the nonlinear k-ϵ model into the three-dimensional code is underway. Description of the Reynolds stress tensor based upon this model is implemented in the basic field equations. The resulting form of the equation of motion is very complicated in its general form. Thus, the differential equations are simplified assuming idealized and standard geometry (e.g., rectangular duct). The structure of the resulting equations of motion considering the nonlinear hypothesis were shown in Equations 3.58-3.60.

The extra source terms (the last two) on the right hand side of Equations 3.58-3.60 are due to the nonlinear hypothesis. Only the terms which are significant for the geometry under consideration (rectangular duct) have been included. These additional nonlinear source terms are included in the existing three-dimensional code.

Preliminary predictions with the new model are currently being made in liquids. The early indications suggest that the magnitudes of the hydrodynamic parameters are identical to the predictions obtained using the standard k-ϵ model, though their distributions are significantly different. The magnitude of the transverse velocities obtained using this approach is approximately 1% of the axial mean-sqare velocity field. Work will begin shortly to predict the transverse velocity field in gaseous systems.

Focus of the research effort is presently directed towards more detailed evaluation of this model in liquid and gaseous systems in turbulent channel flow to compute the magnitude of the secondary flow streams. Based on this evaluation, it will be decided whether the nonlinear k-ϵ model can be used to improve performance of the three-dimensional code. In addition, review of the other turbulence models is continuing for possible incorporation in later versions of the comprehensive code.

3.8.4 Conclusions

The major purpose of this task was to enhance the capability of the three-dimensional comprehensive code to predict the turbulent flows. This was initiated by reviewing and evaluating the available turbulence models. Subsequently, a model was selected for incorporation into this code.

In the last two decades, several sophisticated turbulence models have been proposed, including: Reynolds stress transport, direct numerical simulation,

and large eddy simulation. Though these models are successful in providing better understanding of turbulence, they have not been used for solving practical engineering problems due to their complexity.

Recently, a nonlinear k-ϵ model has been proposed to update the standard k-ϵ model. This model describes the Reynolds stress tensor through a nonlinear expansion of Boussinesq hypothesis. In turbulent flows, where normal stress effects are significant, this method seems to provide better estimates of transport properties. In the case of turbulent flows in ducts and channels, the use of this closure technique simulates secondary flow streams.

This model is currently being evaluated for the three-dimensional code. The governing equations are very complicated when this model is incorporated. However, the equations simplify significantly when used for a simpler geometry. In the case of a rectangular duct, the mean-sqare velocity field simulated via this nonlinear approach is different compared to the predictions obtained using the standard k-ϵ model. The predictions also show distinct zones of secondary transverse flow. Testing is continuing with both liquid and gaseous systems.

3.9 Summary of Submodel Development

Comprehensive combustion computations allow for the coupling of many physical and chemical processes thus providing a tool to study synergestic effects of multiple subcomponents. The overall predictive capability of the 3-D combustion code will only be as good as the weakest submodel. This section has summarized development and independent evaluation on several critical submodels necessary for the 3-D model: radiation, char oxidation, turbulent dispersion of particles, nitrogen oxide formation, carbon-monoxide formation, carbon-monoxide partial equilibrium, coal devolatilization, and turbulence. The radiation and turbulence submodels have been formulated in 3-D geometries. The turbulence submodel is currently under evaluation in a 3-D code. The other submodels have been implemented only in 2-D axi-symmetric geometries. A summary of these seven studies appears here.

3.9.1 Radiation

1. All discrete ordinates radiation flux approximations considered, i.e. S_2, S_4, S_6 and S_8, predict radiative transfer in two-dimensional rectangular enclosures containing absorbing-emitting-scattering media with accpetable accuracy. However, S_2 and S_4 were shown to be more acceptable in two-dimensional enclosures as these consume considerably less computer time with little loss in accuracy for these simpler geometries.

2. In three-dimensional rectangular enclosures, the S_2 predictions are grossly in error. However, comparable prediction accuracy is obtained using S_4, S_6 and S_8 approximations. The S_4 is, once again, considered adequate.

3. Radiative transfer in a three-dimensional rectangular enclosure is highly sensitive to uncertainties in the temperature of the medium, significantly sensitive to the extinction coefficient and the scattering albedo, and rather insensitive to the furnace length and wall emissivity.

3.9.2 Char Oxidation

1. The nonlinear nature of the Arrhenius law has been shown to have significant implications on the method of correlating the Arrhenius parameters to data. A derivation has been presented which traces a rigorous data analysis technique to fundamental features of the data being correlated while preserving as many desirable statistical properties as possible. The resulting method of data analysis differs substantially from the most commonly used to correlate data with the Arrhenius law.

2. The common approach to correlating data with the Arrhenius law comprises both the fit of the data inside of the extrapolation of the results outside of the temperature range over which it is measured. In general, the more common approach overemphasizes the low temperature data in determining the parameters for the Arrhenius expression. This biasing toward the low temperature data and the inability of the common approach to produce parameters with desirable statistical properties has the potential of producing correlations so poor that the Arrhenius law would incorrectly be rejected as the proper fit of the data. This poor correlation of the data is amplified when the Arrhenius law is extrapolated beyond the range of the data on which its parameters are based.

3. The parameters determined from the common approach can lie well

outside of high-confidence contours for the true (population) parameters. A rigorous analysis of these contours shows that they are not simple rectangles,as implied by stating their extreme values. They are also not elliptical, as would be predicted from an extension of techniques used in analyzing linear equations. They are slender loops which illustrate both the nonlinearity of the equation and the correlation of the parameters with each other.

4. A reexamination of many sets of heterogeneous reaction rate data shows that features of past comparisons of trends have been inappropriately interpreted as decreases in char reactivity at high temperatures when, in fact, they are artifacts of data analysis. Reanalysis of several sets of data have been completed with the more rigorous approach.

3.9.3 Turbulent Dispersion of Particles

1. A first-principles approach to describing particle dispersion was developed as an extension of stochastic process modeling and turbulence theory. The model requires no adjustable parameters and is independent of any particular turbulence model.

2. The submodel does require a description of the turbulent flow field in terms of the mean-sqare velocities and Lagrangian autocorrelation functions. Approximations for these in terms of parameters from the k-ϵ model have yielded reasonable results.

3. This submodel has been rigorously evaluated by comparison to exact solutions, the most accurate alternative models, and experimental data. In all cases, the model was both an accurate and efficient method of describing turbulent dispersion. The model predicted the experimental data within its inherent error over a wide range of flow conditions.

4. The turbulent dispersion model forms a useful framework for comprehensive computer codes. Adjustable parameters need to be used in these formulations. Side-by -ide comparisons of the new submodel performance compared with an existing approach allows us to conclude that the new approach increases the computational efficiency and robustness of the simulations while decreasing the total number of required particle simulations.

3.9.4 Nitric Oxide Submodel

1. The simulation of 30 new cases, in addition to the extensive predictions made by Hill (1984) provide a broad further evaluation of the NO_x submodel. The success of the NO_x submodel predictions is attributed to the ability of PCGC-2 to model the overall flame structure, an adequate global NO mechanism and kinetic rate expressions, and the coupling of the chemistry reactions with turbulence in the reactor.

2. Within the accuracy of the predicted temperature and major species and the range of experimental error, the NO_x submodel provided reliable predictions for pulverized fuel gasification and combustion or bituminous and subbituminous coals at moderate and extreme fuel-rich conditions. The impact of pressure was properly predicted for the gasification of Utah bituminous coal.

3. Fuel-rich char oxidation predictions were found to differ substantially from observed effluent concentrations. An investigation suggested that this difference resulted from the effects of temperature and the low volatiles content of the char. Reasonable agreement was demonstrated for variation in primary zone stoichiometric ratio and secondary air staging location for staged combustion cases in a sub-scale reactor, although the model predicted higher NO concentrations in the early region of the reactor, and lower values at the exit.

4. The role of temperature in NO decay was found to be significant. This is expected because the kinetic expressions for homogeneous and heterogeneous decay was exponential in temperature. For the gasification cases, the rate and extent of No decay was highest in the fuel-rich regions where appreciable concentrations of HCN exist. Homogeneous NO decay is proving to be more significant than heterogeneous decay.

3.9.5 Carbon Monoxide Submodel

1. The inability of early coal combustion models to accurately predict species concentrations for CO and CO_2 was thought to be partly caused by ignoring the kinetic considerations of the reaction chemistry. A complete kinetic treatment of all chemical processes occurring in the reactor was found to require too great an increase in computational time to be practical with the current generation of computer technology. Using a partial equilibrium method to

consider the phenomenon was found to account for most of the effects of kinetics, including the issue of coupling, while requiring an acceptable increase in computation time to reach a solution.

2. In general, reactor temperature and species concentrations of CO, O_2, and CO_2, were most affected by use of the non-equilibrium CO model instead of the constant equilibrium model. Water concentrations were also affected to a lesser degree. Other model predictions such as gas velocities and mixture fractions were only slightly affected. The most common effect was to delay the oxidation of CO to CO_2 until later in the reactor causing a larger flame zone, lower temperature peaks, and accompanying changes in the consumption of O_2.

3. Use of the non-equilibrium model also had a significant effect on the robustness or usability of PCGC-2 as a whole. Large increases in computational time were sometimes seen as a result of the CO model. In addition to the time increase, many cases were more difficult to converge requiring greater skill in choosing under-relaxation factors.

4. Choice of rate parameters of use with the non-equilibrium chemistry model had a secondary effect on the predictions and convergence times. Use of the different rate equations studied in this work did not have a noticeable effect on the model predictions but they were rarely significant in comparison to the difference between chemistry options. In general, the Howard equation gave faster and more easily converged solutions due to its greater linearity than did the equation suggested by Dryer.

5. Interpretation of the usefulness and reliability of the new chemistry model has been hampered by inadequacies in many other models that provide necessary information to the non-equilibrium model. These models such as the devolatilization and energy models which were specifically considered in this work, have been shown to have uncertainties that affect final predictions by at least the same order-of-magnitude as the effect of the CO non-equilibrium model and usually by an order-of-magnitude greater.

3.9.6 Coal Devolatilization

1. A generalized framework for coal devolatilization has been developed which includes in its scope most of the presently suggested devolatilization models and is organized around the concept of incorporating fundamental descriptions of coal into a kinetic reaction scheme which predicts the product

distributions.

2. This framework has been included, with the exception of the reactive intermediates in a 2-D comprehensive combustion code.

3. Most of the classical approaches to describing coal devolatilization have been reviewed and many have been set on a more useful and concise philosophical, mathematical, or correlative foundation.

3.9.7 Turbulence

1. In the last two decades several sophisticated turbulence models, namely Reynolds stress transport, direct numerical simulation, large eddy simulation etc. have been proposed. Though these models are successful in providing better understanding of turbulence, they have not been used for solving practical engineering problems due to numerical complexity. This investigation is initiated to review and evaluate the available turbulence models and subsequently incorporate some of the models into the 3-D code.

2. Recently, a nonlinear k-ϵ model has been proposed to describe the Reynolds stress tensor through a nonlinear expansion of Boussinesq hypothesis. In turbulent flows where normal stress effects are significant, this method has been shown to provide a better estimate of the velocity field. The model has successfuly predicted secondary flows in ducts and channels where the standard k-ϵ model has failed.

3. The nonlinear k-ϵ model has been incorporated into a 3-D code for duct geometries, thus simplifying the equations significantly.

4. In the case of a rectangular duct, the profile of the mean velocity field simulated via the nonlinear approach show distinct zones of secondary transverse flow. The testing is being continued with both liquid and gaseous systems.

Section 4

Research Task 4 - Fouling and Slagging

4.1 Introduction

The basic philosophy of this modeling effort is the integration of current technology in modeling ash deposition into a complete fouling/slagging model. The fouling/slagging model can operate as a submodel in the comprehensive combustion code, or as an independent code to predict mineral matter transformation during pulverized coal combustion. Although many mechanisms in mineral matter transformation have not been completely defined, this modeling effort is aimed at integrating current technology. Currently, the fouling/slagging submodel predictions have not been compared to laboratory or full-scale furnace experiments. However, before subcomponents (such as deposition rate calculations or physical property predictions) are included in the fouling/slagging submodel, evaluation of subcomponent predictions by comparison to experimental data should be performed independently.

4.2 Model Development

The initial development of the fouling/slagging submodel consisted of first defining the processes that dominated mineral matter transformations in pulverized coal combustion systems. The first process modeled was particle fragmentation. This is critical in predicting the deposition of smaller sub-

micron particles. The second step was the development of particle impaction model to include all mechanisms important to the transport of particles to surfaces. Then a physical properties submodel was developed to predict heat transfer characteristics of the mineral matter deposit. The last step in the initial development of the fouling/slagging submodel is the inclusion of a particle capture mechanism (currently being developed). The development and incorporation of these processes into the fouling/slagging submodel will be discussed in the following sections.

4.2.1 Particle Fragmentation

The development of the particle fragmentation subcomponent of the fouling/slagging submodel has been completed and details of the model formulation are presented elsewhere (Smith and Smoot, 1987). In summary, the particle fragmentation subcomponent currently is based on tracking the char/ash particle's porosity during the combustion process from a Lagrangian reference. As the char/ash particle burns, the particle structure changes and the porosity increases to a critical porosity (taken here as 70%), then the particle fragments into a set number of smaller particles of the same characteristics. The process of changing porosity and then fragmenting continues. This modeling effort represents a simple attempt to predict particle fragmentation in coal combustion simulations.

4.2.2 Particle Deposition

Deposition of particulates from flowing gas-solids suspension has many practical implications of vital importance. These range from the deposition of submicron particles on the human lungs to ash deposition and slagging in coal-fired systems. Although fouling and slagging due to coal-ash has been regarded as a major problem faced by the industry, apparently no attempt has been made to formulate a theoretical treatment for this problem as part of overall furnace numerical simulations.

The present work describes the first phase of an effort to develop a predictive scheme for ash deposition and slagging on the combustor walls in a pulverized-coal-fired system. The treatment includes contributions due to Brownian and eddy diffusion (also thermal diffusion when a temperature gradient exists), and inertial effects.

Theory

Detailed theoretical treatment for particulate deposition under the effects of inertial, diffusion and thermophoresis are available in the literature (Davies, 1966; Sehmel, 1970; Friedlander and Johnstone, 1957; Im and Chung, 1983; Byers, 1969; Walker *et al.*, 1979; Goren, 1977), and therefore only a brief description is included here. In short, the deposition of particulates from flowing streams is a consequence of a concentration gradient in the vicinity of the confining wall. Particle concentration profile envisaged for the near-wall region is shown in Figure 4.1 where the regions of the fully turbulent core, the buffer layer, and the laminar sublayer are demarcated (the temperature and velocity profiles would follow a similar pattern). The stop-distance, s, is the distance which the particles would penetrate due to the effect of inertia alone. The treatment presented below assumes that the particle concentration is uniform beyond the edge of the buffer layer. The rate of deposition may be obtained from: (Davies, 1966).

$$u^+_{dep} = (\frac{D_p}{\nu} + \frac{\varepsilon_p}{\nu})\frac{dC^+}{dy^+} \tag{4.1}$$

In Equation 4.1, + indicates a dimensionless form. D_p, the Brownian diffusivity of the particle, is estimated as

$$D_p = kT_g M \tag{4.2}$$

The mobility, M, is evaluated from the Millikan drag formula (Fuchs, 1964). The eddy diffusivity, ε_p, is obtained as

$$\varepsilon_p = \varepsilon_g / scp \tag{4.3}$$

where Sc_p^{-1} is obtained from Tachen's (Tachen, 1947) empirical formula

$$Sc_p^{-1} = 1 + \frac{exp(-\frac{\tau_f}{\tau_p} + 1) - 1}{1.72[(\frac{\tau_f}{\tau_p})^2 - 1]} \tag{4.4}$$

which holds for the case where $t \simeq \tau_f \cdot \tau_f$ and τ_p are obtained in the same way as in Im and Chung (1983). The eddy diffusivity for the gas phase is obtained in two steps as follows:

$$\frac{\varepsilon_g}{\nu} = (\frac{y^+}{C'})^3; \qquad y^+ < 5 \tag{4.5}$$

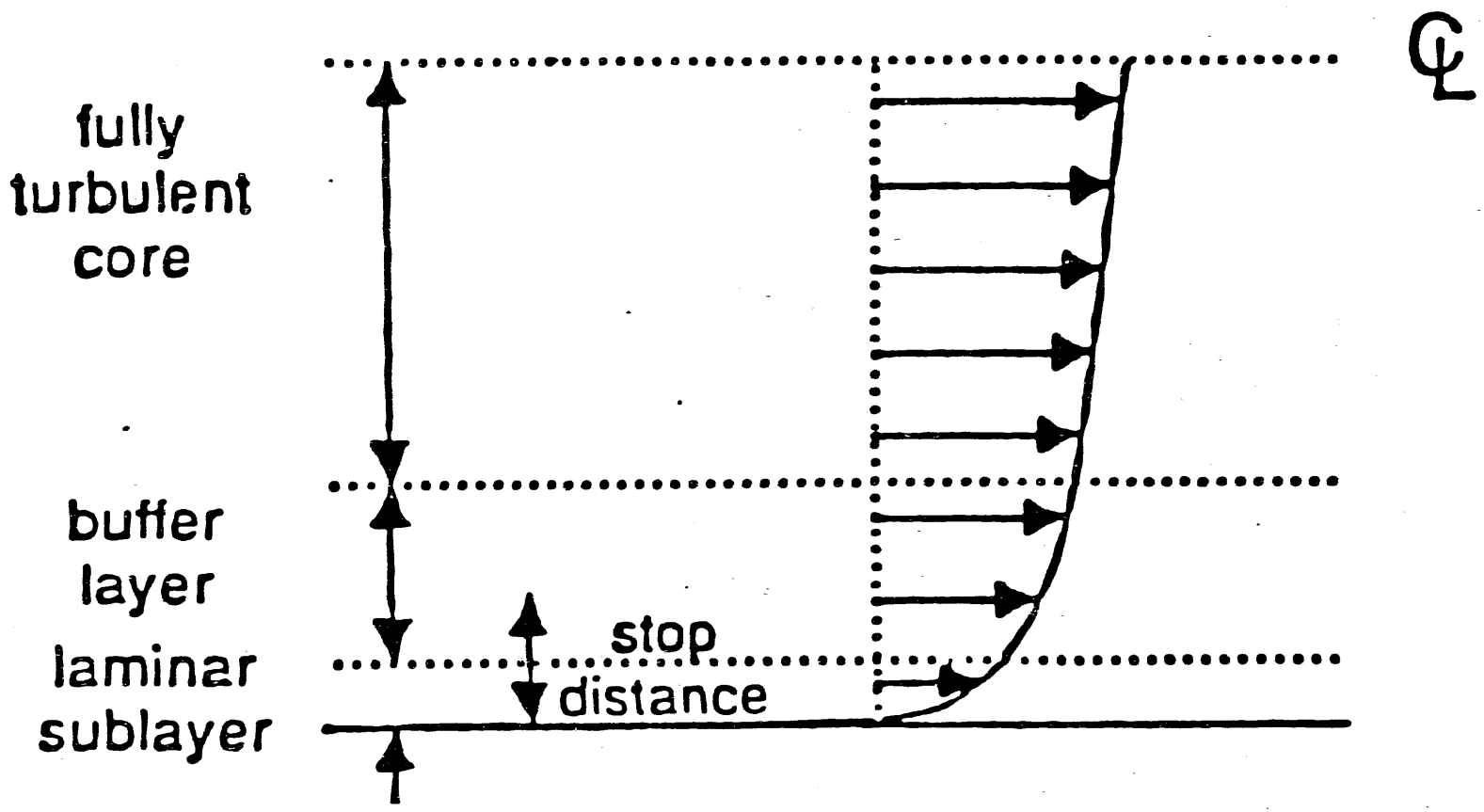

Figure 4.1: The Flow Regimes, and a Typical Concentration Profile.

$$\frac{\varepsilon_g}{\nu} = 0.4(y^+ + k_s^+)\{1 - exp[-(y^+ + k_s^+)/A^+]\}^2; \qquad 5 < y^+, 30 \qquad (4.6)$$

The empirical constant, C', is adjusted so that the same value for the eddy diffusivity is obtained from either Equation 4.5 or Equation 4.6 at the edge of the laminar sublayer (i.e., at $y^+ = 5.0$). Equation 4.6 is taken from Cebeci and Chang, (1978). In order to obtain the deposition velocity, Equation 4.1 is integrated

$$\frac{1}{u_{dep}^+}\int_{(C^+)_{s^+ + r^+}}^{1} dC^+ = \int_{s^+ + r^+}^{5} \frac{dy^+}{(\frac{D_p}{\nu} + \frac{\varepsilon_p}{\nu})} + \int_5^{30} \frac{dy^+}{(\frac{D_p}{\nu} + \frac{\varepsilon_p}{\nu})} \qquad (4.7)$$

In the above equation, $s^+ + r^+$, represents the "effective" stop-distance. The stop-distance is evaluated as

$$s = [v_r'(\frac{1}{Sc_p})^{1/2}]_s \tau_p \qquad (4.8)$$

where v_r', is the radial component of turbulent velocity at the stop-distance (estimated as that at the edge of the laminar sublayer). v_r is obtained as (Tennekes and Lumley, 1972)

$$v_r' \simeq 0.8 u_* \qquad (4.9)$$

u_*, the friction velocity, is related to the skin friction factor of the enclosure (Davies, 1966) which is estimated as (White, 1974)

$$\frac{1}{f} = 2log[\frac{Re(f)^{0.5}}{1 + 0.1(k_s/D_t)Re(f)^{0.5}}] \qquad (4.10)$$

$y^+ = 5.0$ and $y^+ = 30.0$ refer to the dimensionless distances from the wall to the edges of the laminar sublayer and the buffer layer, respectively.

Deposition without Thermophoresis

Integrating the first term, $(INT)_\ell$, of Equation 4.7, we obtain (Davies, 1966)

$$(INT)_\ell = C'(Sc_p)^{1/3}(\nu/D_p^{2/3}[\frac{1}{6}ln\frac{(1+\theta)^3}{1+\theta^3} + \frac{1}{\sqrt{3}}tan^{-1}\frac{2\theta - 1}{\sqrt{3}}]_{\theta_1}^{\theta_2} \qquad (4.11)$$

where

$$\theta = \frac{y^+}{C'}(\frac{\nu}{D_p Sc_p})^{1/3}. \tag{4.12}$$

While integration of the second term, $(INT)_b$, gives (Im and Chung, 1983)

$$(INT)_b = 2.5Sc_p[0.92ln\frac{30+k_s^+}{5+k_s^+} - 0.5(\frac{A^+}{30+k_x^+} - \frac{A^+}{5+k_s^+}) \tag{4.13}$$
$$-0.54\{(\frac{A^+}{30+k_s^+})^2 - (\frac{A^+}{5+k_s^+})^2]\}$$

Taking the integrated form of Equation 4.7 as a whole, we have

$$u_{dep}^+ = \frac{1 - C_{s^+ \cdot r^+}^+}{(INT)_\ell + (INT)_b} \tag{4.14}$$

Since at a distance $s^+ + r^+$ from the wall

$$C_{s^+ + r^+}^+ = \frac{u_{dep}^+}{(v_r')_{s^+ + r^+}^+} \tag{4.15}$$

We obtain upon rearranging

$$u_{dep}^+ = \frac{1}{(INT_\ell + (INT)_b} + \frac{1}{(v_r')_{s^+ + r^+}^+} \tag{4.16}$$

Equation 4.16 shows that three processes contribute to the overall process of deposition: 1) the $(INT)_\ell$ term is a measure of the contribution due to Brownian diffusion, 2) $(INT)_b$ that of eddy diffusion, and 3) the inertial contribution. In situations where $s^+ + r^+$ is greater than 5.0, particle deposition occurs solely due to the effect of inertia.

Deposition with Thermophoresis

In the presence of a thermal gradient, the contribution of Brownian diffusion of the deposition rate is insignificant (Im and Chung, 1983; Byers and Calvert, 1969). Under such conditions, integration of Equation 4.1 with

$$u_{dep}^+ = u_{th}^+ + C_{s^+ + r^+}^+ \quad at\ (S^+ + r^+);\ (s^+ + r^+) \leq 5 \tag{4.17}$$

yields

$$u^+_{dep} = \frac{1}{(INT_b + \frac{1}{u^+_{th}}} \tag{4.18}$$

where u^+_{th}, the thermal velocity of the particle, is given by (Im and Chung, 1983)

$$u^+_{th} = MF_{th} \tag{4.19}$$

with the thermophoretic force, F_{th}, evaluated as (Jacobsen and Brock, 1965)

$$F_{th} = -12\pi\mu r f(Kn)(\frac{\partial T}{\partial y}) \tag{4.20}$$

where

$$f(Kn) = \frac{rC_{tm}K[(\frac{k_g}{k_p} + C_tK)(1 + \frac{4}{3}aC_mKn) - \frac{4}{3}aC_mK]}{(1 + 3C_mK)(1 + 2\frac{K_g}{k_p} + 2C_tK)} \tag{4.21}$$

The temperature gradient is evaluated employing Reynolds analogy, as done in Im and Chung (1983). Once the deposition velocity is known, the rate of deposition may be estimated from a knowledge of the particle concentration at the node point in the computational domain that is close to the wall.

4.2.3 Physical Properties

The next step in model development was the prediction of the physical properties of the ash mineral deposit. The properties predicted were: the phase, the phase composition, heat capacity, thermal conductivity, density, liquid viscosity, liquid surface tension, and radiant surface emittance. A detailed description of the development of the physical properties subcomponent of the fouling/slagging submodel can be found elsewhere (Davies, 1988).

In summary, the liquid and solid properties of the deposit were predicted on the basis of the equilibrium molar liquid mixture. The residual liquid composition (as oxides) was determined from equilibrium considerations. Once the amount of solid phase species has been determined, the residual liquid composition was found by subtracting the total solid phase oxide composition from the bulk ash composition (as oxides).

Phase Equilibrium

The predictions of the phase and phase composition were based on chemical equilibrium. The algorithm used in this study was SOLGASMIX, developed by Gunnar Eriksson (1975). A detailed discussion of the algorithm is presented by Eriksson. In short, the prediction of the solid, liquid, and gaseous equilibrium is accomplished by minimization of the system's Gibbs free energy. A database of Gibbs free energy curve fits obtained from NBS (Eriksson, 1975) was reworked to cover a broader temperature range. Literature data were fit for 57 of the species in the database. The current database contains the Gibbs free energy curve fits for 7 gases, 40 liquids, and 42 solid mineral and complex oxide species.

Thermal Conductivity

Thermal conductivity of the residual liquid mixture was predicted using the correlation of Fin[illegible] (1976) or the data of Mills (1986). A database of the thermal conductivities of the solid species included in the equilibrium database was developed. The effective thermal conductivity of the liquid and solid/gas mixture was predicted using the semiempirical rule of Sugawara and Yoshizawa (1961).

Density, Heat Capacity, and Surface Emittance

Liquid density predictions were based on the particle molar surface tension of the oxide composition of the residual liquid. A database of the solid densities of the mineral species considered in the thermodynamic database was compiled. The effect of bulk density was included in predicting the effective deposit density.

A database of the heat capacities of the mineral species considered in the equilibrium database was compiled. This database formed the basis for predicting the liquid and solid heat capacities.

Data of surface emittance as a function of composition and temperature (evaluated from Boow and Goard [Smith and Smoot, 1982]) was statistically examined using stepwise regression analysis. Some 36 variables considered initially were added or dropped from the model, depending on their statistical significance. With this technique, ten variables were determined to be statistically significant in predicting the surface emittance of ash deposits.

4.2.4 Heat Transfer Calculations

A model was developed to solve the transient, one-dimensional heat conduction equation in a slab. Using the physical properties submodel predictions as a basis for estimating the density, heat capacity and thermal conductivity of the ash deposit, the heat transfer model can solve for the time-dependent temperature profile in the ash deposit. The transient 1-D heat conduction equation was cast into finite difference form and solved using a tridiagonal matrix algorithm. The numerical method used is described in Patanker (1980). At each time-step, the temperature profile required several iterations to converge to an acceptable solution. This is a result of the physical properties being a function of temperature.

The heat transfer submodel was coupled to the deposition submodel and integrated into a comprehensive combustion model to predict the transient build-up and heat transfer characteristics of a coal ash deposit. At each node of the combustion calculation, a different deposit thickness and temperature profile calculation was performed. Ash particle deposition fluxes and net heat transfer fluxes from the combustion zone to the wall surface were all based on clean wall conditions. In the absence of a particle capture mechanism, a constant fraction of particles was assumed to be captured by the depositing surface.

4.3 Results and Discussion

In general, each subcomponent of the fouling/slagging submodel was developed and compared to experimental data as independently as possible. After the inclusion of the subcomponents into the fouling/slagging submodel, calculations were performed in conjunction with a comprehensive coal combustion simulation.

4.3.1 Particle Fragmentation

The effect of particle fragmentation on the prediction of mean particle trajectories in an axi-symmetric reactor is shown in Figure 4.2. Comparison of these two figures clearly shows that particle concentration and deposition are altered when particle fragments are formed. The fragmentation process has

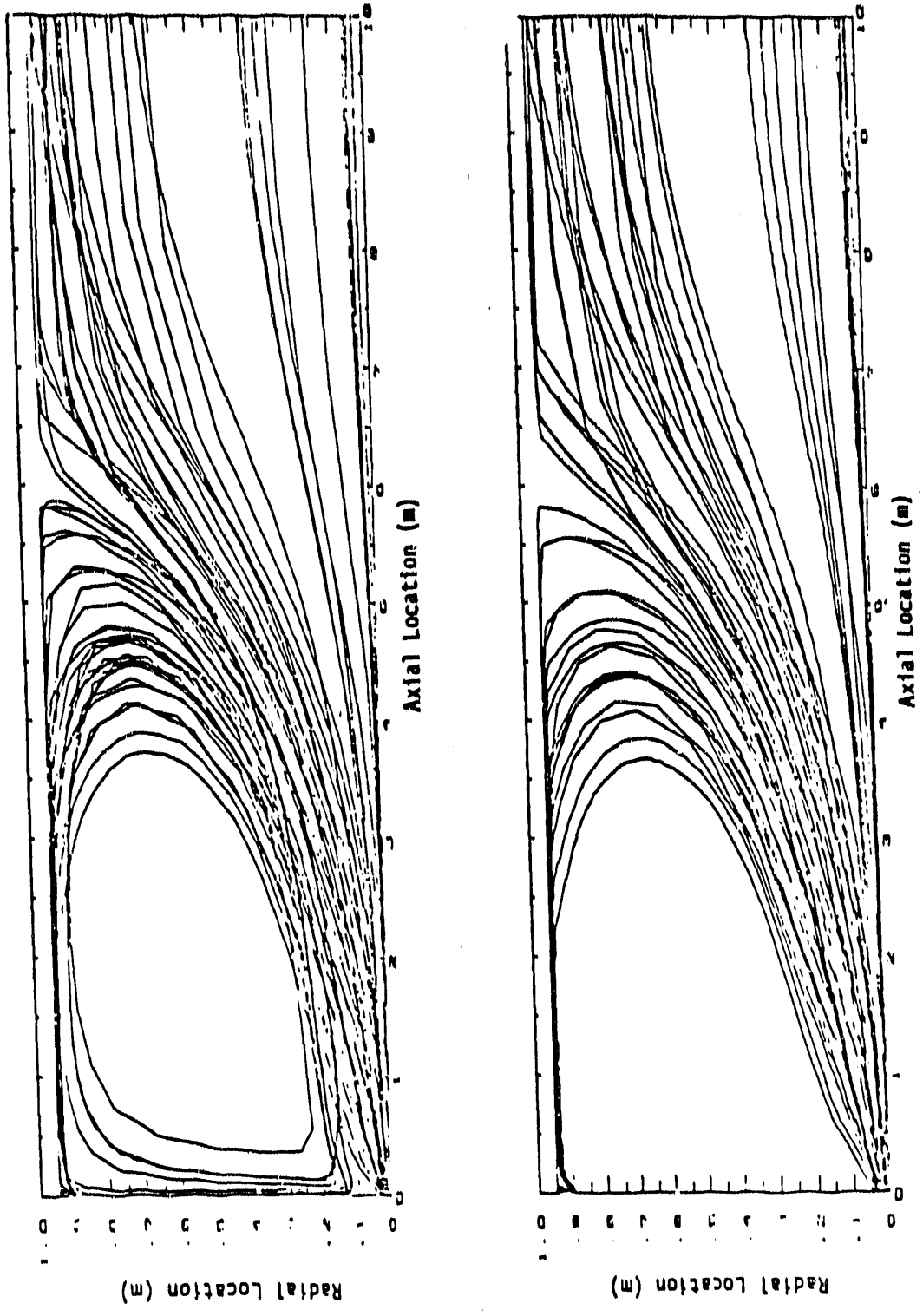

Figure 4.2: a) Predicted Particle Trajectories for the IFRF Case (Michel and Payne, 1980) without Fragmentation. b) Predicted Particle Trajectories with Fragmentation, Four Fragments per Particle.

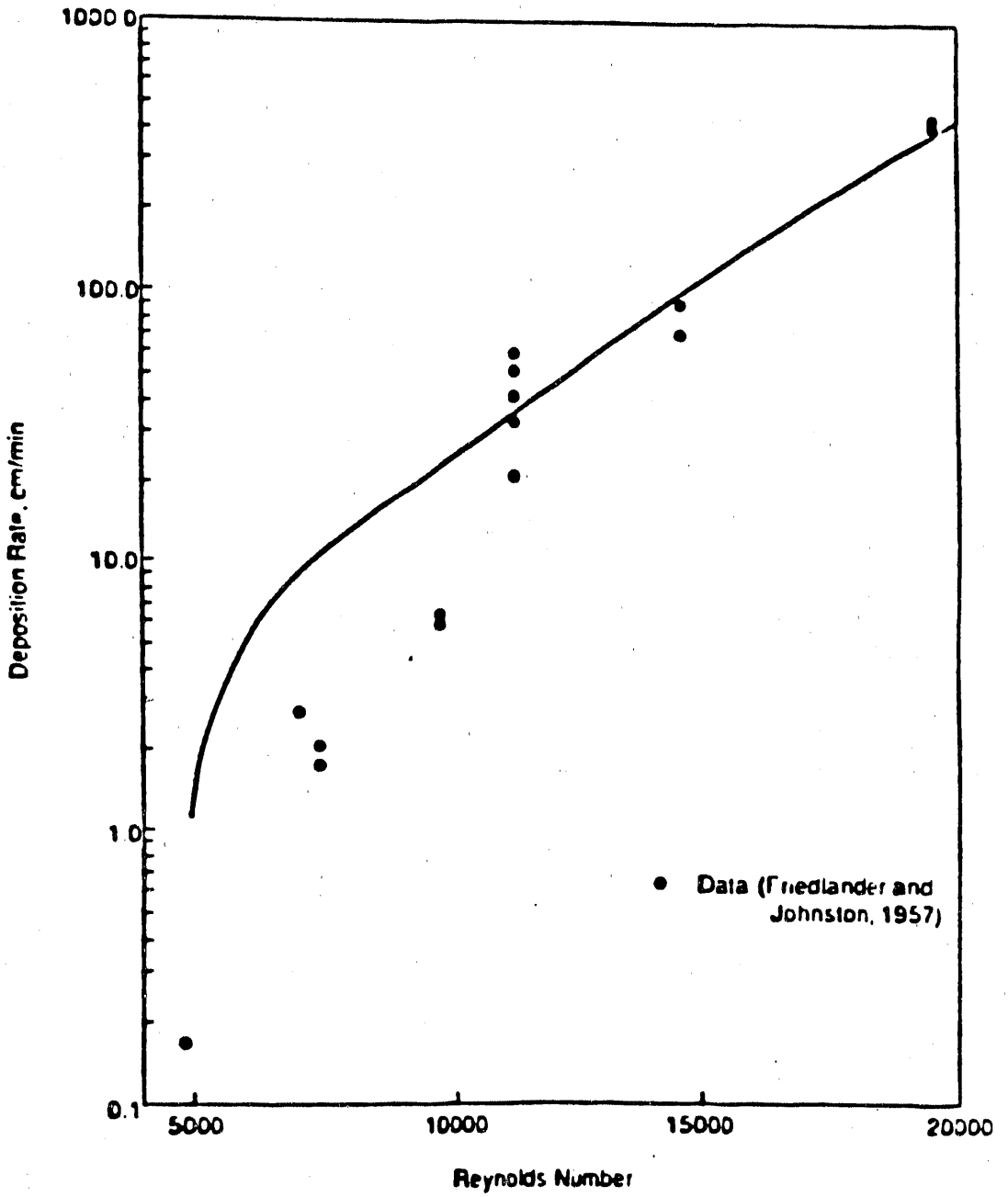

Figure 4.3: Predicted and Measured Deposition Rates of 0.8 μm Iron Particles in a 0.54 cm Diameter Glass Tube ($T_g = T_w = 293K$).

been shown to depend on particle size class and the particle's initial starting location (Smith and Smoot, 1987).

4.3.2 Particle Deposition

Predictions of the deposition model without thermophoresis are compared with the experimental data of Friedlander and Johnstone (1957) in Figures 4.3 and 4.4. These experiments used iron particles suspended in turbulent air flow, with Reynolds numbers of between 5000 and 30000, in glass tubes. The predictions show strong dependence of the deposition velocity on the Reynolds number of the fluid flow and the size of the particles.

Figures 4.5 and 4.6 depict the experimental (Byers and Clavert, 1969) and predicted collection efficiencies for sodium chloride particles onto a water-jacketed copper tube under the influence of thermophoresis. The collection efficiency is the cumulative percent of the incoming particulates that are deposited. Once again, the predictions are in satisfactory agreement with the experimental measurements. However, the predictions show clear minima in the collection efficiency at a particle size of about 1.0 μm, beyond which the collection efficiency increases rather sharply due to the effect of inertia. This eventual increase in collection efficiency is expected, because the stop-distance for larger particles is greater, and would fall beyond the laminar sublayer.

The predictions of a comprehensive combustion code using the deposition model as a subroutine, with and without allowance for particle fragmentation, are presented in Figure 4.7. The test case is that described by Asay (1982). The laboratory furnace used in the experiments was 0.2m in diameter and 1.5m long. A Wyoming subbituminous coal, with an ash content of 6.9% on a dry basis, was fed into the reactor at 10.2 kg/h. The figure shows that the rate of deposition is profoundly affected by the fragmentation of the particulates. This signifies the sensitivity of the deposition rate to particle size, as also observed in Figures 4.4, 4.5, and 4.6. The overall rate of deposition is estimated to be 2.68 kg/day without fragmentation, and 0.66 kg/day when the effect of fragmentation is included.

The results of this study indicate that the rate of deposition of particulates from a flowing stream strongly depends on the particle size and the Reynolds number of the flow. Increasing either of these increases the deposition rate. However, in the presence of thermal gradients, there is a minimum

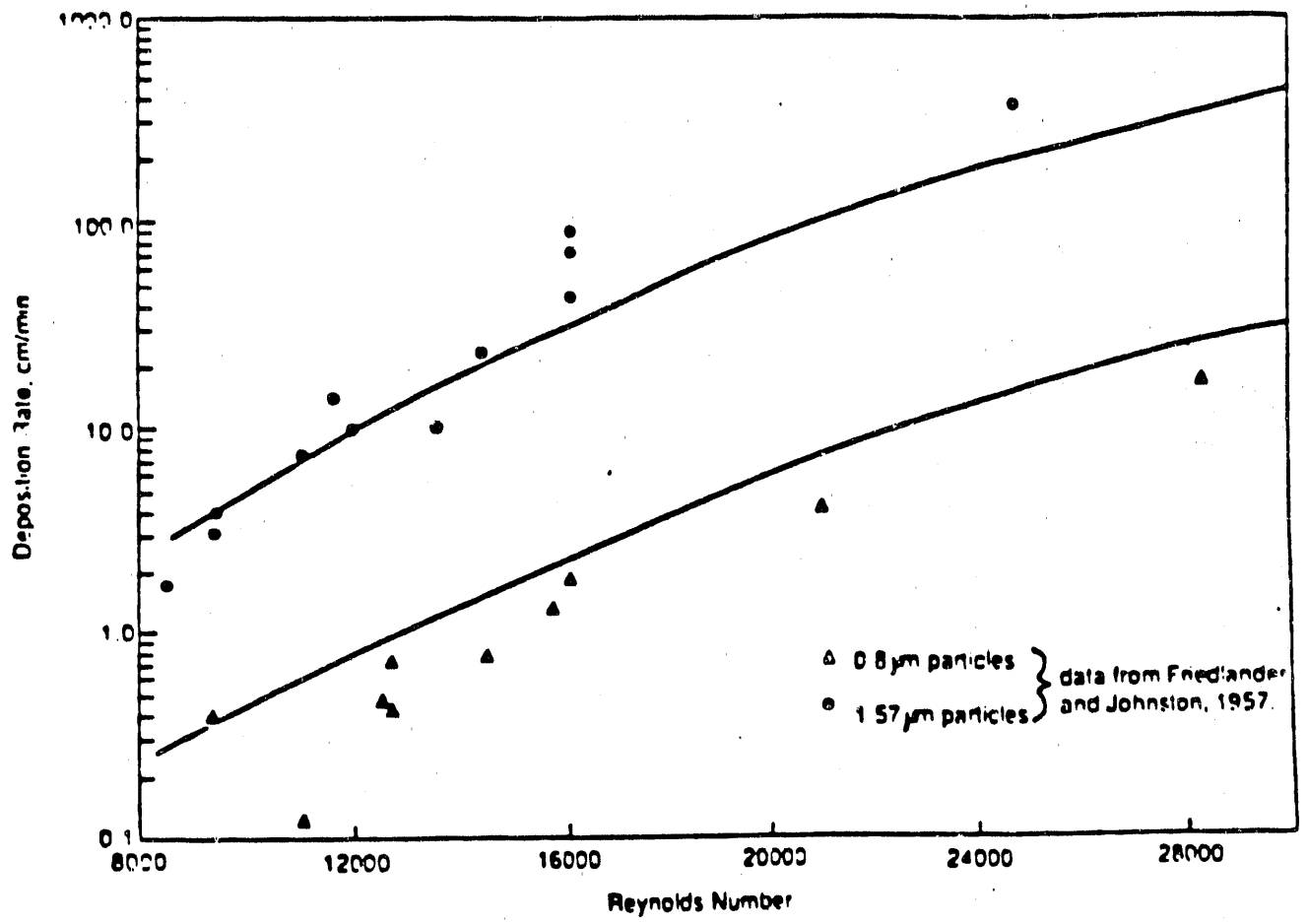

Figure 4.4: Predicted and Measured Deposition Rates of 0.8 μm and 1.57 μm Iron Particles in a 1.3 cm Diameter Glass Tube ($T_g = T_w = 293K$).

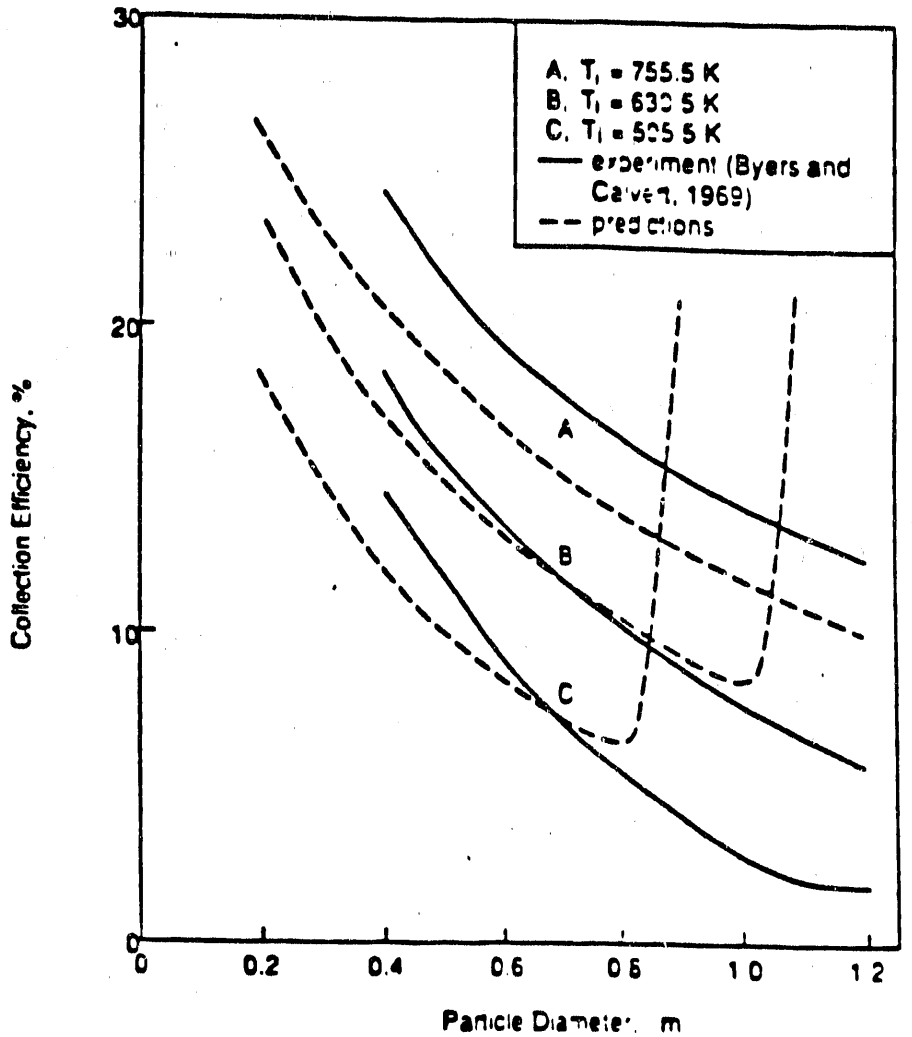

Figure 4.5: Effect of Temperature on the Collection Efficiency (Experimental Data from Byers and Calvert, 1969). $D_t = 7.92mm, L/D = 38.5, Q = 2950cm^3/s, T_w = 300K$.

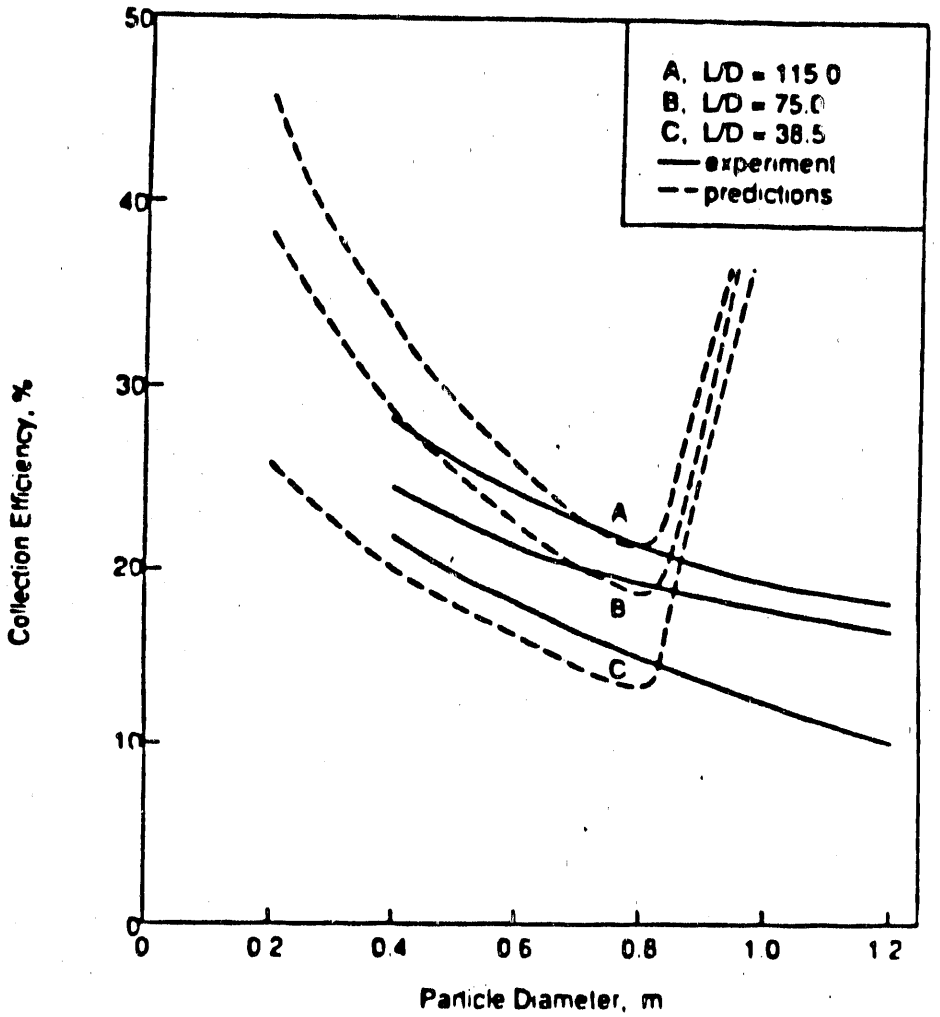

Figure 4.6: Effect of Length/Diameter Ratio on the Collection Efficiency (Experimental Data from Byers and Calvert, 1969). $D_t = 7.92mm, T_i = 755.5K, Q = 3965cm^3/s, T_w = 300K$.

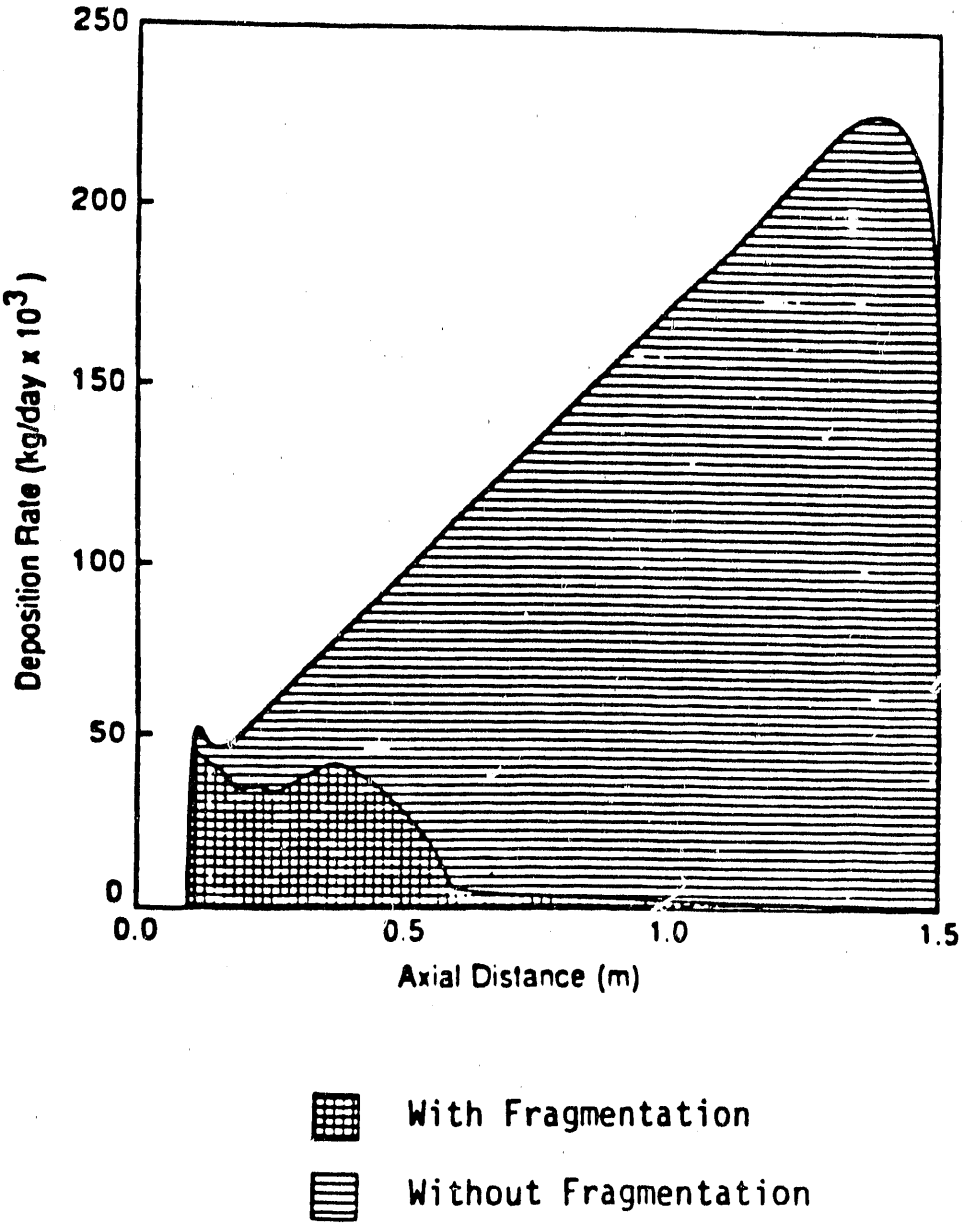

Figure 4.7: Predicted Rates of Particulate Deposition on the Furnace Wall With and Without Particle Fragmentation.

in the deposition rate (corresponding to a "critical" particle size) which depends on the flow characteristics, temperatures, particle density, and thermal conductivity. Particles smaller than this critical size are increasingly prone to deposition by thermophoresis, while larger particles are increasingly susceptible to deposition by inertia.

The significance of the work lies in its applicability to predicting ash deposition in coal-fired combustors. Combined with theoretical models to predict phase transformation, thermal properties and structure of the deposit (the development of which is currently underway) this study may have produced the only comprehensive combustion code capable of predicting slagging and fouling in a coal-fired furnace.

4.3.3 Phase Equilibrium

Predictions using SOLGASMIX, along with the database developed in this study, were compared to the experimental data of a liquidus curve obtained by Weed, et al. (1986). The ash studied by Weed was a Kiluau Iki Basaltic ash with a composition similar to that of coal ashes. Figure 4.8 shows the data comparison between model predictions using both the old database values and the newly developed database. Satisfactory agreement was achieved within the temperature range of Weed's data compared to the NBS database values. However, the general trend of the liquid curve in the lower temperature region (<400 K) was in error due to problems with the NBS curve fits being limited to higher temperature regions.

4.3.4 Thermal Conductivity

By using equilibrium calculations, in combination with thermal conductivity predictions, a comparison was made of model predictions to the thermal conductivity of ashes evaluated by Boow and Goard (Smith and Smoot, 1982). Figures 4.9 and 4.10 show the results of two of the predictions. The comparison for CSIRO No. 5 ash fails due to the premature appearance of a liquid phase. Considering only the solid phase, agreement between predictions and measurements for both ash samples here is within ±15%.

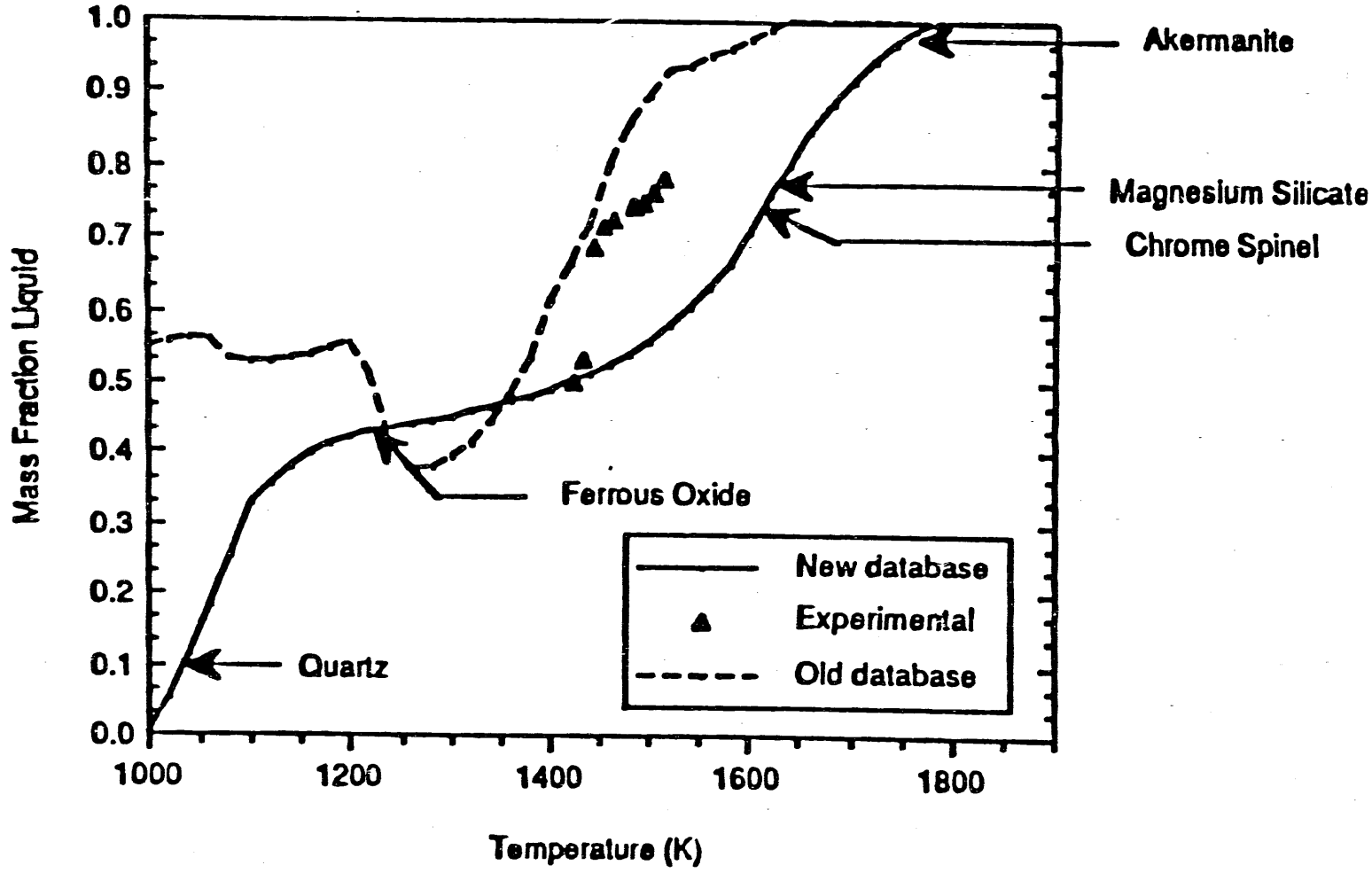

Figure 4.8: Liquidus Curve of Kilauea Iki Basalt Ash [Predictions with SOLGASMIX, Data of Weed, et al. (1986)].

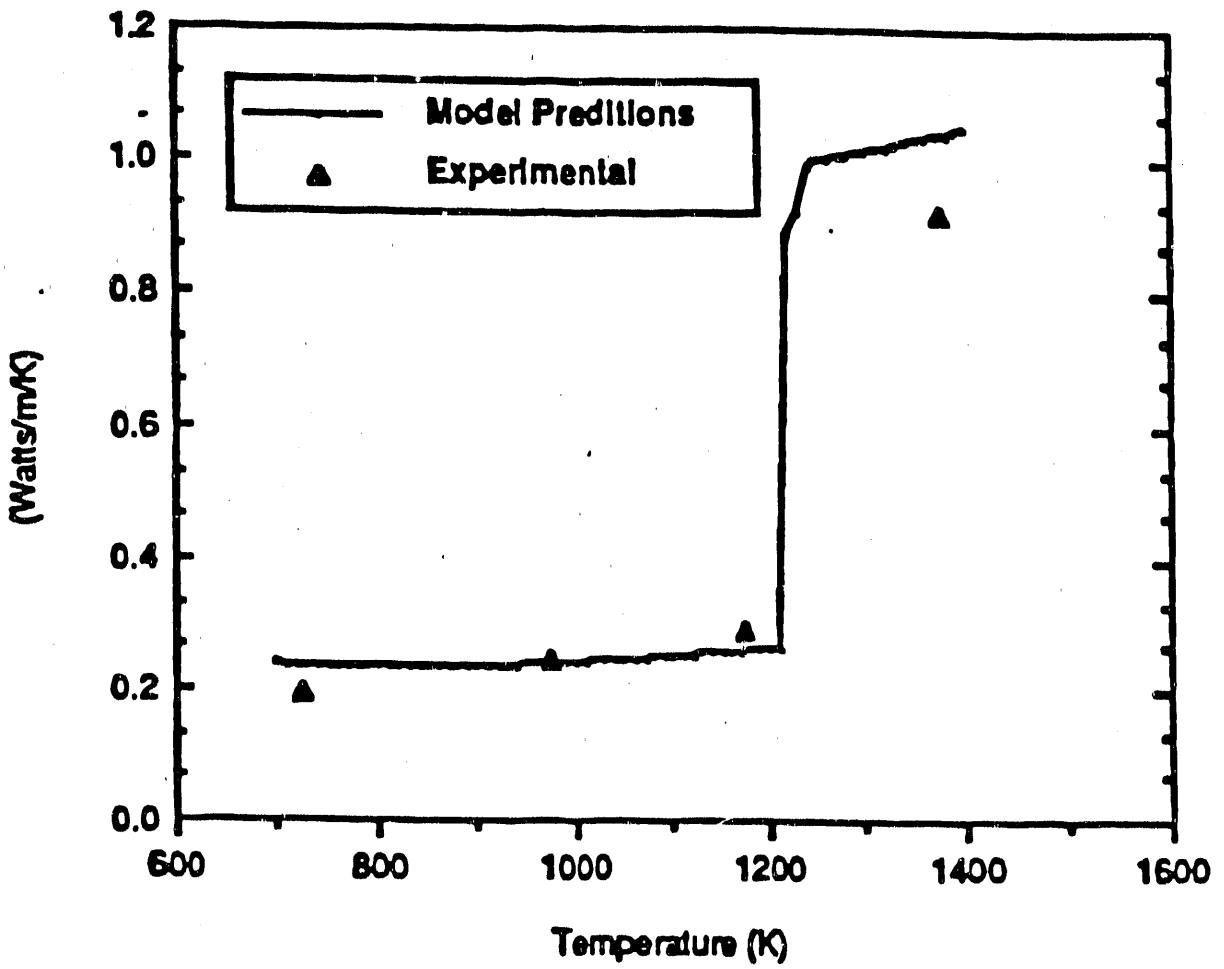

Figure 4.9: Thermal Conductivity Estimate of CSIRO No. 1 Ash Sample.

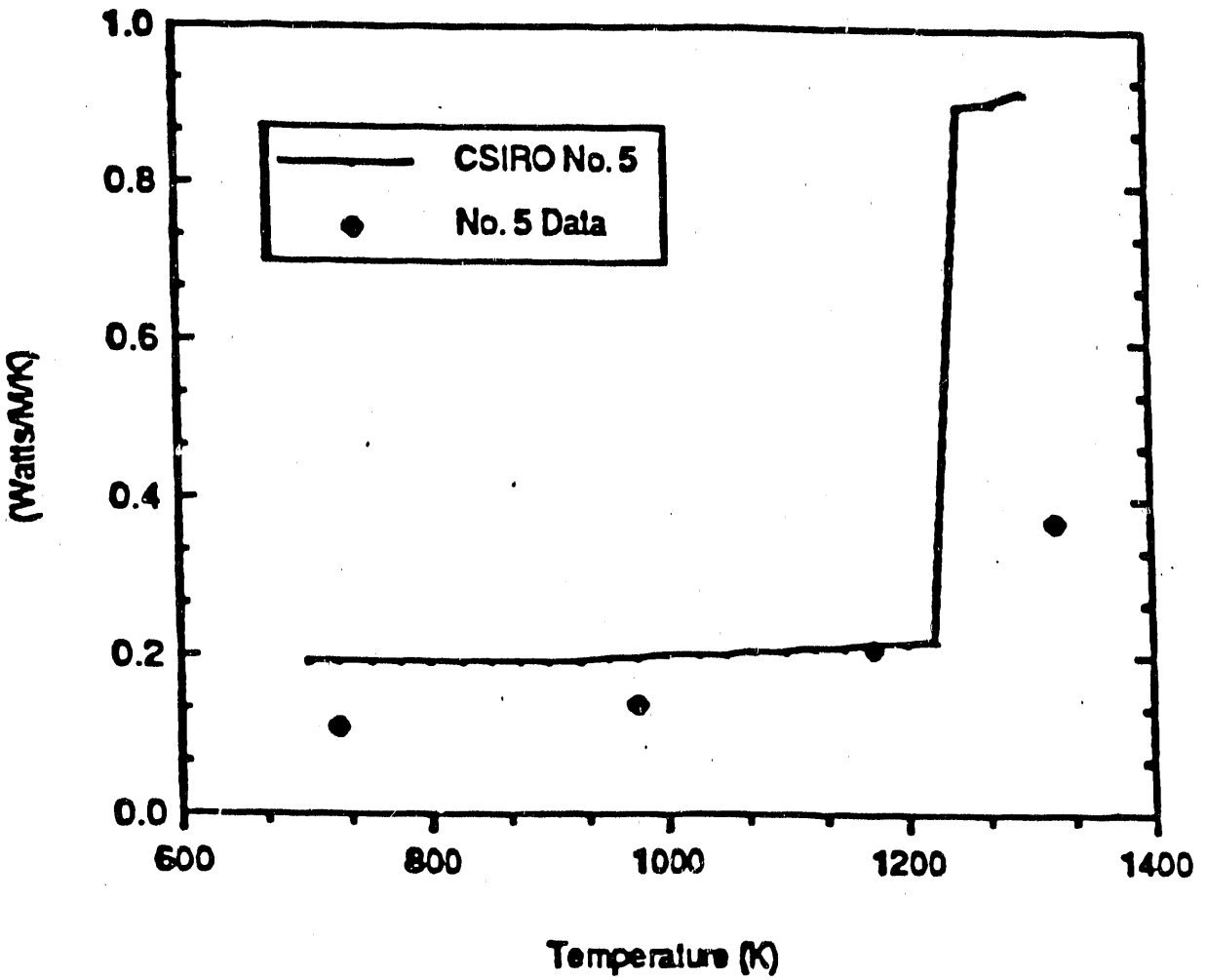

Figure 4.10: Thermal Conductivity Estimate of CSIRO No. 5 Ash Sample.

4.3.5 Density, Heat Capacity, and Surface Emittance

Comparison of the bulk densities of five Australian ashes was performed, and the results are shown in Table 4.1. The root-mean-square difference of model predictions and experimental data were found to be 0.066 grams/cc, or 6.2% of the mean. The accuracy of predicting the deposit heat capacity based on the database developed is believed to be less than 1%. This is based on the error reported in the literature.

Results of the statistical regression of surface emittance as a function of both bulk ash composition and surface temperature are shown in Table 4.2. The parameters that were found statistically significant, along with their respective estimates, are also shown in this table. The statistical set shown in this figure was reduced from a larger set of 36 variables in composition and temperature. The most statistically significant composition variables were found to be SiO_2, CaO and MgO, along with the Sm ratio and the Dolomite percentage. The silica ratio was found to be significant in lieu of the other composition variables. The root-mean-square error of the analysis was 0.09.

4.3.6 Heat Transfer Calculations

Predictions of a comprehensive combustion code using the deposition and heat transfer submodels as subroutines have been completed. The test-case chosen and described by Asay (1982) is a small-scale axi-symmetric furnace 0.2m in diameter and 1.5 m long. A subbituminous coal, with an ash content of 6.9% on a dry basis, was fed into the reactor at 10.2 kg/h. After ten hours of deposition, no liquid was formed on the ash surface. The major mineral species predicted was quartz (SiO_2), with minor amounts of anorthite ($CaAlSi_2O_8$), Nepheline ($NaAlSiO_4$), Hematite (Fe_2O_3), and Akermanite ($Ca_2MgSi_2O_7$). Mean deposit thermal conductivity and density were predicted to be 0.33 Watts/m/K and 1.55 grams/cc, respectively. Figure 4.11 shows the results of predicting the transient deposit thickness, surface temperature and surface emittance, respectively. These calculations were based on an assumed deposit porosity of 0.40.

To investigate the importance of the deposit porosity assumption on model predictions of deposit physical characteristics, a separate test case was run with a porosity of 0.60. The results of this run are shown in Figure

Table 4.1: Prediction of Porous Solid Densities.

Ash	$1 - \psi_s$	Measured Density (grams/cc)		Predicted Density (grams/cc)	
		Bulk	Solid	Bulk	Solid
CSIRO No. 1	.5084	1.52	2.99	1.43	2.82
CSIRO No. 5	.4116	1.28	3.11	1.21	2.95
CSIRO No. 9	.4016	1.02	2.54	1.08	2.70
CSIRO No. 12	.3663	0.89	2.43	0.95	2.59
CSIRO No. 25	.2000	0.59	2.95	0.55	2.75

Table 4.2: Statistically Significant Variables in Predicting Ash Emittance.

Variable	Definition	Estimate of Coefficient
T	Temperature (K)	-2.7158×10^{-3}
T^2	Square temperature	1.4000×10^{-6}
SiO_2	Weight percent silicon dioxide	5.6851×10^{-2}
$(SiO_2)^2$	Square of weight percent silicon dioxide	-5.3927×10^{-4}
CaO	Weight percent calcium oxide	1.8993×10^{-2}
MgO	Weight percent magnesium oxide	2.5837×10^{-2}
Sm ratio	$(MgO + Fe_2O_3 + SiO_2)/(Na_2O + CaO)$	6.2713×10^{-3}
Sm-T	Sm and T integration	-3.9000×10^{-6}
Dol percentage	$100x\ (CaO + MgO)/\ Fe_2O_3 + CaO + MgO + Na_2O + K_2O)$	6.7507×10^{-3}
Dol^2	Square of the dolomite percentage	-7.4100×10^{-5}

*Composition calculated as weight percents normalized as follows:
$SiO_2 + Al_2O_3 + Fe_2O_3 + CaO + MgO + Na_2O + K_2O = 100$

Thickness (mm)

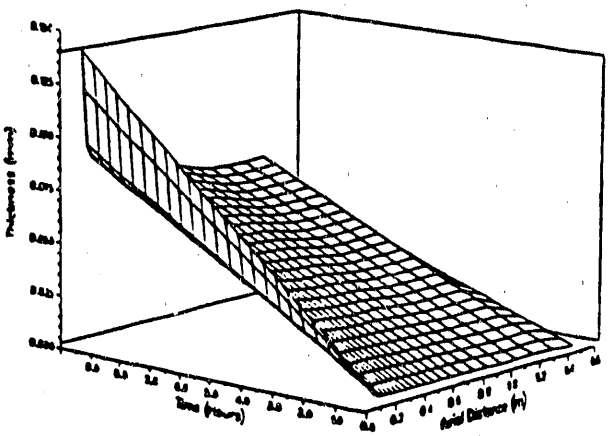

Surface Temperature (K)

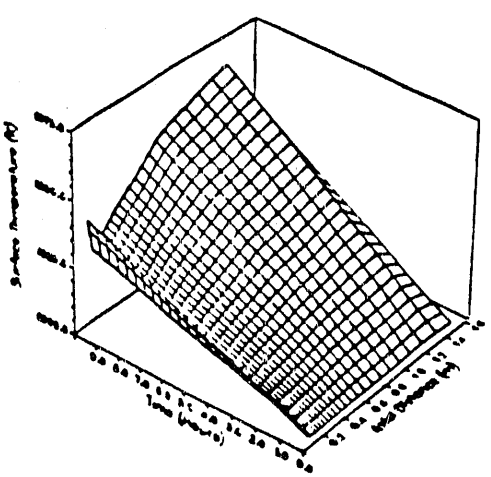

Surface Emittance

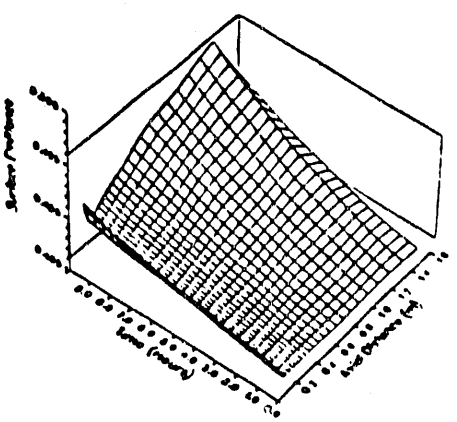

Figure 4.11: Deposit Thickness, Surface Temperature, and Surface Emittance of Asay Case (Deposit Porosity = 0.40).

4.12. Figures 4.11 and 4.12 show that the increase in deposit porosity produced an increase in the predicted surface temperature of more than 150 K. The increase in deposit thickness was directly proportional to the increase of porosity. A 33% increase in porosity produced 57% reduction in the thermal conductivity of the deposit. This study demonstrated that one of the dominating effects in the prediction of the thermal characteristics of ash deposits is knowledge of the deposit porosity.

4.4 Conclusions

Results of fouling and slagging submodel development indicate that the rate of particulate deposition from turbulent streams is highly dependent upon particle size and Reynolds number. An increase in either of these parameters produces an increase in the deposition rate. There exists a minimum in particulate deposition in the presence of a thermal gradient. This minimum corresponds to a "critical" particle size. Increasing the particle size beyond this "critical" point produced sharp increases in the deposition rate.

The thermal characteristics of an ash deposit strongly depend on the deposit porosity. Increases in deposit porosity produced a marked decrease in the deposit effective thermal conductivity, thus increasing the deposit surface temperature. All other properties that are a function of temperature will then be affected by changes in deposit porosity.

The significance of this task lies in its ability to predict particle deposition and thermal characteristics of the deposited material. Currently, a particle capture mechanism is being developed to estimate the fraction of particles that stick to the deposit surface. Upon completion of the capture mechanism, a data comparison can be made to small-scale reactors. In combination with a comprehensive coal combustion code, this type of modeling work could prove beneficial in isolating processes that dominate mineral matter transformations in coal combustion systems.

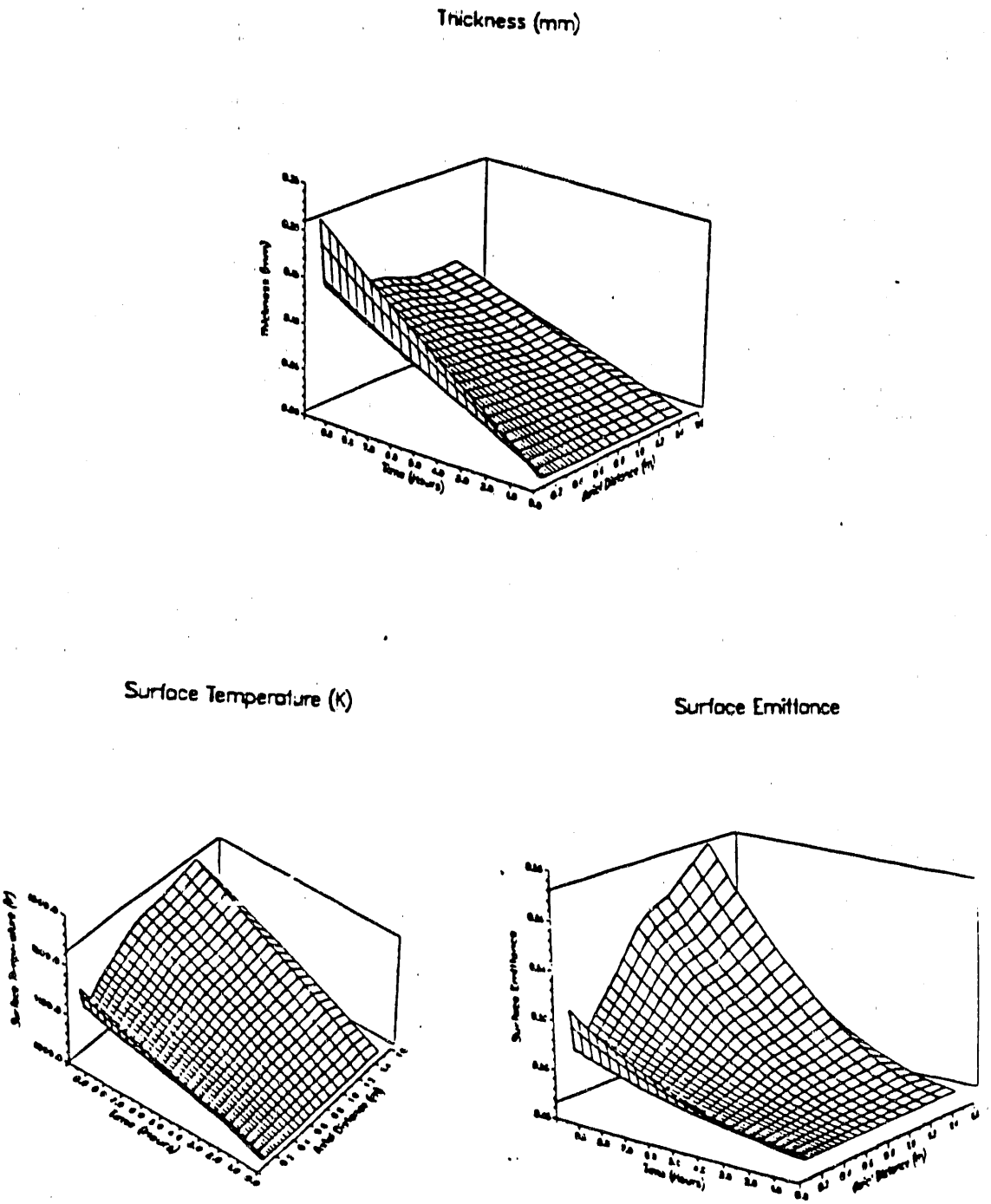

Figure 4.12: Deposit Thickness, Surface Temperature, and Surface Emittance of Asay Case (Deposit Porosity = 0.60).

Section 5

Research Task 5 - Technology Transfer

5.1 Organization

The technology transfer to industry developed under this program was provided for by the industrial collaboration and technology transfer programs of the Advanced Combustion Engineering Research Center. These programs are described in the General Summary Volume (Volume 1) of the Four-Year Progress Report for the Center (reference). The four sources of industrial input to ACERC are shown in Figure 5.1. Consortium representation for these four sources is also shown.

The Advisory Council consisted of nine members, four of whom come from consortium organizations. All consortium members have had representation on the Technical Associates/Affiliates Committee by virtue of the consortium study. Six professionals from consortium organizations participated on the technical working groups that were organized to give direction to each ACERC technical thrust area. Individuals from consortium organizations have participated or will soon participate in the Technical Fellows Program through extended visits (one week to several months) in an ACERC laboratory.

Consortium members have also participated in three Annual Technical Review Meetings held at BYU during the past three and one-half years in which the consortium was active. The most recent of these was held at BYU

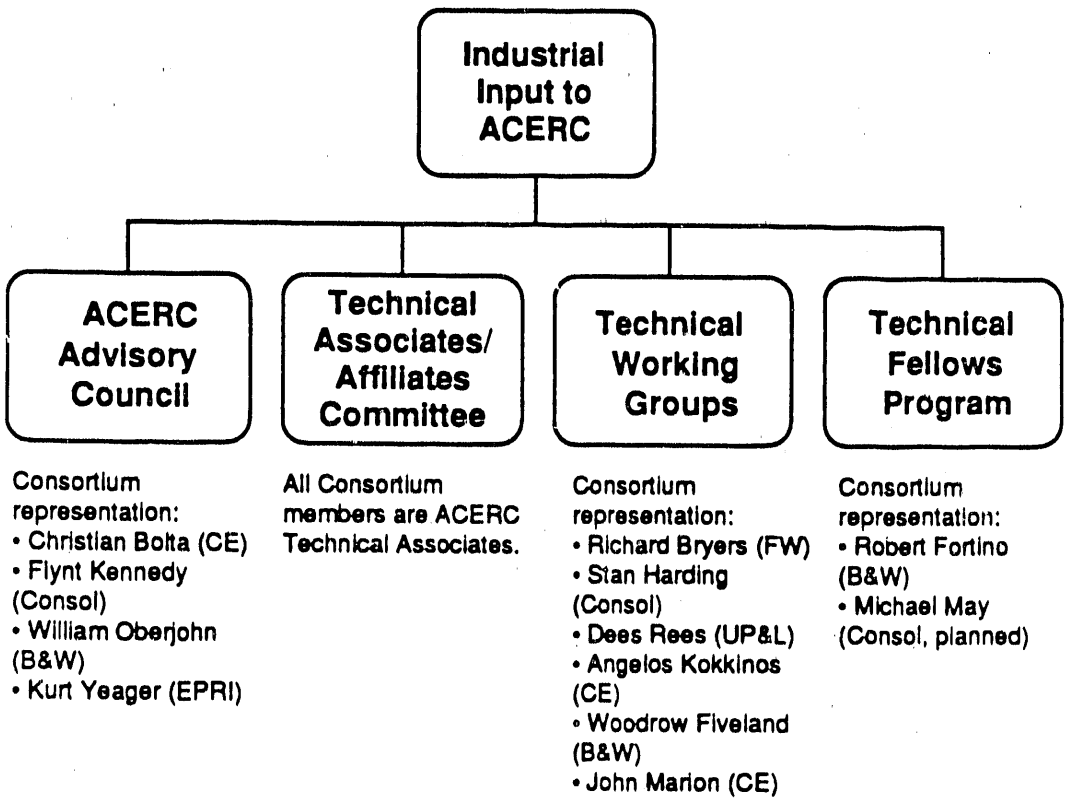

Figure 5.1: Industrial Input to ACERC with Consortium Representation.

on December 8-9, 1988 and had more than 100 people in attendance. At the conference there were technical reports and a poster session, featuring 40 posters covering all ACERC and consortium projects.

Technology transfer was coordinated by the ACERC committee shown in Figure 5.2. The Center Director had overall responsibility and was assisted by the Center Manager. Technology transfer was promoted through publishing textbooks and reports, offering short courses, lectures, and training periods using modern graphics-based engineering workstations, and through the Visiting Professionals and Technical Fellows programs. The Visiting Professionals program brought appropriate technology to the Center through extended visits by invited experts. The Technical Fellows program allowed interested professionals to spend from a few weeks to several months at the Center, working jointly on technical research. Partial support was offered from ACERC to Technical Associates (including all consortium members) to assist in technology transfer to their respective companies by participating in the Technical Fellows program. A brief summary of consortium participation in the Visiting Professionals and Technical Fellows programs is given below.

At the conclusion of the consortium study, all consortium members were eligible to continue membership in ACERC. Such continuation could be secured by either a new research grant/contract or payment of an annual stipend by the consortium member to ACERC.

5.2 2-D Code Distribution

A new version of the two-dimnensional code (87-PCGC-2) was released by ACERC on January 1, 1988 for Consortium/ACERC Associate Member distribution. Improvements in the new code included generalized geometry, slurry combustion, additional inlets, a new radiation model based on the discrete ordinates method, variability in coal heat capacity with temperature, a more robust energy equation option, and an improved user's manual (see below). Organizations that received the new code are shown in Table 5.1. As shown, six of the companies are affiliated with the consortium. The code may be requested by consortium members by contacting Dr. Scott Brewster, Combustion Laboratory, 45 CTB, BYU, Provo, UT 84602 (Telephone 801/378-6240). Only a small license fee is charged to consortium members to cover the costs of legal processing, preparing the tape, and copying the

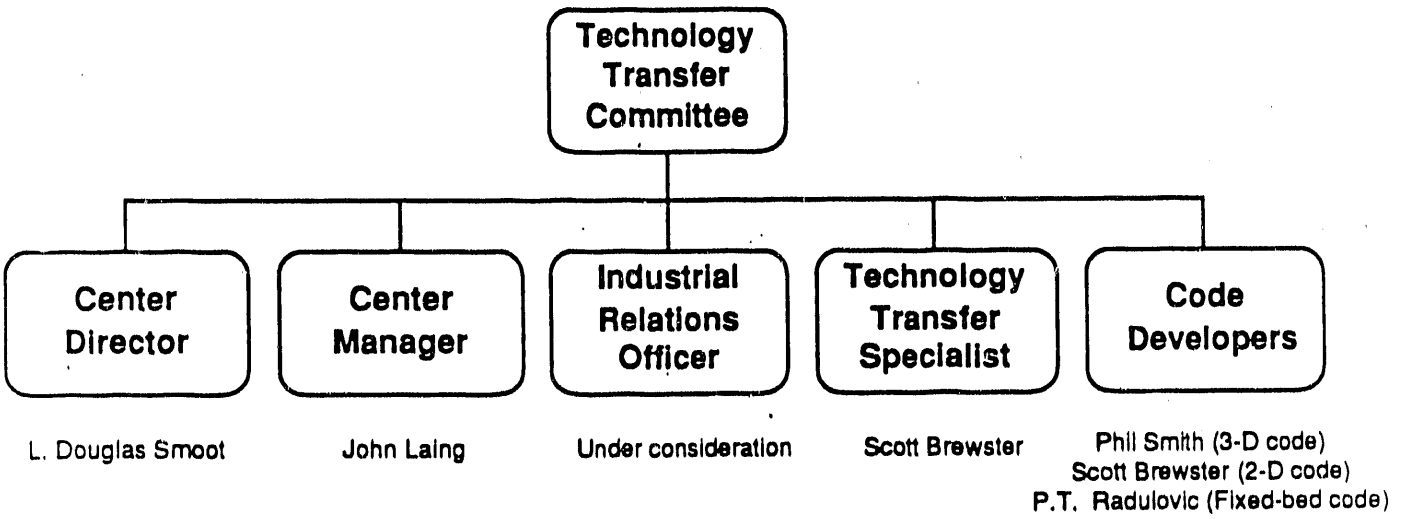

Figure 5.2: ACERC Technology Transfer Committee.

user's manual. A tape containing an updated version of 87-PCGC-2, with corrections made since its initial release, was mailed to all licensed code users.

5.3 2-D User's Manual Update

The user's manual for 87-PCGC-2 was extensively revised and updated to be consistent with the new code. The revised user's manual contains descriptions of the most recent features as well as expanded sections on code use and maintenance. Sample problems for gas combustion, coal combustion and gasification, and slurry combustion were included. Color-coded tables help users find information quickly. An update to the revised user's manual containing corrections and additions made during the first year after the initial release was mailed to all licensed users.

5.4 Technical Visitors

Technical visitors from consortium organizations who have participated in two center programs are listed in Table 5.2.

The most recent Visiting Professional was Dr. Thomas O'Brien from the U.S. Department of Energy Morgantown Energy Technology Center (METC), who came to obtain a detailed knowledge of the 3-D code for subsequent implementation at METC. Dr. O'Brien accomplished this objective, assisting in preparation of the user's manual for the code. In this way, he was able to learn many aspects of the code in a relatively short time, while making a useful contribution to the project. He also implemented the METC chemical equilibrium code for studying complex slag chemistry.

5.5 3-D Code Distribution and Workshop

The 3-D code, PCGC-3, will be distributed to consortium members as part of a workshop. The user's workshop for consortium members for the 3-D code was planned at BYU during the summer of 1990. During this study, the 3-D code (PCGC-3) was demonstrated for gaseous combustion systems as well as for non-reactive flows. Rectangular or cylindrical configurations are allowable. Details on the code workshop were provided to all consortium

Table 5.1: Organizations with 87-PCGC-2.

ORGANIZATIONS WITH 87-PCGC-2

Organization	Code User	Date	Computer/Operating System
Advanced Fuel Research, Inc.[1]	Dr. Peter Solomon	November 1987	Sun-3/Unix
Clemson Univ.[2]	Prof. Tah-Tei Yang	May 1989	Sun-4/Unix
Consol[1]	Dr. Stan Harding	April 1988	Vax/VMS
DOE/METC[1]	Dr. Tom O'Brien	March 1988	Vax/VMS
DOE/PETC[1]	Walter Fuchs	May 1988	Vax/VMS
Dow Chemical[3]	J. P. Henley	June 1988	Vax/VMS
Iowa St. Univ.[2]	Dr. Gerald Colver	April 1988	Vax/VMS
Penn St. Univ.[2]	Dr. Savash Yavuzkurt	March 1988	Vax/VMS
Shell Development Co.[4]	Ron Jensen	January 1989	Vax/VMS
Southern Co. Serv.[5]	Ambavi Bhimani	July 1988	IBM 3090
Tennessee Valley Authority[1]	Greg Marcus	August 1987	Microvax/VMS
Texaco[4]	Dick Jung	January 1989	HP 850S/Unix
Univ. of Alabama[2]	Dr. David Arnold	April 1987	Vax/VMS

[1]Consortium member organizations.

[2]University

[3]ACERC Associate Member

[4]ACERC Affiliate Member

[5]Consortium membership through EPRI.

Table 5.2: Extended Visits from Consortium Organizations to the Combustion Center During Consortium Study Period.

Visitor	Company	Date	Purpose of Visit
Robert Carangelo	Advanced Fuel Research	July 14-18, 1986	Gain general familiarity with PCGC-2
Robert Forcino	Babcock and Wilcox	January-February, 1988	Apply PCGC-2 to particle removal
Robert Carangelo	Advanced Fuel Research	August, 1988	Measure coal gasifier temperature in-situ with FTIR emission/transmission
Dr. Thomas O'Brien	Morgantown Energy Technology Center (DOE)	December 1988-June 1989	Develop 3-D code user's manual

members. A survey was conducted in order to establish the exact dates and workshop approach. At the workshop, a User's Manual will be provided to consortium members and ACERC Associate Members. Associate members were invited to sent up to two participants to the workshop. It was recommended that workshop participants have significant experience in technical basics and computer use of comprhensive models in order to profit from the workshop, since the state of code development is considered to be "specialist-useable".

5.6 Technical Publications

During the study, twelve quarterly technical progress reports and three annual reports were prepared, together with a three volume final report. In addition, several technical papers were presented and published. Technical presentations and publications resulting from the consortium study are shown in Tables 5.3 and 5.4. Several student theses and dissertations also were prepared and are available from the Combustion Laboratory. A complete list of publications is available on request.

Table 5.3: Technical Presentations from Consortium Study.

Authors	Title	Conference	Date
Jamaluddin, A.S. and Smith, P.J.	Prediction of radiative heat transfer in cylindrical furnaces	WSS Combustion Institute	Spring 1986
Smith, P.J. and Fletcher, T.H.	A study of two chemical reaction models in turbulent coal combustion	ASME	December 1986
Smith, P.J., Sowa, W.A., and Hedman, P.O.	Furnace design and comprehensive coal combustion models	ASME	December 1986
Boardman, R.D. and Smoot, L.D.	Evaluation of a NO_x submodel by comparison of experimental systems with model predictions	WSS Combustion Institute	Spring 1987
Jamaluddin, A.S. and Smith, P.J.	Prediction of radiative heat transfer in rectangular enclosures	WSS Combustion Institute	Spring 1987
Smoot, L.D. and Smith, P.J.	Comprehensive modeling of combustion systems	Joint ASME/JSME	March 1987
Smith, J.D., Smith, P.J., and Hill, S.C.	Parametric sensitivity study of an entrained-flow pulverized-fuel combustion model	WSS Combustion Institute	November 1987
Jamaluddin, A.S. and Smith, P.J.	Predicting particulate deposition from turbulent streams	Engineering Foundation Conference on Mineral Matter and Ash Deposition from Coal	February 1988
Smith, P.J., Baxter, L.L., and Jamaluddin, A.S.	Coal combustion modeling: Particulate and gas phase heat transfer effects	AIChE	March 1988
Baxter, L.L. and Smith, P.J.	The effects of interfacial conditions on mass and heat transfer	WSS Combustion Institute	November 1987
Gillis, P.A. and Smith, P.J.	Three-dimensional fluid dynamics modeling in furnace geometries	WSS Combustion Institute	March 1988

Table 5.3: Technical Presentations from Consortium Study (Continued).

Authors	Title	Conference	Date
Baxter, L.L. and Smith, P.J.	Turbulent dispersion of particles	WSS Combustion Institute	March 1988
Davies, P.R. and Smith, P.J.	Modeling ash transormations in pulverized coal combustion chambers	WSS Combustion Institute	October 1988
Smith, P.J., Gillis, P.A., and Christensen, K.R.	Coal-fired pilot plant furnace computer simulations	AFRC	October 1988

Table 5.4: Publications from Consortium Study.

Authors	Title	Conference	Date
Jamaluddin, A.S. and Smith, P.J.	Prediction of radiative heat transfer in cylindrical furnaces	WSS Combustion Institute	Spring 1986
Smith, P.J. and Fletcher, T.H.	A study of two chemical reaction models in turbulent coal combustion	ASME	December 1986
Smith, P.J., Sowa, W.A., and Hedman, P.O.	Furnace design and comprehensive coal combustion models	ASME	December 1986
Boardman, R.D. and Smoot, L.D.	Evaluation of a NO_x submodel by comparison of experimental systems with model predictions	WSS Combustion Institute	Spring 1987
Jamaluddin, A.S. and Smith, P.J.	Prediction of radiative heat transfer in rectangular enclosures	WSS Combustion Institute	Spring 1987
Smoot, L.D. and Smith, P.J.	Comprehensive modeling of combustion systems	Joint ASME/JSME	March 1987
Smith, J.D., Smith, P.J., and Hill, S.C.	Parametric sensitivity study of an entrained-flow pulverized-fuel combustion model	WSS Combustion Institute	November 1987
Baxter, L.L. and Smith, P.J.	The effects of interfacial conditions on mass and heat transfer	WSS Combustion Institute	November 1987
Jamaluddin, A.S. and Smith, P.J.	Predicting particulate deposition from turbulent streams	Conference on Minerals and Ash Deposition	February 1988
Smith, P.J., Baxter, L.L., and Jamaluddin, A.S.	Coal combustion modeling: Particulate and gas phase heat transfer effects	AIChE	March 1988
Baxter, L.L. and Smith, P.J.	Turbulent dispersion of particles	WSS Combustion Institute	March 1988
Brewster, B.S. and Smoot, L.D.	Predicted effects of coal volatiles composition in turbulent flames	WSS Combustion Institute	March 1988
Gillis, P.A. and Smith, P.J.	Three-dimensional fluid dynamics modeling in furnace geometries	WSS Combustion Institute	March 1988
Davies, P.R. and Smith, P.J.	Modeling ash transormations in pulverized coal combustion chambers	WSS Combustion Institute	October 1988
Smith, P.J., Gillis, P.A., and Christensen, K.R.	Coal-fired pilot plant furnace computer simulations	AFRC	October 1988
Smith, P.J. and Gillis, P.A.	Large scale predictability of pulverized coal combustion byproducts	First Int. Congress Toxic Combustion	August 1989
Boardman, R.D., Smoot, L.D., and Brewster, B.S.	Measurement and prediction of thermal NO	WSS Combustion Institute	October 1989

Table 5.4: Publications from Consortium Study.(Continued).

Authors	Title	Journal	Vol.	Page no.	Date
Brewster, B.S., Baxter, L.L. and Smoot, L.D.	Treatment of coal devolatilization in comprehensive combustion modeling	Energy & Fuels	2	362	1988
Boardman, R.D. and Smoot, L.D.	Prediction of nitric oxide in advanced combustion systems	AIChE J.	34	1573	1988
Jamaluddin, A.S. and Smith, P.J.	Prediction of radiative heat transfer in axisymmetric cylindrical enclosures	Comb. Sci. Tech.	62	173	1988
Jamaluddin, A.S. and Smith, P.J.	Discrete-ordinates of radiative transfer equation in non-axisymmetric cylindrical enclosures	Journal of the ASME	96	227	1988
Smith, P.J. and Fletcher, T.H.	A study of two chemical reaction models in turbulent coal combustion	Comb. Sci. Tech.	58	59	1988

Section 6

Technical Summary, Conclusions And Recommendations

A summary of the results obtained during this study, the conclusions drawn from each task, and some recommendations for future work are presented below.

Task 1: Full-Scale Model Development

A practical, computational, combustion furnace model has been developed and entitled PCGC-3 (Pulverized Coal and Gasification Combustion model in three dimensions). This model represents the 3-D embodiment of the submodels and numerical methods developed over the last decade and a half at this laboratory. Throughout the course of this project, the 2-D code has remained a useful tool for evaluating submodels and for analysis of simpler furnaces. As such, the 2- and 3-D codes represent a pair of tools for analyzing combustion chambers.

By the end of this contracted study, the 3-D code had incorporated computational fluid dynamics, gaseous reaction, heat transfer, and non-reacting particulate transport all in turbulent environments. In moving to calculations in larger chambers, a new set of computational constraints have emerged. Differencing schemes, solution procedures, coupling algorithms and other numerical methods have been reevaluated in light of the temporal and spatial scales required in larger furnaces. Graphical interfaces are often the only way

of gaining access to the input and output data of large or complex geometries in combustion. Graphics pre- and post-processors have been developed for this model, under independent funding, and further development is to be continued under ACERC sponsorship.

The problems associated with increasing the scale of the calculation has introduced needs for new procedures and methods. At different furnace scales, different physical processes dominate. The 3-D code has been applied in this study to laboratory and pilot-scale furnaces and smaller. Applications to larger systems arewill be forthcoming under ACERC sponsorship and will require development of appropriate numerical methods and of submodel adequacy. Like scale-up of real physical furnaces, the scale-up of the furnace model has required a systematic development path. Development of complex tools where the understanding of basic physics and chemistry are still evolving requires an iterative approach to the application of the scientific method. The iterative approach includes: hypothesizing an approach, testing and evaluating that hypothesis, drawing conclusions that lead to new hypotheses and thus new testing.

Previous work at BYU laid the foundation for this work. Several comprehensive models (such as PCGC-2) and submodels had been previously developed and evaluated. An extensive literature review was conducted to evaluate applicable numerical algorithms and techniques. A review of existing 3-D combustion models revealed their common basis of using the SIMPLE algorithm and their lack of demonstration with fine grid simulations. Iterative, decoupled, numerical techniques were found to be the most applicable to this problem because of low computer memory requirements and compatibility with turbulence submodels. PCGC-2 was extended to three dimensions for an evaluation of its numerical techniques and a comparison of the SIMPLE-based algorithm variations. The major observations of this development project are:

1. The disparity of scales encountered in industrial geometries requires highly irregular grid structures and requires a finite difference formulation that adequately minimizes false diffusion on the non-uniform grid.

2. A weighted central-difference formulation was used to address irregular grids. This formulation moves control-volume faces to new locations, centering the node-point in the cell. The new formulation dramatically reduces exact solution errors on non-uniform grids.

3. Numerical diffusion on highly irregular meshes has been, in part, caused by the incorrect evaluation of cell face velocities. A nodal differencing scheme was developed which significantly reduced equation error. This nodal scheme was not characterized by the poor convergence properties of higher order upwind differencing schemes.

4. A decrease in computation time was achieved through extensive vectorization of the 3-D code. The reduction was case-dependent, but was approximately a factor of four. A major increase in efficiency resulted from changing the (tri-diagonal maxtrix algorithm) TDMA solver from a line-by-line method to a plane-by-plane method. This change removed the recursion in the TDMA subroutine. Additional convergence acceleration was obtained by over-relaxing the matrix solver to become more implicit.

5. The turbulence submodel can dominate the overall convergence process in highly-turbulent flows. Studies of computational fluid dynamics (CFD) numerical methods are conducted with a coupled turbulence submodel since the importance of turbulence/velocity coupling tends to increase with increasing Reynolds numbers.

6. An exact solution case was formulated to evaluate finite-differencing errors in the model. This procedure led to several improvements in the differencing scheme and facilitated the removal of numerous coding problems. This technique became an important tool in the 3-D model development.

7. Convergence evaluations are aided through a more careful normalization of equation errors. This allows comparison of equation errors and the identification of the equation(s) slowing overall convergence. The proximity of convergence to computer round-off error is also provided through this computation.

8. Domain decomposition methods can greatly reduce computer storage requirements at the expense of computational time. The value of subdomaining is problem- and computer-specific.

9. Grid resolution requirements were established for three test cases. It was found that corner-fired furnaces require substantially fewer node points than wall-fired furnaces. Grid-independent simulations of a tangentially-fired furnace were achieved for grid structures exceeding 15,000 nodes. Complex furnace flows can require up to 500,000 grid points.

10. Several variations of the SIMPLE algorithm were tested for robustness and speed. Convergence rates are strongly dependent on under-relaxation factors. Simulating highly turbulent flows reduces the significance of algorithm selection on solution time. The determination of optimal algorithm and

under-relaxation factors was found to be case-dependent. Higher Reynolds number flows require lower under-relaxation factors. The SIMPLEC, SIMPLER, and SIMPLERC algorithms provided the best compromise between speed and robustness. This study recommends the use of SIMPLERC with an under-relaxation factor of 0.8 for PCGC-3.

11. Numerical constraints on large-scale problems require improved numerical methods to avoid numerical stalling in traditional iterative elliptic solvers and to avoid enormous memory requirements of traditional direct solvers.

12. About one order-of-magnitude enhancement in computational efficiency has been demonstrated for 2-D, axi-symmetric flow problems by using the multigrid process. Even for complex geometries and flow conditions, the multigrid algorithms were shown to avoid numerical stalling to produce constant and fast convergence.

13. Preparing geometry input files for 3-D code calculations is tedious and prone to error unless an automated computer graphics pre-processor is used. Such a tool has been developed and assists significantly in preparing complex files quickly and correctly through a menu-driven, user-friendly, graphics pre-processor.

14. Access to the large output data base from predictions generated by the 3-D code has been facilitated by a graphics-based post-processor.

Task 2: Model Evaluation

An evaluation has been conducted to explore the predictability of the overall 3-D model with its integrated submodels. Separate submodel evaluation (independent of other submodels) has also been conducted. In evaluating coupled components of the modeling strategy we have made extensive use of both the 2-D and 3-D versions of the model. The 2-D code has been a useful and complimentary tool for evaluation of certain aspects of the final 3-D product.

The evaluation included a nonlinear sensitivity analysis of an axi-symmetric laboratory coal-fired furnace, numerical analysis of the 3-D code using several approaches including identification of mesh-size independent solutions for several cases, and comparisons with known exact solutions, extensive 2- and 3-D comparative evaluations with experimental data, and a compilation

and evaluation of available 3-D data. Major observations and conclusions from this evaluation are:

1. A 2-D global, nonlinear sensitivity analysis of a laboratory coal-fired furnace was used to identify specific parameters which have the greatest impact on model predictions. Model predictions for coal burnout, NO_x concentration, local gas temperature, and local coal-gas mixture fraction were used to identify critical parameters. Model parameters examined in this study represent the physical and chemical processes which occur in pulverized fuel (pf) combustion.

2. The parameters required to describe the devolatilization subprocess showed the greatest overall impact from the sensitivity analysis while parameters governing char oxidation were the second most important. Char oxidation had the most impact on model prediction for NO_x concentration. Particle dispersion had a secondary effect on overall model predictions and had the greatest impact on coal burnout and coal-gas mixture fraction predictions. Also, of secondary importance was the effect of coal rank as indicated by the elemental oxygen content of the coal. This affected gas temperature predictions most dramatically.

3. Parameter uncertainties from the sensitivity analysis for the radiation coefficient, turbulence intensity, and the particle swelling factor showed little or no impact on model prediction. This is attributed to the dominant influence of the uncertainty in the other parameters on the sensitivity analysis.

4. While the results obtained in the sensitivity analysis are case-specific, they do focus attention on the critical submodels which appear to dominate the predictions. These results provide direction to future submodel development as well as experimental efforts to obtain accurate values of the physical parameters required by these submodels. This work also illustrates the role of sensitivity analysis as an engineering tool to be used to gain a deeper understanding of the physical process being modeled.

5. An exact solution evaluation was conducted to identify algorithmic and coding errors in the 3-D code. Identified errors were removed and the exact solution reproduced to within the accuracy of truncation error.

6. Residual error within individual equations has been quantified and compared with truncation error. This analysis is used to track convergence in the 3-D code.

7. An evaluation of various 3-D momentum-continuity coupling schemes has been conducted. The schemes explored have included SIMPLE, SIM-

PLER, SIMPLEC, SIMPLEST, and all combinations and permutations of the above schemes. SIMPLERC with under-relaxation of 0.8 resulted in the most efficient and robust combination.

8. A comprehensive, comparative evaluation of the 2-D version of the reacting coal code was completed. This analysis included cases from non-reacting cold flow with and without particles to reacting hot flow with and without coal particles. The analysis was comprised of 33 separate cases all with detailed profile data. The analysis included an evaluation of the experimental data reliability.

9. In the 2-D evaluation, discrepencies between predicted and measured profiles were most apparent in the recirculation zone. The outer regions of the reaction chamber were described very well. Exit compositions and carbon conversions were predicted with almost complete accuracy. Areas of fully-mixed flow were also characterized well.

10. The 2-D comparative evaluation revealed the sensitivity of the calculation to inlet and boundary conditions particularly in inlet mean velocities, turbulence intensity profiles, and heat effects near walls.

11. The 2-D comparative evaluation showed the weakest phenomenological submodels to be the turbulence model, the devolatilization model and the reaction and heat effects model.

12. A full 3-D comparative evaluation was conducted on four simple turbulence models, constant eddy diffusivity, Prandtl mixing length, a k-ϵ model, and a k-ϵ model with relaminarization.

13. The relaminarization model correctly simulated laminar and turbulent pipe flows. The added complexity of this model reduced overall robustness. It is recommended that the relaminarization model should be used judiciously in transitional flows.

14. Two cold-flow cases were chosen to evaluate PCGC-3. These cases were chosen to represent the two major classes of furnaces used in industrial boilers: a tangential or corner-fired system and a wall-fired, swirled burner furnace. This evaluation included local direct comparison with experimental data and provided confidence to be able to move on to incorporate reacting gaseous and particulate systems. Geometric spatial scales and fluid-dynamic temporal scales can be resolved at least for pilot-scale furnaces.

15. Finer mesh calculations than previously demonstrated in computational combustion are needed to resolve physical processes in practical 3-D furnace geometries. One quarter of a million nodes were needed for a four-burner, wall-fired, swirl-flow pilot furnace simulation.

16. A study was conducted to collect available 3-D furnace data for model evaluation. Six sets of data were obtained and documented and evaluated. Recommendations were made for further data collection.

Task 3: Submodel Development

Comprehensive combustion computations allow for the coupling of many physical and chemical processes, thus providing a tool to study synergestic effects of multiple subcomponents. The overall predictive capability of the 3-D combustion code is limited by the quality of submodels. Further development and independent evaluation was conducted on several important submodels necessary for the 3-D model: radiation, char oxidation, turbulent dispersion of particles, nitrogen oxide pollutant formation, carbon monoxide pollutant formation, carbon monoxide partial equilibrium, coal devolatilization, and turbulence. The radiation and turbulence submodels have been formulated in 3-D geometries. The turbulence submodel is currently under evaluation in a 3-D code under independent funding. The other submodels have been implemented only in 2-D axi-symmetric geometries. A summary of these seven studies is presented below.

Radiation:

1. All discrete ordinates radiation flux approximations considered, i.e. S_2, S_4, S_6 and S_8, predict radiative transfer in two-dimensional rectangular enclosures containing absorbing-emitting-scattering media with acceptable accuracy. However, S_2 and S_4 were shown to be more acceptable in two-dimensional enclosures since these consume considerably less computer time with little loss in accuracy for these simpler geometries.

2. In three-dimensional rectangular enclosures, the S_2 predictions are grossly in error. However, comparable prediction accuracy is obtained using S_4, S_6 and S_8 approximations. The S_4 is, once again, considered adequate.

3. Radiative transfer in a three-dimensional rectangular enclosure is highly sensitive to uncertainties in the temperature of the medium, significantly sensitive to the extinction coefficient and the scattering albedo, and rather insensitive to the furnace length and wall emissivity.

Char Oxidation:

1. The nonlinear nature of the Arrhenius law has been shown to have significant implications on the method of correlating the Arrhenius parameters to data. A derivation has been presented which traces a rigorous data analysis technique to fundamental features of the data being correlated while preserving as many desirable statistical properties as possible. The resulting method of data analysis differs substantially from that most commonly used to correlate data with the Arrhenius law.

2. The more common approach to correlating data with Arrhenius law by linearizing the equation overemphasizes the low-temperature data. This poor correlation of the data is amplified when the Arrhenius law is extrapolated beyond the range of the data on which its parameters are based.

3. The parameters determined from the common appraoch can lie well outside of high-confidence contours for the true (population) parameters. A rigorous analysis of these contours shows that they are not simple rectangles,as implied by stating their extreme values. They are also not elliptical, as would be predicted from an extension of techniques used in analyzing linear equations. They are slender loops which illustrate both the nonlinearity of the equation and the correlation of the parameters with each other.

4. A reexamination of many sets of heterogeneous reaction rate data shows that features of past comparisons of trends have been inappropriately interpreted as decreases in char reactivity at high temperatures when, in fact, they are artifacts of data analysis. Reanalysis of several sets of data have been completed with the more rigorous approach.

Turbulent Dispersion of Particles:

1. A first principles approach to describing particle dispersion was developed as an extension of stochastic process modeling and turbulence theory. The model requires no adjustable parameters and is independent of any particular turbulence model.

2. The submodel requires a description of the turbulent gaseous flow field in terms of the mean-square velocities and Lagrangian autocorrelation functions. Approximations for these in terms of parameters from the k-ϵ model have yielded reasonable results.

3. This submodel has been rigorously evaluated by comparison to exact solutions, the most accurate alternative models, and experimental data. In all cases, the model was both an accurate and efficient method of describing turbulent dispersion. The model predicted the experimental data within its inherent error over a wide range of flow conditions.

4. The turbulent dispersion model forms a useful framework for comprehensive computer codes. Adjustable parameters need to be used in these formulations. Side-by-side comparisons of the new submodel perfo mance compared with an existing approach allows us to conclude that the new approach increases the computational efficiency and robustness of the simulations while decreasing the total number of required particle simulations.

Nitric Oxide Submodel:

1. The simulation of 30 new cases, in addition to the extensive predictions made under previous contracts provided a broad further evaluation of the NO_x submodel. The successes of the NO_x submodel predictions is attributed to the ability of PCGC-2 to model the overall flame structure, an adequate global NO_x mechanism and kinetic rate expressions, and the coupling of the chemistry reactions with turbulence in the reactor.

2. Within the accuracy of the predicted temperature and major species and the range of experimental error, the NO_xsubmodel provided reliable predictions for pulverized-fuel gasification and combustion for bituminous and subbituminous coals at moderate and extreme fuel-rich conditions. The impact of pressure was properly predicted for the gasification of Utah bituminous coal.

3. Fuel-rich char oxidation predictions were found to differ substantially from observed effluent concentrations. An investigation suggested that this difference resulted from the effects of temperature and the low volatiles content of the char. Reasonable agreement was demonstrated for variation in primary zone stoichiometric ratio and secondary air staging location for staged combustion cases in a sub-scale reactor, although the model predicted higher NO concentrations in the early region of the reactor, and lower values at the exit.

4. The role of temperature in NO decay was found to be significant. This is expected because the kinetic expressions for homogeneous and heterogeneous decay was exponential in temperature. For the gasification cases, the rate and extent of NO decay was highest in the fuel-rich regions where ap-

preciable concentrations of HCN exist. Homogeneous NO decay is proving to be more significant than heterogeneous decay.

Carbon Monoxide Submodel

1. The inability of early coal combustion models to accurately predict species concentrations for CO and CO_2 was thought to be partly caused by ignoring the kinetic considerations of the reaction chemistry. A complete kinetic treatment of all chemical processes occurring in the reactor was found to require too great an increase in computational time to be practical with the current generation of computer technology. Using a partial equilibrium method to consider the phenomenon was found to account for most of the effects of kinetics, including the issue of coupling, while requiring an acceptable increase in computation time to reach a solution.

2. In general, reactor temperature and species concentrations of CO, O_2, and CO_2 were most affected by use of the non-equilibrium CO model instead of the constant equilibrium model. Water concentrations were also affected to a lesser degree. Other model predictions such as gas velocities and mixture fractions were only slightly affected. The most common effect was to delay the oxidation of CO to CO_2 until later in the reactor causing a larger flame zone, lower temperature peaks, and accompanying changes in the consumption of O_2.

3. Use of the non-equilibrium model also had a significant effect on the robustness or usability of PCGC-2 as a whole. Large increases in computational time were sometimes seen as a result of the CO model. In addition to the time increase, many cases were more difficult to converge requiring greater skill in choosing under-relaxation factors.

4. Choice of rate parameters for use with the non-equilibrium chemistry model had a secondary effect on the predictions and convergence times. Use of the different rate equations studied in this work did not have a noticeable effect on the model predictions but they were rarely significant in comparison to the difference between chemistry options. In general, the Howard equation gave faster and more easily converged solutions due to its greater linearity than did the equation suggested by Dryer.

5. Interpretation of the usefulness and reliability of the new chemistry model has been hampered by inadequacies in many other submodels that provide necessary information to the non-equilibrium model. These submodels

such as the devolatilization and energy models which were specifically considered in this work have been shown to have uncertainties that affect final predictions by at least the same order-of-magnitude as the effect of the CO non-equilibrium model and usually by an order-of-magnitude greater.

Coal Devolatilization:

1. A generalized framework for coal devolatilization has been developed which includes in its scope most of the presently suggested devolatilization models. It is organized around the concept of incorporating fundamental descriptions of coal into a kinetic reaction scheme which predicts the product distributions.

2. This framework has been included, with the exception of the reactive intermediates, in the 2-D comprehensive combustion code.

3. Most of the classical approaches to describing coal devolatilization have been reviewed and many have been set on a more useful and concise philosophical, mathematical, or correlative foundation.

Turbulence:

1. In the last two decades, several sophisticated turbulence models, namely Reynolds stress transport, direct numerical simulation, large eddy simulation, etc., have been proposed. Though these models are successful in providing better understanding of turbulence, they have not been used for solving practical engineering problems due to numerical complexity. This investigation was initiated to review and evaluate the available turbulence models and subsequently to incorporate some of the models into the 3-D code.

2. Recently, a nonlinear k-ϵ model has been proposed to describe the Reynolds stress tensor through a nonlinear expansion of Boussinesq hypothesis. In turbulent flows where normal stress effects are significant, this method has been shown to provide a better estimate of the velocity field. The model has successfuly predicted secondary flows in ducts and channels where the standard k-ϵ model has failed.

3. The nonlinear k-ϵ turbulence model has been incorporated into a simplified 3-D code for duct geometries with independent funding, thus simplifying the equations significantly.

4. In the case of a rectangular duct, the profile of the mean veolcity field simulated via the nonlinear approach shows distinct zones of secondary transverse flow. The testing is being continued under separate funding with both liquid and gaseous systems.

Task 4: Fouling and Slagging

The basic philosophy of this modeling effort is the integration of current technology in modeling ash deposition into a complete fouling/slagging submodel. The fouling/slagging submodel can operate as a submodel in the comprehensive combustion code, or as an independent code to predict the mineral matter transformation during pulverized coal combustion. Although many mechanisms in the mineral matter transformation processes have not been completely defined, this modeling effort was aimed at integrating current technology. Currently the fouling/slagging submodel predictions have not been compared to laboratory or full-scale furnace experiments. However, before subcomponents (such as deposition rate calculations or physical property predictions) are included in the fouling/slagging submodel, evaluation of subcomponent predictions by comparison to experimental data is performed as independently as possible from other subcomponent predictions.

Initial results of fouling and slagging submodel development indicate that the rate of particulate deposition from turbulent streams is highly dependent upon particle size and Reynolds number. An increase in either of these parameters produces an increase in the deposition rate. A minimum in particulate deposition exists in the presence of a thermal gradient. This minimum corresponds to a "critical" particle size. Increasing the particle size beyond this "critical" point produced sharp increases in the deposition rate.

The thermal characteristics of an ash deposit are strongly dependent upon the deposit porosity. Increases in deposit porosity produced a marked decrease in the deposit effective thermal conductivity, thus increasing the deposit surface temperature. All other properties that are a function of temperature, will be effected by changes in deposit porosity.

The significance of this modeling effort lies in its ability to predict particle deposition and thermal characteristics of the deposited material. A particle capture mechanism is being developed with independent support to estimate the fraction of particles that stick to the deposit surface. Upon completion of

the capture mechanism, data comparison can be made to small-scale reactors. In combination with a comprehensive coal combustion package, this type of modeling work could prove very beneficial in describing processes that dominate mineral matter transformations in coal combustion systems.

Task 5: Technology Transfer

During this study, three annual review meetings were held at BYU with all consortium members invited. Also, consortium members were invited to all ACERC review and technology transfer activities. All consortium members were also invited to sent professionals to the laboratory for extended technical exchange. Babcock and Wilcox and Pittsburgh Energy Technology Center participated in this part of the program.

A new version of PCGC-2 was released to consortium members through ACERC with a new User's Manual. Plans for a workshop on the 3-D code, PCGC-3 were identified. Preparation of a User's Manual for the 3-D code was completed under this study (Volume II, Final Report). Twelve quarterly reports and three annual reports were prepared under this study. In addition, several technical presentations and publications were completed, based on work funded in whole or in part through this study. A list of these publications is available upon request from ACERC.

A new technology transfer committee has been organized under ACERC to expand technology transfer activities relating to new ACERC developments.

Bibliography

[1] Abbas, A.S. and Lockwood, F.C., Prediction of a Corner-Fired Utility Boiler. *21st Symposium (International) on Combustion*, The Combustion Institute, pg. 285, 1986.

[2] Asay, B.W., *Effects of Coal Type and Moisture Content on Burnout and Nitrogeneous Pollutant Formation.* PhD thesis, Dept. of Chemical Engineering, Brigham Young University, Provo, UT, 1982.

[3] Atherton, R.W., Schainker, R.B., and Ducot, E.R., On the Statistical Sensitivity Analysis of Models for Chemical Kinetics. *AIChE J.*, 21:441, 1975.

[4] Axworthy, A.E. and Dayan, V.H., *Chemical Reaction in the Converstion of Fuel Nitrogen to NO_x: Fuel Pyrolysis Studies.* Second EPA Stationary Source Combustion Symposium, 1977.

[5] Bartok, W. and Folsom, W.A., *Gas Reburning-Sorbent Injection - A Combined NO_x/SO_x Control Technology.* Joint Symposium on Stationary Combustion NO_x Control, New Orleans, LA, 1987.

[6] Batchelor, G.K., *Austr. J. Sci. Res*, A2:437, 1957.

[7] Baxter, L.L., *Turbulent Transport of Particles.* PhD Thesis, Dept. of Chemical Engineering, Brigham Young University, Provo, UT, 1989.

[8] Baxter, L.L. and Smith, P.J., Coal Devolatilization, manuscript in progress, 1990.

[9] Beck, J.V. and Arnold, K.J., *Parameter Estimation in Engineering and Science*, Wiley, New York, 1977.

[10] Beer, J.M., International Flame Research Foundation: The Effect of Fineness and Recirculation on the Combustion of Low-Volatile Coal. *Journal of the Institute of Fuel*, pg. 286, 1964.

[11] Berry, S., Rice, S., and Ross, J., *Physical Chemistry*, Wiley, New York, 1980

[12] Bird, R.B., Stewart, W.E., and Lightfoot, E.N., *Transport Phenomena.* Wiley, New York, 1960.

[13] Blair, D.W. and Wendt, J.O.L. , *Formation of NO_x and Other Products from Chemically Bound Nitrogen in Coal Combustion.* Technical Report DOE/ET/11314-T1, U.S. Department of Energy, 1981.

[14] Boardman, R.D., *Measurement and Prediction of Nitric Oxide in Stationary Combustors.* PhD thesis in progress, Dept. of Chemical Engineering, Brigham Young University, Provo, UT, 1990.

[15] Boardman, R.D., *Further Evaluation of a Predictive Model for Nitric Oxide Formation During Pulverized Coal Combustion.* Master's thesis, Dept. of Chemical Engineering, Brigham Young University, Provo, UT, 1987.

[16] Bockhorn,H. and Lutz, G., The Application of Turbulent Reaction Models to the Oxidation of CO in a Turbulent Flow. *20th Symposium (International) on Combustion*, The Combustion Institute, pg. 377, 1984.

[17] Boni, A.A. and Penner, R.C., Sensitivity Analysis of a Mechanism for Methane Oxidation Kinetics. *Comb. Sci. Tech.*, 15:99, 1977.

[18] Boyd, R.K. and Kent, J.H., Three-Dimensional Furnace Computer Modeling. *21st Symposium (International) on Combustion*, The Combustion Institute, pg. 265, 1986.

[19] Braaten, M.E., *Development and Evaluation of Iterative and Direct Methods for the Solution of the Equations Governing Recirculating Flows.* PhD thesis, University of Minnesota, 1985.

[20] Brandt, A. and Dinar, N., Multigrid Solutions to Elliptic Flow Problems. *Numerical Methods for Partial Differential Equations*, S. Parter, editor, Academic Press, New York, 1979.

[21] Brandt, A., *Multigrid Techniques: 1984 Guide with Applications to Fluid Dynamics.* Volume 85 of *GMD-Studien*, Gesellschaft für Mathematik und Datenverarbeitung MBH, Bonn, 1984.

[22] Bueters, K.A., Gogoli, J.G., and Habelt, W.E., Performance Prediction of Tangentially Fired Utility Furnaces by Computer Model. *15th Symposium (International) on Combustion*, The Combustion Institute, pg. 1245, 1986.

[23] Burden, R.L., Faires, J.D. and Reynolds, A.C., *Numerical Analysis, second edition.* PWS Publishers, Boston, MA, 1981.

[24] Byers, R.L. and Calvert, R., *Ind. Eng. Chem. Fund.*, 8:646, 1969.

[25] Canavos, G.C., *Applied Probability and Statistical Methods.* Little, Brown and Company, Boston, 1984.

[26] Caracotsios, M. and Stewart, W.E., Sensitivity Analysis of Initial Value Problems with Mixed Nodes and Algebraic Equations. *Comput. Chem. Engineering*, 9:231, 1985.

[27] Carlson, B.J. and Lathrop, K.D., *Transport Theory - The Method of Discrete Ordinates in Computing Methods of Reactor Physics.* Gordon and Breach Science Publishers, New York, 1986.

[28] Castro, I.P. and Jones, J.M., Studies in Numerical Computations of Recirculating Flows. *International Journal for Numerical Methods in Fluids*, 7:793, 1987.

[29] Chandrasekhar, L., Stochastic Problems in Physics and Astronomy. *Reviews of Modern Physics*, vol. 15, 1943.

[30] Chang, K.C., Wolsky, A.M., Berry, G.F., Wang, C.S. and Choi, U.C., *A Modeling Study of Pulverized Coal Combustion in CO_2/O_2 Atmospheres.* Technical Report ANL/CNSV-51, 1986.

[31] Cherian, M.A., Rhodes, P., Simpson, R.J., and Dixon-Lewis, G., Kinetic Modeling of the Oxidation of Carbon Monoxide in Flames. *18th Symposium (International) on Combustion*, The Combustion Institute, pg. 385, 1981.

[32] Chigier, N.A., The Atomization and Burning of Liquid Fuel Sprays. *Progress in Energy and Combustion Science*, 2:97, 1976.

[33] Christensen, K.R. , *An Efficient Axi-Symmetric Flow Model.* Master's thesis, Dept. of Chemical Engineering, Brigham Young University, 1988.

[34] Coffee, T.P. and Heimerl, J.M., Sensitivity Analysis for Premixed, Laminar Steady State Flames. *Comb. and Flame*, 50:323, 1983.

[35] Colson, R.W., *A Carbon Monoxide Partial Equilibrium Model for Turbulent Coal Combustion: Evaluation of the Equilibrium Assumption in Comparison with Energy and Devolatilization Considerations.* Master's thesis, Dept. of Chemical Engineering , Brigham Young University, 1989.

[36] Corrsin, S., *J. Atomos. Sci*, 20:115, 1963.

[37] Crowe, C.T., Review - Numerical Models for Dilute Gas-Particle Flows. *Journal of Fluids Engineering, Transactions of ASME*, 104:197, 1982.

[38] Csanady, G.T., *Turbulent Diffusion in the Environment.* D. Reidel Publishing Co., Dordrecht, Holland, 1973.

[39] Cukier, R.I., Fortiun, C.M., and Shuler, K.E., Study of the Sensitivity of Coupled Reaction Systems to Uncertainties in Rate Coefficients I. Theory. *J. Chem. Phys.*, 59:3873, 1973.

[40] Cukier, R.I., Schaibly, J.H., and Shuler, K.E., Study of the Sensitivity of Coupled Reaction Systems to Uncertainties in Rate Coefficients. I. Analysis of the Approximations. *J. Chem. Phys.*, 63:1140, 1975.

[41] Cukier, R.I., Levine, H.B., and Shuler, K.E., Nonlinear Sensitivity Analysis of Multiparameter Model System. *J. Comp. Phys.*, 26:1, 1978.

[42] Cvetanovič, R.J., Overend, R.P., and Paraskevopoulos, G., *International Journal of Chemical Kinetics,* 7:249, 1975.

[43] Cvetanovič, R.J., Singleton, D.L., and Paraskevopoulos, G., *International Journal of Chemical Kinetics,* 83:50, 1979.

[44] Daniel, C., *Applications of Statistics to Industrial Experimentation.* Wiley, New York, 1976.

[45] Dannecker, K.M. and Wendt, J.O.L., *Fuel Nitrogen Mechanism During the Fuel-Rich Combustion of Pulverized Coal.* AIChE Meeting, San Francisco, 1984.

[46] Davis, M.E., *Numerical Methods and Modeling for Chemical Engineers.* Wiley, New York, 1984.

[47] Deardorf, J.W., A Numerical Study of Three-Dimensional Turbulent Channel Flow at Large Reynolds Numbers. *J. Fluid Mech.*, 41:453, 1970.

[48] Dickinson, R.J., and Gelinas, R.P., Sensitivity Analysis of Ordinary Differential Equations - a Direct Method. *J. Comp. Phys.*, 21:123, 1976.

[49] Dougherty, E.P. and Rabitz, H., A Computational Algorithm for the Green's Function Method of Sensitivity Analysis in Chemical Kinetics. *Int. J. Chem. Kinet.*, 11:1237, 1979.

[50] Draper, N. and Smith, H., *Applied Regression Analysis*, Wiley, New York, 1981.

[51] Dryer, F.L. and Glassman, I., High Temperature Oxidation of CO and CH_4. *14th Symposium (International) on Combustion*, The Combustion Institute, pg. 987, 1972.

[52] Dunker, A.M., Efficient Calculation of Sensitivity Coefficients for Complex Atmospheric Models. *Atmos. Envir.*, 15:1155, 1981.

[53] Dutta, A., Walsh, P.M. and Beer, J.M., Effects of Hydrocarbons, Char and Bed Solids on the Oxidation of Carbon Monoxide in the Freeboard

of a Fluidized Bed Coal Combustor. *20th Symposium (International) on Combustion*, The Combustion Institute, 1984.

[54] Ethier, S.N. and Kurtz, T.G., *Markov Processes.* Wiley, New York, 1986.

[55] Faeth, G.M., Evaporation and Combustion of Sprays. *Progress in Energy and Combustion Science*, 9:1, 1983.

[56] Falls, A.H., McRae, G.J., and Seinfeld, J.H., Sensitivity and Uncertainty of Reaction Mechanisms for Photochemical Air Pollution. *Int. J. Chem. Kinet*, 11:1137, 1979.

[57] Ferziger, J.H., Clark, R.A. and Reynolds, W.C., Evaluation of Subgrid-Scale Turbulence Models Using an Accurately Simulated Turbulent Flow. *J. Fluid Mech.*, 91:1, 1979.

[58] Field, M.A., Gill, D.W., Morgan, B.B., and Hawksley, P.G.W. , *Combustion of Pulverized Coal.* Institute of Fuel for the British Coal Utilisation Research Association, Leatherhead, UK, 1974.

[59] Fiveland, W.A., Personal communication, 1987.

[60] Fiveland, W.A., Discrete-Ordinates Solutions of the Radiative Transport Equation for Rectangular Enclosures. *ASME J. Heat Transfer*, 106:699, 1984.

[61] Fiveland, W.A. and Wessel, R.A., FURMO: A Numerical Model for Predicting Performance of Three-Dimensional Pulverized, Fuel-Fired Furnace. 86-HT-35, *ASME*, New York, 1986.

[62] Fletcher, T.H., *A Two-Dimensional Model for Coal Gasification and Combustion.* PhD thesis, Dept. of Chemical Engineering, Brigham Young University, Provo, UT, 1983.

[63] Fletcher, T.H., *Theoretical Modeling of Reacting Coal Particles in Pulverized Coal Combustion and Gasification.* Master's thesis, Dept. of Chemical Engineering, Brigham Young University, Provo, Utah, 1980.

[64] Frank, P.M., *Introduction to System Sensitivity Theory.* Academic Press, New York, 1978.

[65] Freihaut, J.D., Proscia, W.M. and Seery, D.J., *Fuel-Bound Nitrogen Evolution During the Devolatilization and Pyrolysis of Coals of Varying Rank.* Joint Symposium on Stationary Combustion NO_x Control, New Orleans, LA, 1987.

[66] Freihaut, J.D., W.M. Proscia, and Seery, D.J., *Effect of Heat Transfer on Tar and Light Gases from Coal Pyrolysis.* 194^{th} National Meeting of the American Chemical Society, New Orleans, LA, 1987.

[67] Friedlander, S.K. and Johnson, H.F., *Ind. Eng. Chem.*, 49:1151, 1957.

[68] Gillis, P.A. and Smith, P.J. , *Flowfield Simulations in Industrial Furnace Configurations.* 195th ACS National Meeting, Toronto, 33:215, 1988.

[69] Gillis, P.A. and Smith, P.J., *Three-Dimensional Fluid Dynamics Modeling in Furnace Geometries.* Spring Meeting of Western States Section, The Combustion Institute, Salt Lake City, 1988.

[70] Glass, J.W. and Wendt, J.O.L., *Advanced Staged Combustion Configurations for Pulverized Coal: Fuel Nitrogen conversion During Fuel Rich Combustion of Pulverized Coal and Char.* Technical Report 1 DOE/ET/15184-1152, U.S. Department of Energy, 1981.

[71] Goetz, G.J., Nsakala, N.Y., Patel, R.L., and Lao, P.C., *Combustion and Gasification Characteristics of Chars from Four Commercially Signifcant Coals of Different Rank.* Final Report for EPRI project no. 1654-6, Sept. 1982.

[72] Goldschmidt, V.W., Householder, M.K., Ahmadi, G., and Chuang, S.C., Turbulent Diffusion of Small Particles. *Progress in Heat and mass Transfer*, 6:487, 1972.

[73] Gosman, A.D. and Ioannides, E., *Aspects of Computer Simulation of Liquid-Fueled Combustion.* AIAA Paper No. 81-0323, 1981.

[74] Gosman, A.D., Pun, W.M., Ruchal, A.K., Spalding, D.B., and Wolshstein, R., *Heat and Mass Transfer in Recirculating Flows.* Academic Press, London, 1969.

[75] Gosman, A.D. and Lockwood, F.C., Incorporation of a Flux Method for Radiation Into a Finite-Difference Procedure for Furnace Calculations. *14th Symposium (International) on Combustion*, The Combustion Institute, pg. 661, 1973.

[76] Gosman, A.D., Caretto, L.S., Patankar, S.V., and Spalding, D.B., *Two Calculation Procedures for Steady, Three-Dimensional Flows with Recirculation.* Proceeding of the Third International Conference on Numerical Methods in Fluid Dynamics, 1973.

[77] Gouldin, F.C., Dpesky, J.S., and Lee, S.L., Velocity Field Characteristics of a Swirling Flow Combustor. AIAA Paper No. AIAA-83-0314, 1983.

[78] Grant, D.M., Pugmire, R.J., Fletcher, T.H., and Kerstein, A.R., *A Chemical Model of Devolatilization Using Percolation Lattice Statistics.* Spring Meeting of the Western States Section, The Combustion Institute, Salt Lake City, Utah, March 21-22, 1988

[79] Grotzbach, G., Direct Numerical and Large Eddy Simulation of Turbulent Channel Flows, *Encyclopedia of Fluid Mechanics, volume 6.* Gulf Publishing, 1983.

[80] Hackbush, W. and Trottenberg, U. editors, *Multigrid Methods, Proceedings of the 1981 Multigrid Conference held at Köln–Porz.* Volume 360 of Lecture Notes in Mathematics, Springer–Verlag, Berlin, 1982.

[81] Harsha, P.T., Kinetic Energy Methods. *Handbook of Turbulence, volume 1.* W. Frost and T.H. Moulden, editors, Plenum Press, New York, 1977.

[82] Héberger, K., Kemény, S., and Vidóczy, T., On the Errors of Arrhenius Parameters and Estimated Rate Constant Values. *International Journal of Chemical Kinetics*, 19:171, 1987.

[83] Hein, K. and Leuckel, W., *Results of Detailed Measurements Carried Out in Swirling Pulverized Anthracite Flames During the Series of Trials C-13.* IFRF Document No. f32/a/39, IJmuiden, The Netherlands, 1970.

[84] Hill, S.C., *Modeling of Nitrogen Pollutants in Turbulent Pulverized-Coal Flames.* PhD thesis, Dept. of Chemical Engineering, Brigham Young University, Provo, Utah, 1983.

[85] Hill, S.C., Smoot, L.D., and Smith, P.J., Prediction of Nitrogen Oxide Formation in Turbulent Coal Flames. *20th International Symposium on Combustion*, The Combustion Institute, pg. 1391, 1984.

[86] Hinze, J.O., *Turbulence, 2nd edition.* McGraw-Hill, 1975.

[87] Howard, J.B., Williams, G.C. and Fine, D.H., Kinetics of Carbon Monoxide in Postflame Gases. *16th Symposium (International) on Combustion*, The Combustion Institute, 1977.

[88] Hwang, J.T., Sensitivity Analysis in Chemical Kinetics by the Method of Polynomial Approximation. *Int. J. Chem. Kinet.*, 15:395, 1983.

[89] Hwang, J., Dougherty, E.P., Rabitz, S., and Rabitz, H., The Green's Function Method of Sensitivity Analysis in Chemical Kinetics. *J. Chem. Phys.*, 69:5180, 1978.

[90] Hyde, D.J. and Truelove, J.S., *The Discrete Ordinates Approximation for Multi-Dimensional Radiant Heat Transfer in Furnaces.* Technical Report AERE R-8502, Harwell, U.K., 1977.

[91] Jamaluddin, A.S. and Smith, P.J., *Prediction of Radiative Heat Transfer in Rectangular Enclosures.* Western States Section Meeting, The Combustion Institute, Provo, Utah, 1987.

[92] Jeong, K.M., Hsu, K.J., Jeffries, J.B., and Kaufman, F., *Journal of Physical Chemistry,* 88:1222, 1984.

[93] Jerri, A.J., The Shannon Sampling Theorem-Its Various Extensions and Applications: A Tutorial Review. *Proc. of the IEEE,* vol. 65, 1965.

[94] Jones, W.P. and Launder, B.E., The Prediction of Laminarization With a Two-Equation Model of Turbulence. *International Journal of Heat and Mass Transfer*, vol. 15, 1972.

[95] Jones, W.P. and Launder, B.E., The Calculation of Low-Reynolds-Number Phenomena With a Two-Equation Model of Turbulence. *International Journal of Heat and Mass Transfer*, vol. 16, 1973.

[96] Kalinske, A.A. and Pien, C.L., Eddy Diffusion. *Industrual and Engineering Chemistry*, 36:220, 1944.

[97] Kampe de Feriet, J., *Ann. Soc. Sci.* Bruxelles, 1939.

[98] Kampe de Feriet, J., Compt. Rend. 1948.

[99] Kobayashi, H., Howard, J.B., and Sarofim, A.F., Coal Devolatilization at High Temperatures. *16th Symposium (International) on Combustion*, The Combustion Institute, pg. 411, 1977.

[100] Koda, M., McRae, G., and Seinfeld, J.H., Automatic Sensitivity Analysis of Kinetic Mechanisms. *Int. J. Chem. Kinet*, 11:427, 1979.

[101] Koucky, R.W., Marion, J.L. and Anderson, D.K., *Development of Sorbent Injection Criteria for Sulfur Oxides Control from Tangentially Fired Coal Boilers.* Report from Combustion Engineering, Windsor, CT., December 1987.

[102] Kramer, M.A., Calo, J.M., and Rabitz, H., An Improved Computational Method for Sensitivity Analysis: Green's Function Method with 'AIM'. *App. Math. Modelling*, 5:432, 1981.

[103] Kramlich, J.C., Lester, T.W. and Wendt, J.O.L., *Mechanisms of Fixed Nitrogen Reduction in Pulverized Coal Flames.* Joint Symposium on Stationary Combustion NO_x Control, New Orleans, LA, 1987.

[104] Kuntz, P.J., Mitchell, G.F., and Ginsburg, J., Fourier Analysis of Steady-State Reaction Schemes for Interstellar Molecules. *Astrophys. J.*, 209:116, 1976.

[105] Kuo, K.K., *Principles of Combustion.* Wiley, New York, 1986.

[106] Langevin, P., *Comptes. Rendues*, 146:530, 1908.

[107] Launder, B.E. and Spalding, D.B., *Mathematical Models of Turbulence*. Academic Press, London, 1972.

[108] Laurendeau, N.M., Heterogeneous Kinetics of Coal Char Gasification and Combustion, *Progress in Energy and Combustion Science*, 4:221, 1978.

[109] Leavitt, D.R., *Effects of Coal Dust and Secondary Swirl on Gas and Particle Mixing Rates in Confined Coaxial Jets*. Master's thesis, Dept. of Chemical Engineering, Brigham Young University, Provo, Utah, 1980.

[110] Lee, G.K., Lockwood, F.C., Rizvi, M.A. and Whaley, H., Coal Combustion Model Validation Using Cylindrical Furnace Data. *20th Symposium (International) on Combustion*, The Combustion Institute, pg. 513, 1984.

[111] Lee, J.W., Wendt, J.O.L. and Pershing, D.W., *Pollutant Control Through Staged Combustion of Pulverized Coal*. Technical Report FE-1817-4, U.S. Department of Energy, 1986.

[112] Leonard, B.P., A Stable and Accurate Convective Modeling Procedure Based on Quadratic Upstream Interpolation. *Computer Methods in Applied Mechanics and Engineering*, 19:775-791, 1975.

[113] Leschiziner, M.A. and Rodi, W., Calculation of Annular and Twin Parallel Jets Using Various Discretization Schemes and Turbulence Model Variations. *Journal of Fluids Engineering*, 13:352, 1981.

[114] Lilly, G.P., Effect of Particle Size on Particle Eddy Diffusivity. *Industrial and Engineering Chemistry Fundamentals*, 12:268, 1973.

[115] Lindsay, J.D., *LDA Measurements in a Simulated Gasifier with Swirl*. PhD thesis, Dept. of Chemical Engineering, Brigham Young University, Provo, UT, 1986.

[116] Lockwood, F.C. and Shah, N.G., A New Radiation Solution Method for Incorporation in General Combustion Prediction Procedures. *18th*

Symposium (International) on Combustion, The Combustion Institute, pg. 1405, 1981.

[117] Lockwood, F.C. and Salooja, A.P., The Prediction of Some Pulverized Coal Flames in a Furnace. *Combustion and Flame*, 54:23, 1983.

[118] Lopez, J.C., March, S.C., and Garcia, F.C., *Ingereria Quimica (Madrid)*, 13:147, 1981.

[119] Lowes, T.M., *The Prediction of Radiant Heat Transfer in Axisymmetrical Systems.* Technical Report G02/a/25, International Flame Research Foundation, 1973.

[120] Lowe, A., Wall, T.F., and Stewart,I., A Zoned Heat Transfer Model of Large Tangentially Fired Pulverized Coal Boilers. *15th Symposium (International) on Combustion*, The Combustion Institute, pg. 1261, 1974.

[121] Lumley, J.L., *Turbulence*, Chapter 12. Springer-Verlag, 1978.

[122] Markatos, N.C. and Pericleous, K.A., Laminar and Turbulent Natural Convection in an Enclosed Cavity. *International Journal of Heat and Mass Transfer*, 27:755, 1984.

[123] Menguc, M.P. and Viskanta, R., Radiative Transfer in Three-Dimensional Rectangular Enclosures Containing Inhomogeneous Anisotropically Scattering Media. *J. Quant. Specrosc. Radiat. Transfer*, 33:533, 1985.

[124] Merrick, D., Mathematical Models of the Thermal Decomposition of Coal: 2. Specific Heats and Heats of Reaction, *Fuel*, 62:540, 1983

[125] Michel, J.B. and Payne, R., *Detailed Measurement of Long Pulverized Coal Flames for the Characterization of Pullutant Formation.* IFRF Document Number F09/a/23, IJmuiden, 1980.

[126] Michelfelder, S. and Lowes, T.M., *Report on the M-2 Trials.* IFRF Document F36/a/4, IJmuiden, The Netherlands, 1974.

[127] Modarress, D., Wuerer, J., and Elghobashi, S., *An Experimental Study of a Turbulent Round Two-Phase Jet.* AIAA Paper No. AIAA-82-0964, 1982.

[128] Monin, A.S. and Yaglom., A.M., *Statistical Fluid Mechanics. volume 1.* MIT Press, Cambridge, MA, 1971.

[129] Montgomery, D.C., *Design and Analysis of Experiments*, Wiley, New York, 1984.

[130] Morr, A.R. and Heywood, J.B., Partial Equilibrium Model for Predicting Concentration of CO in Combustion. *Acta Astronautica* 1:949, 1974.

[131] Oh, M.S., *Softening Coal Pyrolysis,* PhD thesis, Dept. of Chemical Engineering, Massachusetts Institute of Technology, Cambridge, MA, 1985

[132] Okubo, A. and Karweit, M.J., *Oceanography*, 14:514, 1969.

[133] Patankar, S.V. *Numerical Heat Transfer and Fluid Flow.* Hemisphere Publishing Corp., Washington, 1980.

[134] Peeters, J. and Mahnen, G. , Reaction Mechanisms and Rate Constants of Elementary Steps in Methane-Oxygen Flames. *14th International Symposium on Combustion*, The Combustion Institute, pg. 133, 1974.

[135] Pershing, D.W. and Wendt, J.O.L., Pulverized Coal Combustion: The Influence of Flame Temperature and Coal Composition on Thermal and Fuel NO_x. *16th Symposium (International) on Combustion*, The Combustion Institute, pg. 389, 1977.

[136] Pierce, T.H., *Theory and Application of Sensitivity Analysis to Enzyme Kinetics.* PhD thesis, Michigan State University, East Lansing, MI, 1981.

[137] Pierce, T.H. and Cukier, R.I., Global Nonlinear Sensitivity Analysis Using Walsh Functions. *J. Comp. Phys.*, 41:427, 1981.

[138] Plackett, R.L. and Burman, J.P., The Design of Optimum Multifactorial Experiments. *Biometrika*, 33:305, 1946.

[139] Rabitz, H., Chemical Sensitivity Analysis Theory with Applications to Molecular Dynamics and Kinetics. *Comput. Chemistry*, 5:167, 1981.

[140] Rabitz, H., Kramer, M., and Dacol, D., Sensitivity Analysis in Chemical Kinetics. *Ann. Rev. Phys. Chem.*, 34:419, 1983.

[141] Raithby, G.D., Skew Upstream Differencing Schemes for Problems Involving Fluid Flow. *Computer Methods in Applied Mechanics and Engineering*, 19:153, 1976.

[142] Raithby, G.D. and Torrance, K.E., Upstream-Weighted Differencing Schemes and Their Application to Elliptic Problems involving Fluid Flow. *Computers and Fluids*, 2:191, 1974.

[143] Rasband, M., *PCGC-2 and The Data Book: A Concurrent Analysis of Data Reliability and code Performance.* Master's thesis, Dept. of Chemical Engineering, Brigham Young University, Provo, UT, 1988.

[144] Ratzel, A.C. and Howell, J.R., *Two-Dimensional Radiation in Absorbing-Emitting-Scattering Media Using the P-N Approximation.* Technical Report 82-HT-19, ASME, 1982.

[145] Rawlins, D.C., *Nitrogen and Sulfur Pollutant Formation During Coal-Water Mixture Combustion.* Master's thesis, Dept. of Chemical Engineering, Brigham Young University, Provo, UT, 1984.

[146] Reece, G.J., Launder, B.E. and Rodi, W., Progress in the Development of a Reynolds Stress Transport Closure. *J. Fluid Mech.*, 68:537, 1975.

[147] Reuven, Y., Smooke, M.D., and Rabitz, H., Sensitivity Analysis of Boundary Value Problems: Application to Nonlinear Reaction-Diffusion Systems. *J. Comp. Phys.*, 64:27, 1986.

[148] Roache, P.J., *Computational Fluid Dynamics.* Nermosa Publishers, Albuquerque, New Mexico, 1976.

[149] Rodi, W., *Progress in Turbulence Modeling for Incompressible Flows.* AIAA 19th Aerospace Science Meetings, St. Louis, Missouri, 1981.

[150] Rodi, W., Examples of Turbulence Models for Incompressible Flow. *AIAA J.*, 20:872, 1982.

[151] Sampath, H. and Ganesan, V., Numerical Predictions of Three-Dimensional Reacting Flows, *Fuel*, vol. 66, 1987.

[152] Samuelsen, G.S. and Brum, R.D., *Two-Component Laser Anemometry Measurements in a Non-Reacting and Reacting Complex Flow Model Combustor.* Fall Meeting of the Western States Section of the Combustion Institute, Sandia National Laboratories, 1982.

[153] Schailby, J.H. and Schuler, K.E., Study of the Sensitivity of Coupled Reaction Systems to Uncertainties in Rate Coefficients. II. Application. *J. Chem. Phys.*, 59:3879, 1973.

[154] Schuhler, C., *Z. Phys. Chemie (Leipzig)*, 263:249 1982.

[155] Schumann, U. and Frederich, R., *Direct and Large Eddy Simulation of Turbulence: Notes on Numerical Fluid Mechanics, volume 15.* Friedr. Vieweg and Sohn, Munchen, Germany, 1985.

[156] Serio, M.A., Solomon, P.R., Hamblen, D.G., Markham, J.R., and Carangelo, R.M., Coal Pyrolysis Kinetics and Heat Transfer in Three Reactors. *21st Symposium (International) on Coal Combustion*, Munich, West Germany, 1986

[157] Shmel'ev, A.S., Asadullin, R.M., and Spivak, S.I., *Russian Journal of Physical Chemistry*, 55:1691, 1981.

[158] Shuen, J.S., Chen, L.D., and Faeth, G.M., *AIChE Journal*, 29:167, 1983.

[159] Singer, J.G., editor, *Combustion, Fossil Power Systems.* Combustion Engineering, Inc., Windsor, CT, 1981.

[160] Sloan, D.G., *Modeling of Swirl in Turbulence Systems.* PhD thesis, Dept. of Chemical Engineering, Brigham Young University, Provo, UT, 1985.

[161] Sloan, D.G., Smith, P.J., and Smoot, L.D., Modeling of Swirl in Turbulent Flow Systems. *Progress in Energy and Combustion Science*, 12:163, 1986.

[162] Smith, J.D., *Foundations of a Three-Dimensional Model for Predicting Coal Combustion Characteristics in Industrial Power Generation Plants.* PhD thesis, in progress, Dept. of Chemical Engineering, Brigham Young University, Provo, UT, 1990.

[163] Smith, J.D., *Prediction of the Effects of Coal Quality on Utility Furnace Performance.* Master's thesis, Dept. of Chemical Engineering, Brigham Young University, Provo, UT, 1984.

[164] Smith, P.J. and Baxter, L.L., *A Study of Turbulent Particle Dispersion in Pulverized Combustion and Gasification.* Western States/Canadian Sections, The Combustion Institute, Banff, Canada, April 1986.

[165] Smith, P.J., Fletcher, T.H., and Smoot, L.D., Model for Pulverized Coal-Fired Reactors. *18th Symposium (International) on Combustion*, The Combustion Institute, pg. 1285, 1981.

[166] Smith, P.J., Hill, S.C., and Smoot, L.D., Theory for NO Formation in Turbulent Coal Flames. *19th Symposium (International) on Combustion*, The Combustion Institute, pg. 1263, 1982.

[167] Smith, P.J., Fletcher, T.H., and Smoot, L.D., Model for Pulverized Coal-Fired Reactors. *18th Symposium (International) on Combustion*, The Combustion Institute, Pittsburgh, PA 1285, 1981.

[168] Smith, P.J. and Gillis, P.A., *Three-Dimensional Fluid Dynamics Modeling in Furnace Geometries.* Western States Section, The Combustion Institute, Salt Lake City, UT, 1988.

[169] Smith, P.J., Gillis, P.A., and Christensen, K.R., *Coal-Fired Pilot Plant Furnace Computer Simulations.* American Flame Research Committee, Pittsburgh,PA, 1988.

[170] Smith, P.J. and Smoot, L.D., *Detailed Model for Practical Pulverized Coal Furnaces and Gasifiers.* Quarterly Technical Progress Report No. 6, Consortium, February 1987.

[171] Smith, P.J. and Smoot, L.D., *Detailed Model for Practical Pulverized Coal Furnaces and Gasifiers.* First Annual Progress Report, Consortium, May 1986.

[172] Smith, P.J. and Smoot, L.D., *Detailed Model for Practical Pulverized Coal Furnaces and Gasifiers.* Second Annual Progress Report, Consortium, May 1987.

[173] Smith, P.J. and Smoot, L.D., *Detailed Model for Practical Pulverized Coal Furnaces and Gasifiers.* Third Annual Progress Report, Consortium, May 1988.

[174] Smith, P.J., Smoot, L.D., and Brewster, B.S., *Revised User's Manual: Pulverized Coal Gasification or Combustion in 2-Dimensions, volume 2.* Final Report DOE Contract No. AC21-85MC22059. Brigham Young University, Provo, Utah, December 1987.

[175] Smith, R.D., The Tract Element Chemistry of Coal During Combustion and the Emissions from Coal-Fired Plants. *Prog. Energy Combust. Sci.*, 6:201, 1980.

[176] Smooke, M.D., Reuven, Y., Rabitz, H., and Dryer, F.L., *Application of Sensitivity Analysis to Premixed Hydrogen-Air Flames.* Technical Report ME-104-86, Dept. of Mechanical Engineering, Yale University, New Haven, CT, 1986.

[177] Smoot, L.D. and Pratt, D.T., editors, *Pulverized Coal Combustion and Gasification.* Plenum Publishing Corp., New York, 1979.

[178] Smoot, L.D. and Smith, P.J., Turbulent Gaseous Combustion Part II: Theory and Evaluation for Local Properties. *Combustion and Flame*, 42:227, 1981.

[179] Smoot, L.D. and Smith, P.J., *Coal Combustion and Gasification.* Plenum Publishing Corp., New York, NY, 1985.

[180] Smoot, L.D. and Christensen, K.R., *Data Book: For Evaluation of Pulverized Coal Reaction Models.* Final Report Volume III prepared for U.S. DOE, Contract No. DE-AC21-81MC16518, 1985.

[181] Smoot, L.D., Azuhata, S., Hedman, P.O. and Sowa, W.A., Effects of Flame Type and Pressure on Entrained Coal Gasification. *Fuel*, 65:1511, 1986.

[182] Smoot, L.D., Brown, B.W. and Hedman, P.O., Effects of Coal Type on Entrained Gasification. *Fuel*, 65:673, 1986.

[183] Smoot, L.D., Smith, P.J. and Hill, S.C., Effects of Swirling Flow on Nitrogen Oxide Concentration in Pulverized Coal Combustion. *AIChE Journal*, 32:1917, 1986.

[184] Soelberg, N.R., Smoot, L.D., Hedman, P.O., Local Measurements in an Entrained Coal Gasifier, *Fuel*, 64:776, 1985.

[185] Sowa, W., Personal communications. 1986. Brigham Young University, Provo, UT.

[186] Spexiale, C.G., On Nonlinear k-l and k-ϵ Models of Turbulence. *J. Fluid Mech*, 178:459, 1987.

[187] Sprouse, K.M. and Schuman, M.D., Predicting Lignite Devolatilization with the Multiple Parallel and Two Competing Reaction Models. *Combustion and Flame*, 43:265, 1981.

[188] Stone, H.L., Iterative Solution of Implicit Approximations of Multidimensional Partial Differential Equations. *SIAM Journal of Numerical Analysis*, 5:530, 1968.

[189] Taylor, G.I., Technical Report, *London Math Soc.*, 1922.

[190] Taylor, G.I., *London Math Soc.*, 2-20:196, 1921.

[191] Taylor, G.I., *Royal Soc. London*, A135:685, 1932.

[192] Taylor, G.I., *Royal Soc. London*, A151:421, 1935.

[193] Taylor, G.I., *Royal Soc. London*, A164:476, 1938.

[194] Tennekes, H. and Lumley, J.L., *A First Course in Turbulence.* MIT Press, Cambridge, MA, 1972.

[195] Thole, C.A. and Trottenberg U., newblock *Basic Smoothing Procedures for the Multigrid Treatment of Elliptic 3D-Operators.* Arbeitspapiere der GMD 141, Gesellschaft für Mathematik und Datenverarbeitung MBH, Bonn, 1985.

[196] Tilden, J.W., Constanza, V., McRae, G.J., and Seinfeld, J.H., Sensitivity Analysis of Chemical Reacting Systems. *Modeling of Chemical Reacting Systems.* K.H. Ebert, P. Deuflhard, and W. Jager, editors. Springer-Verlag, Berlin, 1981.

[197] Tomovic, R. and Vokobratovic, M., *General Sensitivity Theory.* Elsevier, New York, 1972.

[198] Truelove, J.S., *Differential Equation Models of Radiative Heat Transfer.* Technical Report AERE R-8364, Harwell, U.K., 1976.

[199] Truelove, J.S., *Evaluation of a Multi-Flux Model for Radiative Heat Tranfer in Cylindrical Furnaces:* Technical Report AERE R-9100, Harwell, U.K., 1978.

[200] Truelove, J.S., Prediction of the Near-Burner Flow and Combustion in Swirling Pulverized-Coal Flames. *21st Symposium (International) on Combustion*, The Combustion Institute, pg. 275, 1986.

[201] Truelove, J.S., Three-Dimensional Radiation in Absorbing-Emitting-Scattering Media Using the Discrete-Ordinates Approximation. *J. Quant. Spectros. Rad. Transfer*, 1987.

[202] Turan, A., *A Three-Dimensional Model for Gas Turbine Combustors.* PhD thesis, University of Sheffield, England, 1978.

[203] Ubhayakar, S.K., Stickler, D.B., Von Rosenberg, Jr., C.W., and Gannon, R.E., Rapid Devolatilization of Pulverized Coal in Hot Combustion Gases. *16th Symposium (International) on Combustion*, The Combustion Institute, pg. 427, 1976.

[204] Van Doormaal J.P. and Raithby, G.D., Enhancements of the SIMPLE Method for Predicting Incompressible Fluid Flows. *Numerical Heat Transfer*, 7:147, 1984.

[205] Vanka, S.P., Second Order Upwind Differencing in a Recirculating Flow. *AIAA Journal*, 25:1435, 1987.

[206] Varma, S.A., Radiative Heat Transfer in a Pulverized-Coal Flame in *Pulverized Coal Combustion and Gasification.* L.D. Smoot and D.P. Pratt, Eds., Plenum Press, New York, 1979.

[207] Webb, B.W., *Laser Velomiceter Measurements in a Simulated Entrained Flow Coal Reactor* Master's thesis, Dept. of Chemical Engineering, Brigham Young University, Provo, UT, 1982.

[208] Wendt, J.O.L., Pershing, D.W., Lee, J.W., and Glass, J.W., Pulverized Coal Combustion: NO_x Formation Mechanisms Under Fuel-Rich and Staged Combustion Conditions. *17th Symposium (International) on Combustion*, The Combustion Institute, pg. 77, 1979.

[209] Wendt, J.O.L., Fundamental Coal Combustion Mechanisms and Pollutant Formation in Furnaces. *Prog. Energy Combustion Science*, 6:201, 1980.

[210] Windig et al., *Anal. Chem.* 59:317, 1987

[211] Wormeck, J.J., *Computer Modeling of Turbulent Combustion in a Longwell Jet-Stirred Reactor.* PhD thesis, Dept. of Chemical Engineering, Washington State University, Pulman, WA, 1976.

[212] Zhang, Q.F., Shuen, J.S., Solomon, A.S.P., and Faeth, G.M., Structure of Ducted Particle-Laden Turbulent Jets. *AIAA Journal* 23:7, 1985.

END

DATE FILMED

11 / 26 / 90